Azimuthal Anisotropy Measurement of Neutral Pion and Inclusive Charge Hadron Production in Au+Au Collisions at $\sqrt{s_{NN}} = 62$ and 39 GeV

A Dissertation Presented

by

Xiaoyang Gong

to

The Graduate School

in Partial Fulfillment of the Requirements

for the Degree of

Doctor of Philosophy

in

Physics

Stony Brook University

December 2012

Stony Brook University

The Graduate School

Xiaoyang Gong

We, the dissertation committee for the above candidate for the Doctor of Philosophy degree, hereby recommend acceptance of this dissertation.

Roy Lacey – Dissertation Advisor
Professor, Department of Chemistry

Jiangyong Jia – Dissertation Advisor
Assistant Professor, Department of Chemistry

Dmitri Kharzeev – Dissertation Advisor
Professor, Department of Physics and Astronomy

Axel Drees – Chairperson of Defense
Professor, Department of Physics and Astronomy

Maria Victoria Fernandez-Serra
Assistant Professor, Department of Physics and Astronomy

Lijuan Ruan
Associate Physicist, Physics Department
Brookhaven National Lab

This dissertation is accepted by the Graduate School.

Charles Taber
Interim Dean of the Graduate School

Abstract of the Dissertation

Azimuthal Anisotropy Measurement of Neutral Pion and Inclusive Charge Hadron Production in Au+Au Collisions at $\sqrt{s_{NN}} = 62$ and 39 GeV

by

Xiaoyang Gong

Doctor of Philosophy

in

Physics

Stony Brook University

2012

The harmonic flow coefficients v_n with n=2,3,4 are measured for neutral pions and inclusive charged hadrons in Au-Au collisions at $\sqrt{s_{NN}} = 62$ and 39 GeV with the PHENIX detector at the Relativistic Heavy Ion Collider (RHIC). These v_n coefficients characterize the anisotropy of particle productions in the azimuth at different angular scale $(2\pi/n)$, which are sensitive to the transport properties and initial spatial asymmetries of the hot and dense medium created in these collisions. Significant values of v_n are observed for neutral pions (for $n = 2$) and inclusive charge hadron (for $n = 2, 3, 4$) at both collision energies, spanning broad ranges of transverse momentum p_T and collision centrality. These results are compared to measurements at other beam energies from RHIC, and to the recent results at $\sqrt{s_{NN}} = 2760$ GeV from the Large Hadron Collider (LHC). The magnitudes of the v_n are found to be similar over the range of $\sqrt{s_{NN}}$ =39-2760 GeV. However, the

v_2 values for inclusive charge hadron are found to decrease significantly for collisions at $\sqrt{s_{NN}} < 39$ GeV, and essentially reaches 0 at $\sqrt{s_{NN}} \approx 3$ GeV. These results provide important input for studying the transport properties and the initial geometry profiles of the hot and dense matter created in Au+Au collisions at $\sqrt{s_{NN}} = 62$ and 39 GeV. They also serve as important components in the beam energy scan of v_n, which might help locate the critical point of the QCD phase diagram.

Contents

List of Figures

List of Tables

Acknowledgements

I am deeply indebted to my advisors, Roy Lacey and Jiangyong Jia, who are always kind and patient. Without the guidance provided by them this dissertation work simply would not be possible. I would also like to thank the nuclear chemistry group at Stony Brook. Working with a group of smart young people makes the experience of the past four years quite enjoyable. I am lucky to be a member of the PHENIX collaboration. I learned how to work coordinately with others in a large project, and benefited greatly from the discussions in all the meetings and conferences. Last but not least, I am very grateful for the support from my family. They are the very reasons that keep me moving forward.

Abbreviations

ACC	Aerogel Cherenkov Counter
ALICE	A Large Ion Collider Experiment
ATLAS	A Toroidal LHC ApparatuS
ATP	Assembly Trigger Processor
AdS/CFT	Anti de Sitter/Conformal Field Theory
BBC	Beam-Beam Counter
BES	Beam Energy Scan
BNL	Brookhaven National Laboratory
CGC	Color Glass Condensate
CMS	Compact Muon Solenoid
CNT	Central Arm
DAQ	Data Acquisition
DC	Drift Chamber
DCM	Data Collection Module
DIS	Deep inelastic scattering
DST	Data Summary Tape
EC	Enhanced (event plane) Calibrator
EM	Electromagnetic
EMCal	Electromagnetic Calorimeter
EvB	Event Builder

FEE	Front-End Electronics
FEM	Front-End Modules
GeV	Giga-electronVolt
GL1	Global Level-1 (trigger)
GTM	Granule Timing Module
HPSS	High Performance Storage System
IR	Interaction Region
LHC	Large Hadron Collider
LL1	Local Level-1 (trigger)
MB, MiniBias	Minimum Bias
MC	Monte Carlo (simulation)
MIP	Minimum Ionizing Particle
MPC	Muon Piston Calorimeter
MTM	Master Timing Module
NBD	Negative Binomial Distribution
NDF	Number of Degree of Freedom
NSF	Network Storage System
OC	Official (event plane) Calibrator
PC	Pad Chamber
PHENIX	Pioneering High-Energy Nuclear Interaction eXperiment
PID	Particle Identification
PMT	Photomultiplier Tube
PRDF	PHENIX Raw Data Format
PbGl	Pb (lead) Glass
PbSc	Pb (lead) Scintillator
QA	Quality Assurance
QCD	Quantum Chromodynamics

QGP	Quark Gluon Plasma
RCF	RHIC Computing Facility
RHIC	Relativistic Heavy Ion Collider
RICH	Ring Imaging Cherenkov detector
RXI, RXN_i	inner ring of RXN
RXN, RxNP	Reaction Plane detector
RXO, RXN_o	outer ring of RXN
Run10	RHIC run in the 2009-2010 period
SEB	Sub Event Buffer
STAR	Solenoidal Tracker At RHIC
TOF	Time Of Flight
ZDC	Zero Degree Calorimeter
pQCD	perturbative QCD

For detectors with south and north component (denoted by "DET", such as BBC, MPC and RXN), "DETs" and "DETn" refers to the south and north component of the detector.

Notations

p_T	transverse momentum
v_n	n-th order Fourier coefficients, cf. Eqn-1.2, Eqn-1.3
v_n^{raw}	measured n-th order Fourier coefficients, cf. Eqn-3.10
$\text{Res}\{\Phi_n\}$	event plane resolution factors, cf. Eqn-3.10
ϵ_n	n-th order eccentricity, cf. Eqn-1.1
Ψ_n	n-th order event plane
Φ_n	n-th order measured event plane
$\sqrt{s_{NN}}$	center of mass energy per nucleon-nucleon collision
N_{part}	number of participating nucleons
N_{coll}	number of binary collisions
R_{AA}	nuclear modification factor, cf. Eqn-1.7
Au, Cu, Pb	gold, copper, lead
p, d	proton, deuteron
$\pi^{\pm}, K^{\pm}, \bar{p}$	charged pions, kaons, anti-proton
π^0, K_S^0, K_L^0	neutral pions and kaons (Short and Long states)
X_0	radiation length
c	speed of light
u_B	baryon chemical potential
m_T, KE_T	transversal kinetic energy, $\sqrt{m_0^2 + p_T^2} - m_0$
T_C	critical temperature

Chapter 1

Introduction

1.1 Quantum Chromodynamics

The advance of science is driven by the pursuit of answers to several fundamental questions, one of which is what are the basic constituents of matter and how they interact among themselves. The early attempt to answer this question can be traced back to ancient Greece; Empedocles established four ultimate elements, which are later developed by Aristotle to five. By the early 19th century, the concept and existence of a molecule had been widely accepted. The scientific theory of atoms were then developed and summarized by Mendeleev in his famous periodic table in 1869. At the end of 19th century (1896), the discovery of radioactivity, which suggested a sub-structure of atoms, marked the beginning of the revolutionary development of modern science. Scientists have discovered that within each atom, there is a core called the "nucleus" occupying only $\sim 1/10^{15}$ of the space of the atom while accounting for more than 99.9% of its mass. A nucleus consists of one or more "nucleons" that are identified as "protons" with positive charge and "neutrons" with zero net charge. However, nucleons are still not indivisible. In 1968, crucial evidence was provide by the Deep Inelastic Scattering (DIS) experiment at the Stanford Linear Accelerator Center (SLAC) [1] [2] in support of the conjectured "quark" model first proposed by Murray Gell-Mann [3] and George Zweig [4] [5].

Quarks carry a "color" quantum number and the interactions among quarks are described by Quantum Chromodynamics (QCD), a $SU(3)$ gauge theory; the gauge bosons in the theory are called "gluons". Quarks and gluons could be collectively referred to as "partons". Particles that appear to be composed of three quarks are referred to as "baryons", e.g. nucleons mentioned above, while another kind of particles that seem to consist of a pair of quark and anti-quark are referred to as "mesons". The set of particles containing both baryons

and mesons are called "hadrons". To date, there are 6 "flavors" of quarks: "up","down","charm", "strange","top" and "bottom". An illustration of the sub-atomic structure discussed above is demonstrated in Fig-1.1.

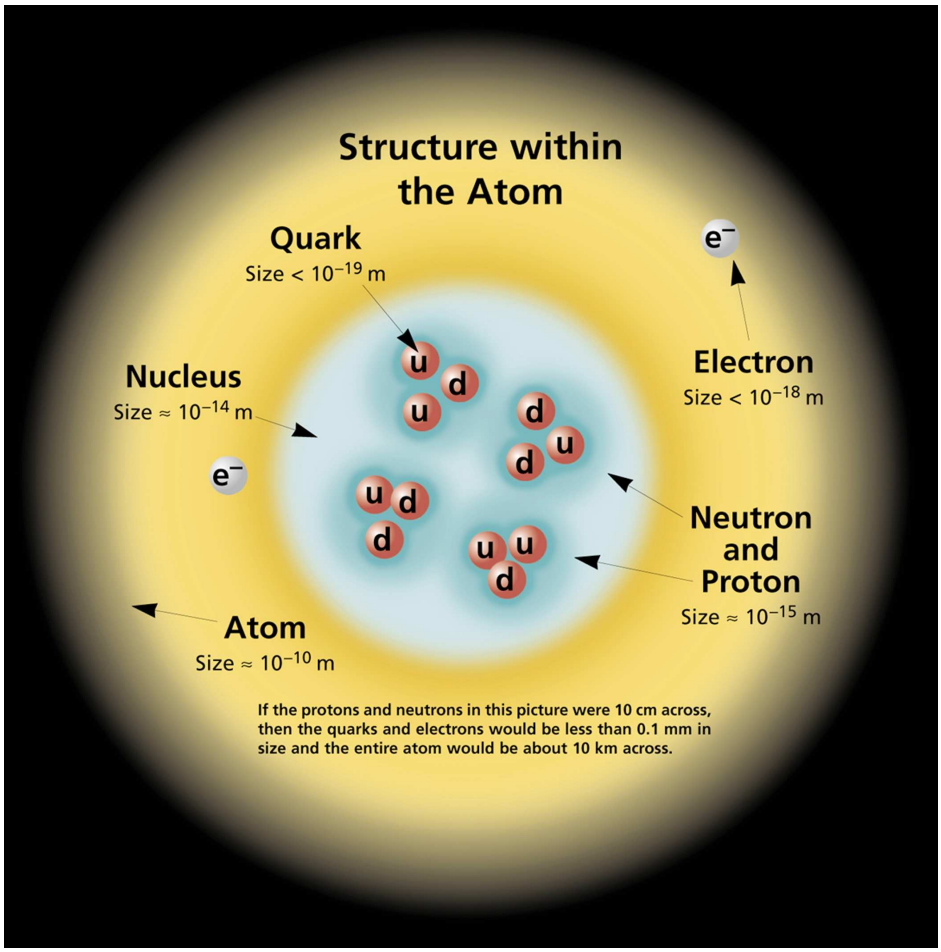

Figure 1.1: Structure within the atom (CPEP[1]).

1.1.1 Asymptotic Freedom

The coefficient characterizing the strength of QCD interactions is not a constant. This "running coupling coefficient" α_s is weaker at high energy scales and becomes stronger at the other end, a phenomenon commonly referred as "Asymptotic Freedom" [6] [7]. According to the wave-particle duality, larger energy scale corresponds to shorter distance and finer structure. Therefore,

[1]http://www.cpepphysics.org/

the asymptotic freedom feature of QCD dictates an anti-screening behavior of interactions among quarks, i.e. the further two quarks are apart, the stronger the interaction between them becomes.

Measurements of α_s at different energy scales are summarized as data points in Fig-1.2. QCD calculations are also shown and denoted by the yellow

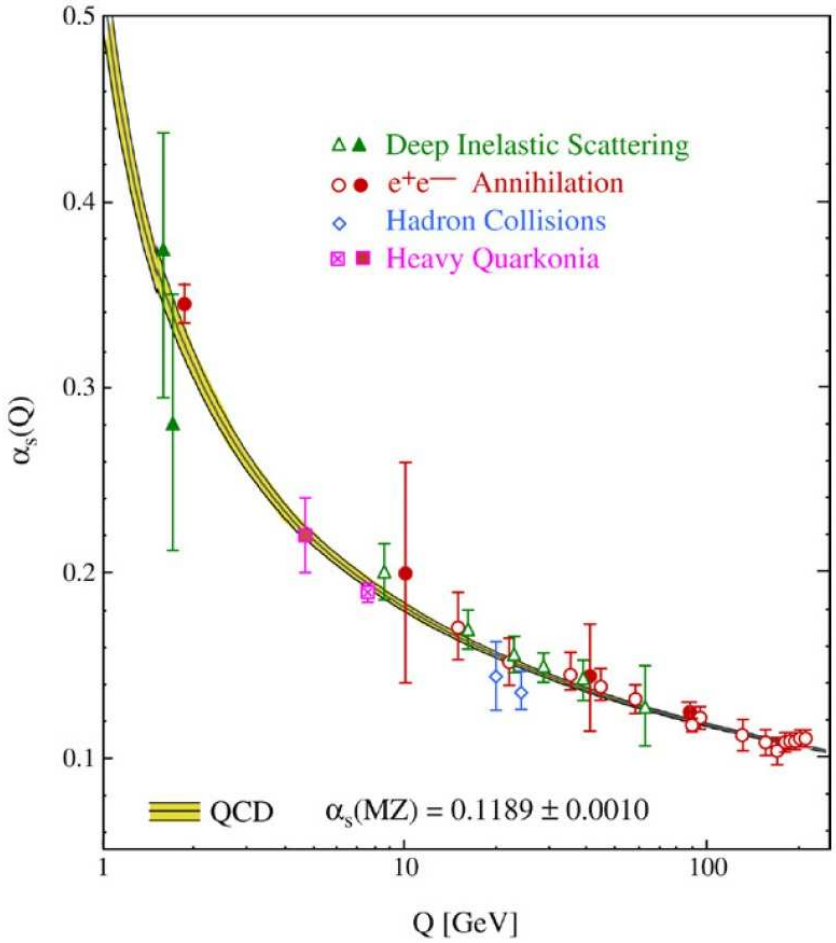

Figure 1.2: Summary of $\alpha_s(Q)$ measurements as a function of energy scale Q [8]. The Open an d filled symbols represent (resummed) NLO, and NNLO QCD calculations respectively.

band, which match experimental results very well. When Q (the momentum exchange in the reaction, indicating the energy scale) is increased by two orders of magnitude, corresponding α_s decreases by a factor of 5.

1.1.2 QCD in Practice

Calculations in particle physics are normally carried out in the perturbative approach: the target variable (e.g. total cross section of a certain reaction) is expanded with respect to orders of the coupling constant. If the coupling constant is a small number, the significance of higher order terms in the expansion is dampened quickly and the summation of the expansion could be performed to just the first few leading orders. In this case, the calculation is greatly simplified.

The above reasoning applies to QCD calculations at high energy scales, such as the hard scattering among partons. However, in experiment partons scatter and move apart and the interactions among them grow large; when the interaction energy exceeds a certain threshold, hadrons are produced. Eventually, these hadrons are measured and analyzed by the experimentalists. Since the interactions are strong, the hadronization process can not be handled in the perturbative approach. To tackle this issue, factorization schemes [9] are proposed to separate the hard and soft part of the process. The hard scattering is handled by perturbative QCD and the hadronization is characterized by a set of particle distribution functions and measured in various experiments. This framework has proven to work well and has been adopted in theoretical derivations and simulation packages for nuclear reactions.

A primary non-perturbative treatment of QCD is referred to as lattice QCD, which is essentially a finite difference method. As the name suggests, space-time is discretized into a lattice and the dynamic evolution of nuclear matter is simulated on this grid. Numerical recipes and super-computers are employed for this computationally intensive analysis; however, at the current level of technology the application of lattice QCD is restricted to relatively small systems, such as the individual hadrons [10]. To describe QCD interactions within larger systems, phenomenological models have been devised. Several applications of these models are presented in later sections (see for example, Sec-1.8.3).

1.2 QCD Phase Diagram

Like other substances, nuclear matter exists in several different states, the properties of which are governed by QCD interactions. Fig-1.3 shows the schematic phase diagram for nuclear matter. The vertical axis represents temperature (T) that is closely related to energy density (ϵ). The horizontal axis represents baryon chemical potential (μ_B), which reflects the net baryon (number of quarks offset by number of anti-quarks) density of the matter. The anti-

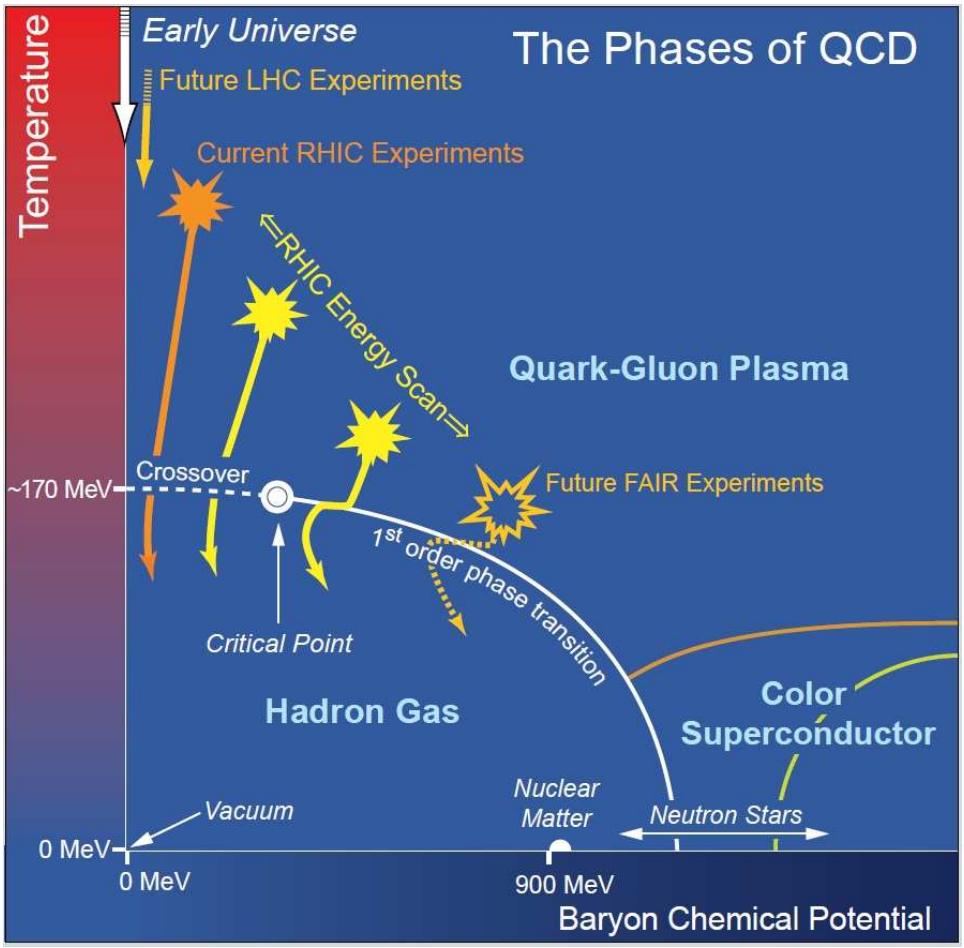

Figure 1.3: Schematic QCD phase diagram for nuclear matter [11]. The solid lines show the phase boundaries for the indicated phases. The solid circle depicts the critical point. Possible trajectories for systems created in the QGP phase at different accelerator facilities are also shown.

screening feature of QCD interaction suggests that when T (thus ϵ) is small, α_s is large and quarks are bound together within short distances. In fact, at low temperature (not really "low" compared to typical daily temperature, 1 MeV corresponds to roughly 10^{10} K), quarks and gluons are always packaged inside the hadrons, a phenomenon called "confinement". This state of nuclear matter could be best described as hadron gas, indicated on the phase diagram in the lower left region.

If atoms are compressed sufficiently (e.g. in the gravitational collapse of stars where electrons outside the nuclei are pushed into the nucleus so that protons are transformed into neutrons), another state of nuclear matter is formed, which typically exists in the core of neutron stars. This high μ_B low T state is located in the lower right corner of the phase diagram, the structure of which is mostly conjectured.

On the other hand, if nuclear matter is heated up, as in the case of various high energy nuclei scattering experiments, asymptotic freedom suggests that the coupling constant α_s would become small enough to allow a deconfined state of nuclear matter. In such a state, nuclei would melt down to a plasma of free (deconfined) quarks and gluons, or Quark Gluon Plasma (QGP) [12]. It is predicted that the universe was in the QGP state within several microseconds after the "big bang". By creating "little bangs", a nickname for relativistic heavy ion collisions, QGP can be produced on earth and is the main subject of current nuclear physics research. Several experimental signatures for the QGP are discussed in Sec. 1.6 - 1.8.

In analogy to the phase diagrams for other substances (such as water), the QCD phase diagram is characterized by its critical point and phase boundaries. Lattice QCD simulations suggested a critical temperature of $T_C \approx 170$ MeV that corresponds to an energy density of $\epsilon \approx 1$ GeV/fm^3 [13]. As depicted on Fig-1.4, the number of degrees of freedom (NDF) increase significantly as the temperature crosses T_C and quickly reaches a constant level, indicating the deconfinement of partons and a phase transition. In the small μ_B region, lattice QCD calculations have shown that the transition from QGP phase to hadron gas phase is a crossover transition [15], illustrated by the dashed line on Fig-1.3; on the other side of the critical point (region with large μ_B), a first order phase transition is expected. The desire to map out the precise locations of these "landmarks" (critical point and phase boundaries) of the QCD phase diagram is a central objective in nuclear physics.

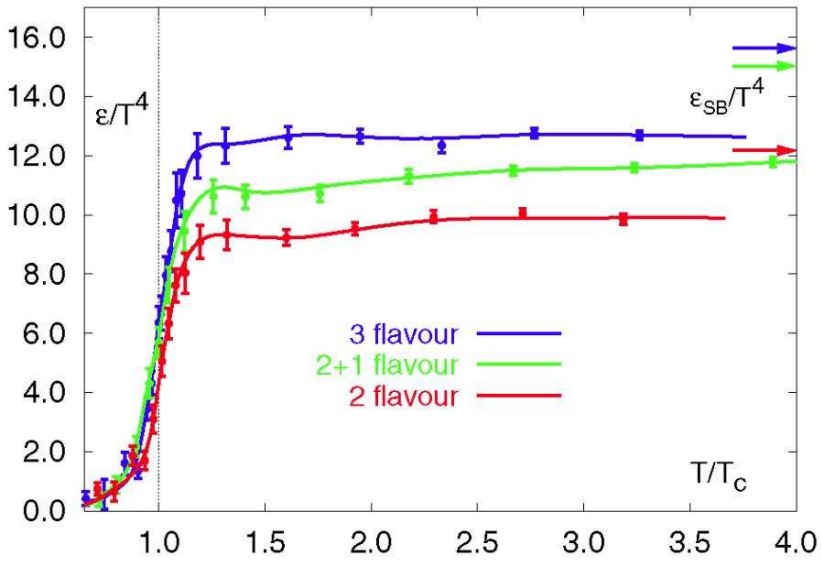

Figure 1.4: Increase of NDF at $\sim T_C$ predicted by lattice QCD [14]. ϵ/T^4 (proportional to NDF) is plotted against T/T_C, where T_C is the critical temperature. The increasing number of flavors indicates the role of strange quarks in the computation. The arrows on the right indicate the Stefan-Boltzmann limit.

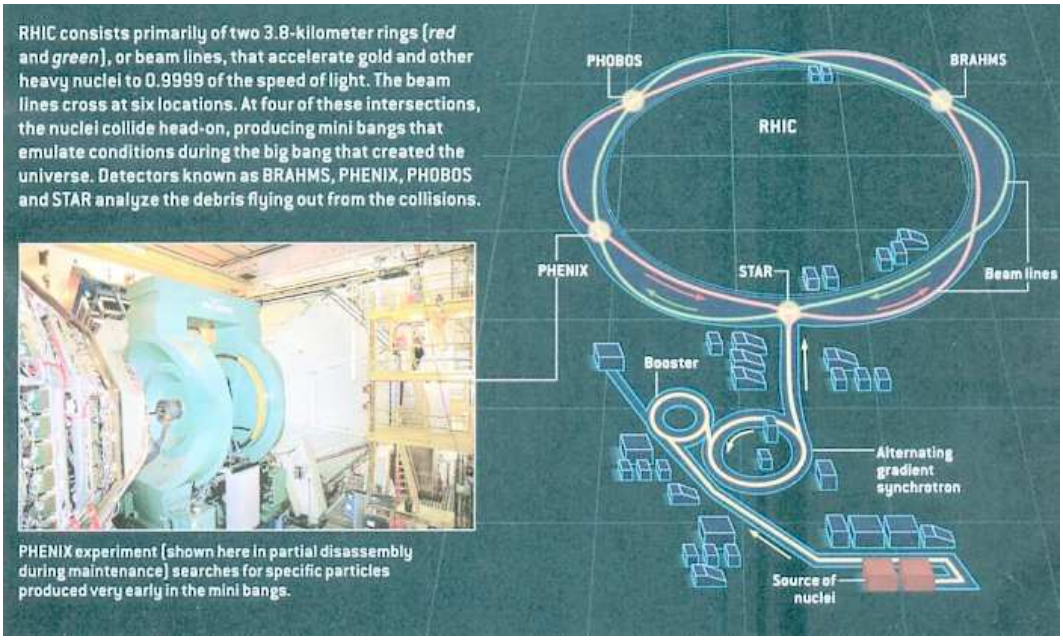

Figure 1.5: RHIC and PHENIX

1.3 RHIC and PHENIX

RHIC stands for Relativistic Heavy Ion Collider. It's located in the Brookhaven National Laboratory (BNL) and serves as one of major facilities for experimental nuclear physics. Nuclei are accelerated to ultra-relativistic speed ($\gamma \sim 100$) and guided to collide head on; the large energy density produced in these collisions is expected to lead to creation of a QGP.

Four detectors were built to collect the collision products, which are typically thousands of particles; they are PHENIX, STAR, PHOBOS and BRAHMS. This thesis study is carried out at PHENIX, which stands for the Pioneering High Energy Nuclear Interaction eXperiment and refers to both the detector and the collaboration of scientists working on the detector. A detailed presentation of the PHENIX detector is given in Chapter-2.

RHIC is a versatile collider. Up to date a good variety of particle species have been accelerated and collided, including Au+Au, p+p, Cu+Cu and d+Au. These nuclei are boosted to various kinetic energies; the center of mass energy per nucleon pair $\sqrt{s_{NN}}$ ranges from 7.7 GeV to 500 GeV. Note that in this thesis natural units are used, which means GeV, GeV/c and GeV/c^2 are used interchangeably (c denote speed of light). This kind of versatility is crucial for experimental nuclear physics. As illustrated on Fig-1.3, RHIC could perform a beam energy scan over a wide region on the QCD phase diagram. Therefore, the machine has the capability to perform experiments which could serve to map out the critical point and phase boundaries.

It's noteworthy that RHIC is the only collider that is able to perform polarized p+p collisions. This unique capability allows experiments on RHIC to explore the origin of nucleon spin. This aspect is not discussed in this dissertation.

1.4 Heavy Ion Collisions

Nuclear matter created in heavy ion collision is encoded with a non-trivial initial geometry profile, which is carried through in the evolution of nuclear matter and eventually reflected in the final state particle distributions. A brief description of the collision geometry and the time-line of heavy ion collision is provided below.

1.4.1 Collision Geometry

The geometry of heavy ion collision is rather complicated, compared to p+p or $e^+ + e^-$ collisions. A general illustration of the collision geometry is given in

Fig-1.6. The parts of the nuclei participating in the collision are marked with

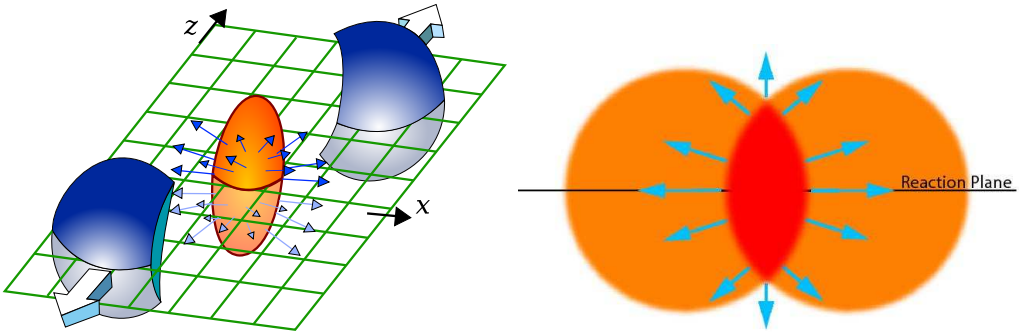

Figure 1.6: Geometry of heavy ion collision. Left Panel: spectators and the collision zone shown with the reaction plane. Right Panel: beam view of the collision in the transverse plane.

denser colors, and there are two "spectators" that are not directly involved in the collision. The beam direction naturally defines the z-axis. Together with the line interval connecting the centers of the two nuclei, a unique plane commonly referred to as the "reaction plane" (RP) is determined. As the two nuclei move, the line interval will be perpendicular to the z-axis at a particular time, referred to as the "crossing time". The length of the line interval at the crossing time is defined as the "impact parameter" (b). It has a smaller value when the two nuclei have a larger overlapping region in the collision. The other plane that is used frequently, the "transverse plane" (TP), is defined to be perpendicular to the z-axis and contains the two nuclei centers at the crossing time.

There is another variable, "centrality", that is commonly used to reflect b and the size of the collision zone. Centrality can be expressed as a percentage: 0% centrality corresponds to $b = 0$ and the largest possible overlapping region, while 100% centrality means the two nuclei touch each other tangentially and b roughly equals to the sum of the radii of the colliding nuclei. Collisions are often categorized as central, mid-central and peripheral; they have small, mediocre and large centrality values correspondingly. The rigorous process of centrality definition based on experimental observables are discussed in Sec-3.3.

Other than its size, the collision zone is also characterized by its shape, which roughly resembles an "almond" as illustrated in Fig-1.6. The almond shape could be quantified by the second order eccentricity, defined in Eqn-1.1. However, it turns out that there are significant fluctuations superimposed on the almond shape and more detailed treatment is necessary (cf. Sec-1.6). A

thorough understanding of the initial geometry proves to be crucial for many heavy ion analyses.

In most cases cylindrical coordinates are employed to describe the spacial information in heavy ion collision. The z-axis is taken as defined above. The azimuthal angle ϕ is defined relative to a certain direction (in which $\phi = 0$) in the lab reference frame. The θ angle is rarely used; instead, it's represented by pseudorapidity η that is defined as $\eta = -\ln[\tan(\frac{\theta}{2})]$.

1.4.2 Evolution of Heavy Ion Collisions

The evolution of heavy ion collisions can be divided into several stages, which are illustrated in Fig-1.7. Although much interest is focused on the QGP

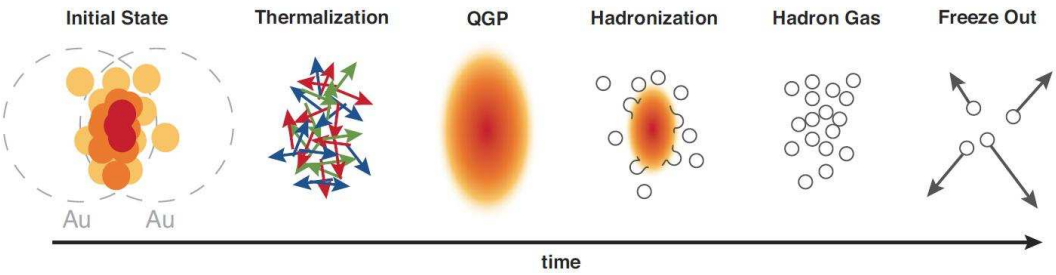

Figure 1.7: Schematic illustration of the evolution of nuclear matter created in heavy ion collisions [16]

stage, what are actually measured are the final collision products of outgoing particles. Therefore to extract information on QGP based on experimental measurements, the three stages after the generation of QGP need to be understood. On the other hand, the initial condition of the nuclear matter serves as an input to model calculations at the QGP stage. As a result, the two stages that precede the QGP stage must be carefully modeled as well.

A brief discussion of each stage is given below. Since physics observables and models have not yet been introduced, the discussion is schematic.

- Initial state: in relativistic heavy ion collisions, incoming nuclei appear to be "pancakes" in the lab frame. Their longitudinal size is contracted by the γ factor, which is around 100 for $\sqrt{s_{NN}} = 200$ GeV collisions. Participating nucleons scatter, generating entropy and producing a nuclear matter with high but non-uniform energy density. The initial geometry profile is determined at this stage. There are two prevailing models that handle initial geometry, Glauber [17] and Color Color Condensate (CGC) [18] [19]; they are discussed briefly in Sec-1.6.2. Important variables characterizing this stage include number of participant nucleons

N_{part}, the number of binary collisions between nucleons N_{coll}, the impact parameter b and eccentricity (cf. Eqn-1.1).

- Thermalization: partons interact among themselves and the system approaches thermal equilibrium. The thermalization time is denoted by τ_0. Hydrodynamics calculations suggest $\tau_0 \leq 1$ fm/c [20], which indicates a surprisingly rapid thermalization.

- QGP: the dense and equilibrated QGP is formed, which continues to expand and cools down.

- Hadronization: the energy density and temperature of the bulk keeps decreasing to a point that the interactions among partons are sufficiently strong to confine the partons into the bound state, i.e. hadrons. A mechanism called "recombination" or "coalescence" is employed to describe this process [21]. Energetic partons might hadronize via "fragmentation", a different scheme that explains the formation of hadron jets. Note that the fragmentation mechanism is first employed to describe jet formation in the collisions of elementary particles where no medium is created (i.e. "vacuum"). In heavy ion collisions, vacuum fragmentation functions are modified by QGP [22].

- Hadron gas: this stage might exist for a brief time. Hadrons are weakly coupled and still exhibit collective behavior. The whole system is still in equilibrium. Due to the relatively weak interactions among hadrons, the system resembles a dilute gas and is best described by transport models such as the Ultrarelativistic Quantum Molecular Dynamics model (UrQMD) [23] [24]. Since information extracted from experiments contains contributions from both hadron gas and QGP, the properties of the hadron gas (e.g. its viscosity) must be understood to enable an isolated treatment of the properties of QGP. Recent studies seem to suggest that the lifetime of this stage is so small that its influence is very limited [25].

- Freeze-out: as the system continues to expand and become dilute, its local thermal equilibrium becomes unsustainable and hadrons eventually stop acting collectively. Interactions among hadrons become even weaker and the typical mean free path of hadrons becomes comparable to the size of the system. The freeze-out process is normally handled by the Cooper-Fyre framework [26] [27].

Our focus is placed on the QGP stage, the measurement of which is discussed in the following sections.

1.5 Probing the QGP: an Overview

The properties of the QGP can not be measured directly. Instead, they are inferred from experimental observables. To be more specific, the properties of the QGP are encoded in phenomenological models based on first principles, such as QCD. The models are then tuned to interpret experimental observations, in which process the properties of QGP are extracted as model parameters. Therefore, two components are crucial:

- precise measurement of physics observables, and
- reliable phenomenological modeling of the observable.

This thesis study is more oriented to the, i.e. experimental measurements.

Experimental observables are normally designed in a way that they are sensitive to a particular aspect of the evolution of the QGP. Several well-established observables are introduced in the sections that follow. But before we check them one-by-one, there are some common features that hold true for all observables, which are discussed below.

- Centrality dependence of the observable: experimentally, centrality is built from multiplicity, i.e. the number of particles created in a collision. However, what's more important is that it is also related to the collision geometry. Events with smaller centrality values are more isotropic in azimuth (cf. Fig-1.6). Alternatively, centralities are characterized as N_{part} and N_{coll}; relations between these variables are illustrated in Fig-3.2 and Fig-3.3.

- p_T dependence of the observable: particles created and measured at RHIC normally have the p_T scale of GeV. High p_T particles ($p_T > 6$ GeV) result from energetic partons, which interact relatively weakly with the QGP medium and result in jets (cf. Sec-1.7.2). Low p_T particles ($p_T < 2$ GeV) are produced by the QGP bulk medium. Consequently, several properties of the QGP such as the partonic level collectivity, temperature and viscosity are encoded in these particles.

- particle species: the most common measurable particles are hadrons. Neutral hadrons such as the π^0 and η are constructed from their decay products of photon pairs (cf. Sec-4.1.1). Charge hadrons can be measured inclusively, i.e. without differentiating between particle species. These measurements have the best statistics and relatively high p_T reach (cf. Sec-5.1). Charge hadrons can also be identified and measured separately, but due to the acceptance limitation of the detectors responsible

for particle identification, the statistics are far less. There are important benefits. The quark content dependence of reaction dynamics is studied by these measurements. In addition, there are particles that do not participate in the strong interactions with the QGP medium, such as direct photons and electrons. They carry information on various stages of the heavy ion collisions and leave the collision zone freely, which means very little distortion on the carried information. These particles are ideal probes of the QGP; however their measurement are very difficult due to the large decay background from various meson and conversion background generated on detector hardware.

In the following sections, several observables that are more relevant to this thesis are introduced and the insights on QGP gained from their measurements are discussed.

1.6 v_n Measurement ($n = 2, 3, 4 \ldots$)

This dissertation is essentially about v_n measurement. Current results of v_n obtained from various experiments are compiled in this section. It is the significant impact of v_n measurement toward our understanding of the QGP that motivates this dissertation study.

1.6.1 The Origin of v_n

The non-trivial initial geometry of the collision zone (Fig-1.6) leads to an azimuthal anisotropy in the profile of the produced particles. If we describe the geometry of the collision zone as an ellipse, then in its short axis direction the pressure gradient is larger, compared to the one in long axis direction. Larger pressure gradients result in larger momentum for the outgoing particles. In this way, the spacial anisotropy in the initial collision geometry is transformed to the anisotropy in the momentum space of the outgoing particles.

If the collision zone is of a perfect elliptical shape, the anisotropy is 2nd order, as the geometry possesses a π rotational symmetry, $f(x) = f(x + \pi)$. While the assumption holds true for an average geometry sampled over many events with the same centrality range, simulations have shown that event-wise there could be a large deviation from this picture. Fig-1.8 shows a participant profile with a triangular shape, indicating a large third order Fourier component of the geometry.

Components of other orders exist too. To quantify the anisotropy, we define

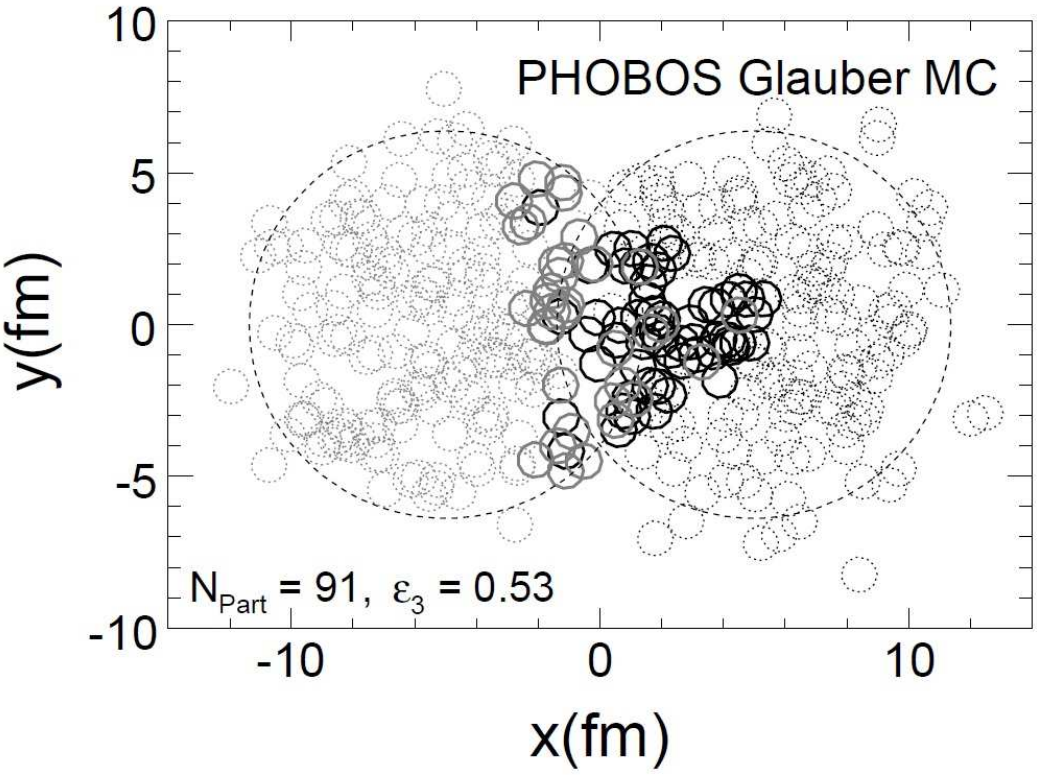

Figure 1.8: Distribution of nucleons showing an initial geometry with third order component [28]. The event is simulated with Glauber Monte Carlo for Au+Au collisions at $\sqrt{s_{NN}}$ = 200 GeV. Participant nucleons are plotted as solid circles and spectator nucleons are indicated by dotted circles.

the n-th order participant "eccentricity" as follows [28]:

$$\epsilon_n = \frac{\sqrt{\langle r^2 \cos(n \cdot \phi_{\text{part}})\rangle^2 + \langle r^2 \sin(n \cdot \phi_{\text{part}})\rangle^2}}{\langle r^2 \rangle} \tag{1.1}$$

assuming that $\langle x \rangle = \langle y \rangle = 0$. r and ϕ_{part} are the polar coordinates of participating nucleons, over which the average $\langle\ \rangle$ is taken. A larger ϵ_n indicates a more prominent n-th order component in the profile, e.g. the one shown in Fig-1.8 has $\epsilon_3 = 0.53$.

The eccentricities in the initial geometry profile would eventually evolve to azimuthal anisotropy for the collision products. A Fourier expansion is routinely employed to analyze this final state anisotropy and the Fourier coefficients v_n are experimental observables and defined as:

$$\frac{\mathrm{d}N}{\mathrm{d}\phi} \propto 1 + \sum_{n=1} 2v_n \cos[n(\phi - \Psi_n)] \tag{1.2}$$

where ϕ denotes azimuthal angles for produced particles and N is the number of particles. Ψ_n is the phase angle of the n-th order term and normally referred to as participant event plane. Since components of different orders in a Fourier expansion are orthogonal, v_n could be conveniently computed as:

$$v_n = \langle \cos[n(\phi - \Psi_n)] \rangle \tag{1.3}$$

where $\langle\ \rangle$ denotes average over particles and events.

1.6.2 QGP as a Perfect Fluid

v_2 is the dominant component of the v_n spectrum in mid-central and peripheral collisions and has been measured prior to the RHIC era. v_2 results of inclusive charge hadrons measured in Au+Au collisions at $\sqrt{s_{NN}} = 200$ GeV by PHENIX is depicted in Fig-1.9. It shows that, for very low p_T v_2 for different centralities doesn't differ, as p_T increases the spreads among v_2 values become larger, consistent with the pressure gradient argument mentioned above. For all centralities, v_2 increases with p_T until some point around 2.5 GeV. v_2 decrease with N_{part}, similar to the 2nd order eccentricity which becomes smaller in central collision.

In the low p_T region, the v_2 values are described well by relativistic hydrodynamic modeling of the QGP. In fact, it was initially modeled as a perfect fluid [30] [31] [32]. Ideal Hydrodynamic calculations, as shown on Fig-1.10, could reproduce results of v_2 measurement well, though subject to the vari-

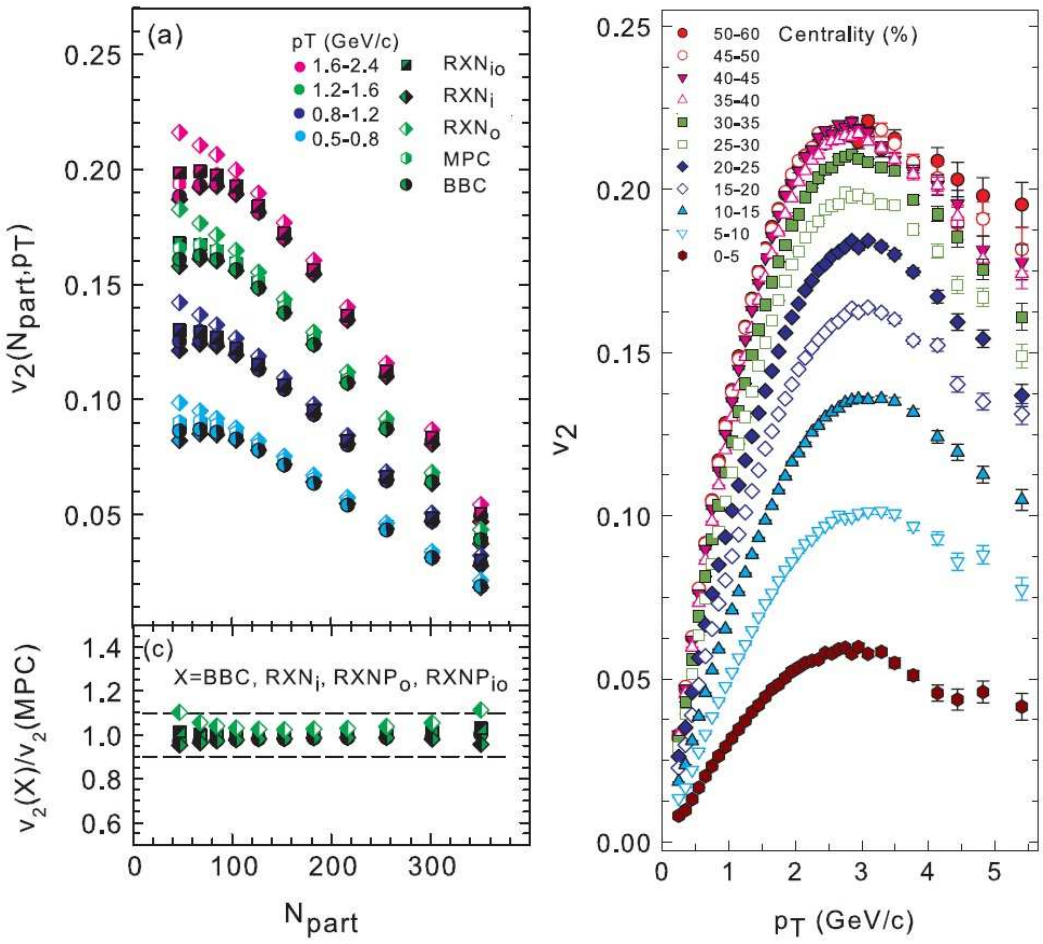

Figure 1.9: v_2 results for Au+Au collisions at $\sqrt{s_{NN}} = 200$ GeV by PHENIX [29]. Left panel: v_2 vs. $N_{\rm part}$ for several p_T selections with Φ_2 constructed with different detectors; the lower panel shows that measurements with different event plane detectors are very consistent. Right panel: v_2 vs. p_T for several centrality selections.

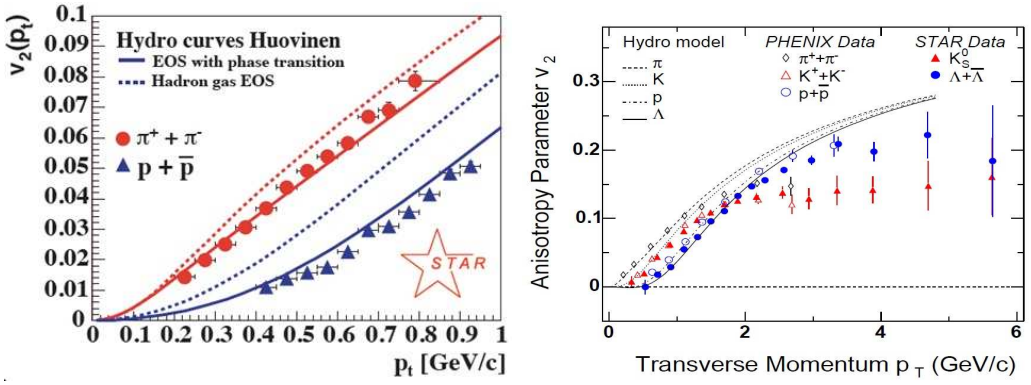

Figure 1.10: v_2 vs. p_T with hydrodynamic model fit [31] [32]. Results are for Au+Au collisions at $\sqrt{s_{NN}} = 130$ GeV (left) and 200 GeV (right); theory curves are from [33] (left) and [34] (right).

ations in the modeling of initial geometry and the equation of state (EOS). This discovery that the QGP is a near perfect fluid, made it an interesting subject that drew much attention from a broader physics community.

A key variable characterizing a property of fluids is the shear viscosity η. Since a dimensionless parameter is usually desired and particle number is not a well-defined quantity for the QGP, the specific shear viscosity is defined as η/s where s is the entropy density. Based on the AdS/CFT duality [35], a conjectured lower bound for η/s of $1/4\pi \approx 0.08$ applys to all relativistic quantum field theories at finite temperature and zero chemical potential [36]. This lower bound suggests that the QGP can not be a perfect fluid with zero viscosity. The question of how the specific viscosity of the QGP approaches this lower limit is an interesting topic that motivates scientists from both the theoretical and experimental communities. To dates, there have been several efforts to extract the specific viscosity for the QGP [37] [38] [39] [40].

One such model calculation is shown in Fig-1.11. It shows that, while model fittings suggest similar η/s values with PHOBOS v_2 and STAR non-flow corrected v_2 values, there is a large uncertainty associated with the initial geometry. η/s values with initial geometry modeled by CGC is twice as large as those with Glauber geometry. The reason is that the CGC model gives a larger eccentricity for the initial geometry profile and thus requires greater viscosity to reproduce the anisotropy of particle production. Calculations of eccentricity in both the Glauber and CGC model framework is documented in [38]. It is noteworthy that η/s values obtained with Glauber geometry are quite close to the conjectured lower bound.

There are other sources of uncertainty in the extraction of η/s, such as

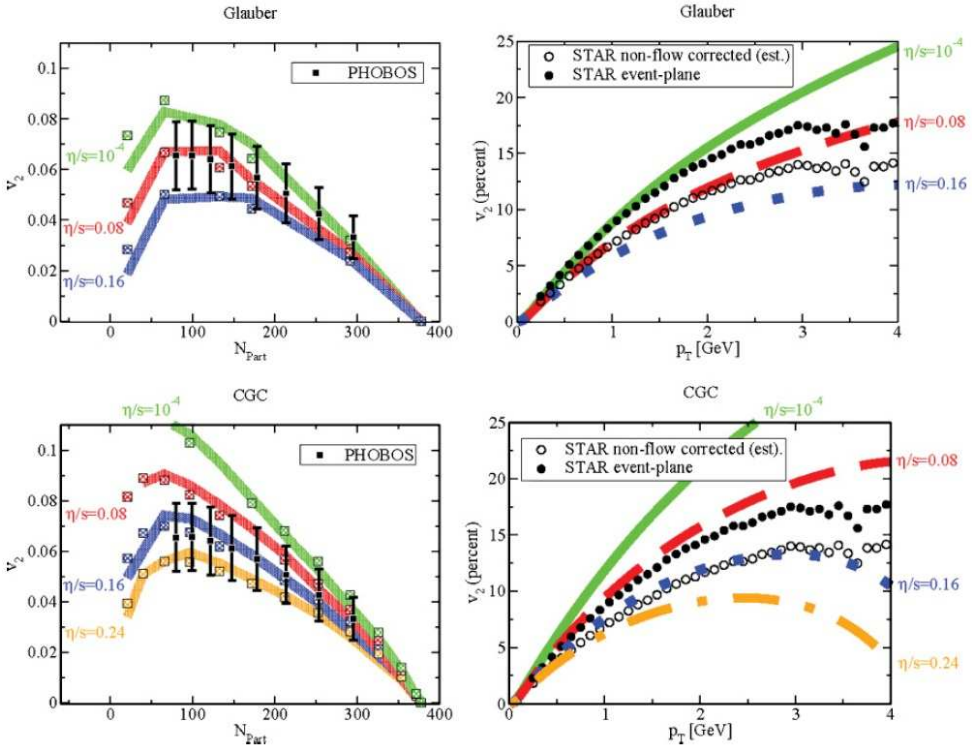

Figure 1.11: v_2 vs. p_T and v_2 vs. $N_{\rm part}$, fit by hydrodynamic calculations with different specific viscosity values. The initial geometry is modeled with Glauber or CGC models [38]. Data points are from the PHOBOS and STAR experiments for Au+Au collisions at $\sqrt{s_{NN}} = 200$ GeV. The errors bars for the PHOBOS data include 90% confidence level systematic uncertainties.

the uncertainty of the EOS [41] that can by seen on Fig-1.10. However, the dominant source is linked to the initial geometry. As we will see, higher order v_n ($n > 2$) values have very strong constraining power on the initial geometry.

1.6.3 Partonic Collectivity

v_2 measurements of identified hadrons exhibit interesting scaling properties that provide additional insights to the understanding of QGP. v_2 vs. p_T for several hadron species are plotted in panel (a) of Fig-1.12. At low p_T ($p_T < 2$

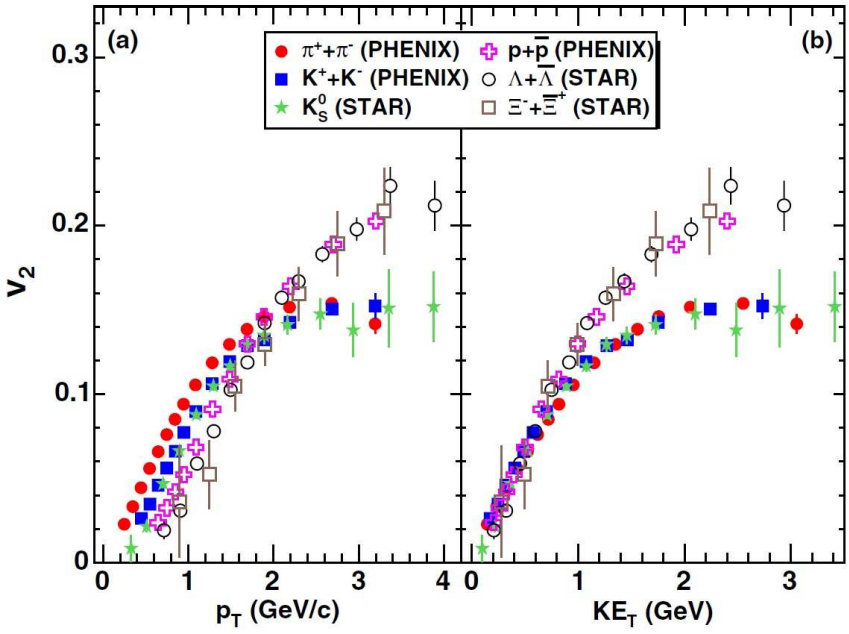

Figure 1.12: (a) v_2 vs. p_T and (b) v_2 vs. KE_T for several identified hadron species [42]. These results were obtained by the PHENIX and STAR experiments for Au+Au collisions at $\sqrt{s_{NN}} = 200$ GeV.

GeV) where hydrodynamics applies, the v_2 values show a clear mass ordering, i.e. heavy hadrons have smaller v_2. In the intermediate p_T range ($2 \sim 4$ GeV, mass ordering is broken and v_2 values for baryons are consistently higher than those for mesons, implying a strong quark content influence.

It is suggested [43] that if v_2 is indeed driven by a hydrodynamic pressure gradient, the v_2 values for different particle species would scale with transverse kinetic energy KE_T, which is defined as $\sqrt{p_T^2 + m^2} - m$ (m for hadron mass). In panel (b) of Fig-1.12, this scaling is clearly shown for $\mathrm{KE}_T < 1$ GeV. It is referred to as "mass scaling" and serves as evidence in support of the

hydrodynamic description of the QGP at low p_T. For $\mathrm{KE}_T > 1$ GeV region, v_2 values exhibit scaling features for baryons and mesons separately.

If the number of valence quarks n_q for each hadron species is taken into account, as in the v_2/n_q vs. KE_T/n_q plot shown on panel (b) of Fig-1.13, an excellent scaling is achieved for the whole KE_T range. This observation,

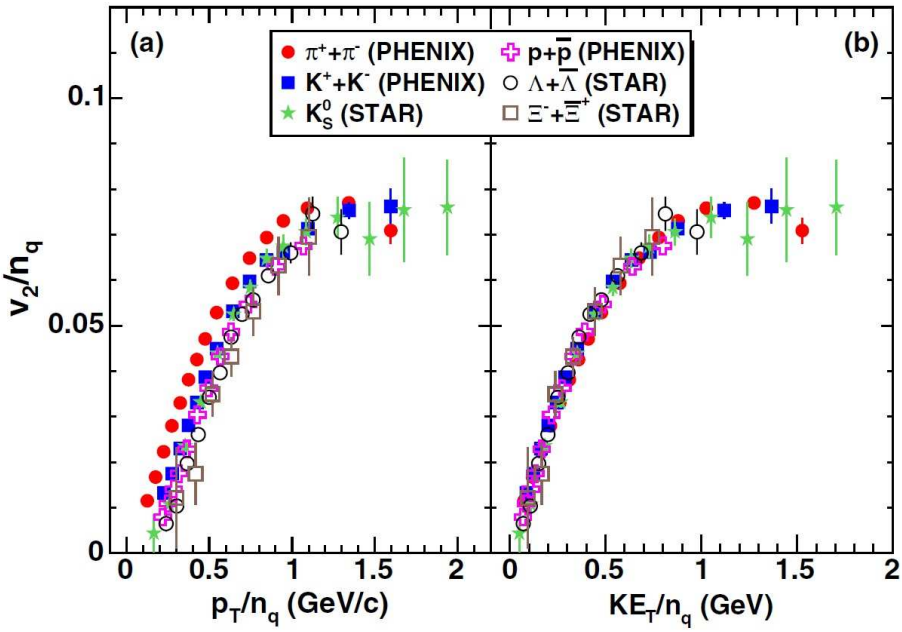

Figure 1.13: (a) v_2/n_q vs. p_T/n_q and (b) v_2/n_q vs. KE_T/n_q for several identified hadron species [42]. A re-compilation of data shown in Fig-1.12.

referred to as "n_q scaling", supports the following two arguments:

1. the degrees of freedom in the flowing QGP are built-up in the early stage of the collision, i.e. the partonic stage;

2. soft hadrons are created via a coalescence (or recombination) mechanism up to intermediate p_T (< 4 GeV) [43] [44] [45] [46].

As technology advances [47] [48], the timing resolution of newly built detectors can be improved. Accordingly, the particle identification capability of both PHENIX and STAR has been enhanced, especially for high p_T particles. Therefore, it became possible to test n_q scaling at even higher p_T. In Fig-1.14, v_2/n_q vs. KE_T/n_q for several hadron species are presented with a high KE_T/n_q reach up to 3 GeV. Panel (a) shows that n_q scaling still roughly holds in the most central $(0-10\%)$ collisions. However in the mid-central $(10-40\%)$ collisions n_q scaling starts to break at $\mathrm{KE}_T/n_q \sim 0.7$ GeV, as

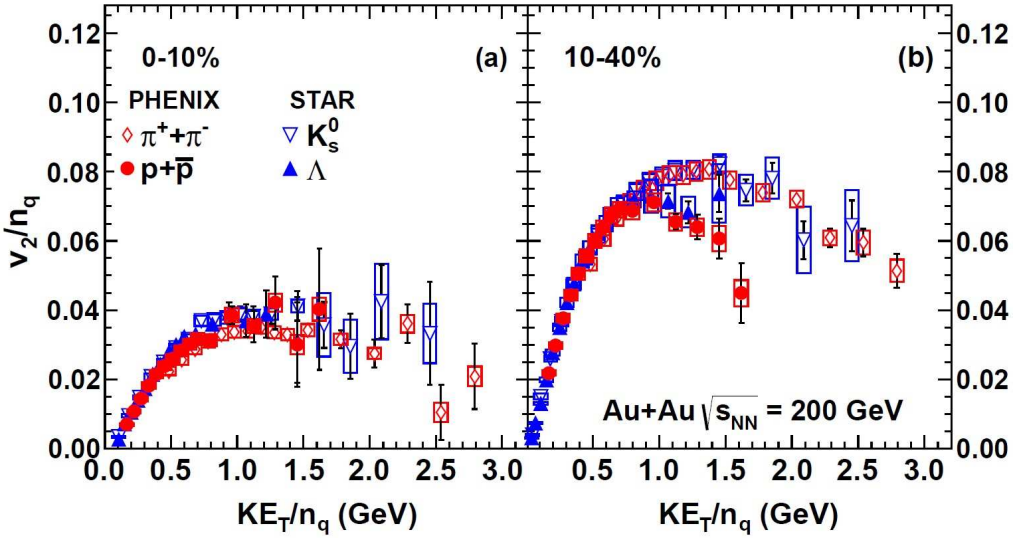

Figure 1.14: v_2/n_q vs. KE_T/n_q with a higher KE_T reach for several identified hadron species [49]. Two centrality ranges, $0-10\%$ and $10-40\%$, are shown. These results were obtained by the PHENIX experiment for Au+Au collisions at $\sqrt{s_{NN}} = 200$ GeV.

shown on panel (b). This observation suggests that while the coalescence (recombination) mechanism dominates in the most central collisions, for peripheral events other hadronization mechanisms begin to compete, such as the fragmentation scheme that mostly applies to energetic partons. Eventually, deviation to n_q scaling is observed.

1.6.4 Measurement of v_n $(n > 2)$

The large fluctuations of the initial geometry profile (cf. Fig-1.8) and the resulting higher order Fourier components (also referred to as "flow harmonics") is only discovered recently [28] but quickly draws a huge amount of attention. Experimentally, v_n has been measured by the PHENIX [50], ATLAS [51], ALICE [52] and CMS [53] collaborations to up to 6th order ($n = 6$). Very consistent results are obtained across the experiments.

v_n values measured at ATLAS are depicted in Fig-1.15. In all centrality selections, sizable v_n $(n > 2)$ values are observed. While v_2 values increase by a factor of 3 from the most central to peripheral collisions, higher order v_n $(n > 2)$ remains mostly the same. This observation is consistent with the fact that v_2 is largely derived from the elliptical shape of the collision zone (eccentricity ϵ_2 is dictated by centrality), while v_n $(n > 2)$ is essentially derived

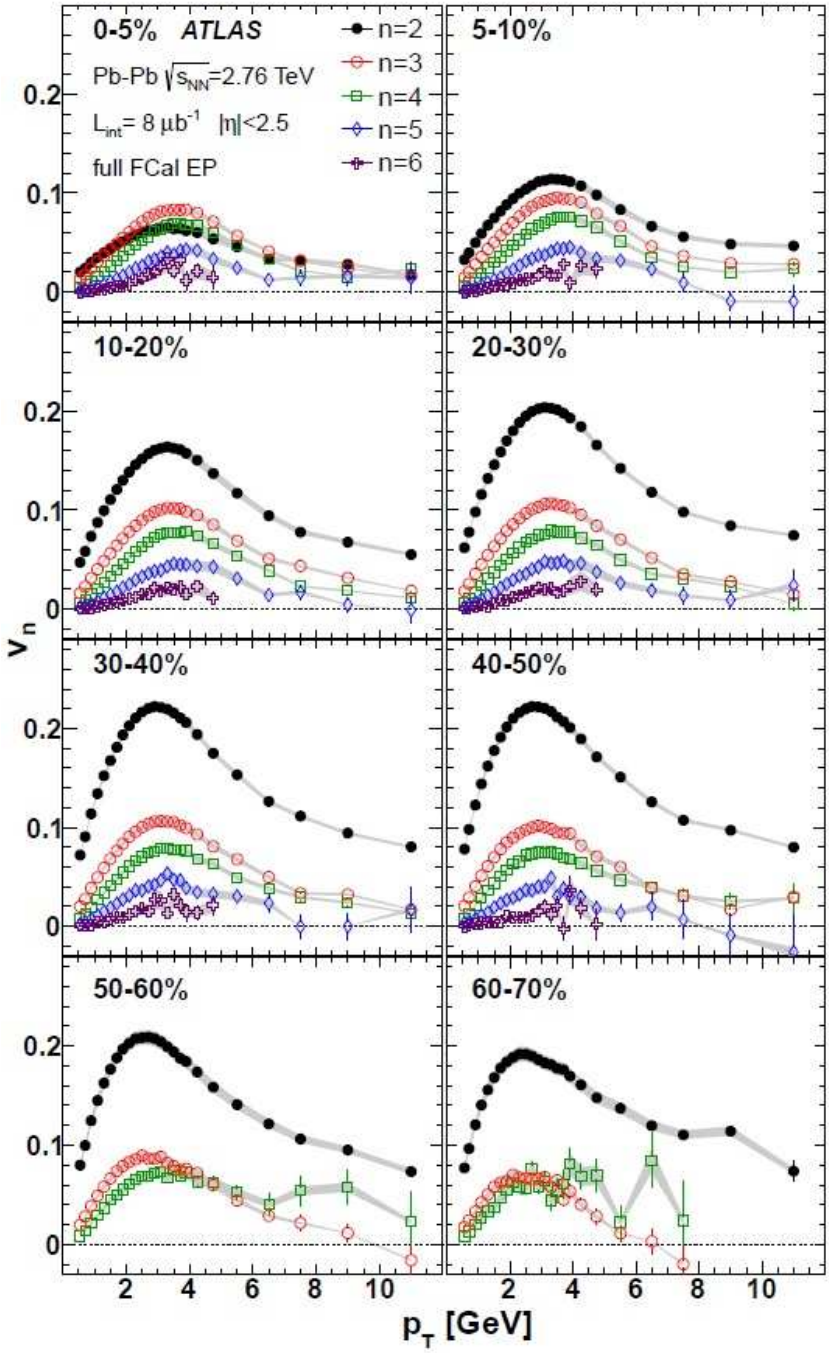

Figure 1.15: v_n vs. p_T measured by ATLAS for Pb+Pb collisions at $\sqrt{s_{NN}} =$ 2.76 TeV. Several centrality bins are shown. Systematic uncertainties are indicated by the gray bands.

from initial geometry fluctuations. Thus, they are relatively insensitive to the collision centrality. In the most central bin $0-5\%$, v_2 values are even smaller compared to v_3 and v_4, indicating that the collision zone is very symmetric without any preference for an elliptical shape.

Another interesting observation is the p_T dependence of v_n. For all orders and centralities, the v_n values increase with p_T till ~ 3 GeV and then decrease, remaining above zero even at very high p_T. This behavior can be explained by a transition from pressure gradient driven v_n to path-length dependent jet energy loss driven v_n [54] [55].

The measurement of higher order harmonics v_n ($n > 2$) can provide additional constraints on the initial geometry models. As indicated in Fig-1.11, one major contributor to the uncertainty of η/s is the initial geometry modeling. Both the Glauber and CGC models describe v_2 and other observables (such as centrality dependence of multiplicity for several hadron species [38]) equally well. The additional requirement of reproducing v_n ($n > 2$) may help control the initial condition. As seen on Fig-1.16, the calculation with initial geometry modeled by CGC is tuned to match v_2 and requires relatively large η/s of $2 \times 1/(4\pi)$; however this value of η/s is too large to reproduce v_3, which is especially evident in the relatively high p_T range (right panels). The calculation of Glauber geometry with η/s of $1/(4\pi)$ (the conjectured lower bound) seems to match data fairly well. Therefore the Glauber model for initial geometry is favored by this analysis.

The aforementioned v_n results were measured with inclusive charge hadrons. Progress has also been made on the v_n measurements of identified hadrons. It seems that $v_n/(n_q)^{\frac{n}{2}}$ scales with KE_T/n_q for various hadron species.

1.7 Dihadron Correlation Measurements

A correlation function $C(\Delta\phi, \Delta\eta)$ for hadron pairs can be defined as [56] [51]:

$$C(\Delta\phi, \Delta\eta) = \frac{N^{\mathrm{same}}(\Delta\phi, \Delta\eta)}{N^{\mathrm{mix}}(\Delta\phi, \Delta\eta)} \tag{1.4}$$

where $\Delta\phi$ is the azimuthal angle separation between the two hadrons and $\Delta\eta$ is the pseudorapidity difference. $N^{\mathrm{same}}(\Delta\phi, \Delta\eta)$ is the number of pairs for a particular $\Delta\phi$ and $\Delta\eta$ bin and when the two hadrons of each pair come from the "same" event. $N^{\mathrm{mix}}(\Delta\phi, \Delta\eta)$ is defined similarly with one crucial difference: the two hadrons in the pairs come from different events ("mixed") with similar event character such as centrality and collision vertex position. $N^{\mathrm{mix}}(\Delta\phi, \Delta\eta)$ carries only trivial correlation reflecting detector acceptance, which is also con-

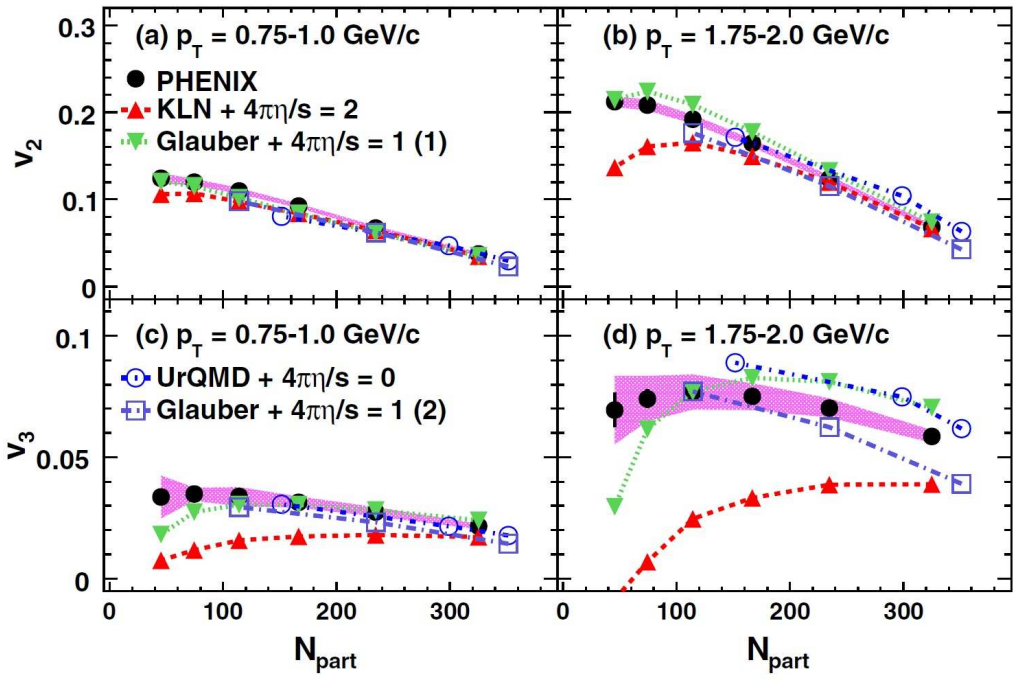

Figure 1.16: Inclusive charge hadron v_2 vs. $N_{\rm part}$ [(a),(b)] and v_3 vs. $N_{\rm part}$ [(c),(d)] measured by PHENIX for Au+Au collisions at $\sqrt{s_{NN}} = 200$ GeV [50]. Two p_T selections are shown. Systematic errors are indicated by the magenta bands. Several model comparisons are shown; they are indicated as "model name"+ "η/s value", e.g. KLN+$4\pi\eta/s = 2$ means that a CGC geometry is assumed with $\eta/s = 2/(4\pi)$.

tained in $N^{\text{same}}(\Delta\phi, \Delta\eta)$ and cancels out in $C(\Delta\phi, \Delta\eta)$. Therefore $C(\Delta\phi, \Delta\eta)$ represents physical correlations only.

In some cases the analysis is relatively insensitive to pseudorapidity; consequently the numerator and denominator in Eqn-1.4 are integrated over $\Delta\eta$ in a certain $\Delta\eta$ range, the results of which are denoted as $N^{\text{same}}(\Delta\phi)$ and $N^{\text{mix}}(\Delta\phi)$, and the ratio $N^{\text{same}}(\Delta\phi)/N^{\text{mix}}(\Delta\phi)$ is defined as azimuthal correlation function $C(\Delta\phi)$.

The two particles in a pair are commonly referred to as trigger and associate particle respectively. The names are interchangeable but normally the particle with higher p_T is referred to as the trigger particle. The correlations between two particles originate from two sources, collective flow and jet:

$$C(\Delta\phi, \Delta\eta) = C_{\text{Flow}}(\Delta\phi, \Delta\eta) + C_{\text{Jet}}(\Delta\phi, \Delta\eta). \tag{1.5}$$

Collective flow has been discussed earlier. A jet is defined as a spray of energetic hadrons moving almost collinearly (in a narrow spacial "cone"). When the nucleon collide, hard scattering of partons inside nucleons may happen and generates energetic parton pairs. These high energy partons shoot out of the QGP medium and eventually hadronize via fragmentation and create jets. Since the two outgoing partons of a hard scattering are likely to be back-to-back, the generated jets are back-to-back and are called dijets.

Due to the nature of jets, $C_{\text{Jet}}(\Delta\phi, \Delta\eta)$ is "localized" in a narrow window of $\Delta\eta \sim 0$ and $\Delta\phi \sim 0$ or π ($\Delta\phi \sim \pi$ for the case that two hadrons come from back-to-back jets, one in each jet). Therefore, it's possible to isolate $C_{\text{Jet}}(\Delta\phi, \Delta\eta)$. On the contrary, $C_{\text{Flow}}(\Delta\phi, \Delta\eta)$ originates from the fact that both particles are correlated to the event planes Ψ_n (see Eqn-1.2). Therefore $C_{\text{Flow}}(\Delta\phi, \Delta\eta)$ is a "global" correlation not restricted to any particular $(\Delta\phi, \Delta\eta)$ region.

In the rest of this section, we first focus on $C_{\text{Flow}}(\Delta\phi, \Delta\eta)$ and discuss the extraction of v_n from it. Then we move on to $C_{\text{Jet}}(\Delta\phi, \Delta\eta)$, which is an important measurement by itself but also related to v_n measurements.

1.7.1 Extraction of v_n from Dihadron Azimuthal Correlation

Since v_n is normally discussed in sufficiently narrow $\Delta\eta$ bins, the dependence of v_n over η is negligible. Therefore, the integrated azimuthal correlation $C(\Delta\phi)$ is discussed in this section. By a simple convolution of the azimuthal angle distributions of the two single particles (Eqn-1.2), we end up with a

distribution of the azimuthal angle difference $\Delta\phi$ as:

$$\frac{\mathrm{d}N_{\mathrm{pairs}}}{\mathrm{d}\Delta\phi} \propto 1 + 2\sum_{n=1}^{\infty} v_n(p_T^a)v_n(p_T^b)\cos(n\Delta\phi) \tag{1.6}$$

Note the $\mathrm{d}N_{\mathrm{pairs}}/\mathrm{d}\Delta\phi$ is just an alias of $C_{\mathrm{Flow}}(\Delta\phi)$ and η is dropped from the equation. According to this equation, it is possible to extract $v_n(p_T)$ from the measurement of $C(\Delta\phi)$ [57]. To reduce the number of variables, the same p_T range for p_T^a and p_T^b is chosen and the coefficients before $\cos(n\Delta\phi)$ become $v_n^2(p_T)$, which is also referred to as $v_{n,n}(p_T)$.

The process of extracting $v_n(p_T)$ from $C(\Delta\phi, \Delta\eta)$ is summarized in Fig-1.17. In panel (a) the full correlation function $C(\Delta\phi, \Delta\eta)$ is shown. On the "near side" ($\Delta\phi \sim 0$), a "ridge" structure can be seen for all $\Delta\eta$; for $\Delta\phi \sim 0$ a "peak" sits on top of this ridge. The peak contains $C_{\mathrm{Jet}}(\Delta\phi, \Delta\eta)$ as mentioned above and the ridge, which represents a global correlation, can be explained by $C_{\mathrm{Flow}}(\Delta\phi, \Delta\eta)$. On the "away side" ($\Delta\phi \sim \pi$), the shape is mostly independent of $\Delta\eta$ and resembles a "shoulder" structure that is more clearly shown by the data points on panel (b). Since we are only interested in the flow correlation, a $|\Delta\eta|$ cut ($|\Delta\eta| > 2$) is applied to suppress the correlations from jets; after an integration over $\Delta\eta$, the resulting azimuthal correlation function (that contains only $C_{\mathrm{Flow}}(\Delta\phi)$) is depicted on panel (b). It is then decomposed according to Eqn-1.6 up to the sixth order. Based on the residual difference shown in the bottom of panel (b), we conclude that the data doesn't have the sensitivity to allow the extraction of $v_{n,n}$ beyond $n = 6$. In panel (c), $v_{n,n}$ values are plotted as a function of $\Delta\eta$ cut. For $\Delta\eta < 2$, $v_{n,n}$ is clearly enhanced by the correlations from jets. For $\Delta\eta$ cut greater than 2 the $v_{n,n}$ values roughly remains the same, demonstrating only a very limited jet contamination. A similar plot for v_n is shown in panel (d); the v_1 values extracted this way is strongly biased by a global momentum conservation effect [58] [59] and is not shown.

It is noteworthy that the v_n values extracted from $C_{\mathrm{Flow}}(\Delta\phi)$ are very consistent with the ones calculated according to Eqn-1.3 [51], in which method the event plane Ψ_n need to be constructed first. The good agreements of v_n values measured with the two independent methods provides evidence that the measurements are very robust.

1.7.2 Difficulties of Full Jet Reconstruction at RHIC

A jets is a spray of energetic hadrons contained in a narrow cone. In the experiments where more fundamental particles are collided (e.g. p+p), the overall multiplicity is typically small. Therefore, the identification of the cone

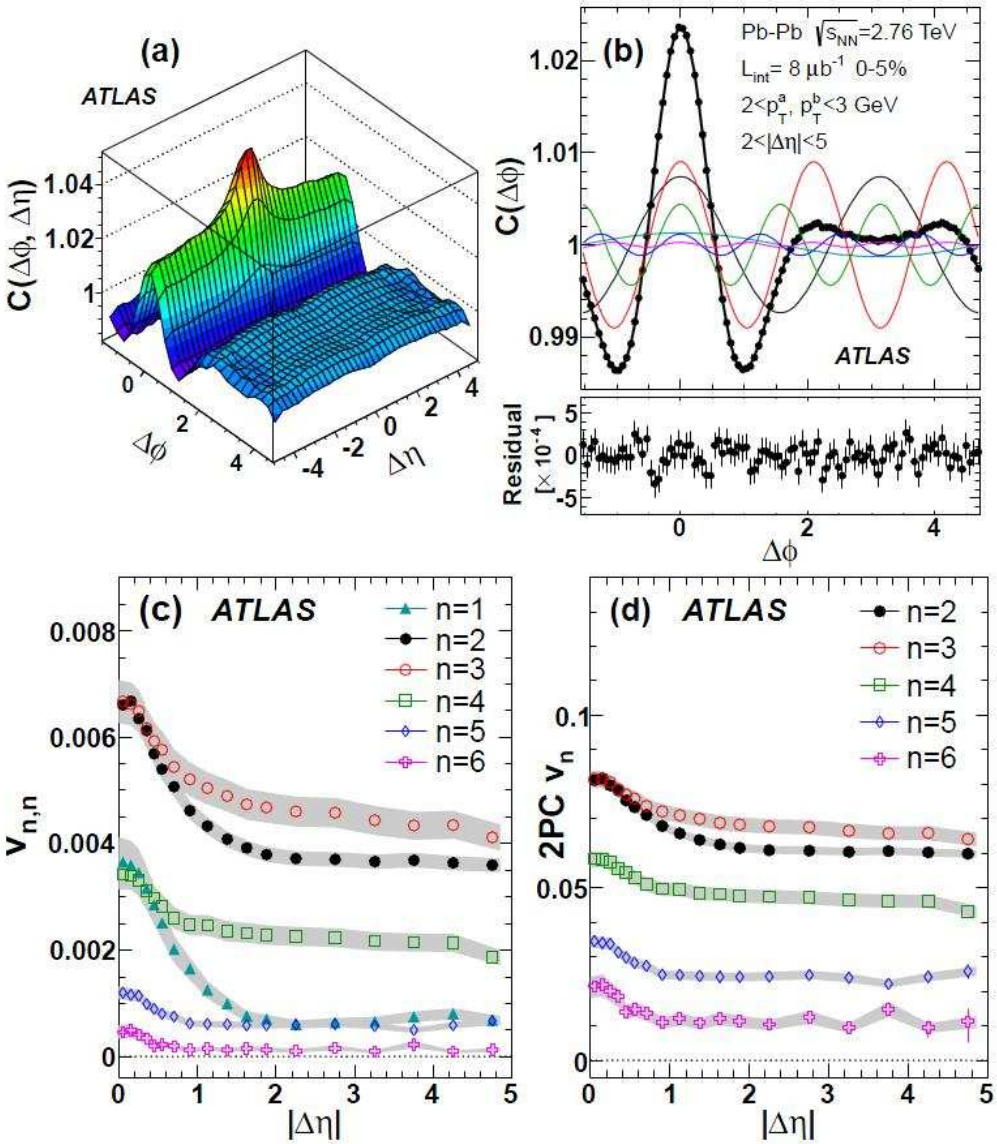

Figure 1.17: Illustration of v_n extraction from dihadron correlations [51]. Both p_T^a and p_T^b are in the range of $2-3$ GeV. Centrality is $0-5\%$. Data is from ATLAS experiment for Pb+Pb collisions at $\sqrt{s_{NN}} = 2.76$ TeV. (a) $C(\Delta\phi, \Delta\eta)$ (b) $C(\Delta\phi)$ integrated for $2 < |\Delta\eta| < 5$; different $v_{n,n}$ components and their sum are shown as curves of different colors. Residual differences between the sum and data points are plotted in the bottom sub-panel. (c) $v_{n,n}$ vs. $|\Delta\eta|$ (d) v_n vs. $|\Delta\eta|$.

of hadrons is unambiguous. However, this picture is complicated in heavy ion collisions at RHIC, where the high multiplicity environment creates a soft background spread over the detector acceptance. The fluctuations of the background, i.e. several hadrons clusterize accidentally, could be falsely recognized as a jet. The probability of this accidental clusterization is low, but hard scatterings are rare events as well. Therefore identified jets might have severe contamination from the background fluctuations. It's noteworthy that at the LHC the situation is yet again different even for the Pb+Pb collisions. The extremely high energy collision at LHC creates jets that are sufficiently energetic to be isolated from the fluctuating background with contaminations under control. Therefore full jet reconstruction is possible [60] [61].

Despite several complications, full jet reconstruction analysis has been carried out at RHIC by both the PHENIX and STAR collaborations. There is very good progress on this front for smaller collision systems such as Cu+Cu and d+Au [62] [63].

1.7.3 Study Jet with Dihadron Azimuthal Correlation

Since a full reconstruction of a jet is difficult, especially in central Au+Au collisions, correlation methods are commonly used by experiments at RHIC to study jets. As mentioned at the end of Sec-1.7.1, v_n are measured and enable a reconstruction of C_{Flow}, which in turn allows C_{Jet} to be extracted from the total correlation function.

There is one notable issue in the process described above: the overall level (magnitude) of C_{Flow} (denoted as ξ) is unknown. A commonly used method for ξ determination assumes Zero (jet) Yield At Minimum ("ZYAM") [64]. Another method, commonly referred to as "absolute background normalization", proposes that ξ results from centrality smearing effects and employs simulations to determine ξ directly [65]. The uncertainty associated with ξ is a major contributor to the overall systematic uncertainties of C_{Jet}.

The most striking phenomenon exhibited by C_{Jet} is commonly referred to as "jet quenching" or "jet suppression" [57] [66] [67]. In Fig-1.18, the vertical axis denotes jet per trigger yield (PTY) that is simply $C_{\text{Jet}}(\Delta\phi)$ divided by number of trigger particles $\text{N}_{\text{Trigger}}$. While PTY for p+p and d+Au collisions clearly reflect the expected features for back-to-back jets, PTY for Au+Au collisions show a very different behavior. On the near side, PTY for Au+Au is unmodified, and is almost the same as that for p+p. However on the away side, the peak that is present in p+p and d+Au collision disappears. This observation strongly suggests that a medium (QGP) is created in Au+Au collision which suppresses the away side jet. Further comparisons between PTY measured in Au+Au and reference measurements from p+p and d+Au show

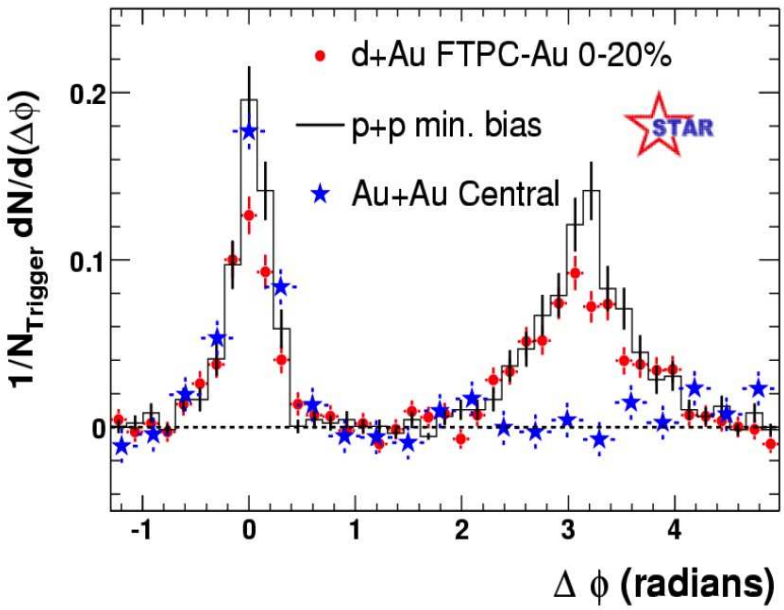

Figure 1.18: Jet per trigger yield vs. $\Delta\phi$ for p+p, d+Au and Au+Au collisions measured by the STAR experiment [66]. Only particles within $|\Delta\eta| < 0.7$ are included in the analysis. Trigger particles have p_T in the range of $4 - 6$ GeV while the associated particles have $2 < p_T < p_T(\text{Trigger})$.

modifications on both the near and away sides [68] [68]. Insights on the stopping power of the QGP (to energetic partons), the mechanism of hadronization, etc. are constrained by these observations.

1.8 $R_{\rm AA}$ and high p_T v_2 measurement

As mentioned in Sec-1.5, high p_T particles originate from fragmentations of energetic partons created in initial hard scatterings. Before hadronization, these energetic partons (sometimes interchangeably referred to as jets) interact with the QGP medium and lose energy, which is demonstrated in Fig-1.18.

v_2 measured at high p_T reflects these same jet-medium interactions; the anisotropy of high p_T particles result from the path-length (the distance a parton travels in the QGP medium) dependence of jet-medium interaction. The energetic partons suffer stronger suppression for larger path-length; thus fewer high p_T particles survive. Since there exists an anisotropy for the medium profile, path-length for different directions will not be the same; the anisotropy of high p_T particles are thus created.

In this section, we first introduce another observable commonly employed to study jet suppression (besides the aforementioned $C_{\rm Jet}$); then the measurement and implication of high p_T v_2 is discussed.

1.8.1 $R_{\rm AA}$ at PHENIX

The "nuclear modification factor" $R_{\rm AA}$ is defined as:

$$R_{\rm AA}(p_T) = \frac{(1/N_{\rm AA}^{\rm evt}){\rm d}^2N_{\rm AA}/{\rm d}p_T{\rm d}y}{\langle T_{\rm AA}\rangle \times {\rm d}^2\sigma_{\rm pp}/{\rm d}p_T{\rm d}y} \tag{1.7}$$

for a particular p_T bin. The numerator of Eqn-1.7 is the yield per event of Au+Au collisions, and ${\rm d}^2\sigma_{\rm pp}/{\rm d}p_T{\rm d}y$ is yield per event for p+p collisions. $\langle T_{\rm AA}\rangle$ is the thickness function of the two Au nuclei and commonly treated approximately as $N_{\rm coll}$. It's straightforward from Eqn-1.7 to see that $R_{\rm AA}$ reflects the comparison of per event yield between Au+Au and p+p, scaled by number of binary collisions in Au+Au.

In the absence of medium effects, $R_{\rm AA}$ is expected to be unity, because in this case a Au+Au collision is simply the superposition of $N_{\rm coll}$ p+p collisions. However if medium modification such as jet suppression exists, $R_{\rm AA}$ would be smaller than one. $R_{\rm AA}$ values measured at PHENIX for various particle species are compiled in Fig-1.19. In the high p_T region, $R_{\rm AA}$ for mesons such as π^0, η and ω are consistent with each other at a value of $0.2 \sim 0.3$, indicating a

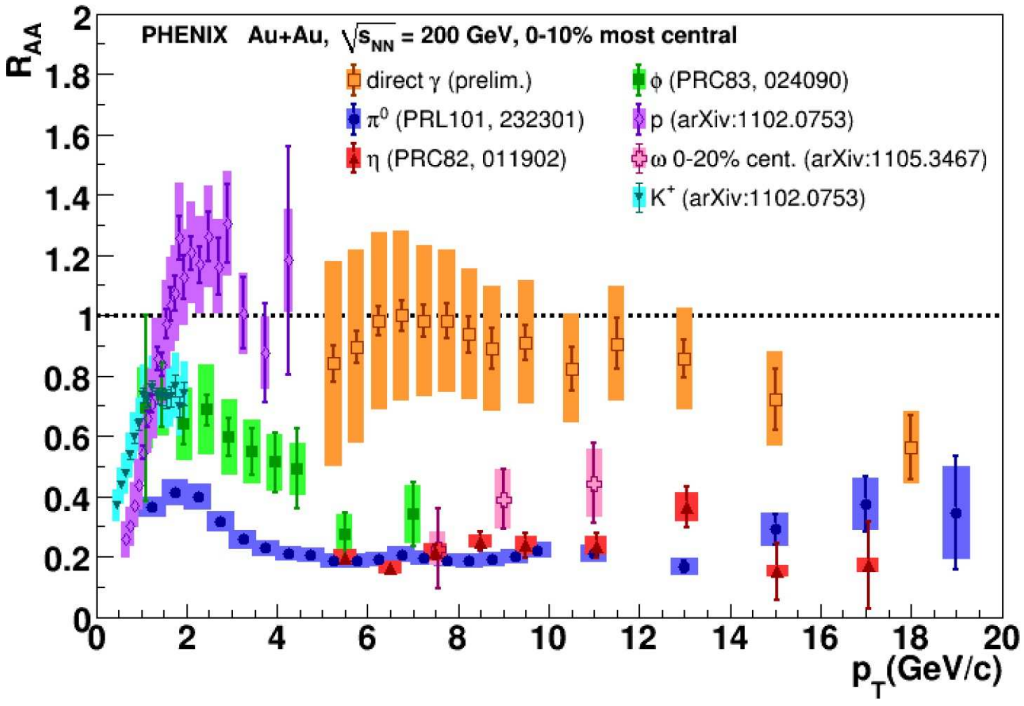

Figure 1.19: R_{AA} measured by PHENIX for various particle species [69] [15] [70] [71] [72] [73].

strong jet-medium interaction that appears to be independent of the mass and quark content of mesons. On the other hand, $R_{\rm AA}$ values for direct photon (γ) are consistent with one, which is expected since photon do not carry color charge and interact with the medium. $R_{\rm AA}$ for other collision system (such as d+Au and Cu+Cu) at several different beam energies are reported in [74] [75] [76].

1.8.2 $R_{\rm AA}$ w.r.t. Reaction Plane

Theoretical characterization of jet-medium interactions is traditionally carried out in a perturbative QCD (pQCD) framework [77]. Based on the measurement of $R_{\rm AA}(p_T)$, initial estimates of parameters like momentum broadening per mean free path $\hat{q} = \langle k_T^2 \rangle / \lambda$ and energy loss per unit path-length $\mathrm{d}E/\mathrm{d}l$ are provided by various models, such as BDMPS-Z/ASW [78], HT [79], and AMY [80]. However, when compared under the same set of circumstances, these models give rather different estimates of the parameters [81]. Therefore $R_{\rm AA}(p_T)$ measurement alone, do not provide sufficient discriminating power to allow for an accurate extraction of jet-medium interaction parameters.

In addition, a Ads/CFT based calculation on jet suppression is proposed in [82] [83], which is favored by measurement such as [84]. This approach is fundamentally different from the pQCD ones and assumes a stronger interaction between jet and medium.

It is clear that a more differential study of $R_{\rm AA}(p_T)$ is necessary to pin down the properties of jet-medium interaction. Since we could roughly control the path-length effect by choosing particles with a different azimuthal angle relative to the reaction plane ($\Delta\phi = \phi - \Psi_{RP}$), the correlation between path-length and jet suppression can be tested by the measurement of $R_{\rm AA}(p_T, \Delta\phi)$ [81]. In Fig-1.20, π^0 $R_{\rm AA}$ for 6 $\Delta\phi$ bins are plotted. For this analysis the initial geometry fluctuations are not taken into consideration and Ψ_{RP} is approximated by Φ_2. From the figure, it can be seen that as the orientation of π^0 goes from in-plane to out-plane, the corresponding value of $R_{\rm AA}$ drops, suggesting a positive correlation between path-length and jet-medium interaction. Actually, a scaling pattern between $R_{\rm AA}$ and path length has been discovered [85] [86].

1.8.3 High p_T v_2

The modulation of $R_{\rm AA}$ vs. $\Delta\phi$ for a particular p_T bin is governed by $v_2(p_T)$. Therefore high p_T v_2 measurements provide another probe to the path-length dependence of jet-medium interaction. In panel (a) of Fig-1.21, it is shown that pQCD based model (WHDG and ASW) calculations underestimate the experimental measurements. Other pQCD models (HT and AMY) give very similar

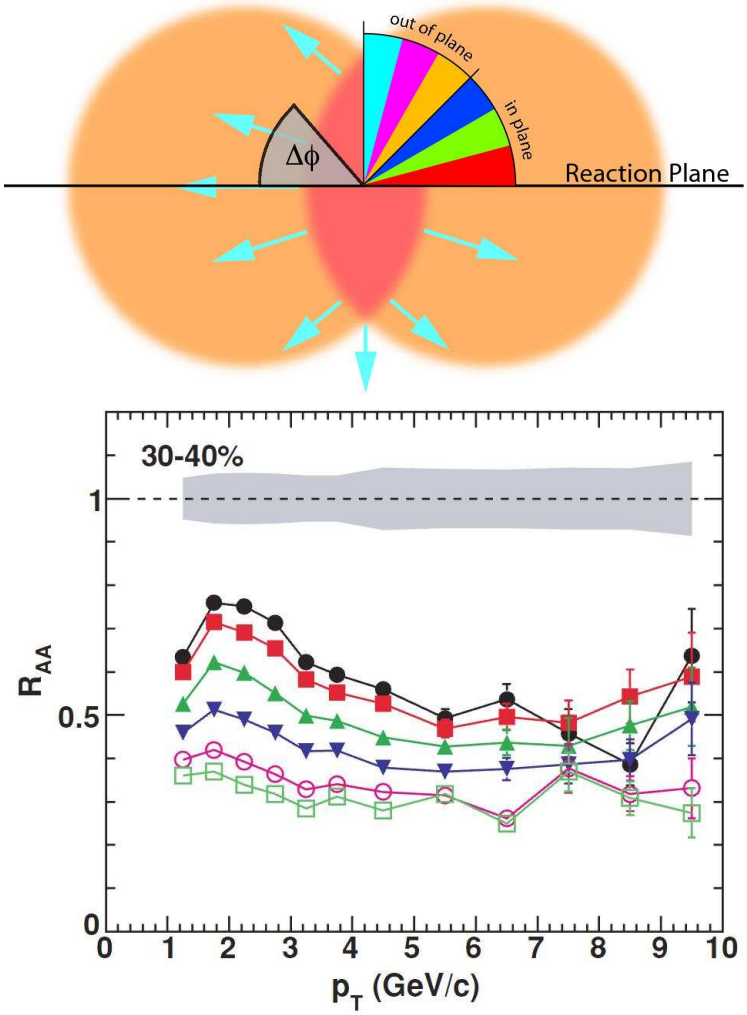

Figure 1.20: Upper panel: cartoon for 6 bins from in-plane (red) to out-plane (cyan); bottom panel: π^0 $R_{\rm AA}(p_T)$ w.r.t. to the event plane [85] measured in Au+Au collisions at $\sqrt{s_{NN}} = 200$ GeV; from in-plane to out-plane, legends are: closed black circle, closed red square, closed green triangle, closed blue inverted triangle, open magenta circle and open green square; systematic uncertainties are indicated by the grey band.

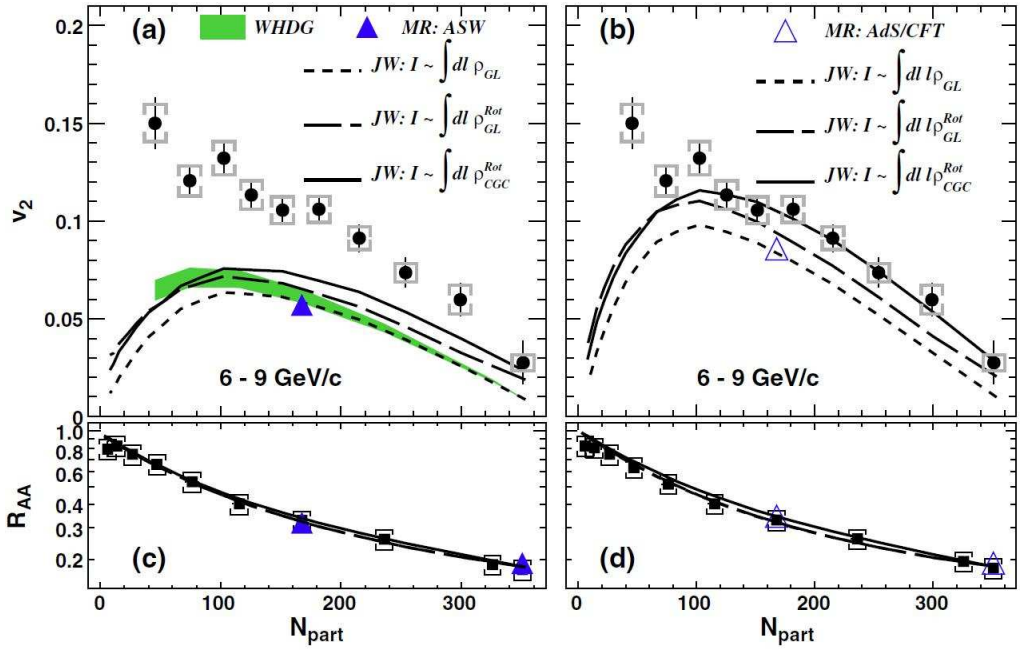

Figure 1.21: v_2 vs. $N_{\rm part}$ at high p_T ($\sim$ 6 - 9 GeV) [87]. The filled circles are data points measured by PHENIX in Au+Au collisions at $\sqrt{s_{NN}}$ = 200 GeV; brackets indicate systematic uncertainties. Panel (a): WHDG [88] (green band), ASW [89] (solid triangle) and JW [90] (lines) model calculations are shown. The JW calculations are implemented with quadratic path-length dependence; Glauber geometry (ρ_{GL}, dashed line), event-by-event rotated Glauber geometry (ρ^{rot}_{GL}, long dashed line) and event-by-event rotated CGC geometry (ρ^{rot}_{CGC}, solid line) are assumed and shown separately. Panel (b): same as (a) except that JW calculations are implemented with cubic path-length dependence and a AdS/CFT modified calculation in the ASW framework (empty triangle) is shown.

results [87]. All of these models have a quadratic path-length dependence. For the JW model, which is also implemented with a quadratic path-length dependence, an underestimate of the data is observed irrespective of the initial geometry model used.

However, calculations which implement an AdS/CFT inspired jet-medium interaction could immediately narrow the gap between data and theory, as shown by the empty triangle on panel (b). The AdS/CFT inspired interaction has an effective cubic path-length dependence. Inspired by this fact, the JW model was re-implemented with this cubic path-length dependence, and the results were found to reproduce the v_2 measurement much better .

Three versions of initial geometry models were assumed. In two of these models (ρ^{rot}_{GL} and ρ^{rot}_{CGC}) event-by-event rotation of the participating nucleons was implemented to account for initial geometry fluctuations. It was observed that the event-by-event rotated CGC geometry best matches the data.

For all of these models, $R_{\rm AA}$ values are well reproduced, as demonstrated on the bottom panels (c) and (d) of Fig-1.21. Therefore, high p_T v_2 measurements can indeed shed additional insights on jet-medium interaction.

1.9 Motivation for this Dissertation Study

Studies of the nuclear matter created in $\sqrt{s_{NN}}$ = 200 GeV Au+Au collisions have revealed several valuable information about the properties of QGP and the underlying interactions among quarks and gluons. In addition, a crossover transition from QGP to hadron gas has been established. A few of these discoveries have been discussed in the previous sections.

As shown in Fig-1.3, experiments of Au+Au collisions at $\sqrt{s_{NN}}$ = 200 GeV (the evolution of nuclear matter in this case is marked as the orange curve "Current RHIC Experiments") mainly access the low μ_B region of the QCD phase diagram. It is natural that the region with higher μ_B should be explored as well. One reason is that the landmark of the QCD phase diagram, the critical point, could lie in this region. Therefore, RHIC has initiated a beam energy scan (BES) program in which Au nuclei are accelerated to collide at $\sqrt{s_{NN}}$ lower than 200 GeV. The program began in 2010 and PHENIX collected data at $\sqrt{s_{NN}}$ = 62, 39 and 7.7 GeV with roughly 700, 350, and 1.2 million MiniBias events in each dataset.

Several experimental observables are introduced to probe the properties of QGP. Most of them are still measurable at lower collision energies, although the detector performances deteriorates with the decrease of multiplicity as $\sqrt{s_{NN}}$ becomes smaller. In this dissertation study, detailed measurements at 62 and 39 GeV of v_2 for neutral pions and v_n for inclusive charge hadrons are

presented. The measurements of neutral pion v_2 is motivated mostly by the fact that neutral pions could be constructed at relatively high p_T, in which case v_2 contains information on path-length dependence of hard parton energy loss and thus sensitive to details of transport models. It's a complementary analysis to the study of jets.

The inclusive charge hadron v_n measurement not only provides v_2 values at low to intermediate p_T with greater precision, but also v_3 and v_4 for the same p_T range. As mentioned in Sec-1.6.4, higher order v_n's have a unique capability for constraining the initial geometry condition of nuclear collisions and allow precise extraction of hydrodynamic parameters such as the specific viscosity. Furthermore, results of these measurements are compared to existing results at 200 GeV and new measurements from the LHC experiments at 2.76 TeV for Pb+Pb collisions. By compiling the same set of observables measured at beam energies across three orders of magnitude, the properties of QGP in distinctive regions of the QCD phase diagram can be assessed.

1.10 A Brief Outline

The following chapters of this dissertation begin with a brief introduction to the PHENIX detector, which should help the reader to understand the technical details of the measurements that follow. Since the analyses presented here are among the very first ones utilizing Run10 datasets, construction and calibration of several event signatures were carried out along with the analyses. These include *centrality* that is essential to virtually all analyses and *event planes*, which are important for analyses sensitive to the geometry of the collision zone. Detailed discussions of these two event signatures are documented in Chapter-3. In the next two chapters the aforementioned two core analyses are discussed. The dissertation is then concluded with a compilation of v_n results from a variety of experiments and results of other efforts from the RHIC BES program.

Chapter 2

The PHENIX Detector

PHENIX is a collaboration of more than 500 scientists actively working toward the goal of a better understanding of the nuclear matter. The term also refers to the detector complex that is designed, maintained and operated by the collaboration to collect and record data measured in the heavy ion collisions.

The status of the detector as of 2010 is illustrated on Fig-2.1. As can be seen, it consists of various components [91], a subset of which may also be considered collectively as a detector themselves. On the upper panel of Fig-2.1 where the beam view is shown, the two central arms (green regions) can be clearly identified. Each arm has roughly $\pi/2$ azimuthal coverage and $|\eta| < 0.35$ pseudorapidity coverage. From inner to outer, we have Muon Piston Calorimeter (MPC [92]), Reaction Plane Detector (referred to as RXN [93] in this dissertation, RxNP in the figure), Hadron Blind Detector (HBD [94]), Drift Chamber (DC [95]), Pad Chamber (PC [95], three layers denoted as PC1, PC2 and PC3), Ring Cherenkov Detector (RICH [96]) and Electromagnetic Calorimeter (EMCal [97]), which is composed of 6 lead scintillator (PbSc) sectors and 2 lead glass (PbGl) sectors. Note that in both arms Time Of Flight (TOF) detectors are installed, though they are built with different technologies and treated separately as TOFW [46] [48] and TOFE [96]. The gray area represents the central magnet [98].

The side view of the PHENIX detector is depicted on the lower half of Fig-2.1. Component detectors sitting at large rapidity and their specific rapidity coverage are best observed from this viewpoint. The multiple layers of plates on both sides (south and north) are Muon Trackers (MuTr [99]) and Muon Identifiers (MuID [99]). Detectors that are more relevant to this dissertation include the Beam-Beam Counter (BBC [100], $3.1 < |\eta| < 3.9$), MPC ($3.1 < |\eta| < 3.9$) and RXN (RxNP in the figure), which consists of a inner ring (RXI, $1.0 < |\eta| < 1.5$) and a outer ring (RXO, $1.5 < |\eta| < 2.8$). At a much larger rapidity sits the Zero Degree Calorimeter (ZDC [101], $|\eta| \sim 6$).

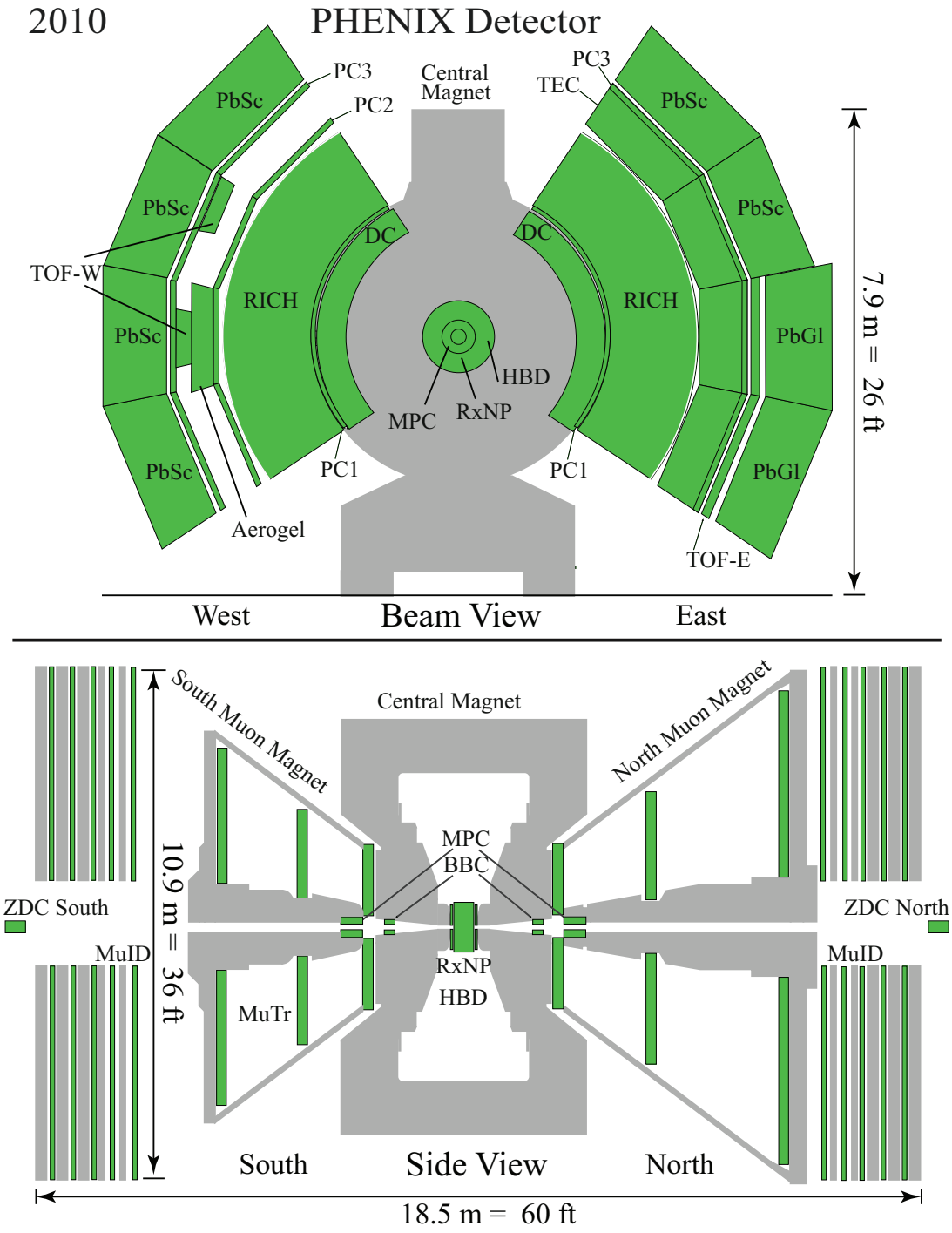

Figure 2.1: The PHENIX detector as of 2010.

A sketch of the PHENIX coordinate system is depicted on Fig-2.2. The X

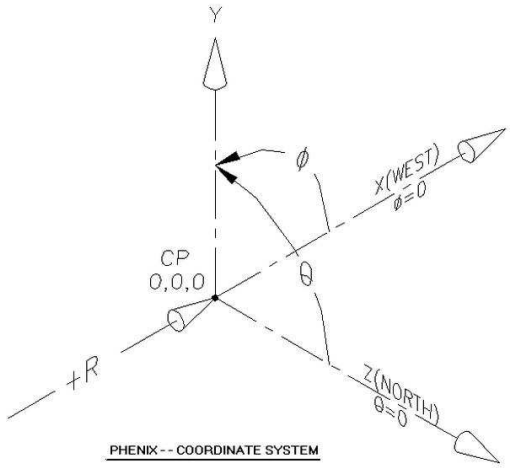

Figure 2.2: PHENIX Coordinate System [102].

and Z axis points to the west and north directions respectively, which is also marked on the beam and side view of Fig-2.1. The coordinates are discussed in Sec-1.4.

2.1 Event Characterization

A nucleus-nucleus collision is also referred to as an "event". In a typical event, hundreds if not thousands of particles are created. In this section, event characterizing variables (also referred to as "global" variables) and relevant detectors are discussed. The variables associated with each particle are then investigated in the sections that follow.

2.1.1 Centrality and Vertex Position Detection

The most fundamental event character is the centrality, which reflects the size and shape of the collision zone (cf. Sec-1.4.1). There is another global variable of essential importance, the position of the collision vertex. The x and y coordinates of the vertex are normally very small and assumed 0 since the beam is contained in the beam pipe with 5 cm radius. Effects of non-zero x and y values are discussed in Sec-5.1.2. However, The vertex position along the beam pipe may vary, which results in sizable values of the z coordinate. An event with $z = 0$ happens right in the middle between the south and north arm (referred to as the "interaction point"), and a non-trivial value of z indicates the collision is off-center. The importance of z is rooted in the following facts:

- during the track construction (from hits on the detector) process, z provides the position of the origin of all tracks (assuming $x = y = 0$);
- components of the PHENIX detector are aligned in such a way that the performance is optimized when detecting events with small z values; actually, the absolute value of z is normally required to be less than 30 cm; otherwise the event is discarded.

2.1.2 BBC

At PHENIX, these two variables are constructed with the BBC detector, the structure of which is illustrated on Fig-2.3. There are two BBC arms installed on the south and north arm of PHENIX respectively (cf. Fig-2.1); each of them is located 144.35 cm (L) away from the interaction point along the beam pipe. One arm is composed of 64 elements. Each element contains a hexagonal quartz Cherenkov radiator part and a meshed dynode photomultiplier (PMT) part. When charged particles generated in the collision hit the radiator, photons are scintillated and multiplied by the PMT, giving an analog signal that is in turn digitized at the front end module of the BBC.

Eventually, the output of each element of the BBC is the particle arriving time t_i and gain of the PMT g_i, along with the (constant) position information for each element. If the averaged arrival time at the south and north arms are T_S and T_N, the vertex position z and global starting time T_0 can be calculated as:

$$z = \frac{T_S - T_N}{2} \times c, \quad T_0 = \frac{T_S + T_N - 2L/c}{2} \tag{2.1}$$

where $L = 144.35$ cm and c is the speed of light. T_0 is another essential quantity that needs to be known for data construction purpose. It signals the time of the collision and serves as the "zero" (starting time) of all other timing information collected from the subsystems which comprise the detector (e.g. at TOF and EMCal). The intrinsic timing resolution of each element of the BBC is 54 ± 4 ps (pico-second). The timing resolution of the whole BBC detector is multiplicity dependent; for a typical event the resolution is 20 ps for T_0. The timing resolution is propagated as the position resolution of 0.6 cm for the z coordinate.

2.1.3 ZDC

Along the beam pipe at even larger rapidity sits the ZDC, a hadronic detector designed to measure neutrons at "zero degree" (polar angle). A side view of the inner detectors at PHENIX (including BBC and ZDC) is depicted on

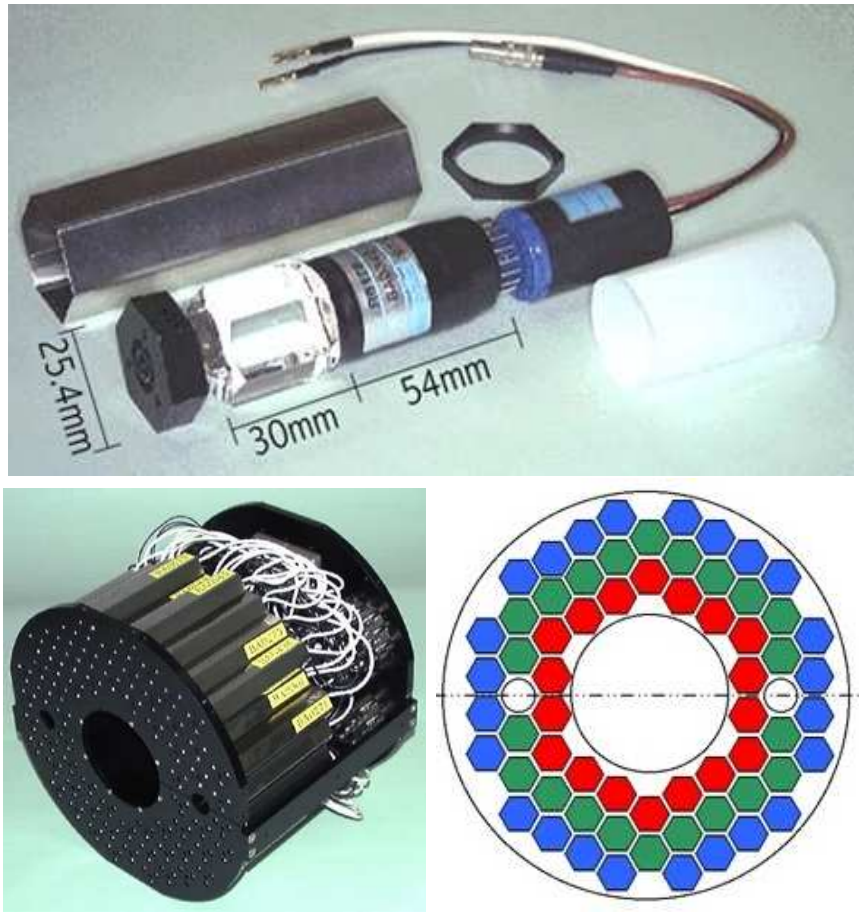

Figure 2.3: The BBC Detector (one arm): upper panel shows one element of the counter that consists of a hexagonal quartz Cherenkov radiator and a meshed dynode photomultiplier. Lower panels: Layout of one arm of the BBC detector which is comprised of 64 elements.

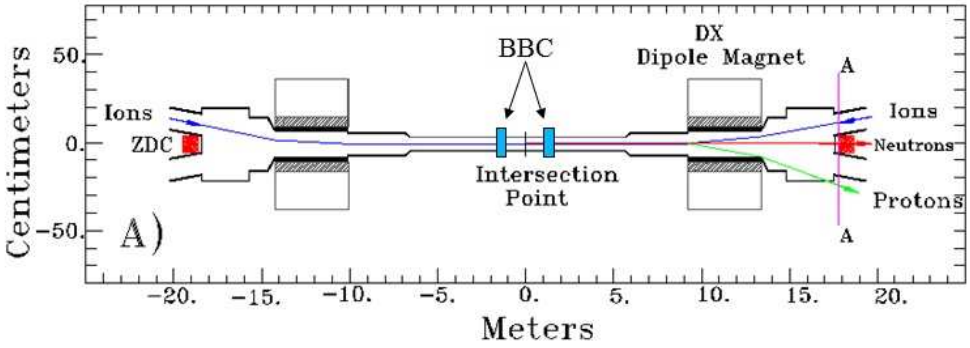

Figure 2.4: Side view of the inner detectors: BBC and ZDC.

Fig-2.4. As can be seen, the two arms of the ZDC sits around 18 meters away from the interaction point ($|\eta| \sim 6$) and placed after the forward dipole magnet, which is designed to bend charged ion or ion segments produced in the collision and guide them back into the beam pipe. Therefore, in the acceptance of the ZDC only evaporated spectator neutrons are undeflected and consequently measured. These neutrons hit the tungsten absrober of the ZDC and generate photon signals, which are further collected and amplified by the connected PMTs.

The main purpose of the ZDC is for luminosity measurements, which are important for absolute measurements and in detector operation. It is not used directly for the measurements presented in this dissertation. The ZDC can also help to define the collision centrality as discussed below.

2.1.4 Centrality Definition

The size of the signal obtained from the BBC is proportional to the centrality of the event: a large centrality means more nucleons participate in the reaction and the number of particles produced will be larger, resulting a greater signal in the BBC. However this is not the case for the ZDC. In central collisions, more participating nucleons means less spectator nucleons, thus the signals at the ZDC are smaller . In peripheral collisions, nuclei remain largely intact and it's hard for neutrons to evaporate. Therefore only few of them arrive at the ZDC and create again a small signal. In mid-central collisions, signals at the ZDC reach their peak. These features are best demonstrated in the left panel of Fig-2.5, where the traditional "clock" method is used to divide centrality bins. The most central bin is located in the lower right corner on the graph and the most peripheral bin in the lower left corner. The right panel presents the division of centrality bins with the "BBC-only" method, in which energy deposited in the ZDC is not utilized to define centrality. Since 2007, centralities in PHENIX are defined with the "BBC-only" method.

2.1.5 Event Plane Detection

Event planes are another set of global variables and they are particularly relevant to this dissertation study. Details of event plane construction are discussed in Sec-3.4. Here we just need to know that a 2π azimuthal coverage is necessary for robust construction of event planes since the acceptance correction is minimized in this situation [104]. This requirement naturally excludes all the central arm detectors. However, we have such detectors at large rapidity. Besides the aforementioned BBC detector, there are two other capable detectors, the MPC and the RXN. All of these detectors have two arms (south

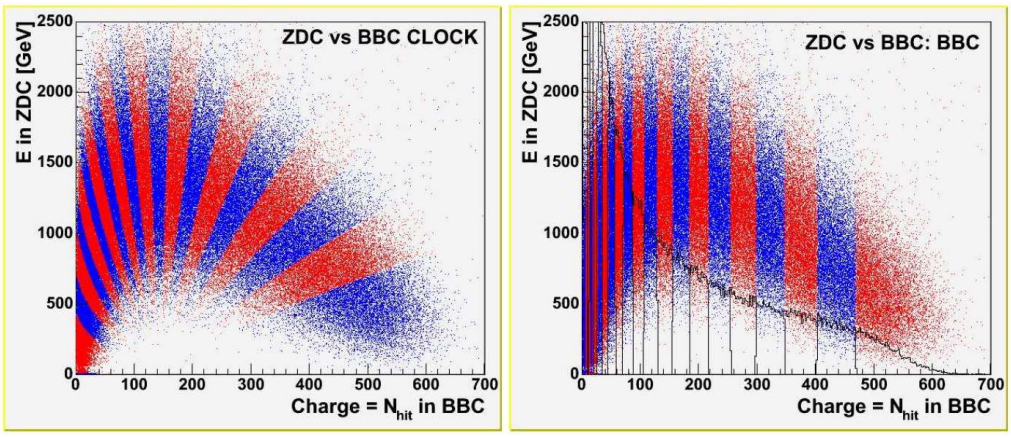

Figure 2.5: ZDC energy vs. BBC charge, utilized for centrality definition [103]. Two methods are presented: the "Clock" method is shown in the left panel and the "BBC-only" method is shown in the right panel.

and north) and event planes can be constructed separately in each of these arms.

2.1.6 MPC

The MPC detector was installed prior to the 2007 run. The two arms are installed in the front holes of the muon arm magnets (the gray area in the muon arms depicted on the lower panel of Fig-2.1). Since the muon arms have slightly different sizes (See Fig-2.1), the two components of the MPC are not identical. The north MPC has η coverage of 3.1 - 3.9 and 216 $PbWO_4$ crystals and the south MPC has coverage of -3.7 - -3.1 and 192 crystals.

The structures and dimensions of the MPC detector are shown on Fig-2.6. The $PbWO_4$ crystal has a very strong stopping power: the Moliere radius is 2.0 cm and the radiation length is around 0.9 cm [106], making $PbWO_4$ a perfect material for calorimetry. A discussion of calorimetry is given in Sec-2.3.1. Scintillated electromagnetic showers are collected and measured by Hamamatsu avalanche photodiodes (APDs) attached to the $PbWO_4$ crystals.

Though designed for neutral pion measurement at large rapidity, in this analysis the MPC is used solely for event plane detection.

2.1.7 RXN

The RXN detector is a designated detector for event plane construction. It was commissioned prior to the 2007 run and decommissioned after the 2010

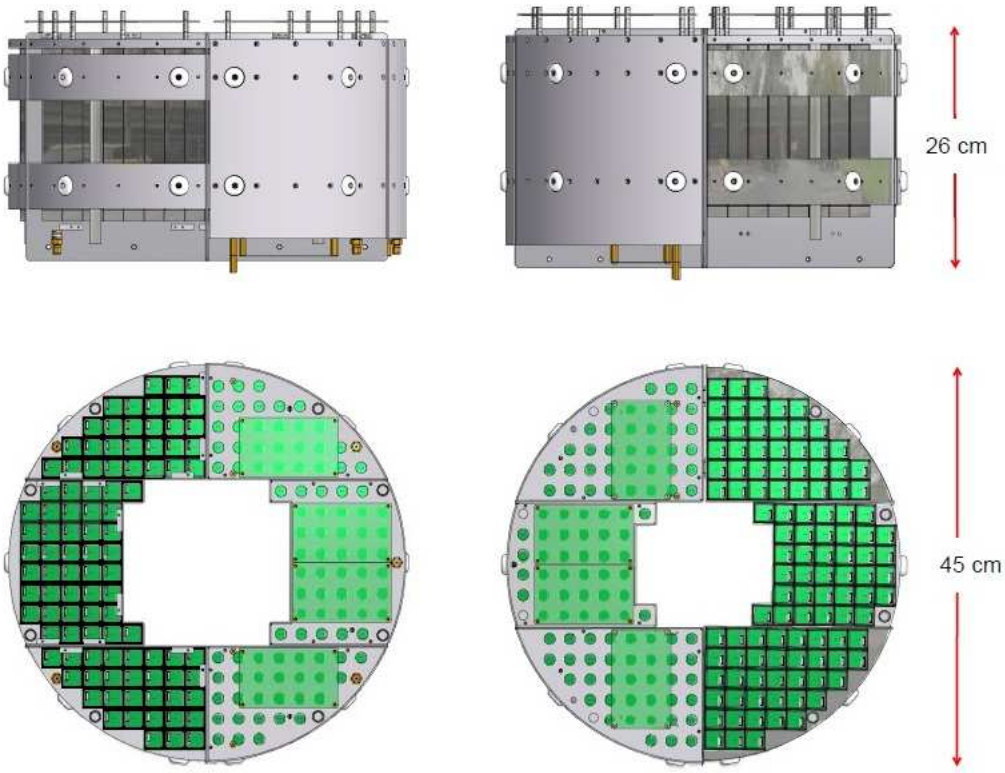

Figure 2.6: Structure and Dimension of MPC [105]; Left (Right) panels show the south (north) arm.

run. The two arms are attached to the nosecone of PHENIX's central magnet, as shown on the upper left panel of Fig-2.7 (and Fig-2.1 for the big picture). It is installed fairly close to the intersection point and just around the beam pipe, therefore it has relatively small rapidity range ($1.0 < |\eta| < 2.8$).

It is a scintillator based detector and the signals are collected and measured by PMTs (the black nodes attached on the green magnet). To enhance the observed signal, converters of 2 cm lead are placed on top of the scintillators, as shown on the right half of Fig-2.7. The structure of the scintillators are graphed on the lower left panel of Fig-2.7. Each arm of the detector is divided into a inner ($1.0 < |\eta| < 1.5$) and a outer ring ($1.5 < |\eta| < 2.8$), which could be treated as separate detectors. The reason behind this η division of RXN is that a large number of particles hit the tip region of the scintillators (cf. left panel of Fig-2.8). The detector response might saturate the readout capability and render the detector ineffective. Therefore, the two ring structure is designed to allow separate readout of the inner and outer region of the detector, and saturation of readout is less likely to happen.

Each ring is further divided into 12 scintillator segments, a very sparse division compared to the 64 elements of BBC and 216 (or 192) $PbWO_4$ crystals of MPC. At the designing stage of RXN, simulations suggested that the performance of Ψ_2 measurements, the primary goal at that time, wouldn't gain much beyond a 12 segments design of the detector (cf. right panel of Fig-2.8). However, higher order Ψ_n measurement were later found to be important [50] and the limited segmentation of RXN leads to a quick drop-off in performance when measurements for higher order Ψ_n are attempted.

2.2 Charged Particles Detection

Charged particles that could be measured experimentally include $\pi^{\pm}$, $K^{\pm}$, $p/\bar{p}$, $e^{\pm}$ and $\mu^{\pm}$. Most heavy hadrons decay quickly and are not directly detected. At PHENIX, except for muons that are observed in the muon arms, all other charged particles are measured in the two central arms.

A charged particle is characterized by its initial momentum (when it's just generated from the collision). The species of the particle would provide additional information since they are created by different mechanisms and subject to different interactions with the nuclear matter. This information is extracted from a full construction of the particle track based on the hits registered on the detectors. The main tracking device in PHENIX is the drift chamber (DC) and pad chamber (PC).

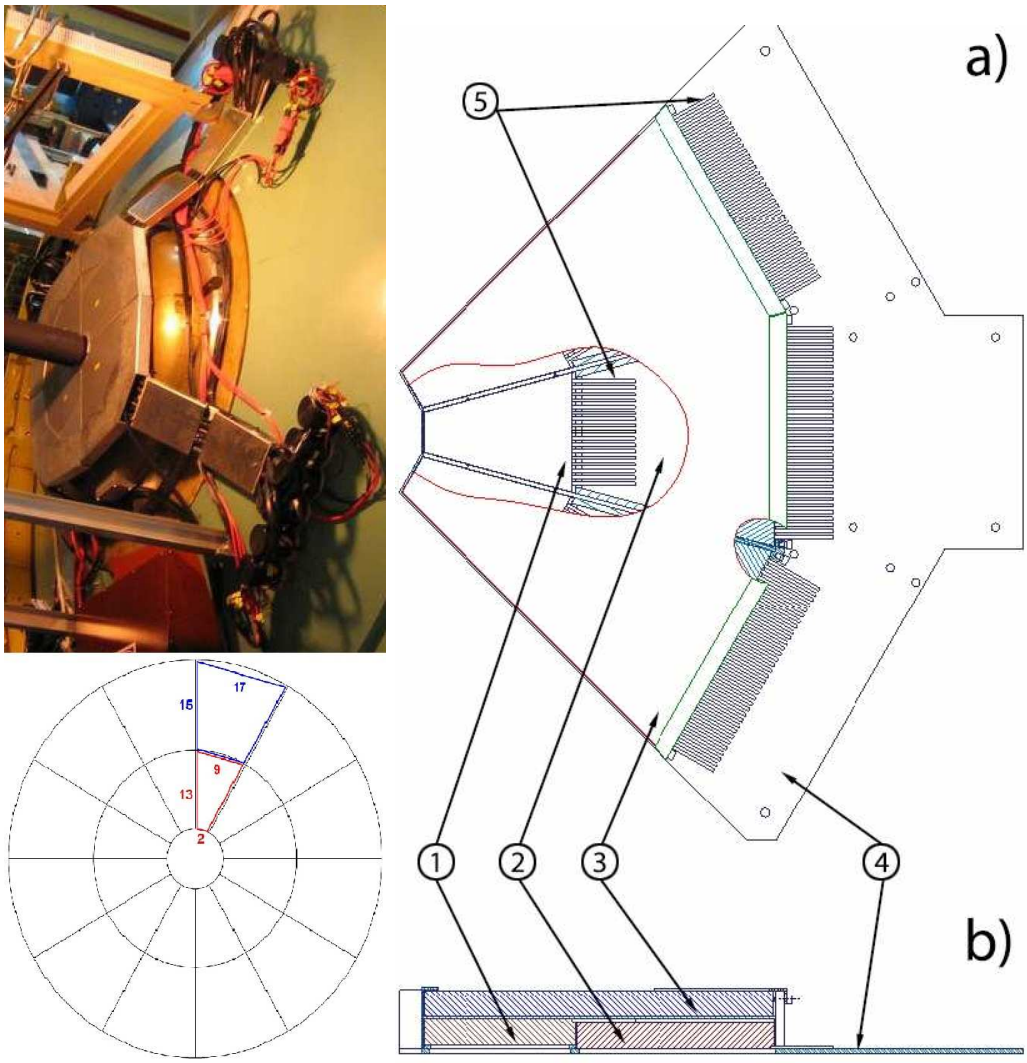

Figure 2.7: The RXN detector [93]. Upper left: RXN north arm installed on the nosecone of PHENIX's central magnet prior to the installation of HBD (cf. Fig-2.1). Lower Left: schematic diagram of one arm, dimensions (in cm) are printed; it's divided into an inner ring and an outer ring; each of them contains 12 scintillator segements. Right: (a) and (b) show the top and side view of 1/4 of an arm; scintillators of inner ① and outer ② are indicated; above them lays the lead converter ③; electromagnetic showers are collected and tranferred by the optical fibers ⑤ to the PMTs. ④ identifies the aluminum tray; .

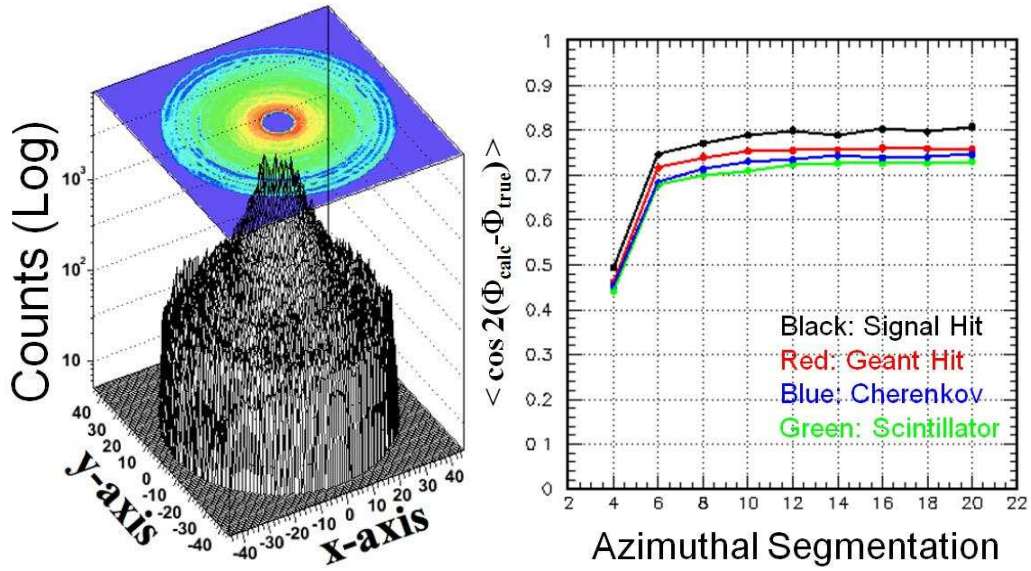

Figure 2.8: Simulation results that help determine the segmentation scheme of RXN. Left panel: distribution of particles in the acceptance of RXN. Right panel: Second order event plane resolutions vs . number of azimuthal segmentations.

2.2.1 DC

DC is a gas detector that consists of two arms (east and west). The general structure and dimension of one arm is plotted on the left panel of Fig-2.9. The volume of the arm is defined by the titanium frame, whose inner surface is 2.02 m from the beam pipe and spans 90° in azimuth. Along the beam pipe (z-axis), the detector is 2.5 meters long, 1.8 meters of which is the active sensor part and occupied by wires. Each arm contains 20 equal sectors; every one of them individually spans 4.5° in azimuth.

The layout of one single sector is depicted on the middle panel of Fig-2.9. Wires in a sector are organized into 3 types of layers: X, U, and V. Wires in each layer have their unique orientation. The X wires run straight from south to north, parallel to the beam pipe. However, the U and V wires are designed to be tilted from the X wires (best seen from right panel of Fig-2.9); the two ends of U and V wires are mismatched by one sector, therefore have 6° angle with the X wires. (The angle could be easily estimated from the geometry.) Along the radial direction, there are 6 wires in each X layer and 4 wires in each U and V layer; the wires thus form planes, as shown in the middle panel. There are also two layers of each type, thus 6 layers in total.

Along the azimuth within one sector, there are 4 sets of anode and cathode

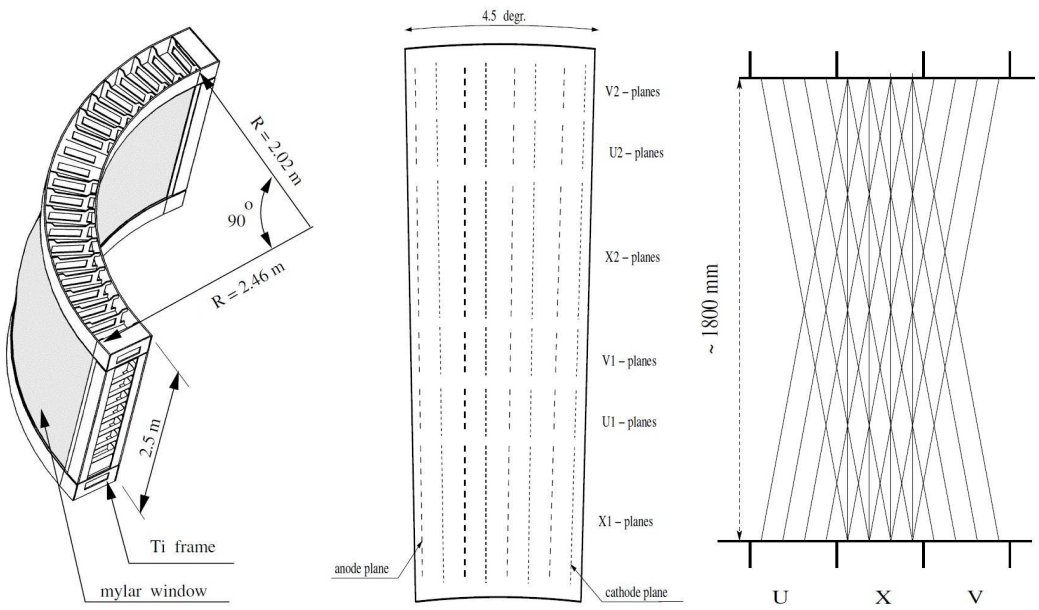

Figure 2.9: The Drift Chamber (DC) [95]. Left panel: general structure and dimensions. Middle panel: side view of one sector; from bottom to top, there are 6 layers of wires: X1, U1, V1, X2, U2 and V2; from left to right, there are 4 anode planes (dashed lines) and 4 cathode planes (dotted lines) of each layer. Right panel: top view of one sector; orientation of wires are best shown here; wires of U and V layers are tilted by 6° relative to wires of X layers.

planes of wires for each layer. High voltage is applied on them and a strong electrical field is created. When a particle passes through the gas filled in the sectors, gas molecules are ionized and clusters of primary ionizations are generated. Electrons of primary ionization drift to the anode wires and create avalanches, a signal on the wire is then registered.

When a X wire fires, the azimuthal angle (or the (x, y) coordinates) of the wire provides an estimation of the azimuth information for the hit. The X wires are indifferent to z coordinate though, because we don't know which part of the wire is hit and the wires run strictly along the z-axis themselves. The (x, y) coordinates of the hit are further refined by an estimation of the distance between the hit and the wire, which is positively related to the drift time and could be measured with the help of global starting time T_0. To find out z coordinate of the hit, Wires in U and V layers are paired and their intersection points (cf. right panel of Fig-2.9) provide basis for z coordinate measurement. The efficiency of a single wire is around 95%. The spatial resolution is $\sim$ 120 micrometer and the angular resolution is 1 mili-radian.

2.2.2 Charged Particle Tracking

In the high multiplicity environment of heavy ion collisions, occupancy of the detector is typical at a high level. An effective algorithm is necessary to find out tracks from thousands of hits on the detector. At PHENIX, this algorithm is based on Hough Transformation [107] [108] of ϕ and α defined in Fig-2.10. (ϕ, α) pairs are generated for all possible combinations of hits. Each combination is considered a track candidate and include:

- 6 X1 and 6 X2 hits that provide 12 (x, y) coordinate measurements (open circles on Fig-2.10);
- 4 UV1 and 4 UV2 hits that provide 8 z coordinate measurements;
- one hit on PC1 (discussed later) that provide one (x, y, z) coordinate measurement.

These pair values of (ϕ, α) are then pushed into a 2D histogram of (ϕ, α); since a true track would leave many hits in the detector, a large number of combinations are made and the bin of (ϕ, α) corresponding to that track would have a large count. Therefore, all (ϕ, α) bins in the 2D histogram with counts over a threshold value are considered to be representing track candidates.

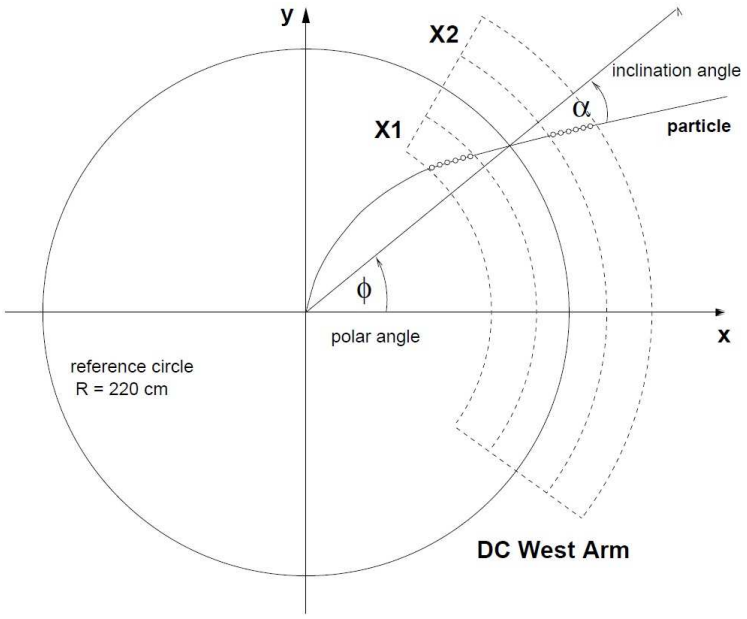

Figure 2.10: Beam view of a sample track in the PHENIX central arm [108]. The reference circle is defined at $R = 220$ cm that roughly cuts the DC in half. The west arm of the DC is drawn on the graph (dotted lines). Charged particles are bent in the magnetic field which exists only outside of the DC. Therefore, tracks in the DC can be identified by associating hits (small open circles) that roughly lie on the same line. The intersection of the track and the reference circle, together with the collision vertex, defines the ϕ angle. The α angle is then naturally defined.

2.2.3 PC

The track candidates are then selected by matching the track projections on the outer layers of the central arm with hits registered on these detectors. The most important detector for this purpose is the Pad Chamber (PC). There are 3 layers of PCs on the west arm and 2 layers on the east arm (cf. Fig-2.1). The three layers are located at a radius of 2.5, 4.2 and 5.0 meters from the beam pipe. PC is a gas detector as well; it has anode wires that lies in a gas volume and two cathode planes above and below the wire plane, as illustrated on Fig-2.11 The upper cathode is segmented into readout "pads", enables a

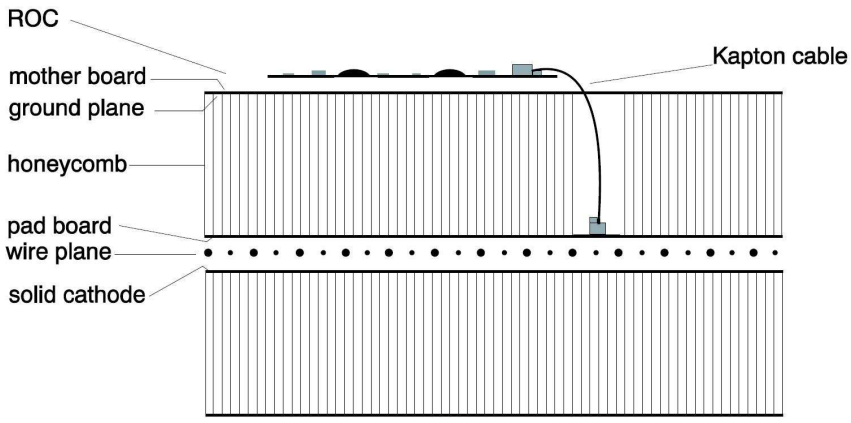

Figure 2.11: Pad Chamber cross-section view [96]. See text.

two dimensional readout in contrast to the one dimensional readout by wires (as those used in DC). The signals are amplified and discriminated by the Readout Cards (ROC's).

The readout method of PC is rather unique [109] [110]. As diagramed in Fig-2.12, readout pixels are arranged in such a way that one layer of pixels are equivalent to three layers of logic pads, and each individual cell is effectively readout. Since we only need one readout channel for a pad, for a large $L \times L$ area we need $(L/d)^2 \times 3$ readout channels, where d is the size of the pad. Compared to the scheme where each cell is in fact read individually and $(3L/d)^2$ readout channels are need, two thirds of readout channels are saved by using the pad scheme. The pad scheme won't work if the multiplicity is too high and the chance that two cells on the same pad fire at the same time is large. However the occupancy is calculated to be $\sim 1\%$ in central Au+Au collisions, thus the aforementioned effect should be small.

The specifications and performance of PC are summarized in Tab-2.1. It's noteworthy that all the PCs have a very small radiation thickness to reduce

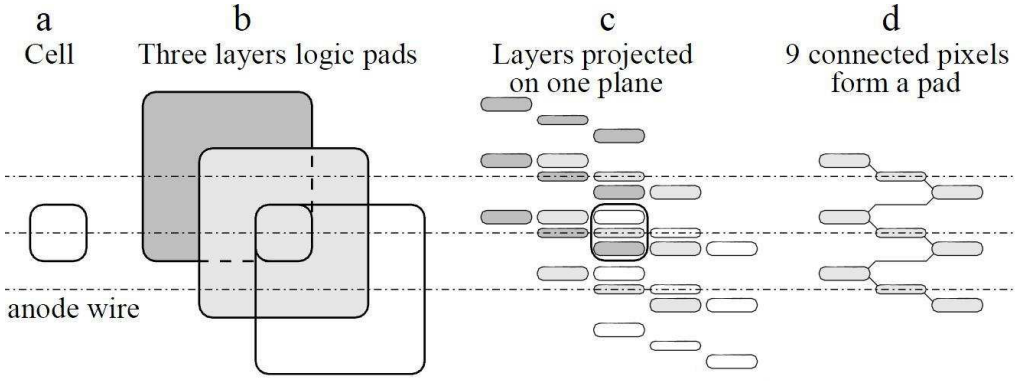

Figure 2.12: Illustration of pad chamber readout scheme [111]: (a) a "cell" and three anode wires (dashed lines) (b) three layers "logic" pads (for illustration purpose only) shifted by one cell both vertically and horizontally; the three pads determined one unique cell by the overlapping region and each cell corresponds to a unique triplets of pads; (d) a "real" pad composed of 9 connected pixels; (c) three layers of real pads are arranged in one plane: note the color correspondence between (b) and (c), grey for left pad, light grey for middle pad and white for right pad; the one to one mapping between a cell and a pad triplet is thus achieved.

Table 2.1: Summary of specifications of pad chamber.

	Wire dist.	Gas gap	Pixel len.	R.T.[a]	z resol.	Perp. resol.
PC1	8.4[b]	6	8.4	1.2%	1.7	2.5
PC2	13.6	10	14.2	2.4%	3.1	3.9
PC3	16.0	12	16.7	2.4%	3.6	4.6

[a] Radiation Thickness.
[b] All the numbers are in millimeters (mm).

photons conversions (to electron-positron pairs). This is particularly important for PC1.

2.2.4 Charged Particle Identification

The principle for charged hadron identification is straightforward. The mass of the particle is calculated and compared to the standard value (e.g the one from Particle Data Group). Based on the following equations:

$$E = \gamma mc^2, \quad p = \gamma mv, \quad \text{and} \quad E^2 - p^2 = m^2, \tag{2.2}$$

the mass-square can be expressed as

$$m^2 = p^2[1/(\frac{v}{c})^2 - 1] \tag{2.3}$$

where c is the speed of light and v is the speed of the particle. Because the track is fully constructed, the calculation of the length integral of the (curved) track is straightforward. Therefore the time of flight (TOF) is the only unknown quantity needed to measure v and subsequently mass-square.

The PHENIX subsystem used to measure the time of flight include a TOF detector in the east arm (TOFE), a TOF detector in the west arm (TOFW), the Aerogel Cherenkov Counter (ACC) and the EMCal (discussed below). Since v is generally very close to c the timing resolutions of these detectors must be very good to allow an accurate measurement of m. When m is calculated, a 2D histogram similar to the one shown in Fig-2.13 is employed to identify pions, kaons and protons. The three branches for pions, kaons and protons are well separated at low momentum, since in this case the difference between v and c is relatively large and the measurement of m is more accurate. At large p a substantial dispersion of m is observed and the boundaries between particles become obscure.

For electron/position identification, the main device is the Ring Imaging Cherenkov detector (RICH). When an electron/position transverses the RICH, Cherenkov photons are radiated, which hit the sensors of the RICH. The number of photons (n_0) collected for each track is therefore an essential variable that helps judge whether the track is a electron/position.

2.3 Photon Detection

Photons in heavy ion collisions are particularly important because:

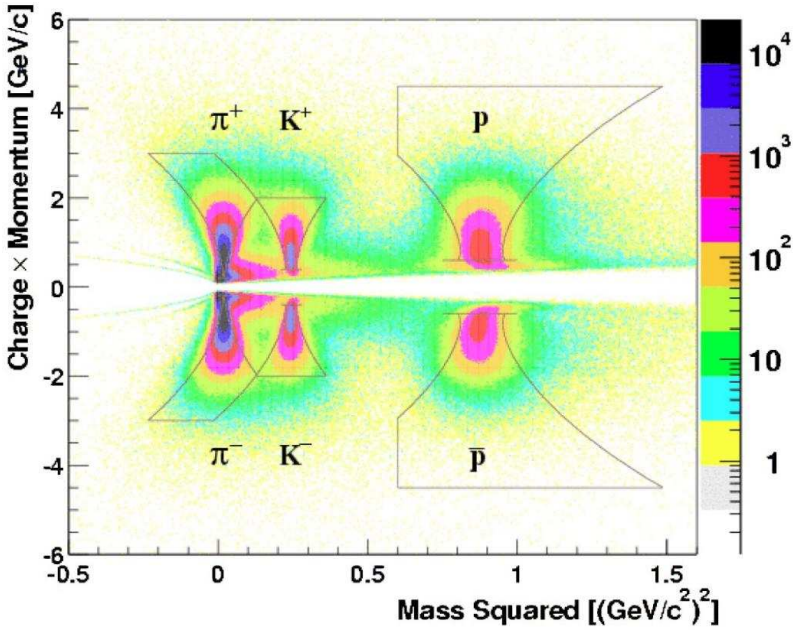

Figure 2.13: Charge × Momentum vs. Mass Square for charged hadron identification [112]. The lines indicate boundaries that enclose pions, kaons and protons respectively.

- thermal photons emitted by the nuclear matter carries information about all stages of the heavy ion collision (cf. Sec-1.4.2);
- photons do not participate in the strong interactions experienced by other particles in nuclear matter, thus information carried out by photons are free from "distortions";

2.3.1 Structure of EMCal

The main subsystem for photon detection in PHENIX is the ElectroMagnetic Calorimeter (EMCal). EMCal is positioned at the outermost layer of the central arms (cf. Fig-2.1). It contains eight sectors, six of which are lead scintillators (PbSc) and two lead glass (PbGl). Each sector is an array of "towers" (detection channel); the layout of towers are summarized in Tab-2.3.1. In total there are 15552 towers of PbSc and 9216 towers of PbGl.

Each PbSc tower is a sampling calorimeter. It has 66 layers of lead absorber and scintillator (cf. Fig-2.14). When the incoming electromagnatically interacting particles hit the Pb absorber, EM showers are created, which then generate photons in the scintillator. The photons are collected by optical

Table 2.2: Layout of one EMCal sector.

Type	PbSc	PbGl
Tower per Super-Module	12×12[a]	6×4
Super-Module per Sector	6×3	16×12
Super-Module per FEM	1×1	2×3
Cross section (tower)	55.35×55.35[b]	40×40
Depth (tower)	375[18][c]	400[14]

[a] (No. along z-axis) $\times$ (No. along azimuth).
[b] in millimeters (mm).
[c] in mm [in X_0].

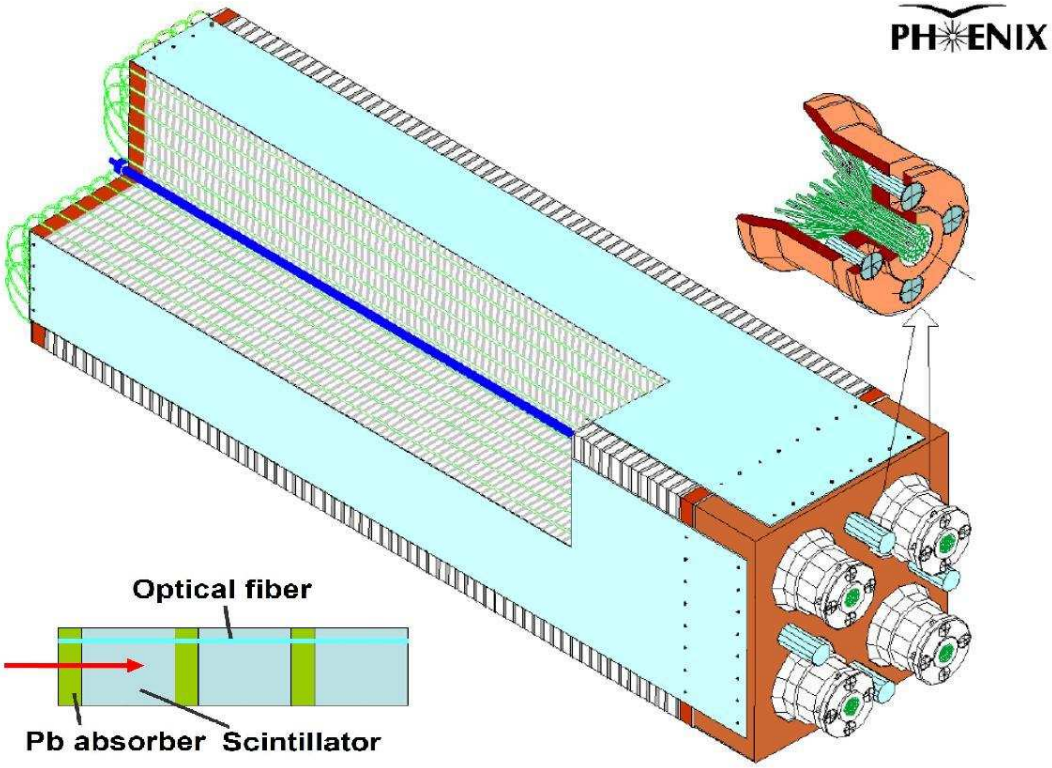

Figure 2.14: Quad-Tower Module of PbSc [99]. Each tower has 66 layers; each layer consists of 1.5 mm of lead absorber and 4.0 mm of scintillator. An optical fiber weaves through the layers and is connected to the PMTs attached at the end of the tower.

fiber and transferred to the PMT, where they are counted and reflected in the strength of the PMT signal.

In contrast to the PbSc towers, the PbGl towers are homogeneous. Each PbGl tower is basically a Cherenkov radiator. When a electromagnatically interacting particle traverses the tower, Cherenkov photons are emitted; the particle's energy is proportional to the number of emitted photons. The photons are collected by the PMT mounted at the end of each tower.

2.3.2 Recognition and Measurement of EMCal Clusters

An EM shower (or cluster) created by the incoming particle won't be confined to a single tower, the shower along with its energy would commonly be shared among neighboring towers. In the high multiplicity environment of heavy ion collisions, it is a non-trivial task to identify particles from the fired towers of EMCal. A pattern recognition process has been developed to do this [113]. It involves three steps as illustrated in Fig-2.15.

After a cluster is established, its energy and position are calculated: the energy is just the sum of energy depositions in all towers which belong to the cluster and the position is calculated as a weighted average of the locations of all participating towers. It's noteworthy that larger weights are assigned to the peripheral towers with less energy depositions, instead of the center tower with the highest energy. With the help of standard beam test, the percentage energy resolutions $(\sigma(E)/E)$ are [99]:

$$\begin{aligned} \text{PbSc}: &\quad 2.1\% \oplus 8.1\%/\sqrt{E(\text{GeV})}, \\ \text{PbGl}: &\quad 0.8\% \oplus 5.9\%/\sqrt{E(\text{GeV})}. \end{aligned} \tag{2.4}$$

The position resolutions for normal incidence are:

$$\begin{aligned} \text{PbSc}: &\quad 1.55 \oplus 5.7/\sqrt{E(\text{GeV})} \ \ (\text{mm}), \\ \text{PbGl}: &\quad 0.20 \oplus 8.4/\sqrt{E(\text{GeV})} \ \ (\text{mm}). \end{aligned} \tag{2.5}$$

Although the position resolution is very good compared to the tower size (cf. Tab-2.3.1), the granularity effect, which could be best understood from Fig-2.16, is not reflected. The 2D position distribution tells us that the measured cluster position tends to be at the centers of the towers. The "hot spots" on the figures are separated by around 5 cm, which is the size of a PbSc tower. The counts at the "hot spots" are more than 5 times of those at the "cold valleys" in between. This effect could have an impacts on certain measurements that are sensitive to cluster position.

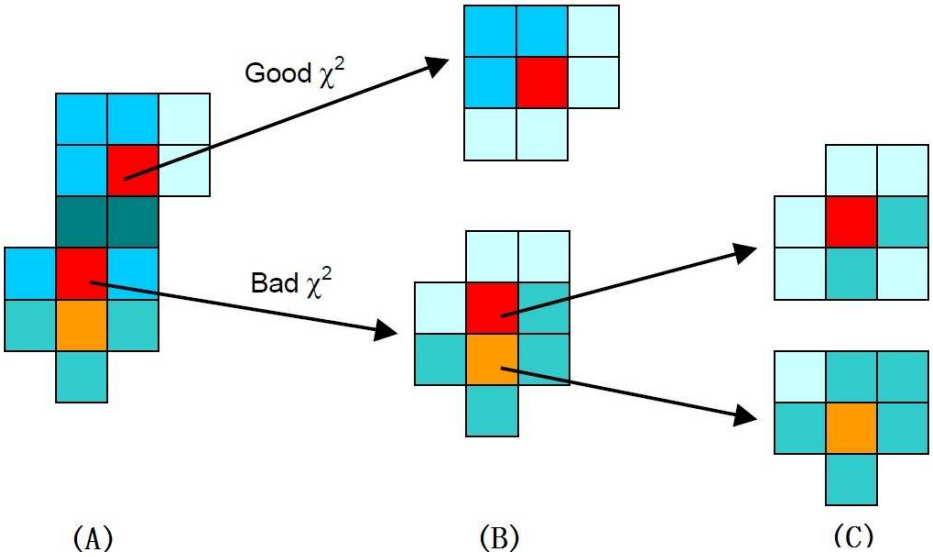

Figure 2.15: EMCal Pattern Recognition [114]. (A) A group of neighboring towers, whose energy depositions pass a pre-defined threshold, are identified. Local maxima (the tower with higher energy than all its neighboring towers) are found within the cluster. Each local maximum is treated as an independent EM shower candidate. (B) The identified showers are compared to the standard EM showers created by photons or electrons and the likelihood indicator χ^2 is calculated [113]. Note that χ^2 values for showers are optimized by splitting energy depositions in the shared towers among showers (the dark green towers in (A)). (C) If an identified shower passes the χ^2 test, it is then an established EM cluster. If not, the shower might be further split and yields more than one partially overlapping clusters.

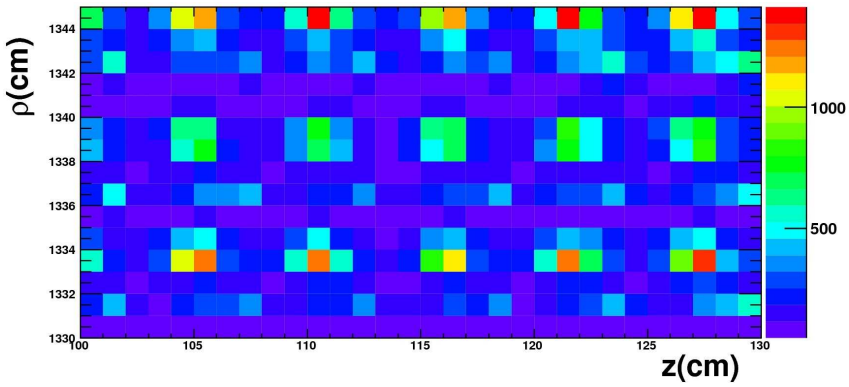

Figure 2.16: EMCal cluster position distribution. 2D histogram of ρ vs. z for part of a PbSc sector, $\rho = R\phi$ and R is the distance between EMCal and beam pipe ($\sim$ 5 meters). Color represents counts. Data from real events.

2.3.3 Photon Identification

EMCal provides an arrival-time measurement of the incident particles and thus has PID capabilities (cf. Sec-2.2.4 for charged particles PID). Timing resolution is crucial for PID and PbSc towers excel in this aspect. Other than identifying different species of charge hadrons, TOF information can also help select photons (and electrons/positrons) since they move at the speed of light.

Another method to separate hadrons from photons/electrons/positrons utilizes the fact that hadrons are Minimum Ionizing Particles (MIPs) and deposit only part of their energy in hadronic showers, as shown in Fig-2.17. Since the

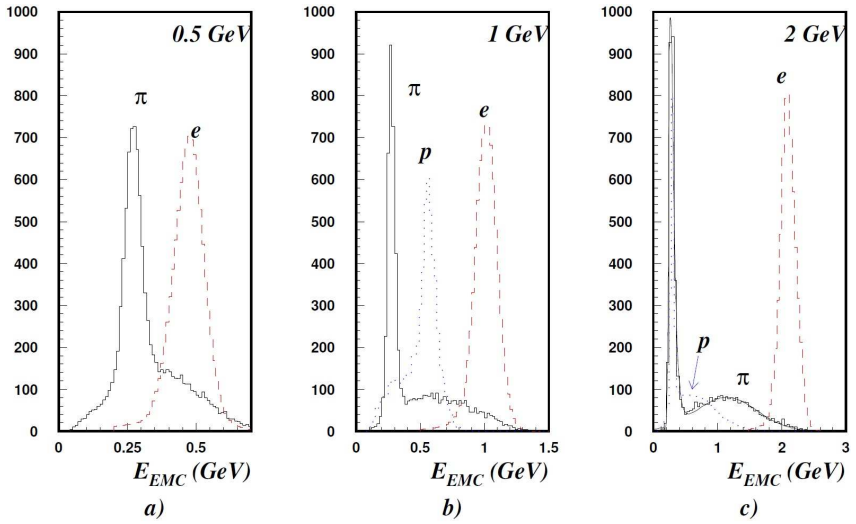

Figure 2.17: Distribution of shower energy (E_{EMC}) for electron, pion and proton test beam of 0.5, 1.0 and 2.0 GeV [97].

momentum for charged particles are measured (cf. Sec-2.2.2 and Sec-5.1.1), the energy (measured at EMCal, E_{EMC}) over momentum ratio E_{EMC}/p may provide information about particle species. For electrons/positrons, $E_{EMC}/p \approx 1$; while for hadrons, E_{EMC}/p are likely to be small.

In addition, the aforementioned χ^2 value indicate the extent to which the cluster created by the particle resembles a standard EM shower; therefore it can be utilized for photon identification. Finally, since PC3 is located right before EMCal, a so called "charge veto" cut can be employed to reject charged hadrons. The idea is that if a shower is located just behind a hit on PC3, then this shower is probably created by a charged particle since photons would not leave any hits on the PC.

2.4 Data Acquisition System

At top energy, the collision rate at PHENIX ranges from a few kHz for Au+Au collisions to around 500 kHz for p+p collisions. The data acquisition (DAQ) system is built to select interesting events and record them. A flow chart of the DAQ is depicted in Fig-2.18. Numbers on the plot might be outdated but

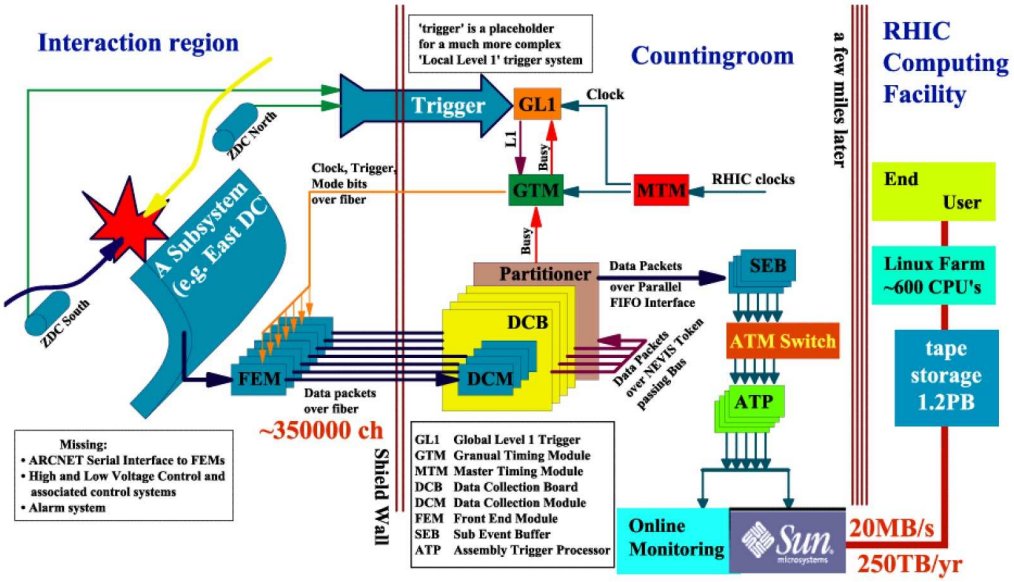

Figure 2.18: Illustration of the PHENIX DAQ [115], see text.

the framework remains the same. There are several components which interact with each other:

- The Master Timing Module (MTM) receive bunch-crossing signals from the 9.4 MHz RHIC clock. It then passes the signals to the Global Level 1 trigger (GL1) and the Granule Timing Modules (GTMs).
- The Frond End Modules (FEMs) are electronics attached directly on the detectors or connected to the detectors with short wires. They are the only part of DAQ that stay in the Interaction Region (IR) where the detector is installed and operated. The analog signals collected by the detector are stored in the FEMs that provide a buffer size of around 40 bunch-crossings. The signals can be digitized automatically in the FEMs for a certain set of detectors, or they are stored in analog form and digitized only after the GL1 signals to do so.
- GTMs are conductors of the FEM operations. When the DAQ is running, they continuously and automatically receive timing signals from

the MTM and send them to the FEMs. Trigger signals from GL1 are also forwarded to the FEMs by the GTMs in a similar fashion. During system diagnosis and troubleshooting, commands to the FEMs are issued via the GTMs as well.

- Only interesting events are recorded, because of both physics considerations and hardware/software limitations. For the purpose, of selection, event triggers are setup. At PHENIX, there are two levels of triggers. The first level consists of various Local Level 1 (LL1) triggers and the GL1 mentioned above. A LL1 trigger is associated with a particular detector. Triggers on BBC and ZDC (see Fig-2.18) are among the most important ones. When a predefined signal appears in the detector, LL1 fires. LL1 triggers from all different parts of the PHENIX detector are pooled (big "trigger" arrow on Fig-2.18) and the GL1 decision is made, which is then forwarded by GTMs to the FEMs to perform operations such as digitization. This process takes some time and it is important for the FEMs to have sufficiently large event buffers.

- Digitized event fragments from FEMs are passed to the Data Collection Modules (DCMs) where data are zero-suppressed (i.e. pedestal level of the signal is subtracted) and packaged; "packets" of PHENIX Raw Data Format (PRDF) is generated here.

- Four DCMs are installed to a Data Collection Board (DCB). GTMs, DCMs and the associate FEMs are organized into partitions. Each partition is a "mini-DAQ" system that has partial capability to work independently.

The rest of the data processing is handled by the PHENIX event builder (cf. Fig 2.19). DCM packets (event fragments) are passed to SubEvent Buffers (SEBs), each one of which deals with a specific part of the event. The fragments are then reorganized by the Gigabit Switch so that fragments from the same event are put together and transferred to the Assembly and Trigger Processors (ATPs), where a full event is created from the pieces. The level 2 trigger may fire at this assembly stage as well. Full events are then buffered and finally recorded on disks as PRDF files [116].

2.5 Computing Framework

Raw data collected at PHENIX each year typically have the size of several hundred TeraBytes (TBs); in 2010 the number exceeded one PetaByte (PB).

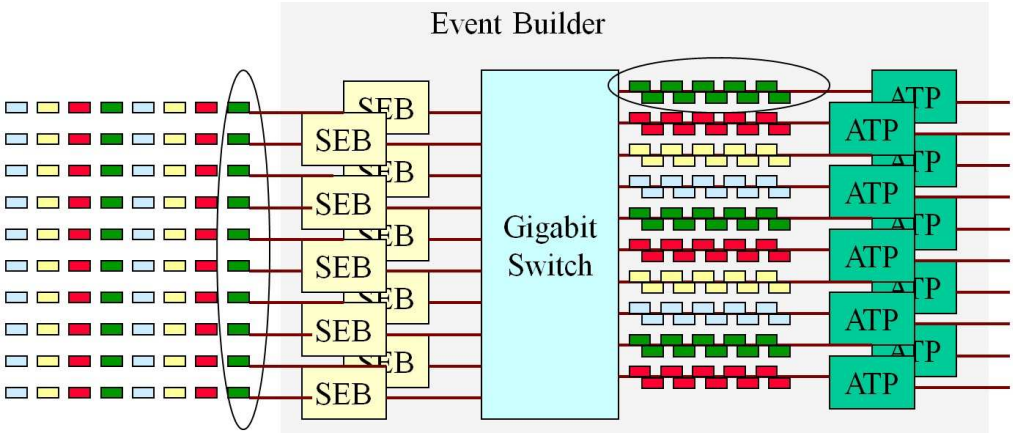

Figure 2.19: PHENIX event builder. Each small block represents an event fragment and neighboring blocks with the same color indicate a full event (e.g. the circled dark green blocks). See text.

The raw data are encoded in the form of PRDF and placed in the mass storage governed by the High Performance Storage System (HPSS[1]).

The PRDF files are too large and contains lots of information which is not directly related to physics analysis. Therefore, they are transformed into a more compact form called Data Summary Tape (DST). This computing intensive task is carried out by about 4000 CPUs working in parallel and usually takes several weeks. The produced DST files, which have the size of less than 100 TB, are placed in the dCache[2] distributed storage system.

Analyzers in PHENIX typically logged into the RHIC Computing Facility (RCF) remotely and perform their daily analysis. RCF utilizes a BlueArc[3] Network Storage System (NSF) that has a large I/O bandwidth and allows hundreds of analyzers to read and write at the same time. However, a system like this is very expensive and is not equipped to accommodate the full set of DST files. Typically only a small fraction (depending on data size) of the DST files are placed on NSF for code testing purposes.

To access the full data, a framework referred to as AnalysisTrain was developed and used by PHENIX analyzers. The train runs weekly and offers an interface for data processing in the form of C++ abstract classes. Analyzers write derived classes and implement their analysis modules. The C++ polymorphism feature makes sure that the users' implementation are invoked by the train. Each piece of data is fetched by the train only once and then passed

[1]http://www.hpss-collaboration.org/
[2]http://www.dcache.org/
[3]http://www.bluearc.com/

through all the analysis modules by request. In this way the I/O stream is minimized. Only the train conductor has the access to dCache where the full data is stored.

Chapter 3

Construction and Calibration of Event Signatures

Several fundamental event signatures are not directly measured as detector responses. These include centrality (along with N_{part} and N_{coll}) and event planes. These variables are essential information of the collision and are necessary for nearly all physics measurements. Their construction and calibration are discussed in this chapter.

3.1 Estimation of N_{part} and N_{coll}

At RHIC, a bunch of nuclei are accelerated and guided to the other bunch of nuclei moving in the opposite direction. A nucleus-nucleus collision may happen during the bunch-crossing, and the collision products that are typically hundreds of particles are collected. During this process, we have no control over the centrality of the nucleus-nucleus collision. Therefore, information about the collision, including the number of participating nucleons (N_{part}) and number of binary collisions (N_{coll}), must be modeled. In this section, the Glauber model [17] is employed to illustrate how these geometric quantities are determined.

3.1.1 Glauber Monte Carlo Simulation

In the Glauber model, a nucleus-nucleus collision is treated as a superposition of nucleon-nucleon collisions. The nucleons are assumed to move in straight lines and in parallel with the trajectory of the nucleus. Moreover, the nucleons are not scattered after colliding with other nucleons (i.e. their trajectories

remain unchanged) and the wounded nucleons can still collide with other nucleons with the ordinary inelastic nucleon-nucleon cross section σ_{inel}.

Nucleons in each nucleus are populated according to the nuclear density profile parameterized by the Woods-Saxon function:

$$\rho(r) = \frac{\rho_0}{1 + \exp(\frac{r-R}{a})} \tag{3.1}$$

where r is the distance to the center of gravity of the nucleus. ρ_0 is the parameter that determines the overall level of the density; it's a common factor for all nucleons and not relevant to this analysis. R is the radius of the nucleus and for Au it's 6.55 fm; a is the diffusiveness parameter and set to be 0.535 fm by default [117].

The Monte Carlo (MC) simulation is employed to best explore the fluctuations associated with the calculation of N_{part} and N_{coll}. A nucleus-nucleus collision modeled by the Glauber model is depicted in Fig-1.8. Nucleons are placed with a probability proportional to the Woods-Saxon function and they may overlap inside each nucleus. The impact parameter b for the two nuclei is randomly generated and then the two nuclei are made to "collide".

A nucleon is considered to be a participant if the transverse distance d between itself and any other nucleon (from the other nucleus) satisfies the condition: $\pi d^2 < \sigma_{\text{inel}}$ (the "black disk" model shown in Fig-3.1 by solid black line). Other schemes include

- a "grey disk" model (dashed grey line) in which the collision happens with probability $\sigma_{\text{inel}}/\sigma_{\text{tot}}$ when $d < \sqrt{\sigma_{tot}/\pi}$, and
- a Gaussian model in which the probability of collison is a continuous function (red dotted line) in the form of $1 - [1 - p_1 \exp(-p_2 b^2)]^2$ with $p_1 = 0.755$ and $p_2 = 0.89$ fm^{-2}.

The calculations with these two models provide a way to estimate systematic uncertainties in the simulation. σ_{inel} for 62(39) GeV collisions is estimated to be 37(34) mb and we allow a ± 3 mb variation to help estimate the uncertainties associated with σ_{inel}. After nucleon-nucleon collisions are defined, N_{part} is just the total number of wounded nucleons and N_{coll} is the total number of nucleon pairs that collide with each other.

3.1.2 Results: N_{part} and N_{coll} in Various Centrality Bins

The N_{part} distribution generated from the above procedures is used as an input to the calculation of trigger efficiency and the subsequent centrality

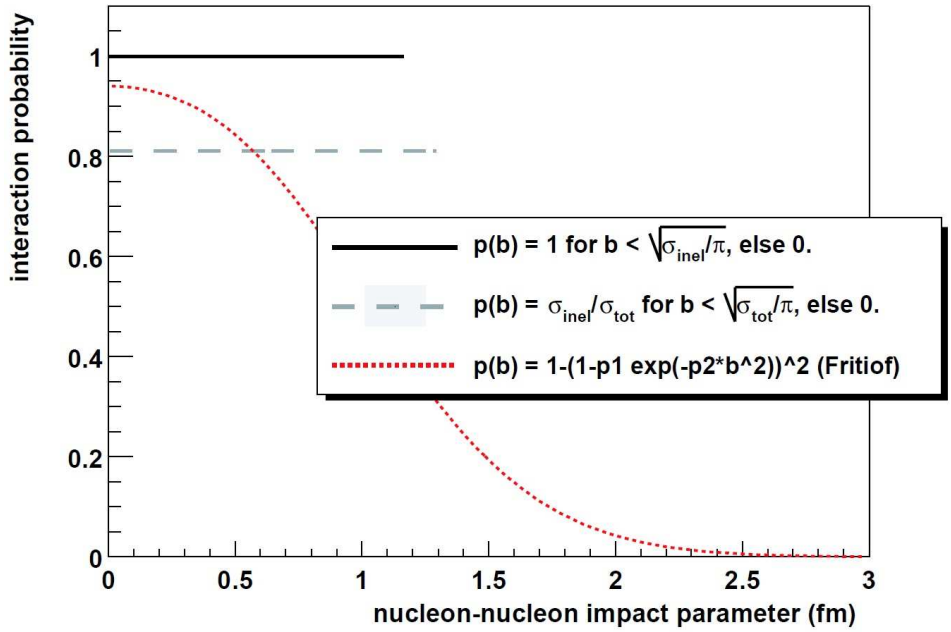

Figure 3.1: Different criteria of defining a nucleon-nucleon collision in the Glauber MC [118]. See text. The nucleon-nucleon impact parameter b in this graph is denoted by d in the text to avoid confusion.

definition. When centrality is defined, each simulated collision can be tagged with a centrality value and distributions of $N_{\rm part}$ and $N_{\rm coll}$ can be found out for a particular centrality range. For 10% step centrality bins, the $N_{\rm part}$ and $N_{\rm coll}$ distributions are plotted in Fig-3.2 and Fig-3.3 respectively. Due to fluctuations, events with larger centralities don't necessarily have greater $N_{\rm part}$ and $N_{\rm coll}$ values. Therefore, the distributions of $N_{\rm part}$ and $N_{\rm coll}$ for neighboring centrality bins may overlap. It's also observed that the distributions for $\sqrt{s_{NN}}$ = 62 and 39 GeV look very similar, which is expected.

The averaged values of $N_{\rm part}$ and $N_{\rm coll}$ in various centrality bins are summarized in Tab-3.1.2 and Tab-3.1.2. These values are important because most physics observables are measured in a certain centrality range. With the listed average values here we could have a rough idea of the $N_{\rm part}$ and $N_{\rm coll}$ values for that centrality range. In addition, these values provide a good basis for experiment comparisons since centrality itself might be defined with different methods for different experiments. The systematic errors are estimated based on the comparisons of independent simulation results with the model parameters set to their upper and lower bounds. These parameters include σ_{inel}, R and a in Eqn-3.1 and trigger efficiency (centrality definition). Different models of nucleon collisions (Fig-3.1) are also compared.

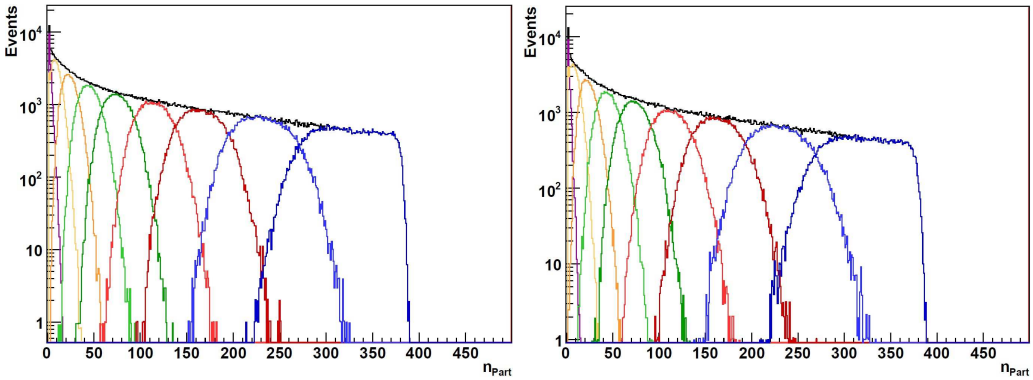

Figure 3.2: N_{part} distributions for 10% step centrality bins [117]. Left(Right) panel for $\sqrt{s_{NN}} = 62$ (39) GeV. Central collisions generally have larger N_{part}.

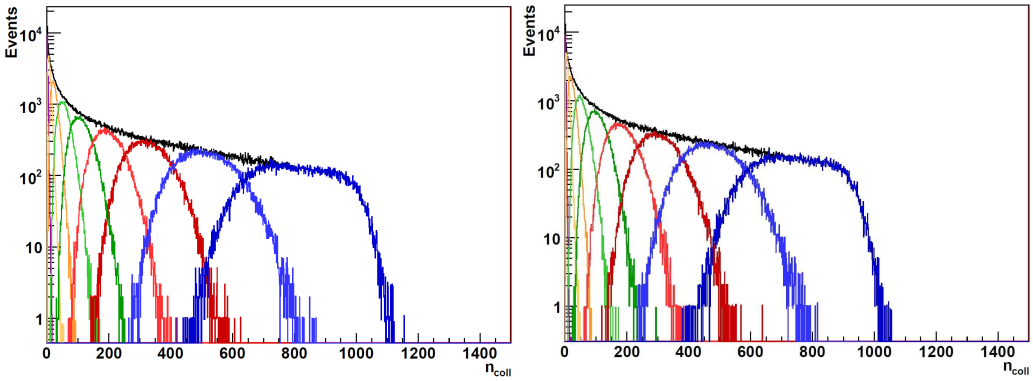

Figure 3.3: N_{coll} distributions for 10% step centrality bins [117]. Left(Right) panel for $\sqrt{s_{NN}} = 62$ (39) GeV. Central collisions generally have larger N_{coll}.

Table 3.1: Averaged N_{part} and N_{coll} values for 10% step centrality bins. $\sqrt{s_{NN}} = 62$ GeV [117].

Centrality Bins	$\langle N_{\text{part}} \rangle$	Sys.Err.	$\langle N_{\text{coll}} \rangle$	Sys.Err.
$0 - 10\%$	319.6	4.1	843.0	100.5
$10 - 20\%$	229.7	4.5	535.8	58.1
$20 - 30\%$	163.8	5.0	337.2	32.9
$30 - 40\%$	113.4	4.7	203.3	20.1
$40 - 50\%$	74.6	3.7	114.3	11.8
$50 - 60\%$	45.2	3.4	57.8	6.7
$60 - 70\%$	24.1	2.6	25.2	3.5
$70 - 86\%$	8.0	0.8	6.6	0.8

Table 3.2: Averaged N_{part} and N_{coll} values for 10% step centrality bins. $\sqrt{s_{NN}} = 39$ GeV [117].

Centrality Bins	$\langle N_{\text{part}} \rangle$	Sys.Err.	$\langle N_{\text{coll}} \rangle$	Sys.Err.
$0 - 10\%$	316.6	4.3	777.2	95.0
$10 - 20\%$	227.2	5.3	496.7	54.8
$20 - 30\%$	161.7	5.4	313.8	31.9
$30 - 40\%$	112.2	4.5	191.0	21.2
$40 - 50\%$	73.8	4.2	108.1	12.7
$50 - 60\%$	44.8	3.2	55.4	6.3
$60 - 70\%$	23.7	3.3	24.2	4.4
$70 - 86\%$	7.7	1.4	6.2	1.4

3.2 Trigger Efficiency Study

An event is triggered by the response of one or more detectors (cf. Sec-2.4). For example, for PHENIX the BBC LL1 is triggered by one or more hits detected in both arms (south and north) of the BBC. In central collisions, the event is almost surely triggered due to the high multiplicity. However for peripheral collisions, though outgoing particles are still produced, they might not hit the particular trigger detector and the event is unnoticed. In other words, trigger efficiency drops to non-trivial values (less than 100%) for peripheral events.

Trigger efficiency is defined w.r.t. the Minimum Biased (MB) events, which are collisions satisfying the least set of requirements to be considered meaningful. For Run10 Au+Au collisions of 39 and 62 GeV, a MB event is defined by the the coincidence of the following two observations in a collision:

- two or more hits at both arms of the BBC;
- vertex position $z < 30$ cm.

At PHENIX, the integrated trigger efficiency for the inclusive MB events is set to be the upper limit of centrality. Therefore, it is a prerequisite for centrality definition.

To find out trigger efficiency, distributions of hits collected in PC1, PC3, RXI, RXO and BBC are compared to those built from simulations where no events are lost. The simulations are carried out in the following steps [119].

- N_{part} distributions similar to those shown in Fig-3.2 (the inclusive black lines) are generated by Glauber MC. After normalization, this distribu-

tion gives the probability $\mathrm{P}(N_{\mathrm{part}})$ of an event with a particular N_{part} value.

- the hits registered on each detector is positively correlated to N_{part}. The number of hits generated by each participating nucleon is modeled by a Negative Binomial Distribution (NBD).

- a convolution of $\mathrm{P}(N_{\mathrm{part}})$ and NBD gives the simulated hits distribution. To be more specific, for each simulated event we pick up a N_{part} value with probability $\mathrm{P}(N_{\mathrm{part}})$ and then generate hits from the i-th nucleon n_i from NBD. Therefore the number of total hits for that event is $N_{\mathrm{hits}} = \sum_{i=1}^{N_{\mathrm{part}}} n_i$. This process is iterated for sufficiently many times and the results are organized as a histogram of N_{hits}, which is the demanded simulated distribution.

In the above procedures, two tacit assumptions are made. The first one assumes each nucleon creates hits independently and the number of total hits of an event is simply the linear sum of the hits created by individual nucleons. This assumption is not true and corrections need to be applied [119]. The second assumption is that in real events the η-distribution of tracks must remain relatively the same for different centrality ranges, so that the number of hits in the detector is only related to centrality. This assumption fails for the BBC at low beam energies of 39 and 62 GeV. Therefore the BBC is not used in this study.

The calculation of trigger efficiency is illustrated on Fig-3.4. Under the

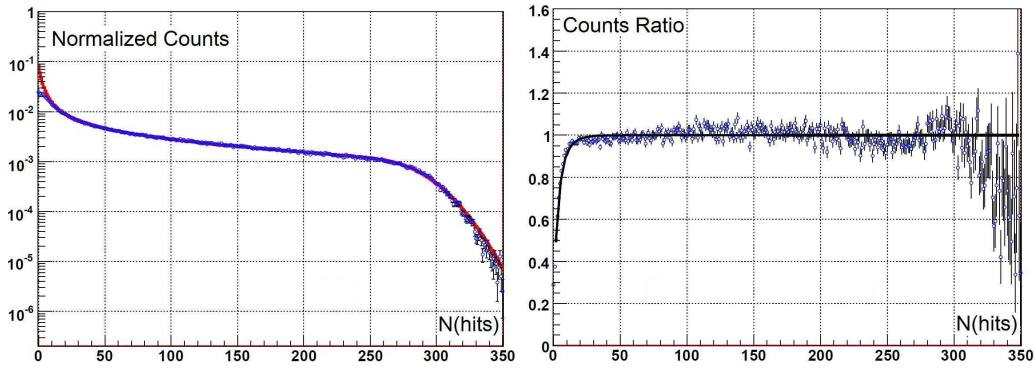

Figure 3.4: Illustration of trigger efficiency calculation [119]. Comparisons between PC1 hits measured in real events (red) and generated via simulations (blue). Left panel: normalized counts vs. N_{hits}. Right panel: the ratio of Counts(real data)/Counts(simulation). In peripheral collisions where N_{hits} is small, the ratio drops sharply, reflecting the loss of efficiency.

assumption that efficiency is 100% in central collisions, parameters in the simulation (mostly in the NBD model) are optimized to reproduce a $N_{\rm part}$ distribution that best matches the one from real data at the large $N_{\rm part}$ region (left panel of Fig-3.4). As a results, the ratio on the right panel is very consistent with 1 for $N_{\rm part} > 30$. In the small $N_{\rm part}$ region, the ratio falls below unity, indicating missing events. The integrated trigger efficiency is calculated as total number of events from real data divided by total number of events from simulation.

The calculated efficiency values with hits from different detectors are summarized in Tab-3.2. For events with large $N_{\rm part}$, the simulated hits distribu-

Table 3.3: Summary of trigger efficiency study [119].

Detector	Eff.(39 GeV)[a]	χ^2/NDF	Eff.(62 GeV)	χ^2/NDF.
PC1	85.16 ± 0.31	1.40	85.84 ± 0.23	1.53
PC3	85.56 ± 0.36	1.18	84.72 ± 0.84	1.73
RXI	85.59 ± 0.26	1.06	86.03 ± 0.14	1.35
RXO	87.41 ± 0.25	2.54	86.09 ± 0.20	1.35
Mean	85.90 ± 0.87	N/A	85.67 ± 0.56	N/A

[a] error reflects statistical errors of real data.

tions match the real ones very well, as indicated by the very small χ^2/NDF values. The systematic uncertainties are estimated based on re-calculation of trigger efficiency with different Glauber parameters and the comparisons among different methods to correct the linear superposition assumption. The uncertainty values are estimated to be 2.0% for both 39 and 62 GeV.

In summary, the percentage efficiency values are estimated as 85.9 ± 2.0 for 39 GeV and 85.7 ± 2.0 for 62 GeV

3.3 Centrality Definition

The trigger efficiency is rounded to an integer number and serves as the total number of centrality divisions; each division represents 1% of centrality. The centrality definition is then a matter of allocating events into the the centrality divisions.

For PHENIX, centrality was initially calculated with the clock method (cf. Fig-2.5). After 2007, a more straightforward "BBC-Only" method was employed. Centrality definition of Run10 62 and 39 GeV is implemented with the "BBC-Only" method.

3.3.1 BBC-Only Method

The basic idea of the "BBC-Only" method is simple: the distribution of BBC total charge $D_{BBC}(Q)$ is built based on MB events; it is then divided evenly (in terms of the number of events in each division) into the total number of centrality divisions; in the case of Run10 62 and 39 GeV, the number is 86.

To implement the even division, event counts are accumulated bin by bin on $D_{BBC}(Q)$, from the one with the highest BBC charge value. Eventually the process reaches a $D_{BBC}(Q)$ bin so that the accumulated event counts pass 1/86 of the total number of events; the lower delimiter of this bin is recorded and any event with BBC charge larger than this value is marked with centrality 99%. The process proceeds until all 86 delimiters are found.

From the above process, we see that the minimum increment of BBC charge is the bin size of $D_{BBC}(Q)$, which introduces a discretization error in the centrality definition proportional to:

$$\frac{\text{number of events in one bin of } D_{BBC}(Q)}{\text{number of events in 1\% of centrality}}. \tag{3.2}$$

The denominator is just 1/86 of the total number of events and a constant; and the numerator is directly related to the bin size of $D_{BBC}(Q)$. Therefore, to reduce the discretization error in the definition of centrality, the $D_{BBC}(Q)$ histogram must have very fine binning in the BBC charge. Traditionally, the bin size is set to 0.1. However at the relatively low beam energy of 62 and 39 GeV, the charge signal deposited in BBC for each event is less. To adjust accordingly, a smaller bin size of 0.01 was implemented.

An exemplary plot of $D_{BBC}(Q)$ is shown in Fig-3.5. Note the y-axis represents event counts and is of logarithm scale. In the region where the BBC charge values are large, the counts are relatively small and each centrality division would span a wide range of BBC charge values. However event counts grow exponentially as the BBC charge values decrease, and the centrality divisions become more and more narrower. It is in this region that a fine binning of BBC charge is essential (cf. Eqn-3.2). As we will see later, even with the BBC charge bin width of 0.01, the centrality division is not uniform and fluctuations are observed in peripheral collisions, which have small BBC charge values.

Though it seems straightforward, two subtleties complicate the process. The first one is that for events with different collision vertex position z, BBC charge distributions are naturally different. Consequently, centrality is defined for events with different z values separately. The z values of MB events lie in the range of $(-30, 30)$ cm and are divided into 12 equal length bins. Centrality

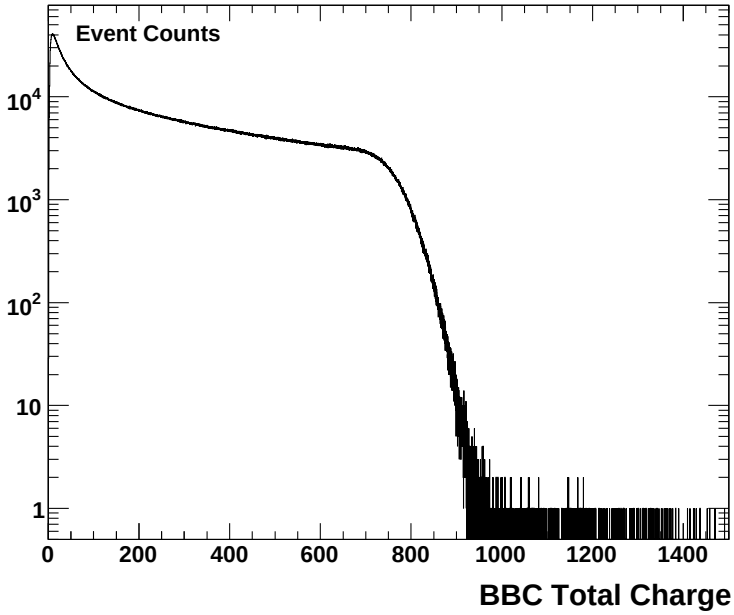

Figure 3.5: BBC total charge distribution, $\sqrt{s_{NN}} = 62$ GeV, collision vertex position $z \in (-5, 0)$ cm.

is then defined individually for events in each z bin. For example, centrality of events with vertex position $z \in (-5, 0)$ cm is defined based on Fig-3.5.

Since there are 12 z-vertex bins to categorize events, and for events in each bin a set of 86 constants are needed for centrality definition, a total number of 1032 constants are recorded in the centrality calibrator.

3.3.2 Run by Run Variation

Before the second subtlety is introduced, we want to clarify the meaning of the term "Run". This word refers to two similar concepts:

- if it's followed by two digits like "Run10", then it refers to the running period of RHIC between year 2009 and 2010.
- if it is used to refer a six digit number such as "315000", then it actually points to a specific segment of data and that number is similar to a time stamp since it increases monotonically as time passes by. For example "Run 228411" is a piece of data collected in Run7 and "Run 311553" in Run10. Whenever the DAQ is stopped and started again, a new run number is assigned.

The size of the data segment corresponds to the continuous running time of the DAQ and is subject to large variations. The DAQ could be forced to stop immediately after the run begins because of a severe subsystem malfunction, or it could run as long as the the beam lasts (not more than 1 hour in this case). The data quality among segments are not consistent as well. It is generally related to the beam condition such as the level of backgrounds in the beam. In addition, sometimes the DAQ is kept running even though one or more subsystems are not fully functional; the data segment might not be used if those subsystems are heavily involved in the analysis of interest.

Centrality definition analysis requires sufficient statistical significance, therefore data segments are combined, provided no significant variation among the run segments are observed. Since the analysis is based on the BBC charge signal, the second subtlety is therefore the variation of the BBC performance among run segments. If the BBC has a uniform performance over a certain period, data segments in that period can be combined together to provide a unique centrality definition for all events from those segments.

Under the assumption that the shape of $D_{BBC}(Q)$ from each data segment is invariant, the mean value of $D_{BBC}(Q)$ provides a scalar character of the BBC performance. The run number dependence of the BBC mean charge is shown in Fig-3.6 for all the run segments of Run10 $\sqrt{s_{NN}} = 62$ GeV. From

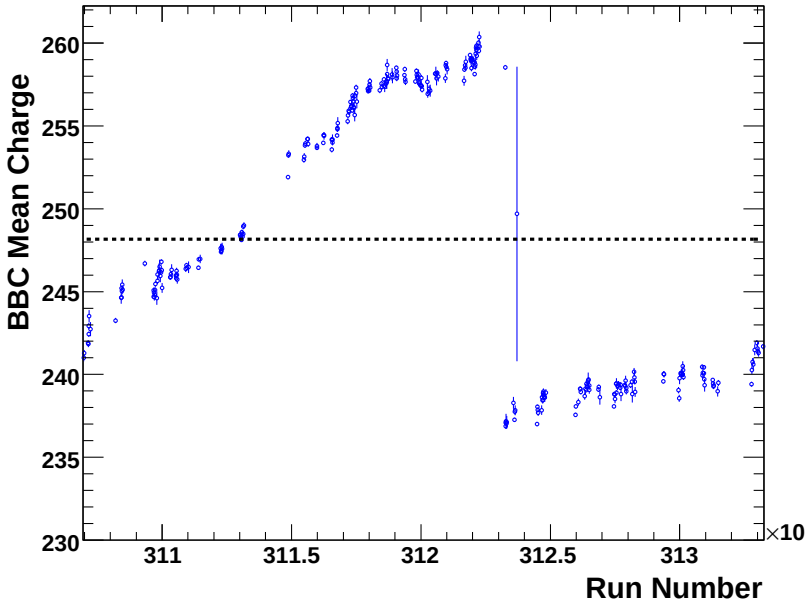

Figure 3.6: BBC mean charge vs. run number, $\sqrt{s_{NN}} = 62$ GeV. The dotted line at 248.15 indicates the averaged BBC mean charge for all the runs.

the graph we see a non-trivial structure: as the run number rolls forward, the BBC mean charge values experience a monotonous increase, followed by a sudden drop and then another monotonous increase. The dotted line shows the averaged BBC mean charge at 248.15; the maximum deviation from the average can be as large as 4% (thus 8% difference between the maximum and minimum). However, if the runs are divided into the following three groups,

- Group-A: 310600∼311400
- Group-B: 311400∼312327
- Group-C: 312326∼313400

then within each group the variation is less than 1.5%.

3.3.3 Scale of BBC Charge

Even if the run-by-run variation is small, if all the segments in a group are directly aggregated, we could still encounter a misalignment problem. A naive example is that if the BBC charge values for one run are consistently 1% lower than all other runs, for that run there would be roughly no event with 99% centrality.

A scaling technique is implemented to overcome the misalignment issue. We denote the BBC mean charge from run i as $\bar{q}_i$ and the the average of that group as $\bar{q}_{\text{ave}}$; if BBC charge values (of all events) in run i are uniformly scaled by $\bar{q}_{\text{ave}}/\bar{q}_i$, the scaled distribution $D^i_{BBC}(\text{Scaled } Q)$ would have a mean value of $\bar{q}_{\text{ave}}$. Since we assume that the shape of $D_{BBC}(Q)$ for all runs is the same, $D^i_{BBC}(\text{Scaled } Q)$ should be the same for all runs. These distributions can then be aggregated and the centrality delimiters found. For centrality determination, the BBC charge values for each run are scaled with the above factor first and then compared to the delimiters for centrality values. In this way, the charge distribution would be divided evenly and we define consistent centrality values for all the runs within a run group.

In summary, the following two measures are employed to deal with variations in BBC charge:

- centrality is defined in vertex-z bins with 5 cm width;
- BBC charge is scaled run-by-run.

Centrality is then calculated with the procedures discussed in Sec-3.3.1. The second item in the above list potentially has a significant impact on the centrality definition, due to the size of the scaling factors. This scheme is thus referred to as "scale-and-divide" in the following sections.

3.3.4 Cross Check of Centrality Definition

The centrality distributions for Group-A, Group-B, Group-C and the inclusive 62 GeV are shown on Fig-3.7. It can be seen that a very good flatness (com-

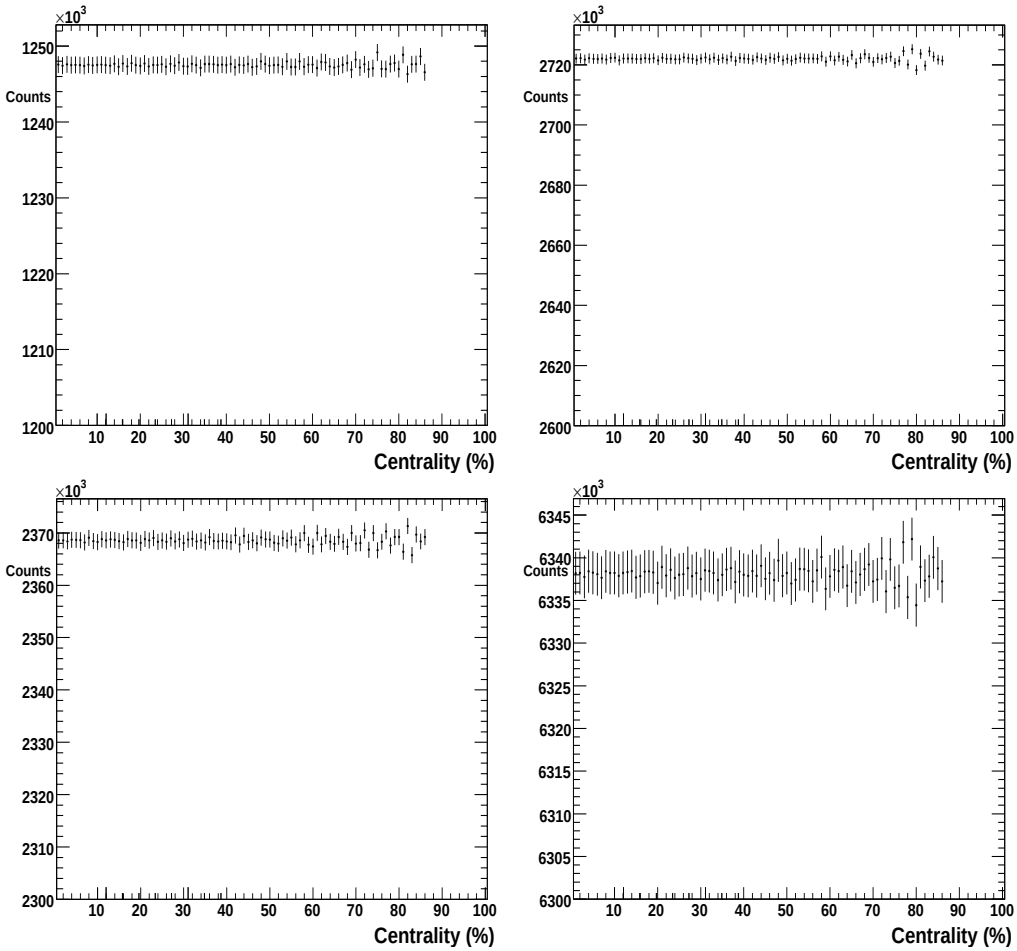

Figure 3.7: Centrality distribution, $\sqrt{s_{NN}} = 62$ GeV. Panels: top-left, Group-A; top-right, Group-B; bottom-left, Group-C; bottom-right, all 62 GeV runs

pared to the size of error bars) is achieved for all distributions, indicating a robust centrality definition. In peripheral collisions, fluctuations are observed; however they are less than 0.1%, and thus negligible.

The flatness observed in Fig-3.7 is expected; it only tells us that the centrality definition method discussed above is implemented correctly. To check the robustness of the scale-and-divide scheme, we need to see whether the flatness of the centrality distribution is preserved in individual runs or run groups that are smaller than the ones (Group-A,B,C) based on which centrality is de-

fined. If the method is pathological, non-flatness of the centrality distribution is expected for the runs with large scaling factors.

A test was designed to investigate the arguments above and the setup is best illustrated in Fig-3.8. Two target run groups are identified as:

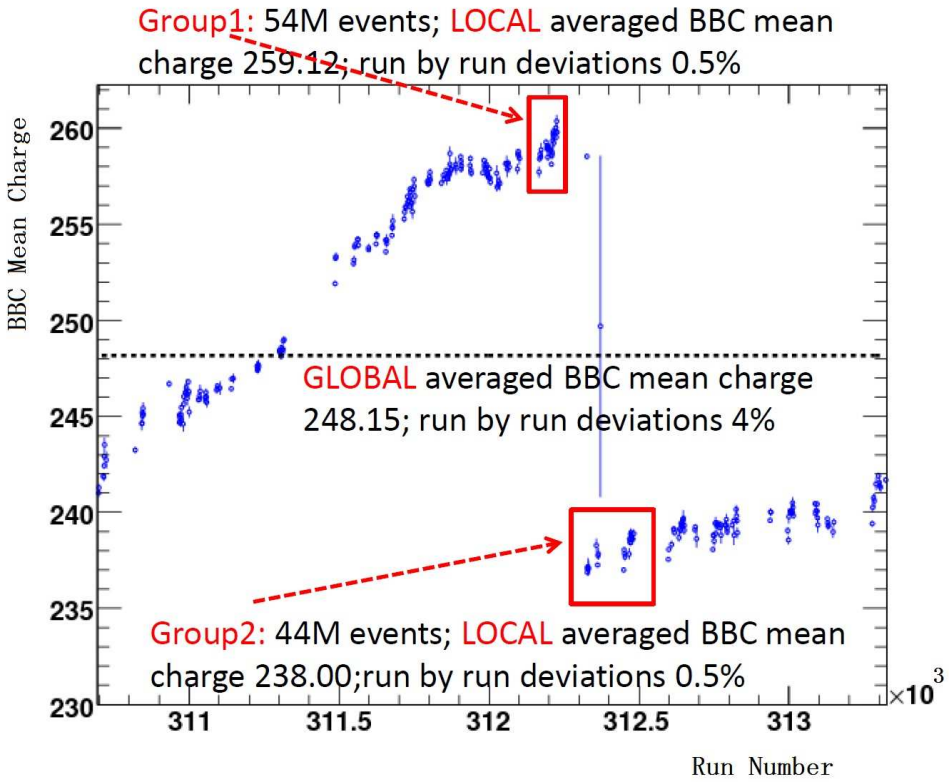

Figure 3.8: Setup of the centrality robustness check. The figure is the same one as shown on Fig-3.6.

- Group1: 312167∼312226;
- Group2: 312327∼312483.

They are indicated by red boxes on Fig-3.8 and represent runs with the highest and lowest BBC mean charge respectively. Centralities for the runs in these two groups are defined in 3 schemes; in each scheme, the average of BBC mean charge $\bar{q}_{\rm ave}$ is chosen individually and the corresponding scaling parameters $\bar{q}_{\rm ave}/\bar{q}_i$ are largely different:

- LOCAL definition - $\bar{q}_{\rm ave}$'s are determined in each of the target groups (259.12 for Group1 and 238.00 for Group2).

- GLOBAL definition - a universal $\bar{q}_{\text{ave}}$ is calculated based on all the runs, the values is 248.15.

- ABC definition - $\bar{q}_{\text{ave}}$'s are found in the aforementioned three run groups, Group-A,B,C.

The $\bar{q}_{\text{ave}}$'s used in LOCAL and GLOBAL are indicated on Fig-3.8 as well. What's more important are the run-by-run variations relative to $\bar{q}_{\text{ave}}$; they are the scaling factors that we want to investigate and have the values of 0.5%, 4.0% and 1.0% for LOCAL, GLOBAL and ABC scheme respectively. In addition, to see the effects of bin size, in the LOCAL and GLOBAL scheme the minimum BBC charge increment is 0.1 while in ABC scheme the the bin size is narrowed down to 0.01.

The centrality distributions for events in Group1 and Group2 using the three schemes are respectively diagramed on Fig-3.9. The observations are listed below:

- For peripheral collisions, we see that the usage of narrow bin size 0.01 significantly reduces the fluctuations as shown by the distributions with ABC centrality definition scheme.

- For central and mid-central events, the distributions for the LOCAL scheme gives a flat distribution; this is expected since run-by-run deviations inside the run groups are less than 0.5%. The flatness of the ABC centrality distributions are better than the GLOBAL ones; it is consistent with the natural expectation that the flatness of centrality definition is positively correlated to the scaling factors, i.e. run-by-run variations relative to the average.

If we focus on the ABC scheme that we implemented as the chosen one for the 62 GeV dataset, we see that the non-flatness in centrality definition is quite limited, even for the small run groups (Group1 and Group2) with the largest possible deviations to $\bar{q}_{\text{ave}}$'s.

To advance one step further, the direct influences of centrality non-flatness on physics observables are studied. Our choice of the observable here is the raw π^0 spectrum, detailed analysis of which is documented in Chapter-4. The cross-check is to compare the raw π^0 spectrum obtained within the two run groups (Group1 and Group2); for each run group two centrality definition schemes are used: Global and Local, with scaling factors around 4.0% and 0.5% respectively; these two schemes are chosen because they give the largest contrast. The results are shown in Fig-3.10. Since the non-flatness (bin-by-bin variations) might be averaged out when the the results are integrated for

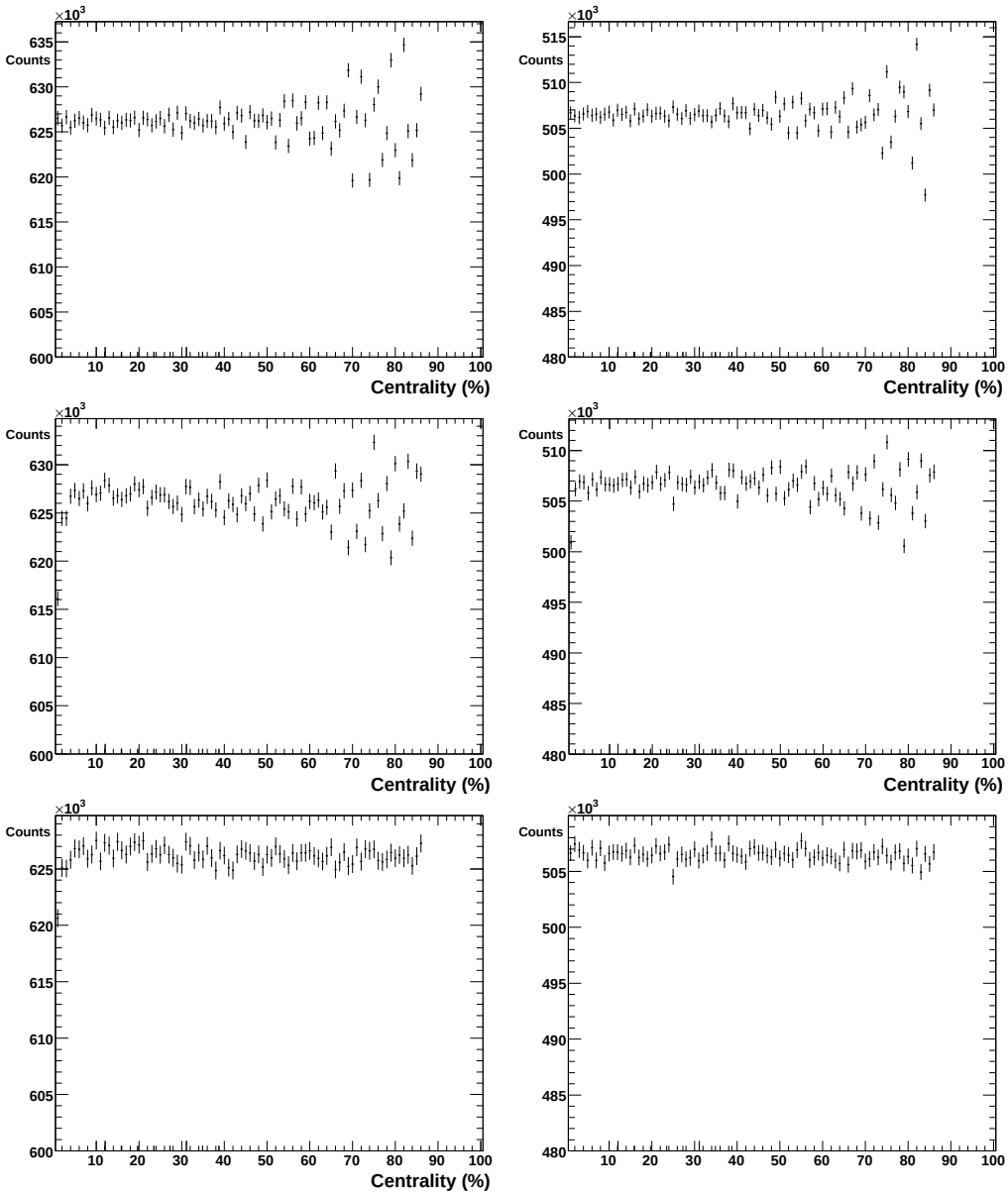

Figure 3.9: Centrality distribution cross-check for $\sqrt{s_{NN}} = 62$ GeV. Panels on left/right show the distributions for Group1/Group2. The top/middle/bottom panels correspond to the LOCAL/GLOBAL/ABC schemes.

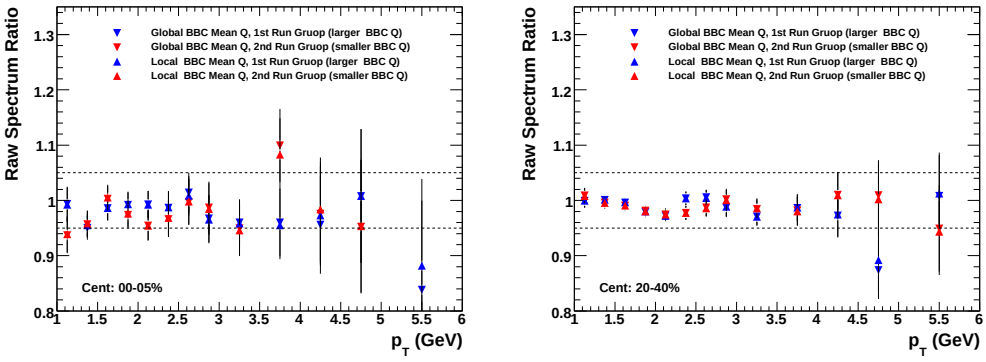

Figure 3.10: Centrality definition cross-check with raw π^0 spectrum. The spectra are divided by the inclusive 62GeV dataset to better illustrate the comparison. $\sqrt{s_{NN}} = 62$ GeV. centrality: $0-5\%$ for left panel and $20-40\%$ for right panel. See text.

a certain centrality range, two centrality ranges are presented in Fig-3.10, a narrow one $(0-5\%)$ and a much wider one $(20-40\%)$. The point here is to compare different centrality definition scheme, represented by up and down triangles for LOCAL and GLOBAL scheme respectively. We see that very good agreement is achieved. The differences between blue and red, and the deviations of the ratios from unity reflect the run-by-run variation of the π^0 spectrum themselves and not relevant here. Investigations for other centrality ranges exhibit the same patterns.

In summary, we conclude that with the ABC scheme implemented, the centrality distribution for 62 GeV dataset are mostly flat (for inclusive 62 GeV dataset, cf. Fig-3.7 bottom right panel; for smaller run groups, cf. Fig-3.9 bottom panels). We further demonstrate that even if a few percent of non-flatness is allowed, physics observables are not affected, partially due to the fact that the results are almost always integrated over a certain centrality range and possible effects are smeared out.

So far only the centrality definition for 62 GeV has been considered. For 39 GeV the case is much easier since the run-by-run variation of the BBC mean charge is less than 1% around the averaged value of 148.25 (cf. Fig-3.11 left panel). Based on our previous study, no further run group division was necessary. The centrality distribution for the inclusive 39 GeV dataset is shown on the right panel of Fig-3.11.

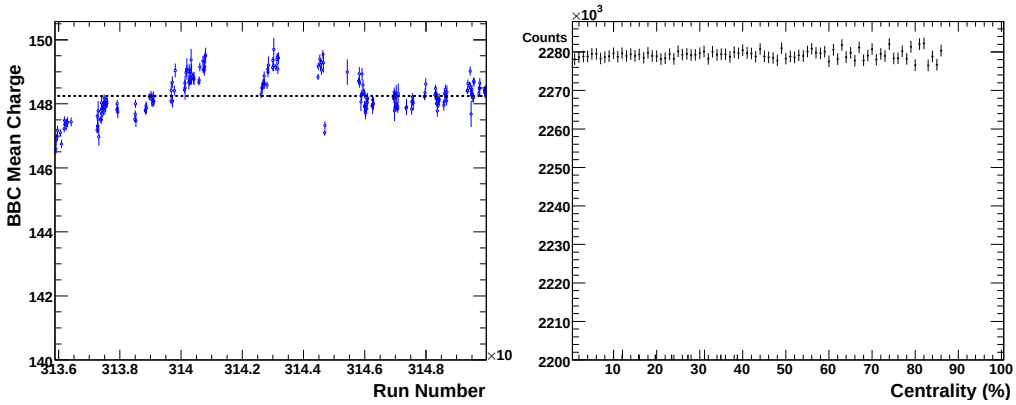

Figure 3.11: Centrality definition for $\sqrt{s_{NN}} = 39$ GeV. Left panel: run number dependence of BBC mean charge. Right panel: centrality distribution.

3.3.5 Quality Assurance

Quality Assurance (QA) refers to the process of discovering and excluding bad segments of data. As mentioned in Sec-3.3.2, a subsystem failure (or other possible reasons) may results in data segments that are inappropriate for a certain analysis. Since centrality is almost universally used, the identification of runs with ill-defined centrality is particularly important and beneficial to other analyses using the dataset.

There are different approaches to define bad centrality distributions. One of them is to check the flatness by observing the χ^2/NDF value of a horizontal line fit to the centrality distribution. The run number dependence of the χ^2/NDF values could then tell us the bad runs that have much large χ^2 values. Another method is to check the fraction of events for a particular centrality range. For example $5/86 = 5.8\%$ of the total events are expected to fall into the $0 - 5\%$ centrality range. The run number dependence of the fractions for four centrality ranges are depicted in Fig-3.12. We could easily identify the outliers that would be excluded. A closer look at them reveals abnormal BBC charge distributions, most likely due to some sort of BBC malfunctioning. A more comprehensive QA, including investigations of run-by-run dependence of the following variables:

- number of events,
- the center and width of collision vertex z distribution,
- aforementioned χ^2/NDF reflecting flatness, and
- event fractions in Fig-3.12

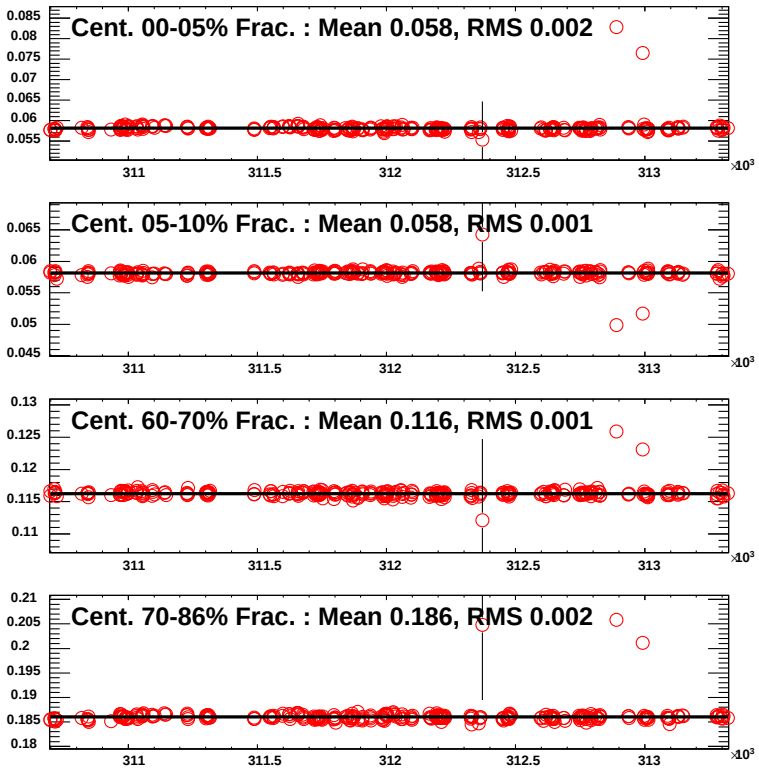

Figure 3.12: Fraction values vs. Run Number. Centrality definition QA for $\sqrt{s_{NN}} = 62$ GeV. Fraction values (number of events in the centrality range divided by the total number of events) for four centrality ranges are shown: $0-5\%$, $5-10\%$, $60-70\%$ and $60-86\%$. The mean and RMS values are printed.

are employed to expose the bad runs for Run10 62 and 39 GeV. The identified bad runs were not analyzed.

3.4 Event Plane Construction

The event planes Ψ_n are another set of event signatures and they in particular reflect the initial geometry of the collision. The correlations between different orders of event planes are interesting and discussed in [29]. Moreover, the correlations between individual tracks and Ψ_n provide estimations of v_n that is the main topic in this dissertation. The principles and procedures for Ψ_n construction are discussed in this section.

It's noteworthy that there exist methods to measure v_n without constructing Ψ_n first, such as the decomposition of two particle correlation functions (cf. Sec-1.7.1). v_n measured in this Ψ_n independent method are used as cross checks for the study performed in this dissertation.

3.4.1 Observed Event Planes

Without obtaining the precise profile of the initial collision zone, the directly extraction of Ψ_n is impossible. However, an approximate orientation for Ψ_n can be measured from the collision products. These so-called observed event planes are denoted by Φ_n and are built from tracks in a certain rapidity range or the response of a particular detector. Since v_n's are normally measured at mid-rapidity (small $|\eta|$), these tracks are chosen to be located at large $|\eta|$ to avoid auto-correlations for the v_n measurement. Φ_n are defined via Q-vectors, which are two-component vectors in the transverse plane [120]:

$$Q_{n,x} = \sum_i \omega_i \cos(n\phi_i), \quad Q_{n,y} = \sum_i \omega_i \sin(n\phi_i). \tag{3.3}$$

The index i refers to a track or a detector segment/pixel and the sum goes over all possible i. ϕ_i is the azimuth of the i-th element and ω_i is the associated weight, which could be the p_T of a track or the gain for the detector segment. The n-th order Q-vector possesses the desired feature of a n-fold symmetry, i.e. if all azimuthal angles are shifted by any multiple of $2\pi/n$, the Q-vector remains unchanged. If we define $\omega \equiv \sum_i \omega_i$, $Q_{n,x}$ and $Q_{n,y}$ could be treated as weighted average of cosine and sine values of the azimuthal angles:

$$Q_{n,x} = \frac{\langle \cos(n\phi) \rangle}{\omega}, \quad Q_{n,y} = \frac{\langle \sin(n\phi) \rangle}{\omega} \tag{3.4}$$

The connection between the Q-vectors and Ψ_n could be best seen from Eqn-1.2, the right hand side (RHS) of which could be expanded as

$$\text{RHS} = 1 + \sum_n 2v_n[\cos(n\phi)\cos(n\Psi_n) + \sin(n\phi)\sin(n\Psi_n)]. \tag{3.5}$$

Therefore, given the orthogonality of different orders of cosine and sine terms in a Fourier expansion, the averages in Eqn-3.4 turn out to be

$$\begin{aligned} \langle\langle\cos(n\phi)\rangle\rangle &= \int \frac{\mathrm{d}N}{\mathrm{d}\phi}\cos(n\phi)\mathrm{d}\phi \propto v_n\cos(n\Psi_n), \\ \langle\langle\sin(n\phi)\rangle\rangle &= \int \frac{\mathrm{d}N}{\mathrm{d}\phi}\sin(n\phi)\mathrm{d}\phi \propto v_n\sin(n\Psi_n). \end{aligned} \tag{3.6}$$

The double brackets $\langle\langle\ \rangle\rangle$ indicate that the average is taken as an integral of the continuous ϕ and corresponds to the ideal case of infinite tracks in a η range or an infinitely large detector resolution, which is obviously not true in practice. However, we could define the observed event planes Φ_n with the same idea:

$$\begin{aligned} \langle\cos(n\phi)\rangle &\propto v_n\cos(n\Phi_n), \\ \langle\sin(n\phi)\rangle &\propto v_n\sin(n\Phi_n), \end{aligned} \tag{3.7}$$

and Φ_n could be calculated based on measurements:

$$\tan(n\Phi_n) = \frac{\langle\sin(n\phi)\rangle}{\langle\cos(n\phi)\rangle}, \quad \text{thus} \quad \Phi_n = \frac{1}{n}\tan^{-1}\left(\frac{Q_{n,y}}{Q_{n,x}}\right). \tag{3.8}$$

By definition Ψ_n must have the aforementioned n-fold symmetry, and their approximations Φ_n defined as Eqn-3.8 are consistently equipped with the symmetry. To enforce unique values of Ψ_n and Φ_n, their values are "folded" up or down to the range of $[-\pi/n, \pi/n)$.

3.4.2 Event Plane Resolution Factors

How well does Φ_n approximate Ψ_n? The answer is important since it's directly related to the v_n measurement. An expression of v_n more closely related to the measurement is shown in Eqn-1.3, where Ψ_n is involved. In practice, only Φ_n is observable; if it's inserted into Eqn-1.3 in the place of Ψ_n, with some

derivations one finds that:

$$\begin{aligned}
&\langle\cos[n(\phi-\Phi_n)]\rangle \\
=&\langle\cos[n(\phi-\Psi_n)-n(\Phi_n-\Psi_n)]\rangle \\
=&\langle\cos[n(\phi-\Psi_n)]\cos[n(\Phi_n-\Psi_n)]\rangle+\text{S.T} \\
=&\langle\cos[n(\phi-\Psi_n)]\rangle\langle\cos[n(\Phi_n-\Psi_n)]\rangle+\text{S.T} \\
=&\langle\cos[n(\phi-\Psi_n)]\rangle\langle\cos[n(\Phi_n-\Psi_n)]\rangle,
\end{aligned} \tag{3.9}$$

where S.T. denote the corresponding sine term. The average $\langle\ \rangle$ is taken over all events and tracks. The first two steps in Eqn-3.9 are trivial; the third equal is valid only if there is no auto-correlations between ϕ and Φ_n. To ensure it, ϕ and Φ_n are measured at η ranges far apart. The sine term naturally vanishes by the definition of Ψ_n in Eqn-3.9.

The expression in the first row of Eqn-3.9 is a measurable quantity and denoted as v_n^{raw}. The two components in the last row are v_n and a correction factor, commonly referred to as the event plane resolution factor $\text{Res}\{\Phi_n\}$. With these new notations, Eqn-3.9 could be re-written as:

$$v_n=\frac{\langle\cos[n(\phi-\Phi_n)]\rangle}{\langle\cos[n(\Phi_n-\Psi_n)]\rangle}\equiv\frac{v_n^{\text{raw}}}{\text{Res}\{\Phi_n\}}. \tag{3.10}$$

In order to measure v_n, $\text{Res}\{\Phi_n\}$ must be determined.

3.4.3 Sub-Events

A "sub-event" refers to tracks in a certain rapidity range. For example, all the tracks that hit the BBC north arm (and the hits left there) form a sub-event; the hits in the south arm form another sub-event. Event planes could be constructed for each sub-event individually. Since most detectors that are used for event plane construction in PHENIX have both a north and south arm, we denote Φ_n constructed at the north(south) arm as $\Phi_n^N(\Phi_n^S)$. By comparing Φ_n^N and Φ_n^S, their resolution factors could be derived.

For each event, Φ_n^N and Φ_n^S are constructed and their difference is recorded. After accumulating a sufficiently large number of events, the expression

$$\langle\cos[n(\Phi_n^N-\Phi_n^S)]\rangle$$

could be calculated with precision, where the average $\langle\ \rangle$ is taken over events.

The expression is further decomposed in the same fashion as Eqn-3.9:

$$\begin{aligned}
&\langle\cos[n(\Phi_n^N - \Phi_n^S)]\rangle \\
=&\langle\cos[n(\Phi_n^N - \Psi_n) - (\Phi_n^S - \Psi_n)]\rangle \\
=&\langle\cos[n(\Phi_n^N - \Psi_n)]\cos[(\Phi_n^S - \Psi_n)]\rangle + S.T \\
=&\langle\cos[n(\Phi_n^N - \Psi_n)]\rangle\langle\cos[(\Phi_n^S - \Psi_n)]\rangle + S.T \\
=&\mathrm{Res}\{\Phi_n^N\}\mathrm{Res}\{\Phi_n^S\}
\end{aligned} \tag{3.11}$$

The reasonings of the derivations are the same as those for Eqn-3.9. Normally south and north component of a detector sit in the same $|\eta|$ range and their designs are the same. If the performances of the two components are indeed the same, we have

$$\mathrm{Res}\{\Phi_n^N\} = \mathrm{Res}\{\Phi_n^S\}$$

and the resolution factors for $\Phi_n^N(\Phi_n^S)$ are calculated from Eqn-3.11.

However, using event planes constructed at only one half of a detector is not satisfactory. It's easy to imagine that the resolution factors are positively correlated to the multiplicity in the η range where Φ_n's are built. If the full detector were utilized, the multiplicity would be doubled and the resolutions improved. Is there a way to calculate resolution factors for the full detector $\mathrm{Res}\{\Phi_n^{SN}\}$ based on the resolutions of the half detector $\mathrm{Res}\{\Phi_n^S\}$ or $\mathrm{Res}\{\Phi_n^N\}$? The answer is yes, provided we have the correct modeling of the Q-vectors.

3.4.4 Modeling of Q-vectors

The dispersion of Φ_n around Ψ_n originates from the fluctuations of the Q-vectors. The distribution of Q-vectors could be modeled as an off center 2D Gaussian that is diagramed in Fig-3.13. The expectation and standard deviation of the 2D Gaussian is represented by $\langle Q\rangle$ and σ respectively. We are indifferent to the magnitudes of Q-vectors; only the angular dispersion ($\Delta\phi$ on Fig-3.13) matters. One quantity that characterizes the $\Delta\phi$ dispersion is the $\Delta\phi$ value when the arrow line on the figure is tangential to the circle. Following this idea, the χ factor is defined as

$$\chi = \frac{\langle Q\rangle}{\sigma}, \tag{3.12}$$

and a higher χ value corresponds to a smaller angular dispersion, thus a greater resolution factor.

Before the direct connection between χ and $\mathrm{Res}\{\Phi_n\}$ is discussed, it is worth the effort to quantify the effect of multiplicity on the χ factors. Assum-

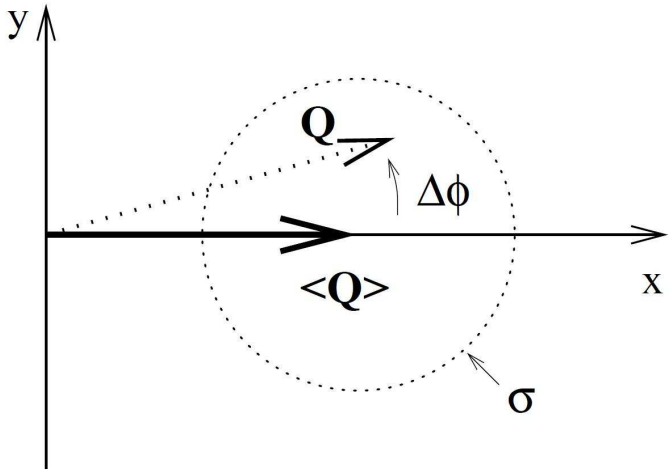

Figure 3.13: Distribution of Q-vectors [121]. $\langle Q \rangle$ is the expectation of the 2D Gaussian and σ (the radius of the dotted circle) denotes the standard deviation. One sample of Q (the dotted arrow) is also plotted.

ing the 2D Gaussian distribution for a single particle's Q-vector is $G(\mu_0, \sigma_0^2)$, for a certain η range with N particles, the corresponding Q-vector follows a distribution of $G(N\mu_0, N\sigma_0^2)$, the χ factor of which is $\sqrt{N}u_0/\sigma_0$. Therefore, the χ factor for a Q-vector associated with N particles is $\sqrt{N}$ times the one for a single track.

The other factor that affects χ_n is the size of anisotropy (v_n) of the particles that are used to build the event planes. If there is no azimuthal anisotropy at all ($v_n = 0$), $\langle Q \rangle$ is then zero and χ_n is naturally zero. When the anisotropy is large, the value of u_0/σ_0 would be sizable and eventually leads to good resolution factors.

Summarizing these two factors, the centrality dependence of χ_n can be understood qualitatively. In central collisions, the size of the azimuthal anisotropy is small; though the multiplicity is high, the value of χ_n is limited. For mid-central collision, a large azimuthal anisotropy emerges without significant loss of multiplicity and the value of χ_n reaches a peak value. Finally for peripheral collision, azimuthal anisotropy doesn't increase much compared to the one in mid-central, but the multiplicity drops quickly and χ_n values decrease as well. Since we will show shortly that Res$\{\Phi_n\}$ varies monotonically with χ_n, the arguments claimed here also apply to Res$\{\Phi_n\}$, as demonstrated in Fig-4.18 and Fig-5.6.

The centrality dependence of χ_n and Res$\{\Phi_n\}$ suggests that Res$\{\Phi_n\}$ and v_n be measured in fine centrality bins to reduce the smearing effect when varying χ_n values in a centrality range are averaged. Therefore, 5% centrality

steps were adopted for central and middle central collisions; for peripheral collisions the multiplicity drops and a wider centrality step of 10% was employed.

The following formula is employed to calculate Res$\{\Phi_n\}$ from χ_n [120]:

$$\text{Res}\{\Phi_n\} = \frac{\sqrt{\pi}}{2\sqrt{2}}\chi_n \exp(-\frac{\chi_n^2}{4})[I_0(\frac{\chi_n^2}{4}) + I_1(\frac{\chi_n^2}{4})], \tag{3.13}$$

where I denotes modified Bessel function. A plot of the equation is shown in

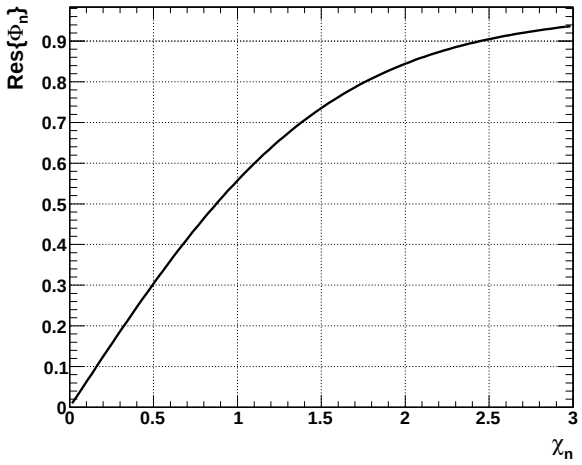

Figure 3.14: Res$\{\Phi_n\}$ vs. χ_n, cf. Eqn-3.13.

Fig-3.14. Features that are noteworthy include:

- Res$\{\Phi_n\}$ is a monotonic function of χ_n, which allow the reversal of Eqn-3.13 to get χ_n from the resolution;
- for small values of χ_n, the relation between Res$\{\Phi_n\}$ and χ_n is almost linear, e.g. a $\sqrt{2}$ larger χ_n approximately leads to a $\sqrt{2}$ larger Res$\{\Phi_n\}$.
- for large values of χ_n, Res$\{\Phi_n\}$ saturates and approaches the 100% limit slowly.

3.4.5 Two Sub-Events Method

With the help of Eqn-3.13, the calculation of Res$\{\Phi_n\}$ for a full detector is then reduced to the problem of evaluating χ_n. Assuming that the south and north sub-event are identical, the procedures to calculate Res$\{\Phi_n^{SN}\}$ are outlined below:

1. measure resolution factors for the half detector sub-event (Res$\{\Phi_n^S\}$ or Res$\{\Phi_n^N\}$, cf. Sec-3.4.3);

2. extract the corresponding χ_n^{half} from Eqn-3.13 with an iteration method;

3. since χ_n scales with $\sqrt{N}$, χ_n for the full detector is $\chi_n^{\text{full}} = \sqrt{2}\chi_n^{\text{half}}$;

4. insert χ_n^{full} to Eqn-3.13 for the resolutions of the full detector Res$\{\Phi_n^{SN}\}$.

It is commonly referred to as the two sub-events method.

Instead of using step 2 listed above, there is another approach to extract χ_n^{half} from Res$\{\Phi_n^S\}$ (or Res$\{\Phi_n^N\}$). If the angle difference in Eqn-3.11 is denoted as $\Delta\Phi_n$, i.e. $\Delta\Phi_n = \Phi_n^S - \Phi_n^N$, the distribution of $\Delta\Phi_n$ is proven to be [121]:

$$\frac{\mathrm{d}N}{\mathrm{d}\Delta\Phi_n} = \frac{e^{-\frac{\chi_n^2}{2}}}{2}\left\{\frac{2}{\pi}(1+\frac{\chi_n^2}{2}) + z[I_0(z)+L_0(z)] + \frac{\chi_n^2}{2}[I_1(z)+L_1(z)]\right\} \quad (3.14)$$

where $z = \frac{\chi_n^2}{2}\cos(n\Delta\Phi_n)$. I_n is n-th order modified Bessel function and L_n the modified Struve function. $\Delta\Phi_n$ takes value in $[-2\pi/n, 2\pi/n)$ and the $\Delta\Phi_n$ distribution (Eqn-3.14) is normalized to 1 in that range, thus becomes a probability density function. Note that χ defined in [121] is $1/\sqrt{2}$ of the one in [120]. The distribution itself could be measured, and χ_n is extracted via a fit.

The benefit of this method is that we could examine the Q-vector modeling and the reasonings above by checking the quality of fitting. Several exemplar fitting curves are put on Fig-3.15. For all three centrality selections, the fitting curves match the data points very well. Small deviations do appear, and the functional form seems to overestimate the dispersion by under-predicting the probability at $|\Delta\Phi| \sim 0$ and over-predicting at $|\Delta\Phi| \sim \pi/2$. The deviations are more notable for mid-central collisions where the resolution factors tend to maximize (middle panel in Fig-3.15).

In $\sqrt{s_{NN}} = 200$ GeV collusion, these deviations are more prominent due to the greater event multiplicity at the higher beam energy and the resulting better event plane resolutions. A study at 200 GeV [122] shows that a relaxed model of Q-vector that has 3 parameters [123] (standard deviation of $Q_{n,x}$, $Q_{n,y}$ and correlation between $Q_{n,x}$ and $Q_{n,y}$) achieves a better fit, as shown on Fig-3.16. However, the resolution factors calculated from the relaxed model aren't improved. Therefore, the traditional 2D Gaussian modeling of the Q-vector was adopted.

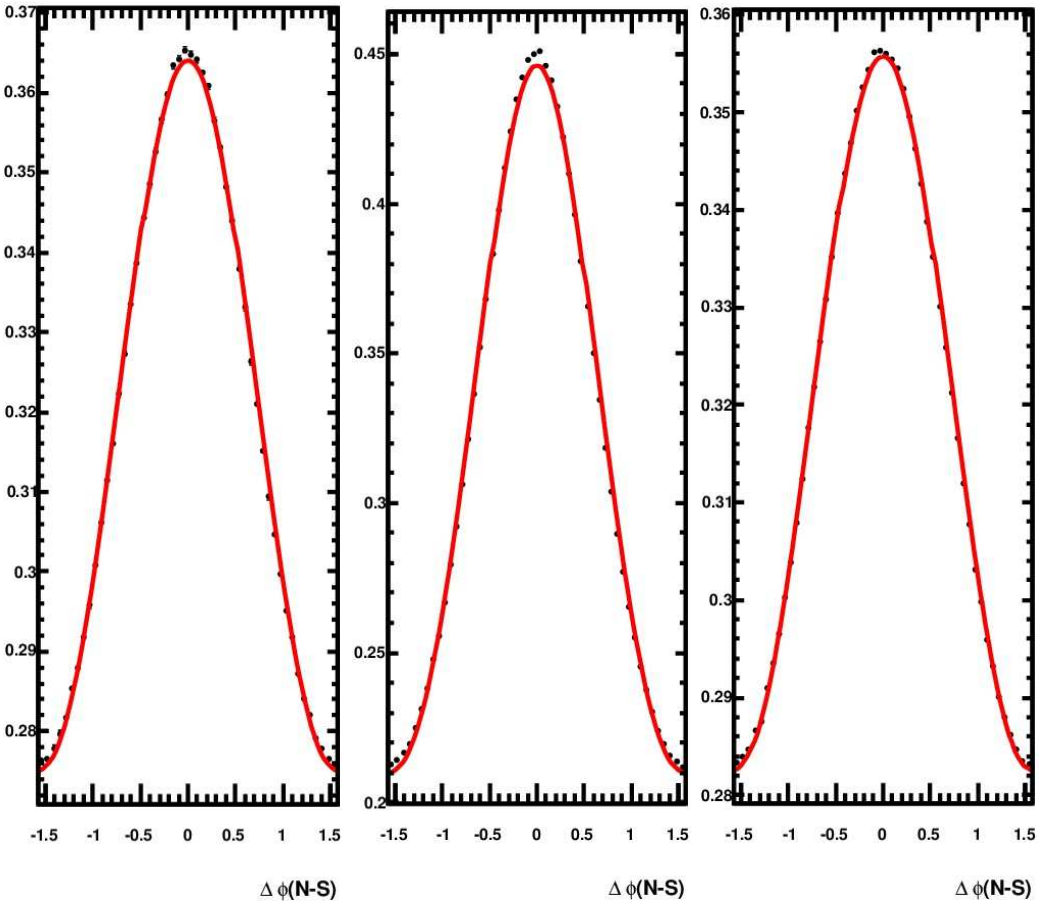

Figure 3.15: Functional (Eqn-3.14) fit to the distribution of $\Delta\Phi_2$. $\Delta\Phi_2$ is measured with RXN at $\sqrt{s_{NN}} = 62$ GeV. Three centrality selections are show: from left to right are $0-5\%$, $30-35\%$ and $50-60\%$.

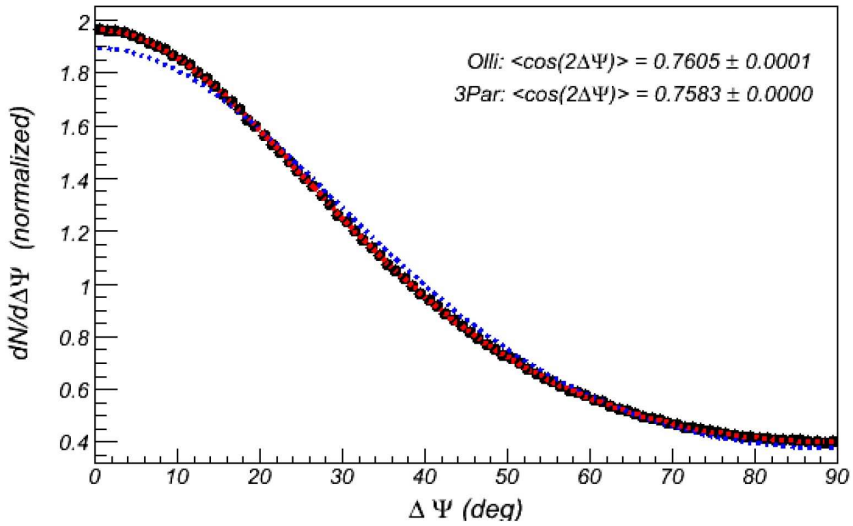

Figure 3.16: $\Delta\Phi_2$ distribution fitted by a relaxed 3-parameter model of Q-vectors [122]. $\Delta\Phi_2$ is folded to the range of $0 \sim \pi/2$ (not $-\pi/2 \sim \pi/2$ as shown in Fig-3.15) because of the symmetry. Black dots show data; blue dots indicate the traditional 2D Gaussian Q-vector modeling and red dots represent the relaxed 3-parameter modeling [123]. Values of $\mathrm{Res}\{\Phi_2\}$ from both methods are printed.

There are other methods that are capable of finding $\mathrm{Res}\{\Phi_n\}$ for the full detector without the necessity of modeling the Q-vector, such as the one discussed in the next section.

3.4.6 Three Sub-Events Method and Jet-Bias

Eqn-3.11 applied to any two sub-events that are correlated only via their individual correlation to Ψ_n. Therefore, if three such sub-events are available, the resolution factor for each of the sub-event could be calculated as:

$$\mathrm{Res}\{\Phi_n^A\} = \sqrt{\frac{\langle\cos[n(\Phi_n^A - \Phi_n^B)]\rangle\langle\cos[n(\Phi_n^A - \Phi_n^C)]\rangle}{\langle\cos[n(\Phi_n^B - \Phi_n^C)]\rangle}}. \tag{3.15}$$

This is the formula for the three sub-events method.

The three sub-events method calculates resolution factor for any sub-event from physics observables directly and is model independent. Therefore, it's considered very robust. However, to find three sub-events that are free from undesired correlation is no trivial task:

1. the sub-events must be located at different rapidity ranges to avoid auto-correlation;

2. moreover, there should be a sufficiently large rapidity gap between any two sub-events to avoid non-flow effects like jet-bias.

Jet-bias is one major contributor to the systematic uncertainty of v_n analysis. Particles from the same jet cone are correlated (jet correlation, cf. upper left panel of Fig-1.17, and Sec-1.7.3) and this correlation is not from the azimuthal anisotropy discussed here. The jet cone has a sizable azimuth and rapidity coverage, and if two detectors are frequently hit by particles from the same jet cone, the observed correlation between the corresponding event planes (cf. Eqn-3.15) would suffer a jet-bias, which could be as large as a few percent of the total correlation.

The two sub-events method normally utilizes the south and north components of the detector; they are well separated in η and considered free from jet contamination. In the three sub-events method, two of the sub-events are inevitably located on the same side (south or north) of the detector; therefore, jet correlation needs to be carefully assessed. Additional limitations come from the fact that at the relatively low collision energy of 62 and 39 GeV, the detector capability for event plane construction deteriorates (mainly due to the reduction of multiplicity), especially for higher order ($n > 2$) event planes. Some detectors that are fully functional at 200 GeV become ineffective (cf. Fig-5.4) and we are left with very few detector choices for event plane construction.

3.4.7 Effective Three Sub-Events Method

One assumption of the 2 sub-events method is that the south and north component of a detector are identical. Strictly speaking, this requirement is hardly met by any detector but normally it's a good approximation. However, there are occasions where the two components are fundamentally different. For MPC detector, the south and north arms have slightly different designs (cf. Sec-2.1.6). For the RXI detector, the south and north arm are designed to be the same but the south arm had a broken PMT and thus worse performance at event plane determination. Consequently, the 2 sub-events method can not be used for these detectors. Another method was developed to help determine the event plane resolution factors.

The idea is that in the cases where more than 2 sub-events are not available at large absolute rapidity $|\eta|$, the event plane in the central arm (CNT) can be utilized, which under normal circumstance is not a good practice because:

- v_n are measured at mid-rapidity and to avoid auto-correlation, Φ_n are commonly constructed at large rapidity;
- the PHENIX central arm doesn't have 2π coverage, and large acceptance effects on Φ_n^{CNT} are to be expected.

The use of Φ_n^{CNT} in our case is special as well. It is not used directly in the analysis but rather serves as a common factor that gets canceled out. Following the logic of Eqn-3.11, we have

$$\begin{aligned}\langle\cos[n(\Phi_n^S - \Phi_n^{\mathrm{CNT}})]\rangle &= \mathrm{Res}\{\Phi_n^S\}\mathrm{Res}\{\Phi_n^{\mathrm{CNT}}\} \\ \langle\cos[n(\Phi_n^N - \Phi_n^{\mathrm{CNT}})]\rangle &= \mathrm{Res}\{\Phi_n^N\}\mathrm{Res}\{\Phi_n^{\mathrm{CNT}}\}\end{aligned} \tag{3.16}$$

and if the ratio of the two equations is taken, we end up with the ratio of event plane resolutions between south and north arm:

$$\frac{\mathrm{Res}\{\Phi_n^S\}}{\mathrm{Res}\{\Phi_n^N\}} = \frac{\langle\cos[n(\Phi_n^S - \Phi_n^{\mathrm{CNT}})]\rangle}{\langle\cos[n(\Phi_n^N - \Phi_n^{\mathrm{CNT}})]\rangle}. \tag{3.17}$$

The combined information of Eqn-3.11 and this ratio suffices to determine $\mathrm{Res}\{\Phi_n^S\}$ and $\mathrm{Res}\{\Phi_n^N\}$.

For the next step, we extract χ_n^S and χ_n^N from the resolution factors (cf. Eqn-3.13). To obtain χ_n factor for the full detector sub-event, we assume the full detector acts as the optimized combination (cf. Sec-3.5.1) of south and north arm and has the factor

$$\chi_n^{\mathrm{Full}} = \sqrt{(\chi_n^S)^2 + (\chi_n^N)^2}. \tag{3.18}$$

Note that if $\chi_n^S = \chi_n^N$, we get a factor of $\sqrt{2}$ and are reverted to the situation of the traditional two sub-events method.

3.5 Event Plane Combination

Event plane combination gathers information from separate event planes (from different sub-events) and compile them into a single set of event planes. It is an effective method to obtain more precise event plane determination. The process could happen at two different stages.

1. The first one is the Q-vector building stage: hits from multiple detectors are combined to contribute to the same set of Q-vectors (cf. Eqn-3.3, the summation of index i traverses through detector segments for multiple detectors). Event planes built from the so-defined Q-vectors naturally

reflect pooled information of multiple detectors; event planes constructed at RXN, which is the combination of RXI and RXO, are categorized as Φ_n combined at this first stage.

2. The second stage of event plane combination happens after Q-vectors are built. This kind of combination involves weighted sum of Q-vectors from different detectors and is the main topic of this section.

3.5.1 Combination of Q-vectors

There are several reasons that the combination of event planes are better implemented after Q-vectors for individual detectors are already built:

- Q-vectors are low level objects that are automatically handled by the software framework in PHENIX (more specifically, the Master Recalibrator and particulary its components for event plane construction). Since the combination of event plane has limited usage, it's not wise to modify the low level framework and implement the combination at the first stage.

- For the first approach, since the detector responses that are used as weighting factors (ω_i in Eqn-3.3) might be quite different for different detectors, global scaling factors must be applied to the gains of each detector before the they are assigned as weighting factors and participate in the combination. For the RXN detector, its inner ring and outer ring have essentially the same architecture and no additional scaling is necessary. However, it is not the case for a general combination, such as the combination of MPC and RXI implemented in [87]. Moreover, the performance of the combined event planes are directly related to the scaling factors. In an extreme case, greater scaling factors are applied to the detector with worse resolutions; consequently the combined event planes may have resolutions even less than one of the original detectors with good performance. On the other hand, if the detector gains are correctly scaled to the optimized level, the combination would be most beneficial. However, it is not easy to see how to determine the optimized scaling in this case.

For simplicity of notation, subscript n indicating Fourier orders is not explicitly shown in this section.

As described in Sec-3.4.4, a Q-vector is modeled to follow a 2D Gaussian distribution $G(\mu_0, \sigma_0^2)$. Note that the mean μ_0 is not denoted as a vector since the direction of μ_0 is irrelevant to the analysis, as we can always rotate the

coordinate frame so that the direction of μ is the x-axis (cf. Fig-3.13). If we have two Q-vectors from separate detectors, the combined event planes are determined by the combined Q-vector that follows:

$$\begin{aligned} G(\mu, \sigma^2) &= \alpha_1 G(\mu_1, \sigma_1^2) + \alpha_2 G(\mu_2, \sigma_2^2) \\ &= G(\alpha_1\mu_1 + \alpha_2\mu_2, \alpha_1^2\sigma_1^2 + \alpha_2^2\sigma_2^2), \end{aligned} \tag{3.19}$$

where α_1 and α_2 are arbitrary weighting factors. Again, since μ_1 and μ_2 are in the same direction the sum $\mu = \alpha_1\mu_1 + \alpha_2\mu_2$ is a direct sum instead of a vector one. The variance $\sigma^2 = \alpha_1^2\sigma_1^2 + \alpha_2^2\sigma_2^2$ equation is validated by the summation properties of Gaussian distribution.

Our goal is to achieve the optimized combination. Therefore, the χ factor for the combined event plane distribution

$$\chi = \frac{\alpha_1\mu_1 + \alpha_2\mu_2}{\sqrt{\alpha_1^2\sigma_1^2 + \alpha_2^2\sigma_2^2}} = \frac{\gamma_1\chi_1 + \gamma_2\chi_2}{\sqrt{\gamma_1^2 + \gamma_2^2}}, \quad \gamma = \alpha\sigma \tag{3.20}$$

needs to be maximized. An algebraic derivation shows that the achievable maximum of χ is

$$\chi = \sqrt{\chi_1^2 + \chi_2^2} \tag{3.21}$$

and the condition for the optimized combination is

$$\frac{\gamma_1}{\gamma_2} = \frac{\chi_1}{\chi_2}, \quad \text{or} \quad \frac{\alpha_1}{\alpha_2} = \frac{\chi_1\sigma_2}{\chi_2\sigma_1}. \tag{3.22}$$

However, only χ_1 and χ_2 in the equation above are known (extracted from resolution measurement). To implement the optimized combination, additional conditions are necessary.

3.5.2 Normalization of Q-Vectors in PHENIX

For PHENIX, Q-vectors are normalized so that the standard deviations of Q_x and Q_y are unity. In this section, we explore the implications of this normalization requirement.

Q-vectors are normalized in 5% step centrality bins. We assume these centrality bins are sufficiently narrow so that the multiplicity in each bin remains roughly the same. Therefore the expectation of Q-vectors, $\boldsymbol{\mu}$, has a fixed length (denoted as μ) for all the events, under the assumption that all fluctuations are disregarded. Note that in this section the analysis is taken across different events, thus we have a vector representation of the expectation ($\boldsymbol{\mu}$). we also assume that in the lab frame the polar angle of $\boldsymbol{\mu}$ is θ, which is

uniformly distributed in $0 \sim 2\pi$.

The dispersion of Q-vectors around $\boldsymbol{\mu}$ follows a 2D Gaussian distribution. Therefore the probability of a Q-vector (denoted as $\boldsymbol{Q}$) appearing at (Q, α) in the transverse plane when $\boldsymbol{\mu}$ has a polar angle θ is

$$\mathrm{d}P(\boldsymbol{Q}, \boldsymbol{\mu}) = \frac{1}{2\pi\sigma^2} \exp[-\frac{(\boldsymbol{Q}-\boldsymbol{\mu})^2}{2\sigma^2}]\mathrm{d}\boldsymbol{Q}\mathrm{d}\boldsymbol{\mu}. \tag{3.23}$$

After the application of the following expressions:

$$\begin{aligned}
(\boldsymbol{Q}-\boldsymbol{\mu})^2 &= Q^2 + \mu^2 - 2r\mu\cos(\alpha-\theta), \\
\mathrm{d}\boldsymbol{Q} &= Q\mathrm{d}Q\mathrm{d}\alpha, \quad \mathrm{d}\boldsymbol{\mu} = \frac{\mathrm{d}\theta}{2\pi},
\end{aligned}$$

Eqn-3.23 is re-written as a function of 3 scaler parameters:

$$\mathrm{d}P(Q, \alpha, \theta) = \frac{1}{2\pi}\frac{1}{2\pi\sigma^2} \exp[-\frac{Q^2+\mu^2}{2\sigma^2}]Q\mathrm{d}Q\mathrm{d}\alpha \cdot \exp[\frac{Q\mu}{\sigma^2}\cos(\theta-\alpha)]\mathrm{d}\theta.$$

The dependence on θ could be integrated out since only the distribution of $\boldsymbol{Q}$ is relevant. The integration of θ from 0 to 2π on the part after "$\cdot$" of the equation above yields $2\pi I_0(\mu Q/\sigma^2)$, where I_0 is zeroth order modified Bessel function. Consequently,

$$\mathrm{d}P(Q, \alpha) = \frac{1}{2\pi\sigma^2} I_0(\frac{\mu Q}{\sigma^2}) \exp[-\frac{Q^2+\mu^2}{2\sigma^2}]Q\mathrm{d}Q\mathrm{d}\alpha.$$

If we introduce $\chi = \mu/\sigma$ and $l = Q/\sigma$, the above expression can be re-written as the multiplicity of a radial term and an angular term:

$$\begin{aligned}
\mathrm{d}P(Q, \alpha) &= \mathrm{d}P(l, \alpha) = \mathrm{d}P(l)\mathrm{d}P(\alpha) \\
\mathrm{d}P(l) &= I_0(\chi l) \exp[-\frac{(l^2+\chi^2)}{2}]l\mathrm{d}l \\
\mathrm{d}P(\alpha) &= \frac{\mathrm{d}\alpha}{2\pi}
\end{aligned} \tag{3.24}$$

We can see that the distribution of $\boldsymbol{Q}$ is independent of the polar angle α; in other words, it has a continuous rotational symmetry. The magnitude of $\boldsymbol{Q}$ has a probability distribution $\mathrm{d}P(l)/\mathrm{d}l$, an illustration of which is diagramed in Fig-3.17.

From Eqn-3.24, we can try to write down the expression for the standard deviation of Q_x and Q_y (denoted by $\sigma(Q_x)$ and $\sigma(Q_y)$). Because they are

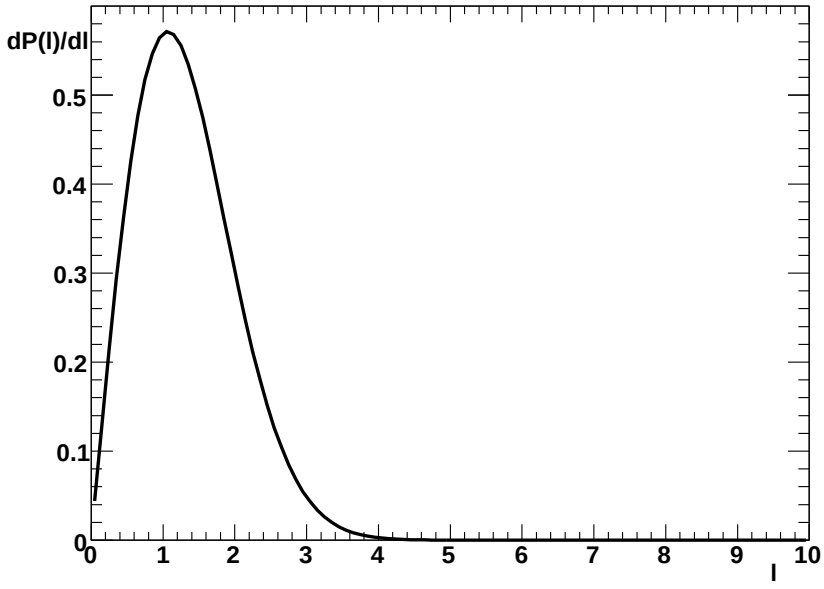

Figure 3.17: $\mathrm{d}P(l)/\mathrm{d}l$ vs. l

symmetric, only derivations for $\sigma(Q_x)$ are shown. By definition,

$$\sigma^2(Q_x) = \langle x^2 \rangle - \langle x \rangle^2 = \int x^2 \mathrm{d}P(Q,\alpha) - [\int x \mathrm{d}P(Q,\alpha)]^2 \tag{3.25}$$

and $x = Q\cos\alpha = l\sigma\cos\alpha$. $\langle x \rangle$ vanishes by symmetry (or explicitly $\int \cos\alpha \mathrm{d}P(\alpha) = 0$). Therefore

$$\sigma^2(Q_x) = \sigma^2 \int l^2 \mathrm{d}P(l) \int \cos^2\alpha \mathrm{d}P(\alpha) = \frac{\sigma^2}{2} \int l^2 \mathrm{d}P(l). \tag{3.26}$$

We could further define

$$\begin{aligned} \mathrm{IP}_n &\equiv \int l^n \mathrm{d}P(l) = \int I_0(\chi l) \exp[-\frac{(l^2+\chi^2)}{2}] l^{n+1} \mathrm{d}l \\ &= 2^{\frac{n}{2}} \Gamma(1+\frac{n}{2}) L_{\frac{n}{2}}(-\frac{\chi^2}{2}) \end{aligned} \tag{3.27}$$

where L_n is the n-th order Laguerre polynomial. If $n = 2$ we have $L_1(x) = -x + 1$; together with $\Gamma(2) = 1$ it is easy to see that $\mathrm{IP}_2 = 2(1 + \frac{\chi^2}{2})$. It's also obvious that $\mathrm{IP}_0 = 1$, which is the normalization condition of the probability distribution $\mathrm{d}P(l)/\mathrm{d}l$.

Under the condition of $\sigma(Q_x) = 1$, we have

$$\sigma^2(Q_x) = \sigma^2(1 + \frac{\chi^2}{2}) = 1. \tag{3.28}$$

This restriction helps us finalize the optimal combination weighting factors (cf. Eqn-3.22) as:

$$\frac{\alpha_1}{\alpha_2} = \frac{\chi_1}{\chi_2}\sqrt{\frac{\chi_1^2 + 2}{\chi_2^2 + 2}} \tag{3.29}$$

It should be emphasized that this formula is obtained under the condition of $\sigma(Q_x) = \sigma(Q_y) = 1$.

3.5.3 MC Simulation

In this section, a MC simulation is setup to compare the following three schemes of combining event planes from two detectors.

- "natural" scheme: Q-vectors from the two detectors are not normalized and directly combined by a straight addition; this scheme actually corresponds to the combination of event planes at the first stage, i.e. the combined Q-vectors are built from hits of both detectors.
- "direct" scheme: Q-vectors from the two detectors are normalized first (cf. Sec-3.5.2) and then combined by a straight addition.
- "weighted" scheme: Q-vectors from the two detectors are normalized first and then combined by a weighted addition with the weighting factors in Eqn-3.29.

The setup of the simulation is quite naive. Particles are separately generated in each "detector", which is a purely virtual concept. The azimuthal distribution of particles for each event follows a presumed profile with a v_2 component. The v_2 values are put by hand for the two detectors (v_2^{Det1} and v_2^{Det2}) and not necessarily the same. Ψ_2 is generated randomly following an uniform distribution between $0 \sim 2\pi$. The number of tracks in each detector is also put by hand, in this way a wide range of χ values could be obtained (remember $\chi \propto \sqrt{N}$).

Results of the simulation are summarized in Fig-3.18. Two configurations of the simulation are tried out and the results are discussed separately.

1. $v_2^{\mathrm{Det1}} = v_2^{\mathrm{Det2}} = 0.05$, left panels of Fig-3.18:
   in this case, the intrinsic azimuthal anisotropy in the two detectors are

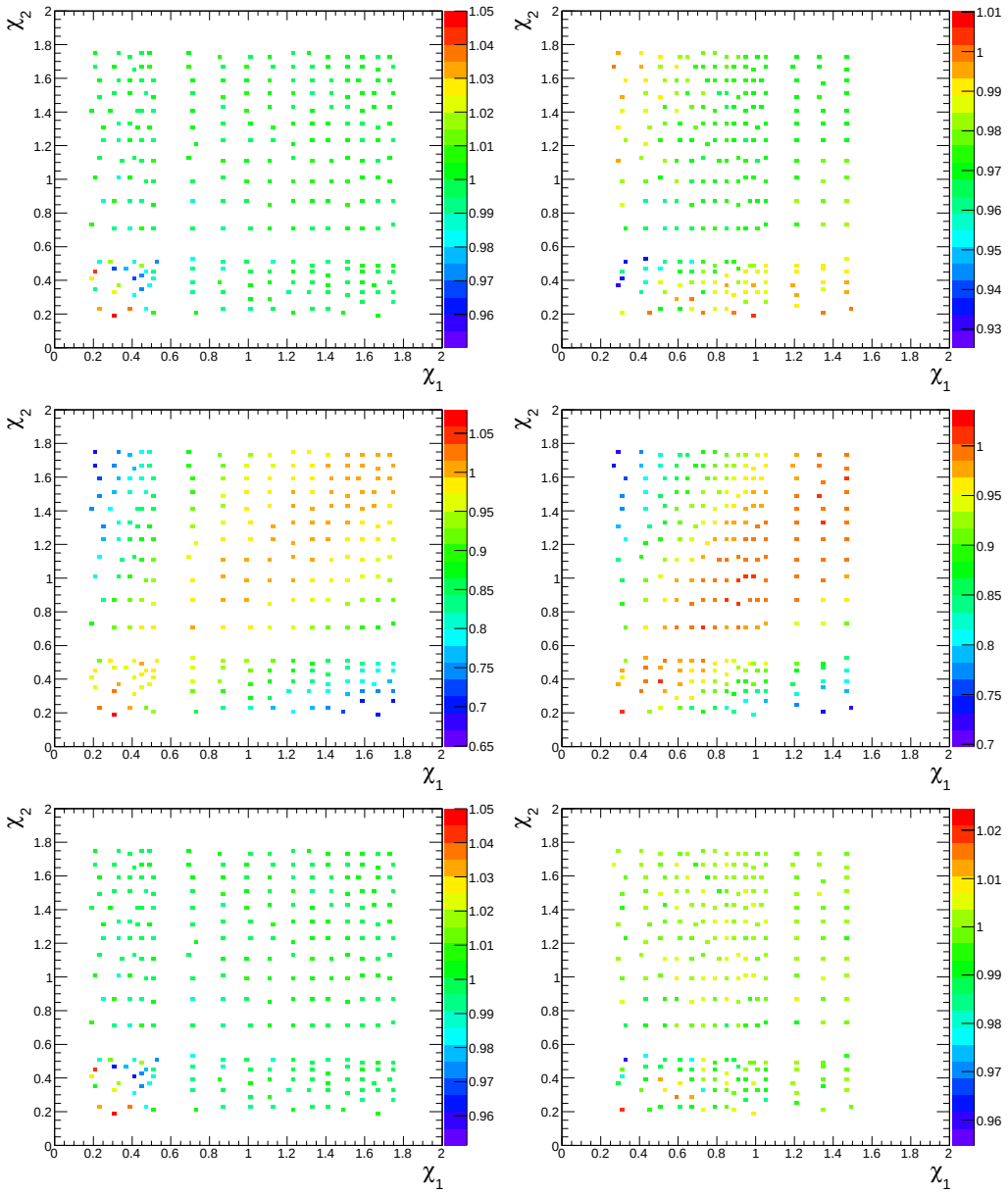

Figure 3.18: Comparisons of different event plane combination schemes. Two axes indicate the χ factors of the two detectors respectively. The color of the point represents the ratio value of achieved χ divided by the optimal value (cf. Eqn-3.21). Left panels: v_2^{Det1}=v_2^{Det2}=0.05; right panels: v_2^{Det1}=0.03, v_2^{Det2}=0.05; top/middle/bottom panel shows natural/direct/weighted scheme respectively. See text.

the same and the only factor that affects χ value of a detector is the multiplicity N. A combination following the natural scheme basically increases the multiplicity to N_1+N_2. Because $\chi \propto \sqrt{N}$, the optimal combined χ value (cf. Eqn-3.21) is automatically obtained and the combination with natural scheme should have the same good performance as the one with weighted scheme. Indeed, in Fig-3.18 we see the ratios are around 1 for the whole χ_1 and χ_2 range. For the direct scheme, the weighting factors are equal, which deviates from the optimal condition (cf. Eqn-3.29) when $\chi_1 \neq \chi_2$. At the lower right or upper left corner where α_1 and α_2 are largely different, the performance of the direct combination could be more than 20% worse than that of the optimal combination.

2. $v_2^{\mathrm{Det1}} = 0.03$, $v_2^{\mathrm{Det2}} = 0.05$, right panels of Fig-3.18:
The observations for this configuration are slightly more complicated. The optimal combination is still reproduced by the weighted scheme, and the performance for the direct scheme remains largely unchanged compared to the first setup. For the natural scheme, there are around 3% performance loss when χ_1 and χ_2 are similar. The loss is absent when one detector dominates, i.e. $\chi_1 \gg \chi_2$ or $\chi_1 \ll \chi_2$.

In summary, the direct combination of normalized Q-vectors needs to be avoided, especially when there is large performance discrepancy between the two detectors. The natural combination scheme seems to work very well (at most 3% loss in the simulation), but as mentioned in the prologue of Sec-3.5, this scheme is not always available in practice. Finally, the weighted combination scheme exhibits the expected good performance and should be adopted.

3.6 Event Plane Calibration

Up till now, we have assumed perfect detectors which lead to Φ_n values which are uniformly distributed between $[-\pi/n, \pi/n)$. However, detectors are imperfect and suffer from a variety of issues (dead channel/segment/pixel, unbalanced responses, etc.) which can influence the distribution of Φ_n. Instead of applying corrections to the foregoing derivations in Sec-3.4 and Sec-3.5, a calibration process was implemented to make manual adjustments so that the calibrated Φ_n are uniformly distributed. This process affects both v_n^{raw} and $\mathrm{Res}\{\Phi_n\}$ (cf. Eqn-3.10), and the effects are largely canceled out in the final results of v_n.

As mentioned in Sec-3.4.4, Φ_n construction is sensitive to centrality. In addition, the south and north arm of the detectors might react differently

depending on the z-vertex value of the collision. Therefore, the calibration was implemented for 5% centrality bins for all available centrality and 5 cm z-vertex bins in the range of $(-30, 30)$ cm. It's noteworthy that the above requirement of bin-by-bin calibration needs centrality definition as a prerequisite. To account for run-by-run variations, the calibration was performed for each run segment separately.

3.6.1 Overview of the Process

The calibration process consists of two stages:

1. re-centering of the Q-vectors;
2. flattening of the event plane distributions.

We denote raw event planes without any calibration as Φ_n^r; after re-centering, they become Φ_n^o and when the flattening is applied as well, they are referred to as Φ_n^c. The comparisons among event planes at these three stages are depicted in Fig-3.19 for RXI and RXO, for the south and north arms. The calibration is very effective, especially when Φ_n^r is severely distorted as is the case for the RXIs (top-left panel of Fig-3.19). The peak to valley ratio for Φ_n^r for the RXIs is more than 10; this strong bias results from the fact that one PMT in the RXIs was broken. It can be seen that the re-centering process removes the major distortion from Φ_n^r (cf. Φ_n^o); after the application of flattening, the distribution of Φ_n^c is almost flat. For detectors that have a relatively uniform response, such as RXOs (bottom-left panel of Fig-3.19), the calibration process still makes the Φ_n distribution flatter.

A detailed description of the calibration process is presented in the following sections.

3.6.2 Re-centering of Q-Vectors

If a detector module malfunctions (e.g. the dead segment in RXIs) the originally uniform Q-vector distribution, which in the ideal case is modeled as Eqn-3.24 and is rotationally symmetric around the origin, would have a strong preference toward the opposite direction of the dead segment and appear off-centered; consequently, Φ_n^r tends to point to the shifted center of the Q-vector and is distorted. The re-centering process is therefore aimed at bringing the center of the Q-vector distribution back to the origin. The normalization of Q-vectors, i.e. setting the standard deviations of Q_x and Q_y to unity (cf. Sec-3.5.2), is also performed at this stage.

The procedures to implement re-centering are as follows;

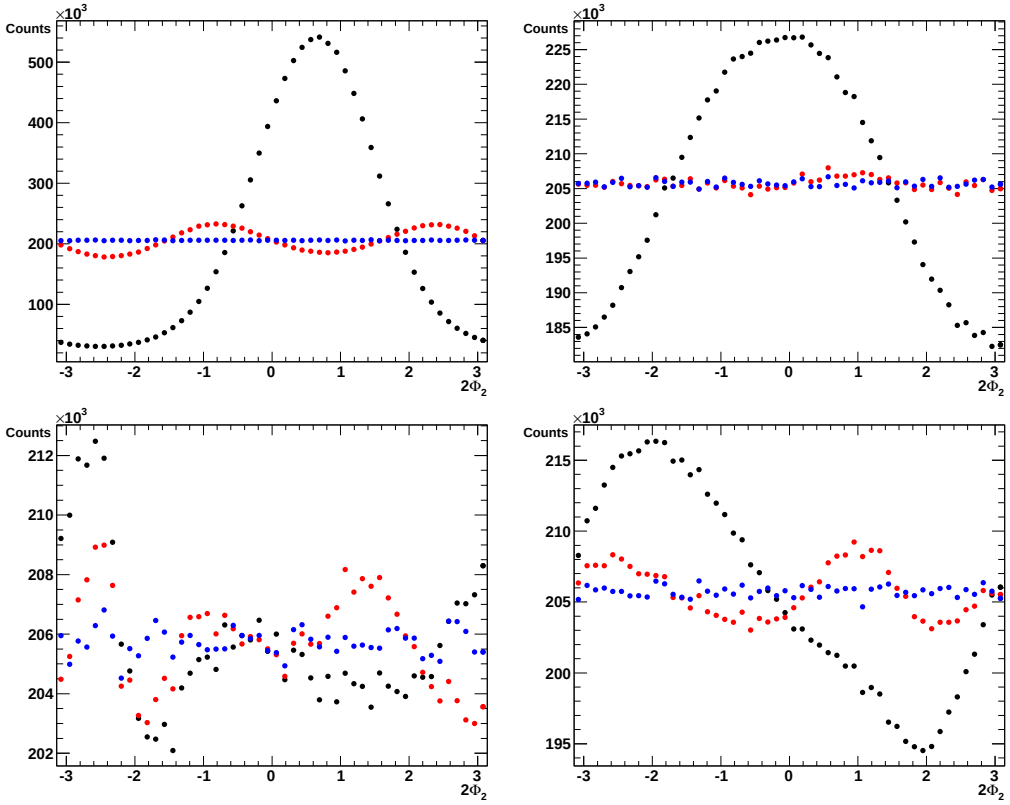

Figure 3.19: Distribution of $n\Phi_n$ ($n = 2$) at different stages of calibration. The black, red and blue dots indicate Φ_2^r, Φ_2^o and Φ_2^c respectively (see text). Top/Bottom panels show RXI/RXO. Left/Right panels show the south/north arm. Results are based on approximately 30 data segments which passed the QA (cf. Sec-3.6.5) for $\sqrt{s_{NN}} = 62$ GeV, centrality: $20 \sim 40\%$.

- First, histograms of Q_x and Q_y are built and filled with data.
- From these histograms, the mean and standard deviations of Q_x and Q_y ($\langle Q_x \rangle$ and $\langle Q_y \rangle$, $\sigma(Q_x)$ and $\sigma(Q_y)$) are calculated and recorded.
- In a second pass over the data, the Q-vectors are adjusted as

$$Q_x^o = \frac{Q_x - \langle Q_x \rangle}{\sigma(Q_x)}, \quad Q_y^o = \frac{Q_y - \langle Q_y \rangle}{\sigma(Q_y)}. \tag{3.30}$$

  Q_x^o and Q_y^o are then re-centered and normalized; they are also used to calculate Φ_n^o.

Distributions of the re-centered Q_x^o and Q_y^o are plotted on Fig-3.20 for RXIs (left panel) and RXOs (right panel). Though re-centered, the Q-vector distri-

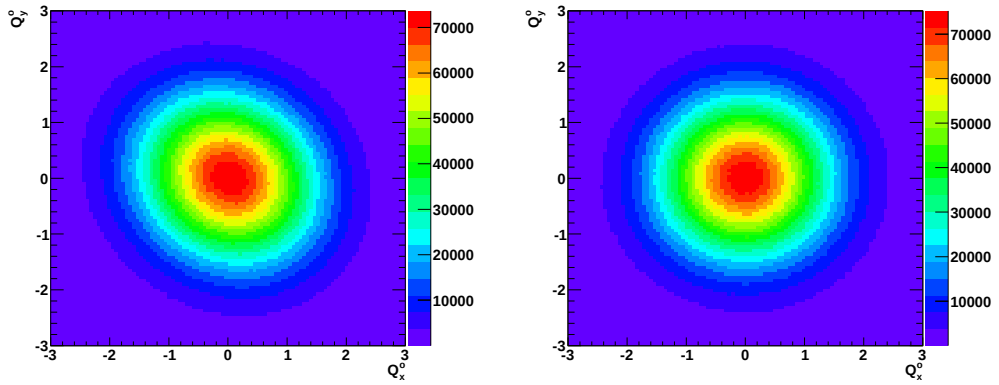

Figure 3.20: Q-vector distributions after re-centering. Axes show Q_x^o and Q_y^o respectively. The left/right panel shows the distribution for RXIs/RXOs. Results are shown for $\sqrt{s_{NN}} = 62$ GeV and a centrality of $20 \sim 40\%$.

bution for RXIs is still distorted and will be further corrected in the flattening process. Note that this picture is consistent with Fig-3.19, which shows that RXOs is quite robust; therefore its Q-vector distribution is not distorted, unlike that for RXIs.

3.6.3 Flattening of Φ_n^o

Instead of implementing further corrections on the Q-vector, flattening is a direct operation on the observed event plane Φ_n^o. The procedures for flattening are as follows:

- when Q_x^o and Q_y^o are obtained, Φ_n^o is calculated as well and filled into histograms of $\sin(nk\Phi_n^o)$ and $\cos(nk\Phi_n^o)$; k starts from 1 and goes up to a certain order of choice;

- the following two quantities are calculated and recorded after filling of the histograms mentioned above is completed:

$$A_{nk} = -\frac{2}{nk} < \sin(nk\Phi_n^o) >, \qquad B_{nk} = \frac{2}{nk} < \cos(nk\Phi_n^o) >; \tag{3.31}$$

- a new pass on the data is then started in which the fully calibrated event planes Φ_n^c are calculated as

$$\begin{aligned} \Phi_n^c &= \Phi_n^o + \Delta\Phi_n, \qquad \text{where} \\ \Delta\Phi_n &= \sum_k [A_{nk}\cos(nk\Phi_n^o) + B_{nk}\sin(nk\Phi_n^o)]. \end{aligned} \tag{3.32}$$

The flattening process, especially Eqn-3.31 and Eqn-3.32, are justified with the following derivation. Our target is to remove the modulation observed in the $dN/d\Phi_n^o$ distribution (cf. Fig-3.19). Therefore $dN/d\Phi_n^o$ is Fourier decomposed as

$$\frac{dN}{d\Phi_n^o} = \frac{n}{2\pi}(1 + \sum_k [a_{nk}\cos(nk\Phi_n^o) + b_{nk}\sin(nk\Phi_n^o)]) \tag{3.33}$$

in the range of $0 \sim 2\pi/n$. Notice that the expansion is normalized to unity and acts as a probability density. Then we find

$$\begin{aligned} \langle\cos(nk\Phi_n^o)\rangle &= \int_0^{\frac{2\pi}{n}} \frac{dN}{d\Phi_n^o}\cos(nk\Phi_n^o)\mathrm{d}\Phi_n^o = \frac{a_{nk}}{2} \\ \langle\sin(nk\Phi_n^o)\rangle &= \int_0^{\frac{2\pi}{n}} \frac{dN}{d\Phi_n^o}\sin(nk\Phi_n^o)\mathrm{d}\Phi_n^o = \frac{b_{nk}}{2} \end{aligned} \tag{3.34}$$

After flattening, we expect that $dN/d\Phi_n^c = n/2\pi$, a flat distribution; thus we correct Φ_n^o and have $\Phi_n^c = \Phi_n^o + \Delta\Phi_n$. The distribution of Φ_n^o can be re-written and expressed in terms of Φ_n^c and $\Delta\Phi_n$

$$\frac{dN}{d\Phi_n^o} = \frac{dN}{d\Phi_n^c}\frac{d\Phi_n^c}{d\Phi_n^o} = \frac{n}{2\pi}(1 + \frac{d\Delta\Phi_n}{d\Phi_n^o}). \tag{3.35}$$

The formula for $\Delta\Phi_n$ can be inferred by the comparison between Eqn-3.35 and Eqn-3.33. The expression of $d\Delta\Phi_n/d\Phi_n^o$ is the immediate result of the

comparison and its primitive function $\Delta\Phi_n$ has the form of:

$$\Delta\Phi_n = \sum_k [\frac{a_{nk}}{nk}\sin(nk\Phi_n^o) - \frac{b_{nk}}{nk}\cos(nk\Phi_n^o)]. \tag{3.36}$$

Put together Eqn-3.32 and Eqn-3.36 and compare, we arrive at

$$A_{nk} = -\frac{b_{nk}}{nk} = -\frac{2}{nk} < \sin(nk\Phi_n^o) >$$
$$B_{nk} = +\frac{a_{nk}}{nk} = +\frac{2}{nk} < \cos(nk\Phi_n^o) >$$

which proves Eqn-3.31. In practice, if flattening is applied up to the m-th order in terms of k, then approximately the first m Fourier components in the Φ_n^o distribution should be removed (flattened).

In Fig-3.21, flattening coefficients are illustrated. Note that RXIs has much

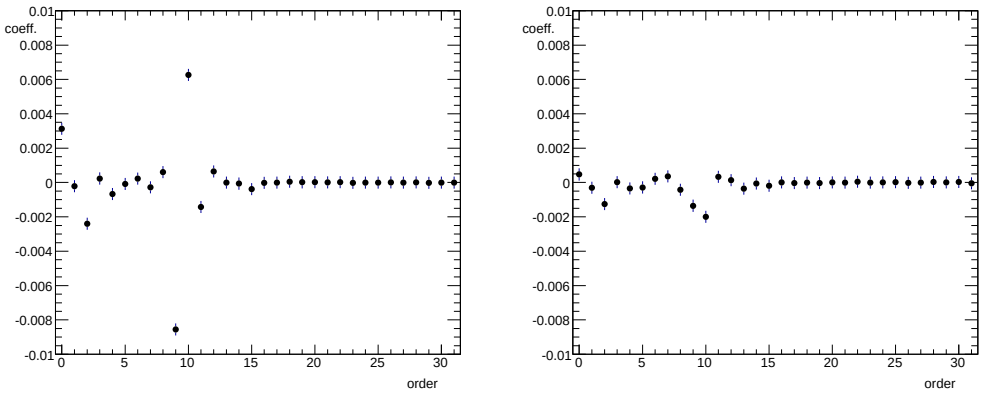

Figure 3.21: Illustration of flattening coefficients A_{nk} and B_{nk} up to 8th order ($k = 1, 2 \ldots 8$) for $n = 2$. Left/Right panel shows RXIs/RXOs. The first 8 bins are B_{nk} and the next 8 bins are A_{nk}. The remaining 16 bins show B_{nk} and A_{nk} after flattening, i.e. calculation is based on Φ_n^c instead of Φ_n^o. After flattening, all coefficients are approximately zero, indicating the removal of non-flatness. Results are shown for $\sqrt{s_{NN}} = 62$ GeV, centrality of $30 \sim 35\%$, and z-vertex in the $(0, 6)$ cm range.

larger flattening coefficients compared to RXOs, as expected. The latter 16 bins on the diagrams show that the flattening process has done a good job and the residual non-flatness is very limited.

3.6.4 Examination of the Calibrated Event Planes

There are multiple methods to check the robustness of the calibrated event planes. The most direct one is to examine the event plane distribution by eye and see whether it is uniform. This check is done in separate centrality bins since event plane construction is multiplicity sensitive. Normalized distributions of the event planes for several detectors located at different rapidities, are shown in Fig-3.22 (BBC, MPC) and Fig-3.23 (RXI, RXO). In central

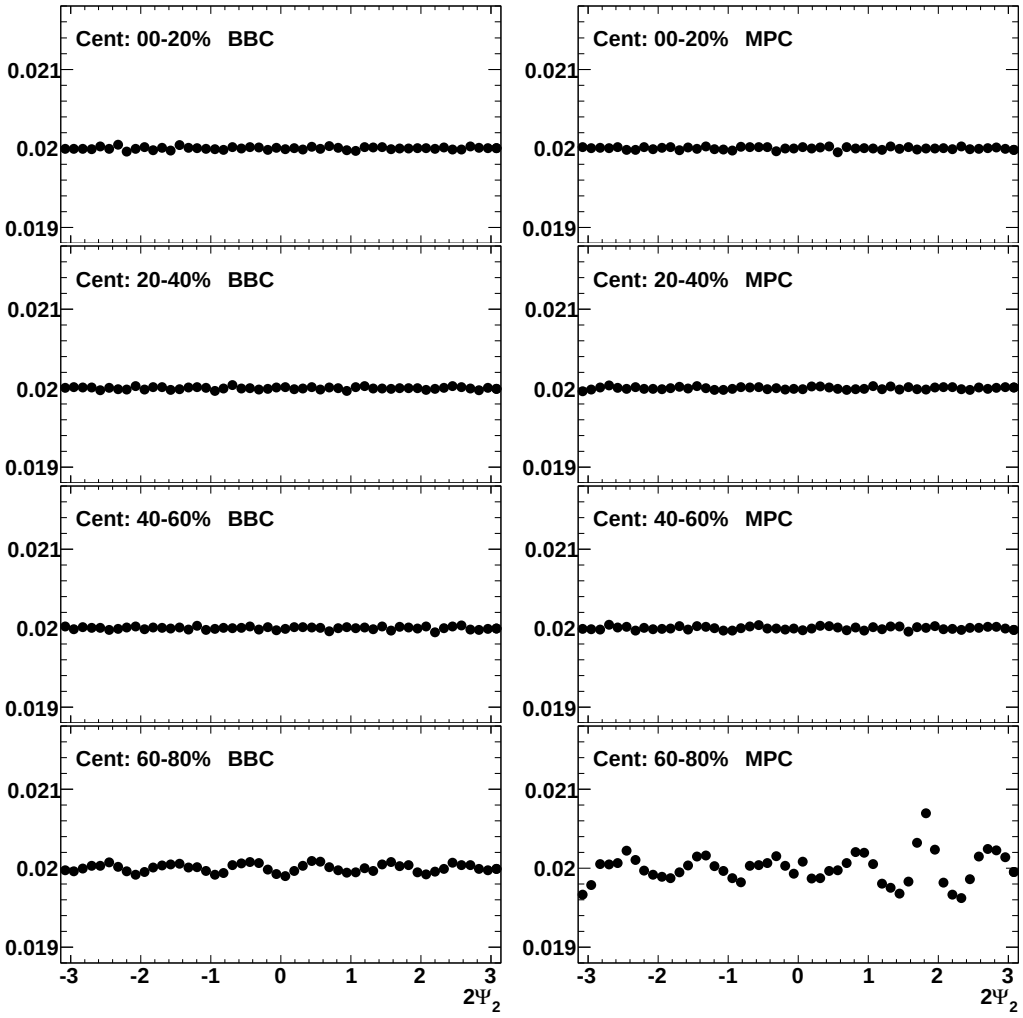

Figure 3.22: Calibrated event plane distributions for four centrality bins, for BBC and MPC for $\sqrt{s_{NN}} = 39$ GeV. The distributions are normalized.

collisions, the event plane distributions for all detectors are flat. However as we move to peripheral collisions, the small structures begin to appear. Note

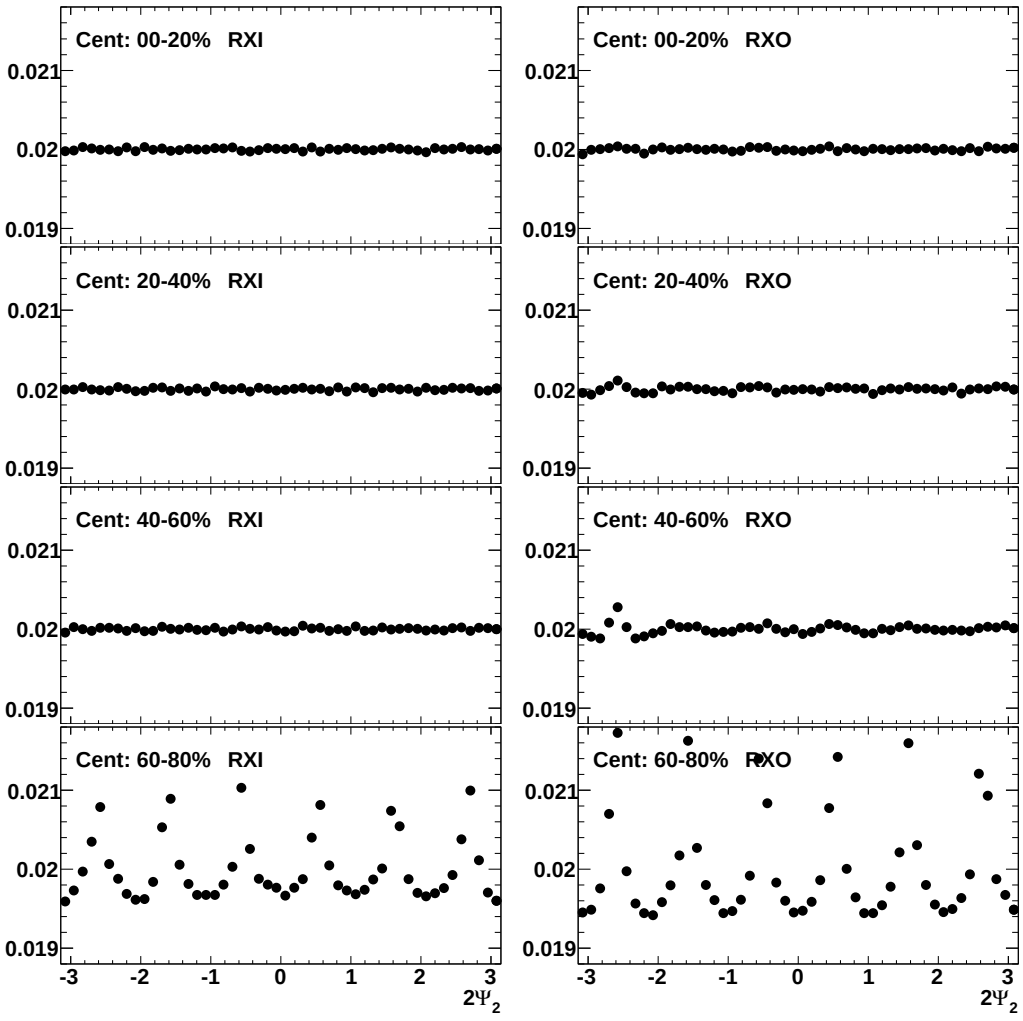

Figure 3.23: Calibrated event plane distributions for four centrality bins, for RXI and RXO for $\sqrt{s_{NN}} = 39$ GeV. The distributions are normalized.

that for the distributions in Fig-3.22 and Fig-3.23, the flattening is applied up to 5th order. Consequently, the residual structures in the distributions have a shape which mainly results from the 6th order Fourier component.

The deviations from uniform distributions are much more prominent for RXI and RXO, compared to BBC and MPC. The reason is probably that the azimuthal segmentation of the RXN detectors are much less (cf. Sec-2.1.5) than those for the BBC and MPC. The spikes in Fig-3.23 for RXI and RXO remind us of those observed in Fig-2.16, both of which are caused by detector granularity. Note as well that RXO has sizeable distortions. The wavy structures begin to appear for the centrality $20-40\%$ and becomes prominent for more peripheral collisions. Besides the reason above that applies for both RXI and RXO, the particle multiplicity incident on RXO is much less than that for RXI. Since event planes are determined with all particle hits on the detector, less multiplicity results in a magnification of the granularity effect. This argument is evidently shown by the centrality dependence of flatness rendered by all detectors. With the increase of centrality, multiplicity decreases and the non-flatness starts to emerge. In the case of RXO, this effect is most prominently demonstrated.

Except for the $60-80\%$ centrality bin for RXO, all other deviations from uniform distributions are within 5%. The impact of this non-flatness of the event planes was evaluated.

It's also worth checking the centrality dependence of $\langle\cos[n(\Phi_n^S-\Phi_n^N)]\rangle$ and $\langle\sin[n(\Phi_n^S-\Phi_n^N)]\rangle$ (abbreviated as $\langle\cos\rangle$ and $\langle\sin\rangle$). Both of them are directly measured. $\langle\cos\rangle$ is the multiplication of $\mathrm{Res}\{\Phi_n^S\}$ and $\mathrm{Res}\{\Phi_n^N\}$ according to Eqn-3.11. $\langle\sin\rangle$ should be zero by definition and omitted in the derivation of Eqn-3.11. $\langle\cos\rangle$ and $\langle\sin\rangle$ are plotted in Fig-3.24 for the $n=2$ case. On the $\langle\cos\rangle$ graphs, we see that the centrality dependence of event plane resolution behaves in the way discussed in Sec-3.4.4. $\langle\cos\rangle$ values beyond 60% centrality are small and might not be trustworthy according to the observations in Fig-3.22 and Fig-3.23. The $\langle\sin\rangle$ values shown in the right panels of Fig-3.22 have a different behavior for the four detectors. The centrality dependence of $\langle\sin\rangle$ values for BBC and MPC are mostly flat and consistent with zero. However, for RXI and RXO the dependence is characterized by structures similar to those on the left panel for $\langle\cos\rangle$ values. The reason for the resemblance is unknown, but the size of $\langle\sin\rangle$ values are on the level of about 1% of the $\langle\cos\rangle$ values, so the effects of the $\langle\sin\rangle$ values should be very limited.

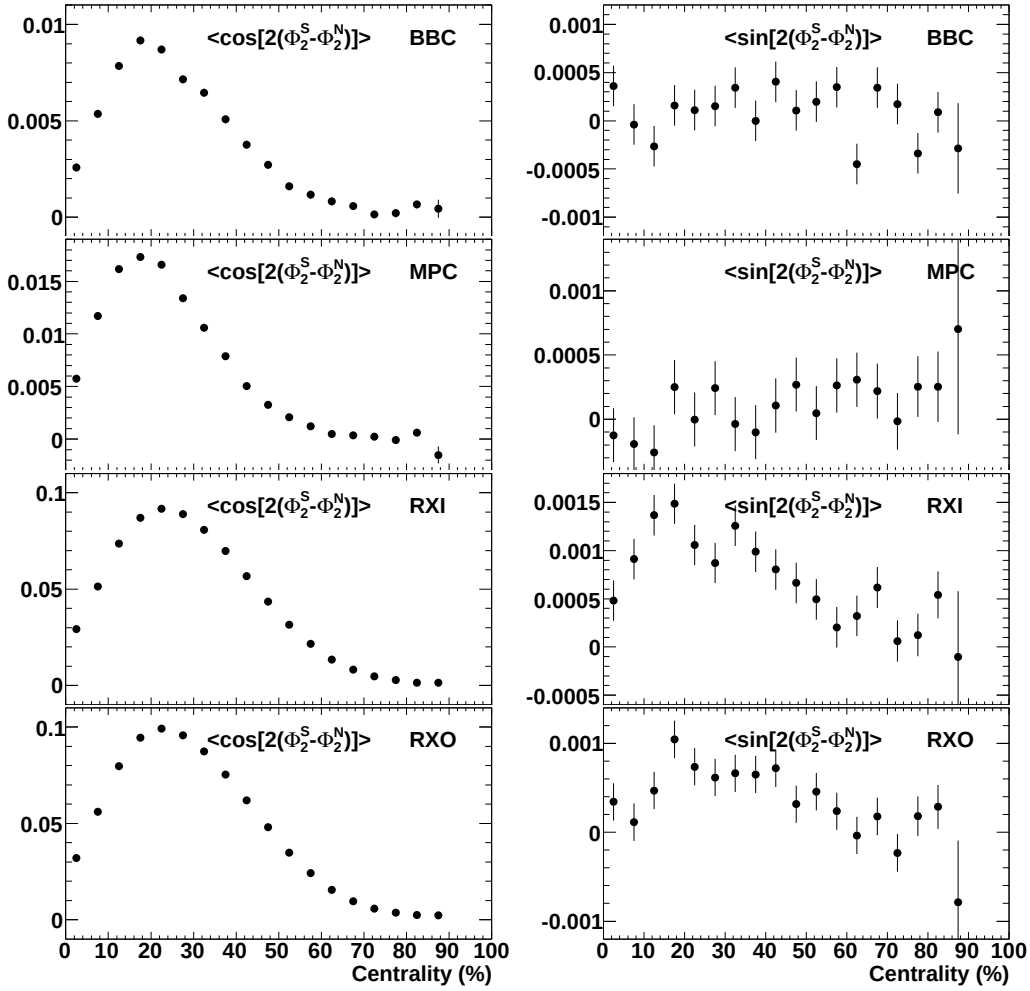

Figure 3.24: Centrality dependence of $\langle\cos[2(\Phi_2^S - \Phi_2^N)]\rangle$ and $\langle\sin[2(\Phi_2^S - \Phi_2^N)]\rangle$. Measurements for BBC, MPC, RXI and RXO are plotted for $\sqrt{s_{NN}} = 39$ GeV.

3.6.5 QA of Calibrated Event Planes

As we performed quality assurance (QA) for centrality definition in Sec-3.3.5, the same type of study, i.e. observing run-by-run variation of several key indicators of measurement robustness, is carried out on calibrated event planes to rule out data segments with "bad" event planes. The check shown here is aimed at the flatness of the event planes, which is quantified by the χ^2/NDF values of flat line fits to the event planes.

Values of χ^2/NDF for BBC, MPC, RXI and RXO are graphed in Fig-3.25 for 62 GeV collisions. While event planes constructed and calibrated for BBC,

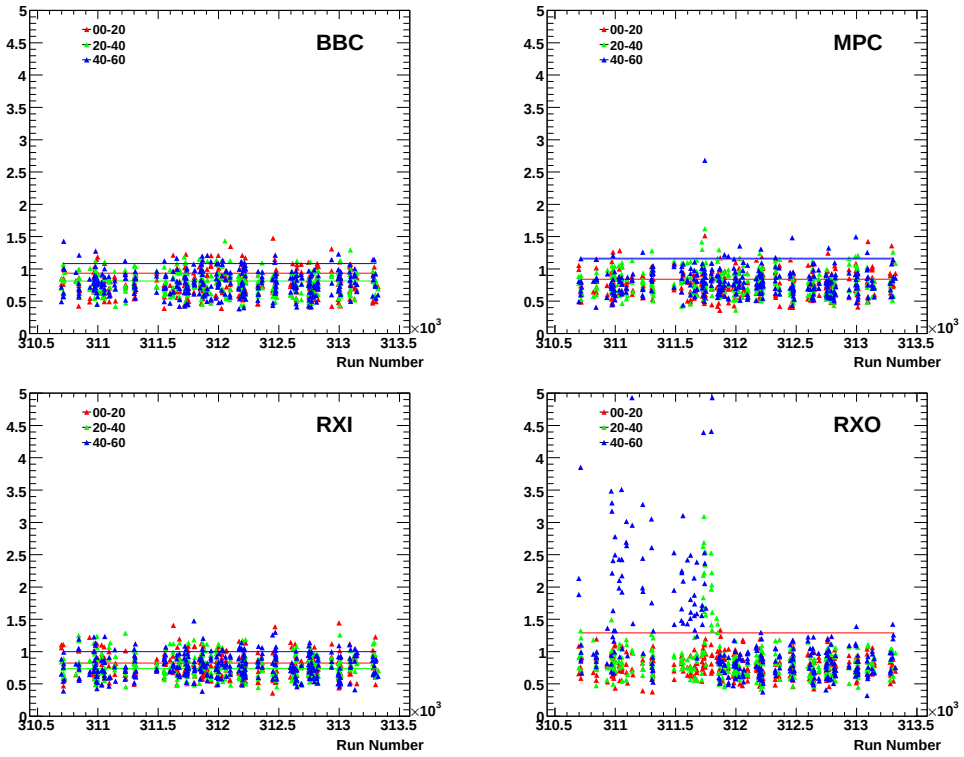

Figure 3.25: QA of event plane flatness. χ^2/NDF values of flat line fits to the event plane distributions are plotted for each run. Three centrality bins are shown as red $(0-20\%)$, green $(20-40\%)$ and blue $(40-60\%)$. Horizontal lines show averaged values of the whole dataset. Event planes at BBC, MPC, RXI and RXO are investigated, $\sqrt{s_{NN}} = 62$ GeV.

MPC and RXI seem to have good flatness, large χ^2/NDF values of RXO appear for about half of the runs, especially for mid-central and peripheral collisions. A closer investigation reveals that the RXO north arm is "innocent"; the non-flatness originates from the south arm and the χ^2/NDF values of RXOs are

plotted in Fig-3.26. We see that even more runs have extraordinary χ^2/NDF

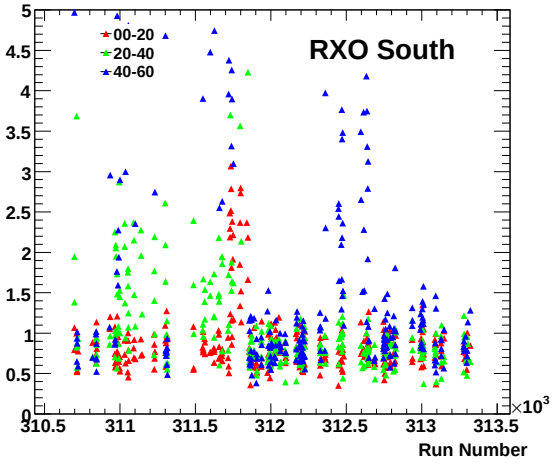

Figure 3.26: QA of event plane flatness. Same graph as those on Fig-3.25, for RXO south arm.

values. If we try to draw a line between the good and bad runs, and define runs with χ^2/NDF larger than 1.5 in the $40-60\%$ centrality bin (blue dots on the figure) as bad runs the rest as good ones, 184 runs are marked as good and the rest 128 are bad. Event planes for the aggregated good and bad runs are shown on left and right panel of Fig-3.27 respectively. While the general shape of Φ_2^r distributions are quite similar for the good and bad runs, a spike structure is observed at $2\Phi_2 \sim -1.5$ for the bad runs. This kind of highly localized structure is very difficult to remove by the calibration procedure and thus largely remains for the Φ_2^c distribution, which in turn results in larger χ^2/NDF values. The specific reason for the spike structure is unknown, but it's likely due to an overheated, constantly firing segment of RXO.

For the bad runs, the residual non-flatness in Φ_2^c for RXOs is around 1% in the $20-40\%$ centrality bin and develops to 4% in $40-60\%$ centrality, while for the good runs the non-flatness remains less than 0.5%. The effect of non-flatness at this level should be small, but for safety reason it's tested with π^0 v_2 measurement, details of which is documented in Chapter-4. From the comparisons shown on Fig-3.28, the differences between good and bad runs are within the statistical fluctuations of π^0 v_2 measurement.

Other indicators of event plane robustness that are examined for run-by-run variaton include $\langle\cos[n(\Phi_n^S - \Phi_n^N)]\rangle$ and $\langle\sin[n(\Phi_n^S - \Phi_n^N)]\rangle$, which are more closely related to the resolution factors and thus directly influence final results. For the $n = 2$ version, run number dependence of $\langle\cos\rangle$ values are plotted on Fig-3.29. The $\langle\cos\rangle$ values across run segments line up very well, in contrast

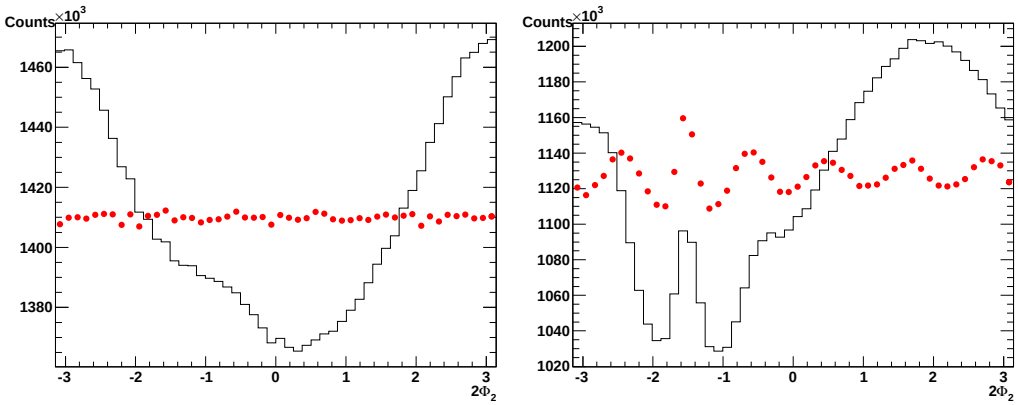

Figure 3.27: Comparisons between Φ_2 distributions from good and bad runs. Left/Right panel shows Φ_2 of aggregated good/bad runs. Black curve indicates uncalibrated Φ_2^r and red dots for fully calibrated Φ_2^c. Centrality: $20-40\%$, $\sqrt{s_{NN}} = 62$ GeV.

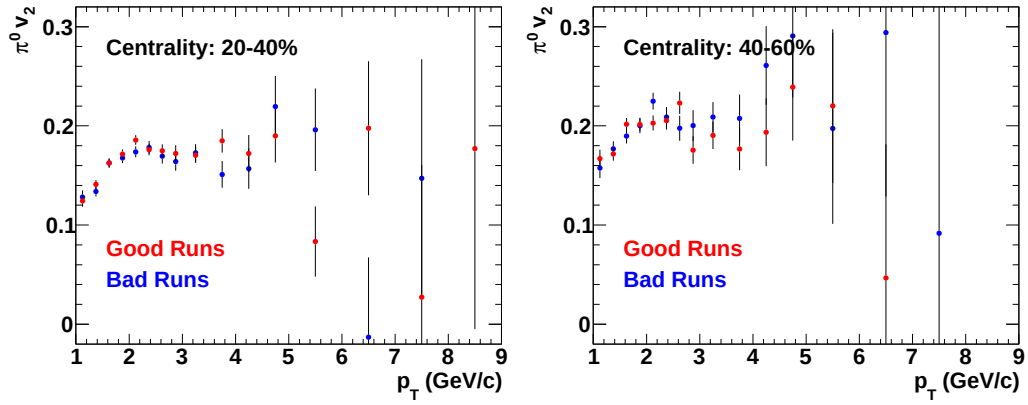

Figure 3.28: π^0 v_2 vs. p_T, measured for runs with different levels of event plane flatness. The bad runs (blue dots) have 1% non-flatness in $20-40\%$ centrality (left panel) and 4% in $40-60\%$ centrality (right panel). The good runs have less than 0.5% non-flatness in both centrality selections. $\sqrt{s_{NN}} = 62$ GeV.

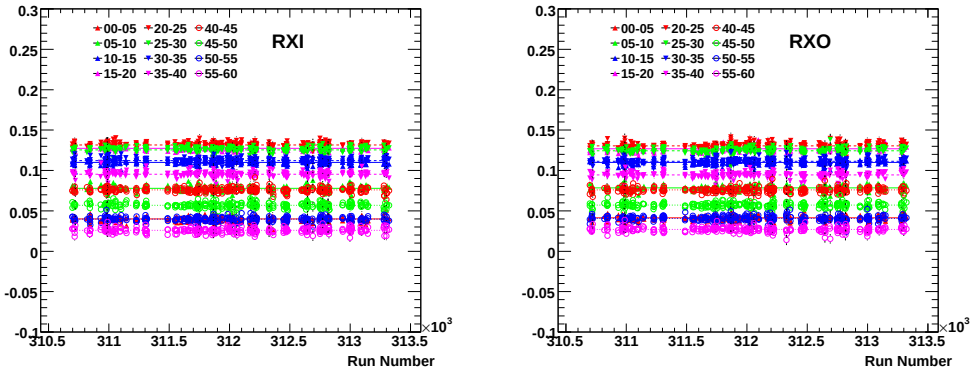

Figure 3.29: QA of $\langle\cos[2(\Phi_2^S - \Phi_2^N)]\rangle$, the values of which are plotted in 12 centrality bins (see legend) for RXI (left panel) and RXO (right panel) for each run segment. Horizontal lines indicate averaged values for the aggregated dataset. $\sqrt{s_{NN}} = 62$ GeV.

to the observations for the flatness indicator χ^2/NDF (cf. Fig-3.25). This fact suggests that the wave structure with the size of several percent doesn't have a substantial effect on the resolution factors; it is more or less averaged out during the process of the $\langle\cos\rangle$ calculation. No outliers are found from the run number dependence of $\langle\sin\rangle$ values as well, which are not diagramed.

The QA check for 39 GeV was also performed. The results show very consistent event plane characters across the runs. Even for the flatness (χ^2/NDF) test, only a very small fraction of runs have a large deviation from expectation.

Chapter 4

Neutral Pion v_2 Analysis

Neutral pions (π^0's) are commonly employed to probe high p_T phenomenon, and v_2 for π^0 has been shown to be sensitive to jet-medium interactions (cf. Sec- 1.8.3). Such interactions could be different for different collision energies. In this chapter, details of π^0 v_2 measurement for Run10 Au+Au collisions at $\sqrt{s_{NN}}$ = 62 and 39 GeV are documented. The results are compared to the existing measurements at the beam energy of 200 GeV.

4.1 Introduction to π^0 Analysis

According to the Particle Data Group [124], π^0 has the mass (m_{π^0}) and mean life time (τ_{π^0}) of

$$m_{\pi^0} = 134.9766 \pm 0.0006 \text{ MeV}, \quad \tau_{\pi^0} = (8.4 \pm 0.4) \times 10^{-17} \text{ s}.$$

The very short lift time indicates that π^0 quickly decays after traveling $c\tau_{\pi^0} \approx$ 25.2 nanometers (nm). This distance, though much large than the size of the collision zone that is typically on the scale of femtometers (fm), is negligible compared to the vertex position resolution of the BBC. Therefore, the decay vertex of π^0 is indistinguishable from the collision vertex and there is no way for a direct observation of the π^0.

4.1.1 Construction of π^0 from Photon Pairs

The dominant decay channel of the π^0 is $\pi^0 \rightarrow 2\gamma$, with a branching ratio of $(98.823 \pm 0.034)\%$. Therefore, π^0's are constructed from two photons. Since π^0's are among the most abundant particles produced in heavy ion collisions, a large number of photons are detected for each event by the EMCal (cf. Sec-2.3).

The kinematics of π^0 decay is quite simple and fully explained by conservation laws. The energy and momentum of π^0 candidates are calculated based on photon measurement as

$$E(\pi^0) = E(\gamma_1) + E(\gamma_2), \quad \boldsymbol{p}(\pi^0) = \boldsymbol{p}(\gamma_1) + \boldsymbol{p}(\gamma_2). \tag{4.1}$$

Then the invariant mass is calculated $m_{\rm inv} = E^2 - \boldsymbol{p}^2$ and compared to m_{π^0}. If $m_{\rm inv}$ falls in a certain neighboring region around m_{π^0}, the photon pair is possibly generated by a real π^0 decay. In practice, $m_{\rm inv}$ is calculated for all possible photon pairs and filled into the $m_{\rm inv}$ histogram (foreground distribution), such as the one indicated by red dots on the left panel of Fig-4.1. Since

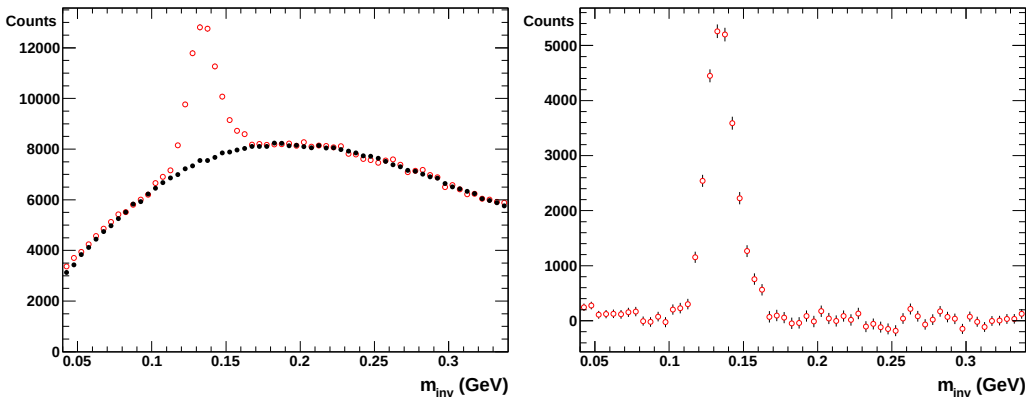

Figure 4.1: An example of π^0 yield measurement by statistical subtraction for photon pairs of $2.0 < p_T < 2.25$ GeV and $\sqrt{s_{NN}} = 62$ GeV. Left panel: red dots indicate $m_{\rm inv}$ calculated from inclusive photon pairs in the same event (accumulated over many events); black dots show the estimation of combinatorial background via the event mixing technique. Right panel: π^0 peak after background subtraction.

$m_{\rm inv}$ might also be calculated from two uncorrelated photons (such as photons from two different π^0 decays, where each photon is from a different decay), a large combinatorial background (black dots) serves as a pedestal for the π^0 peak. Consequently, an event mixing technique was employed to estimate the combinatorial background. The overall size of the background is adjusted to match the foreground in regions far away from the π^0 peak. The background-subtracted distribution is shown in the right panel of Fig-4.1; it shows a clear π^0 peak. Note that the natural width of π^0 mass is only 7 eV which would be negligible on the figure; the width of the peak in Fig-4.1 results from the detector resolution.

The π^0 peak on the right panel of Fig-4.1 is the cornerstone of the π^0 analy-

sis. The peak is routinely fitted with a Gaussian function and the position and width of the peak are determined as the expectation and standard deviation of the Gaussian function. They are the most effective indicators of the quality of π^0 peaks. An integration of the data points in the peak region gives the π^0 yield.

4.1.2 Limitation on π^0 Measurement

The equation to calculate m_{inv} could also be written as

$$m_{\text{inv}}^2 = 2E(\gamma_1)E(\gamma_2)(1 - \cos\theta) \tag{4.2}$$

where θ is the opening angle between the two photons. The EMCal position resolution (cf. Sec-2.3) naturally leads to θ angle resolution; together with the EMCal energy resolution for $E(\gamma_1)$ and $E(\gamma_2)$, the resolution of m_{inv} can be estimated. Moreover, the separation between the two photon clusters has a lower limit. If the two clusters heavily overlap it would be impossible to separate them in the EMCal, and they would appear as a single cluster. This lower limit for γ-pair separation gives a lower bound on θ, denoted by θ_L. Expanding the $\cos\theta$ term in Eqn-4.2 for small θ values while keeping only the first order terms, the following relation could be derived with the help of Eqn-4.1:

$$E^2(\pi^0) = E^2(\gamma_1) + E^2(\gamma_2) + \frac{2m_{\text{inv}}}{\theta^2} \leq E^2(\gamma_1) + E^2(\gamma_2) + \frac{2m_{\text{inv}}}{\theta_L^2}$$

For arbitrary θ, $E(\pi^0)$ could reach infinitely large values for small θ. The lower limit θ_L puts an upper limit on $E(\pi^0)$ and thus the p_T of π^0 that can be measured; at PHENIX this limit is $p_T \sim 20$ GeV.

For low energy photons, the responses of the calorimeters are nonlinear and correspondingly large uncertainties are introduced for the photon energy and position measurement. For this reason, π^0's are constructed only for photon pairs with p_T larger than 1 GeV.

4.1.3 Selection of Photons and Photon Pairs

The full MiniBias dataset of Run10 62 and 39 GeV were used for the analysis. For each event, clusters in EMCal were selected as photons according to certain rules (commonly referred to as "cuts"). The cuts to help select photons are not mandatory since the target particle is π^0, the yield of which is found out by the subtraction shown in Fig-4.1. However, a cleaner background helps to reduce the statistical errors in the π^0 yield. Imagine on average n π^0's are

created for each event and N ($N > 2n$) clusters on EMCal are identified as photons. $N^2/2$ photon pairs are thus filled into the m_{inv} histogram and $aN^2/2$ ($a < 1$, a fraction parameter) photon pairs fall in the π^0 peak region. Assuming a Poisson distribution for the counts in each bin of the m_{inv} histogram, the statistical fluctuation of the background is roughly $N\sqrt{a/2}$. Therefore, the percentage statistical error is proportional to N/n. Therefore the suppression of contamination in the photons (smaller N) is quite beneficial to the analysis.

One important cut to select photon is the χ^2 value. As discussed in Sec-2.3, this value reflects the resemblance between a detected cluster and a modeled "standard" EM shower. The χ^2/NDF distributions (the NDF normalization is tacitly assumed in our analysis) for EM showers and hadron showers are plotted on Fig-4.2. As we can see, the distribution of the hadron shower is

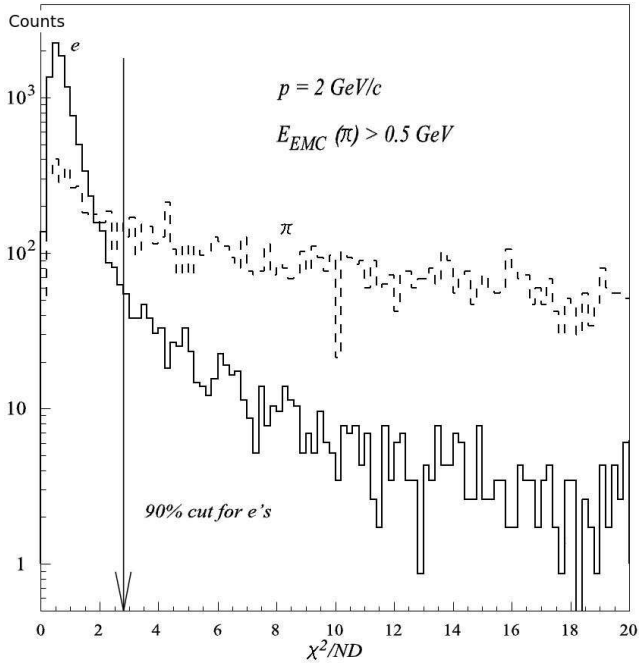

Figure 4.2: χ^2/NDF distributions for clusters created by electrons (EM showers) and charged pions (hadron showers) [125]. Note the logarithm vertical axis.

much flatter when compared to the EM shower. Therefore, enforcement of an upper limit on χ^2 values could effectively reduce the hadron contamination. In our analysis, a $\chi^2 < 3$ cut was implemented.

There are other cuts that are routinely applied to photon identification. If charged particles register in the EMCal, they are likely to leave their a signal in PC3 as well (cf. Fig-2.1, PC3 is located in front of the EMCal); therefore

the exclusion of coincident hits on both PC3 and EMCal was used to reject charge particles (commonly referred to as "charge veto" cut). In addition, information from the RICH helps to identify electrons/positrons which can be rejected as well. The EMCal is also able to provide particle TOF information, which could be employed to reject heavy particles like neutrons. Since this analysis is one of the earliest that utilized the Run10 62 and 39 GeV datasets, these latter cuts were not adopted.

Besides identification cuts on individual photons, there are cuts on the photon pairs that could further reduce the combinatorial background. One natural requirement is that both photons must be measured in the same sector because different sectors show a slightly different response to photons. Some π^0's are cut off by this requirement, but only a small fraction. For energetic π^0's where statistics are more valued, the opening angles of the decay photon pairs are small. Eqn-4.2 suggests that $\theta = m_{inv}/E(\gamma)$ for small θ values. For a photon energy of 3 GeV, $\theta \approx 0.05$ radian or 3 degrees, and its projection in the transverse plane is even smaller. Compared to the 22 degree span of one EMCal sector, the loss of π^0's from this cut is negligible.

Another routinely utilized photon pair cut is the energy asymmetry of the photon pair, defined as

$$\alpha = \frac{|E(\gamma_1) - E(\gamma_2)|}{E(\gamma_1) + E(\gamma_2)}$$

and takes on values between 0 and 1. By pure kinematics, the asymmetry distribution of true π^0 decay photon pairs should be flat. However, for high p_T π^0 construction, mis-identified low energy clusters tend to produce fake π^0's with large α values, as shown on Fig-4.3. Therefore, the requirement

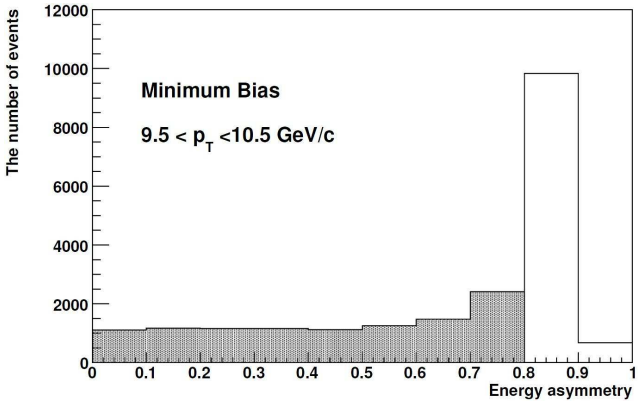

Figure 4.3: Photon pair asymmetry distribution [125].

of $\alpha < 0.8$ was implemented in the analysis. Other pair cuts not discussed

include the cluster distance cut, the opening angle cut and so on.

4.2 EMCal Calibration

The response of the EMCal needs to be calibrated to ensure robust photon measurement for π^0 construction. In this section we discuss the creation of tower masks to exclude undesired towers and the tower-by-tower energy scale calibration. Calibrations of quantities that are not closely related to this analysis, such as the EMCal time of flight and matching variables, are not presented.

4.2.1 Creation of Tower Masks

For an ideal detector, the photon distributions in the EMCal, for a sufficient number of events, should be uniform and all towers are expected to fire roughly equal number of times. However, some towers fire far too often and are referred to as "hot" towers; on the contrary, some towers don't fire at all and are referred to as "dead" towers. Still some towers fire more frequently only in a certain energy range, they are referred to as "warm" towers. Hot and warm towers are particularly harmful to π^0 analysis because they could pair with themselves or other photons and generate false counts in the π^0 peak region, resulting inaccurate π^0 yield measurement.

The method to find out these undesired towers is straightforward. Since they are defined purely by the abnormal firing frequency, histograms of firing frequency are built, like the ones presented on Fig-4.4. These histograms are then fitted with Gaussian functions, the mean and width values of which are calculated. Afterwards, a quantitative cut is applied to exclude towers with firing frequency several RMS away from the mean value. The whole process was applied to the surviving towers for some additional iterations.

The method above removes most of the bad towers. However, it might fail to detect warm towers that have a normal firing frequency for low and intermediate tower energy but produce too many high energy hits. High energy clusters are rare; therefore histograms like those on Fig-4.4 don't have enough statistical significance to isolate bad towers. In this case, those warm towers are identified by observing the satellite peaks around the π^0 peak and picked out by hand. This process is best illustrated on Fig-4.5. Generally, it's safe to say that the bad towers are mostly removed when only the π^0 peak is present in the low invariant mass region, as demonstrated by the right panel of Fig-4.5.

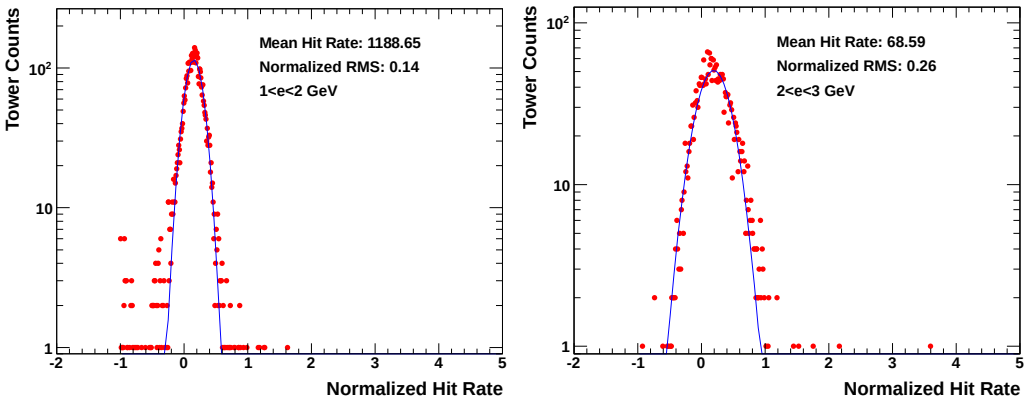

Figure 4.4: Firing frequency distribution of EMCal towers in one sector. The averaged number of hit rate is printed on the figure and used to normalize the horizontal axis. The width of the fitting Gaussian (RMS) is also printed in the unit of the horizontal axis. Left panel shows one PbGl sector for clusters with energy between 1 to 2 GeV. Right panel shows one PbSc sector for clusters with energy between 2 to 3 GeV. The vertical axis represents number of towers and we see one PbGl sector has more towers than one PbSc sector. $\sqrt{s_{NN}} = 62$ GeV.

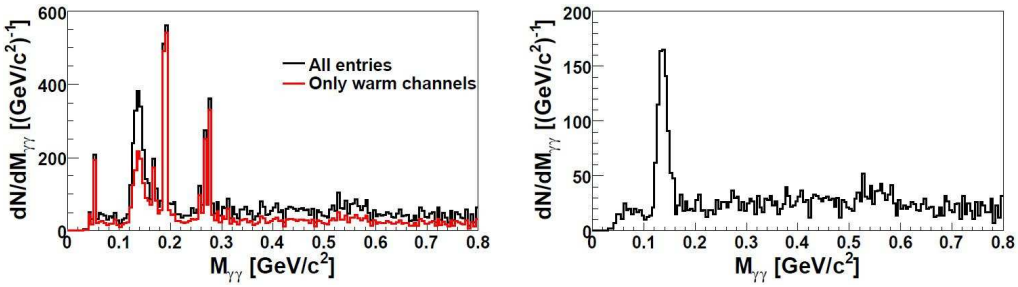

Figure 4.5: Invariant mass distribution showing satellite peaks [126]. Left panel: black line indicates the inclusive invariant mass distribution for photon pairs with p_T in the range of 5 to 6 GeV; red line shows contribution from identified warm towers. Right panel: invariant mass distribution after the subtraction of warm tower contribution. $\sqrt{s_{NN}} = 62$ GeV.

4.2.2 Tower-by-Tower Energy Calibration

The most important calibration for the EMCal is the tower-by-tower energy scale calibration. The necessity of the calibration originates from the fact that energy measurement performance is not uniform across towers. Some towers produce higher than normal cluster energy and others behave in an opposite way. If the two cluster invariant mass histogram is generated with uncalibrated tower energy, the position of the π^0 peak might be shifted from its expected value and its width significantly broadened. The reason for this is that the inclusive π^0 peak results from a superposition of π^0 peaks from all tower pairs, and the position of these π^0 peaks could be shifted due to a non-uniform energy scale. Moreover, in this scenario, if the inclusive π^0 peak is integrated to find the π^0 yield, the background contamination from the broadened π^0 peak would be significant. Therefore, in the tower-by-tower energy calibration, a scaling constant is assigned to each tower so that the produced two cluster invariant mass histogram has the π^0 peak centered at m_{π^0} and the narrowest possible width.

To implement the calibration, a m_{inv} histogram is built for each EMCal tower, i.e. 15552 histograms for PbSc and 9216 histograms for PbGl (cf. Sec-2.3). Each histogram is filled with m_{inv} values calculated with the cluster from the corresponding tower and any other cluster in the same sector. All of these histograms are then fitted with a functional form that has both background and π^0 peak components. Due to the large number of histograms, the fitting process is automated. Towers with clear π^0 peak fits are passed (cf. top panels of Fig-4.6). The rest are checked by eye to see if they are mis-calibrated (cf. middle panels of Fig-4.6) or pathological (e.g, hot, warm, dead towers). The scale factor assigned to each tower is obtained by dividing m_{π^0} with the π^0 peak center of the histogram so that when multiplied by the tower energy, the π^0 peak is shifted to the correct position. Because the procedure relies heavily on the π^0 peaks, it is referred to as the π^0 method.

After one pass of calibration, the energy scales of the two clusters used to calculate m_{inv} are changed. This can lead to an over-correction and a π^0 peak position which deviates from m_{π^0}. Therefore, additional iterations of calibrations were employed. Normally after 3 to 4 passes, the scale factors converge to their correct values.

A complementary method for the tower-by-tower correction, the slope method, was also employed. It served as a cross-check to the aforementioned π^0 method and helped to recover mis-calibrated towers. In this method, the cluster energy distribution is built individually for each tower and fitted with a simple exponential form of $p_0 \exp(p_1 E)$. The inverse slope $1/p_1$ is considered to some extent to be the mean energy of the tower. Since each EMCal sector

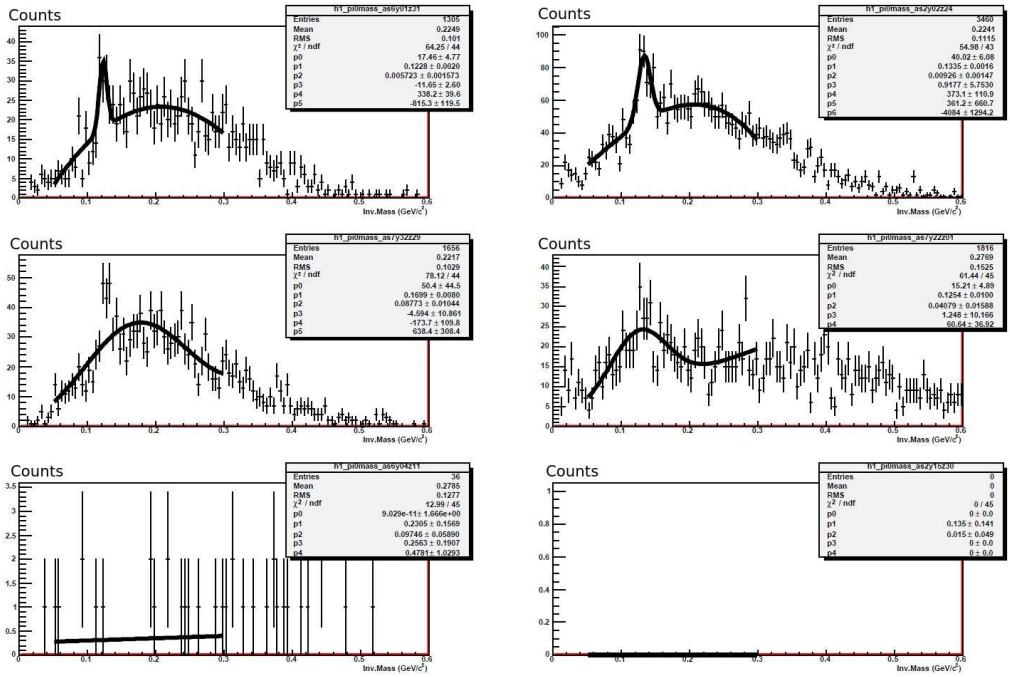

Figure 4.6: EMCal tower-by-tower energy calibration via π^0 method [126]. Each panel shows a typical histogram of the two cluster m_{inv} distribution with a fitted curve. Each histogram is for a specific tower, i.e. one of the two clusters must be associated with that tower. Top panels: m_{inv} distributions for good towers. Middle panels: mis-calibrated towers. Bottom panels: dead towers.

is a flat plane and only the center of the sector is aligned to the interaction point, photons hitting the sector would have an incident angle that is smallest and 0 for the tower at the sector center and largest for peripheral towers of the sector. For photons with equal energy, clusters created with a large incident angle would have a smaller cluster energy. Therefore, $1/p_1$ of a tower is modeled to be proportional to the distance between the tower and the sector center. For PbSc and PbGl sectors, the distance is calculated with following formula

$$\begin{aligned} \text{PbSc}: &\quad \sqrt{(y-18)^2+(z-36)^2} \\ \text{PbGl}: &\quad \sqrt{(y-24)^2+(z-48)^2} \end{aligned}$$

in the unit of tower size. x and y are tower indices in the x and y direction; the formula should be self-evident after referring to Tab-2.3.1 for the tower configuration within a sector.

For PbSc towers, the inverse slope vs. distance plot is shown in the left panel of Fig-4.7. A straight line fit is plotted to indicate the linear relation as

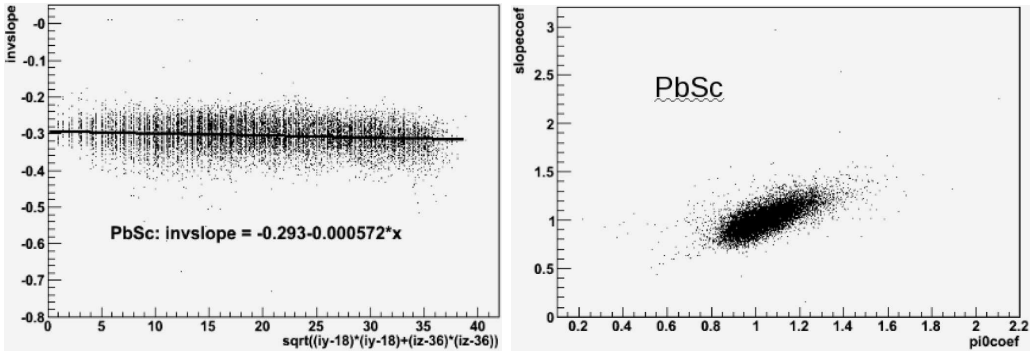

Figure 4.7: EMCal tower-by-tower energy calibration via slope method [127]. Left panel: inverse slope vs. tower distance to sector center. Right panel: correlation between scaling factors found from the two methods. Both panels show PbSc towers.

proposed above. The scale factor for each tower is then defined as the ratio of inverse slope value on the fitted line divided by the measured inverse slope. On the right panel of Fig-4.7, a very good correlation between the scale factors obtained with the two methods is found. Therefore, if there are mis-calibrated towers in the π^0 method, with well defined scale factors for the slope method, they are recovered and assigned with scaling factors from the slope method.

The Run10 EMCal calibrations were done with the first 358M events of Au+Au $\sqrt{s_{NN}} = 200$ GeV collisions (for Run10, PHENIX collected 200, 62, 39

and 7.7 GeV collision data sequentially). The calibration constants generated at 200 GeV are proven to behave well for 62 and 39 GeV as well (cf. Sec-4.4.2). The effectiveness of these calibrations were assessed immediately after the completion of the calibration; the results are shown in Fig-4.8 and Fig-4.9 for π^0 peak position and width respectively. For π^0 peaks constructed in all

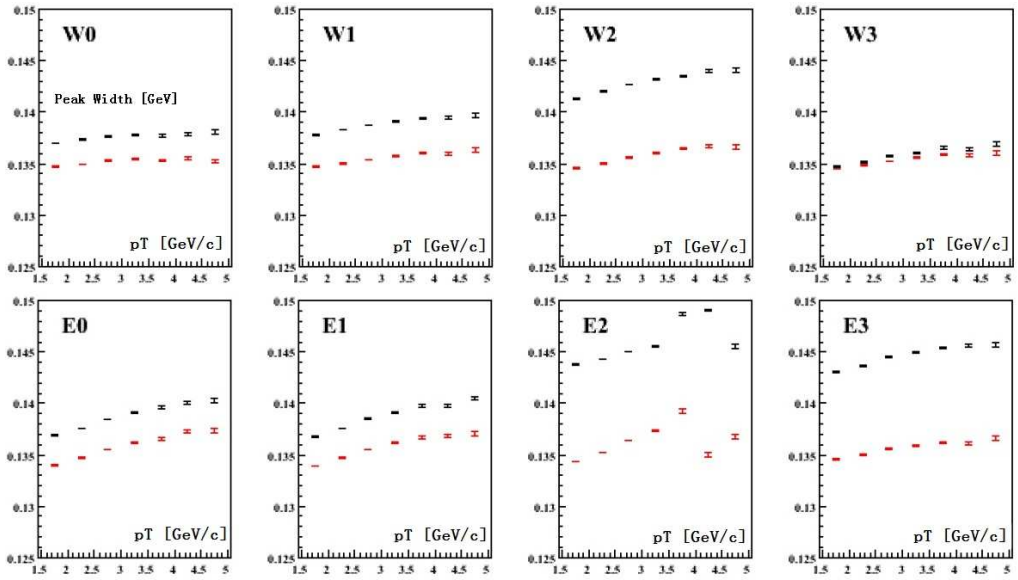

Figure 4.8: π^0 peak position vs. π^0 p_T, before and after calibration. Black/Red dots correspond to values before/after the calibration. 8 EMCal sectors on east (E) and west (W) arms are shown separately; E2 and E3 are PbGl sectors. Results are shown for Run10 Au+Au collisions at $\sqrt{s_{NN}} = 200$ GeV.

sectors, the peak position is shifted to the desired value (m_{π^0}) and the width of the peak is reduced.

Another feature demonstrated in Fig-4.8 and Fig-4.9 is that after calibration, the π^0 peak position and width values are much more consistent among the 8 sectors. This observation provides crucial support if we want to combine the 8 sectors and find π^0 yield from the unified invariant mass distribution. However, differences among sectors do exist. Therefore, a run-by-run sector-by-sector calibration was proposed to be implemented after the tower-by-tower calibration [125]. In the additional calibration, a scale factor for each sector is calculated for each data segment. In this way, the π^0 peak positions of all sectors are guaranteed to align with each other. This additional calibration procedure was not implemented for the analysis presented here. Instead, π^0 v_2's are calculated individually for each sector and the differences among the 8 sectors are quoted as part of the systematic uncertainty.

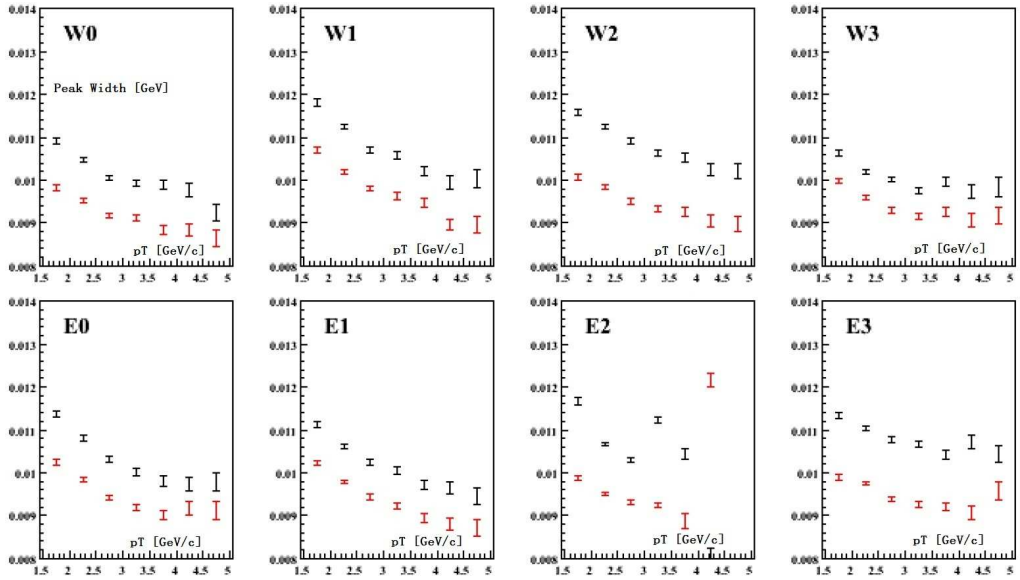

Figure 4.9: π^0 peak width vs. π^0 p_T, before and after calibration. Specifications are the same as Fig-4.8.

4.3 QA of π^0 Peak

In this section the run-by-run variation of π^0 peak is checked. One possible issue of QA analysis is the deficiency of statistics for each data segment. Since the run-by-run variation is normally just a few percent, the error bars for each point on the QA plot (corresponding to one data segment) should not be larger than that. Consequently, neighboring runs are grouped together to form larger data pieces for the statistics starving QA analysis like the one presented here. In our case, every 24 original run segments are considered a run group and aggregated into a data piece, which is assigned an artificial run number starting from 999900.

The results of run group QA analysis of π^0 peak position and width values are diagramed in Fig-4.10. The benefit of utilizing run groups is very obvious, as reflected by the small error bars on the data points. The last run group has less statistics since the number of residual runs for the last run group is normally less than 24. For each EMCal sector, the variations among run groups are typically less than 1%. Therefore, it's safe to aggregate all of these runs to exploit the statistics to the full extent.

The purpose of the QA analysis is to insure uniform performance among run segments and reject possible bad runs. The run group study suggests that the π^0 peak is consistently constructed across the dataset. But to reject bad

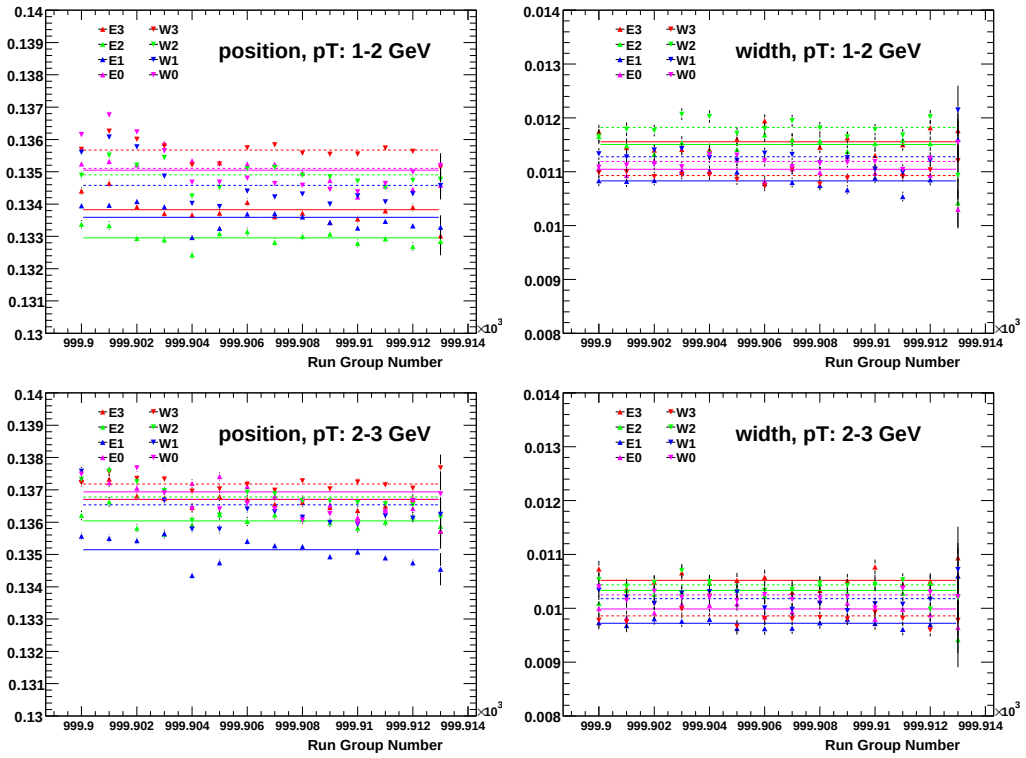

Figure 4.10: Run group QA of π^0 peak for 8 sectors separated into two p_T bins. Left/Right panel shows peak position/width. Horizontal lines indicate averaged values with aggregated runs. Results are shown for the centrality selection of $0-60\%$ for $\sqrt{s_{NN}} = 62$ GeV.

runs, the QA for individual runs must be examined, which is not performed in the first place due to the lack of statistics. However, one feature observed in Fig-4.10 is that the discrepancies among sectors are small. Comparing the flat lines on the figure that indicate averaged values, the π^0 peak position and width values agree within 1% and 5% respectively among different sectors. The differences are not large compared to the QA sensitivity here and therefore the 8 sectors are combined to gain statistics. With improved statistics, the π^0 QA studies of individual run segments are shown in Fig-4.11. The error bars on

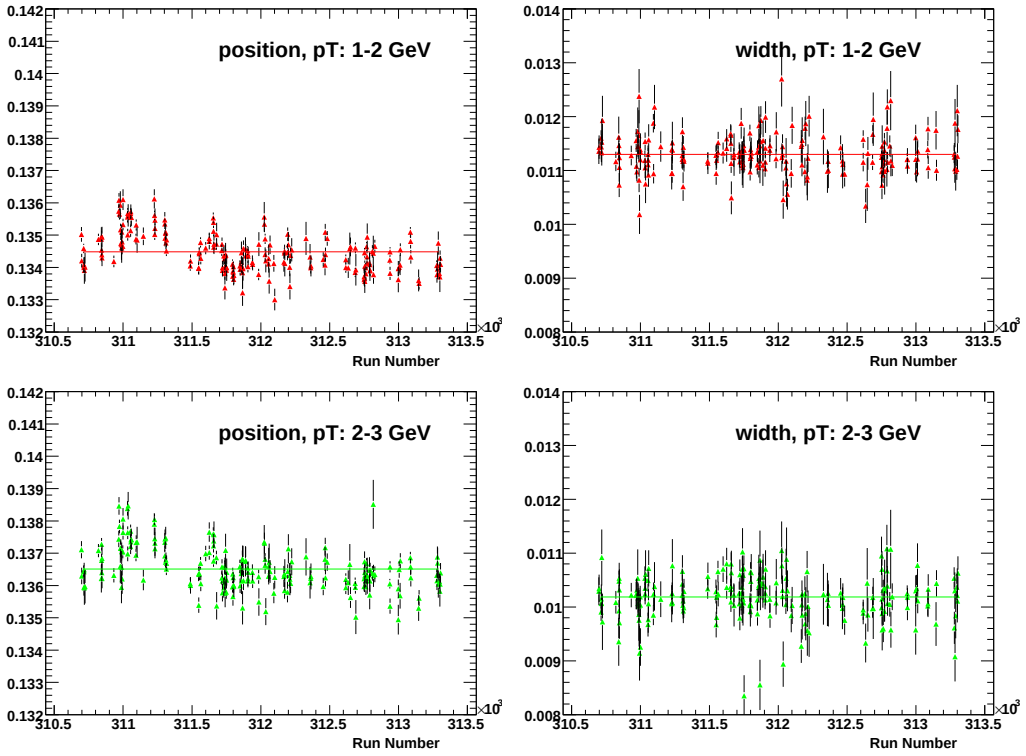

Figure 4.11: Single run QA of the π^0 peaks for the combined sectors in two p_T bins. The left/right panels show peak positions/widths. Horizontal lines indicate averaged values with aggregated runs. Results are shown for the centrality selection of $0-60\%$ for $\sqrt{s_{NN}} = 62$ GeV.

data points are relatively large, roughly on the same scale with the run-by-run fluctuations. Outliers on the figures were marked for additional checking, and problematic data segments were rejected.

The same set of π^0 QA analysis was also implemented for the $\sqrt{s_{NN}} = 39$ GeV dataset. Together with the centrality QA (cf. Sec-3.3.5) and the event plane QA (cf. Sec-3.6.5), the major components for the π^0 v_2 analysis were

completely checked across the dataset. Robust run segments were aggregated and serve as the input for the analysis that follows.

4.4 Extraction of π^0 Yield

The azimuthal anisotropy of particle production reflects the azimuthal dependence of particle yields. Therefore a robust extraction of π^0 yield is a crucial step for the π^0 v_2 measurements.

4.4.1 Measurement of π^0 with Individual and Combined EMCal Sectors

Each of the eight sectors of EMCal can be treated as an individual detector. Actually, π^0's were indeed constructed in each sector separately. However, a combination of the eight sectors increases the statistics by 8 fold. Therefore, we tend to combine the eight sectors whenever possible.

The prerequisite for sector combination is that the π^0 peaks for the m_{inv} histograms are sufficiently similar for all sectors. Side-by-side comparisons of the π^0 peak position and width values for the eight sectors are plotted in Fig-4.12. We observe the same general features for the p_T dependence among

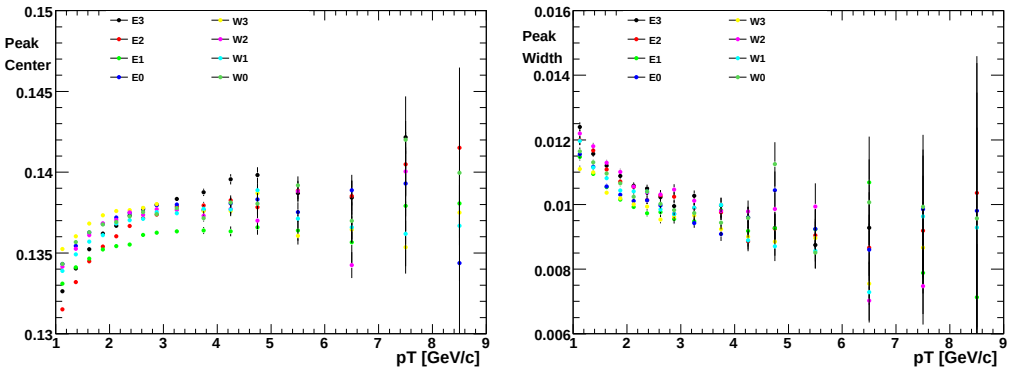

Figure 4.12: Comparison of the π^0 peak among 8 EMCal sectors. Left/Right panel shows the p_T dependence of the positon/width of the π^0 peak. Results are shown for the centrality selection of $0-60\%$ for $\sqrt{s_{NN}} = 62$ GeV.

the 8 sectors for both π^0 position and width. The peak position shows a small increase with p_T but has an average around m_{π^0}. The inclusion of an energy dependent scale factor in the calibration process for each tower may solve the small rise with p_T; however there is no strong motivation supporting

this difficult task and it's therefore not carried out. The peak width decreases with p_T, which is easy to understand as the background particles are normally "soft", i.e. having low p_T.

What's more relevant here is whether the 8 sectors are sufficiently similar to each other so that we could combine them without introducing substantial contamination, which refers to irrelevant photon pairs coincidentally identified as π^0's (fake π^0's). The fakes don't carry a v_n signal and would thus lower the measured π^0 v_2 if included. The discrepancies among peak position values are $1 \sim 2$ MeV, which is small compared to m_{π^0} but not so small relative to the ~ 10 MeV peak width. Instead of a direct quantitative evaluation of the contamination followed by derivations of the effects on v_2, we perform v_2 measurements separately for each sector as well as for the combined sectors. By comparing the differences among these measurements, we obtain an estimation of the uncertainty on the combined result. The following 3 schemes of combination were implemented:

- combine all 8 sectors to gain the best statistics;
- group 6 PbSc sectors and 2 PbGl sectors separately; within each group the mechanism of calorimetry is the same and a cross comparison of the two groups may reveal the effects on π^0 v_2 of the calorimetry mechanism;
- group 4 sectors on the east arm and 4 sectors on the west arm separately. This equal division of sectors allows us to check possible accidental effects with the best statistics.

4.4.2 Quality Check of π^0 Yield Measurement

To obtain the π^0 yield, π^0 peaks were built for various p_T, centrality and EMCal sector combinations. Examples of these π^0 peaks are shown in Fig-4.13 and Fig-4.14 for the combined PbGl and PbSc sectors respectively. We note that the peaks are generally very clean, except for those at very high p_T where only a handful of π^0's are produced. No satellite peaks appear, indicating that all hot and warm towers are excluded. π^0 peaks built on PbGl and PbSc also look very similar.

To allow a comprehensive survey of the π^0 peak quality, the π^0 peaks were quantified by their position and width values via Gaussian fits. The results of the survey are illustrated in Fig-4.15 and Fig-4.16 for the peak position and width values. The EMCal sectors are combined as East and West arm, PbGl and PbSc, as well as all inclusive. For each sector combination, the p_T dependence of the peak position and width are graphed for several centrality bins, represented by different colors. At high p_T, π^0's are scarce and the

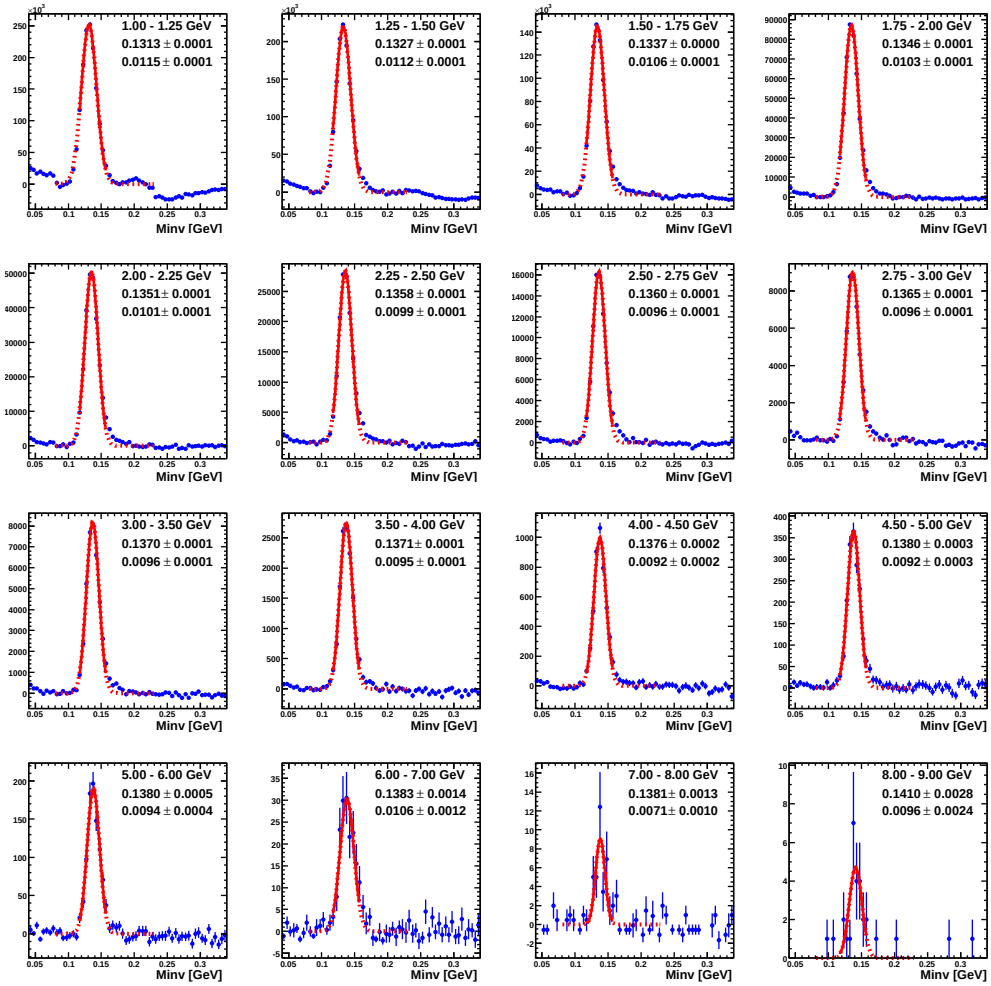

Figure 4.13: π^0 peaks in the PbGl sectors for various p_T selections. The Gaussian fit is represented by red dots. The solid red line indicates the integration region for yield calculation. Note that the integration is performed on data points, not the fitting curve. The peak position and width values are indicated on each panel. Results are shown for the centrality of $20-40\%$ for $\sqrt{s_{NN}} = 62$ GeV.

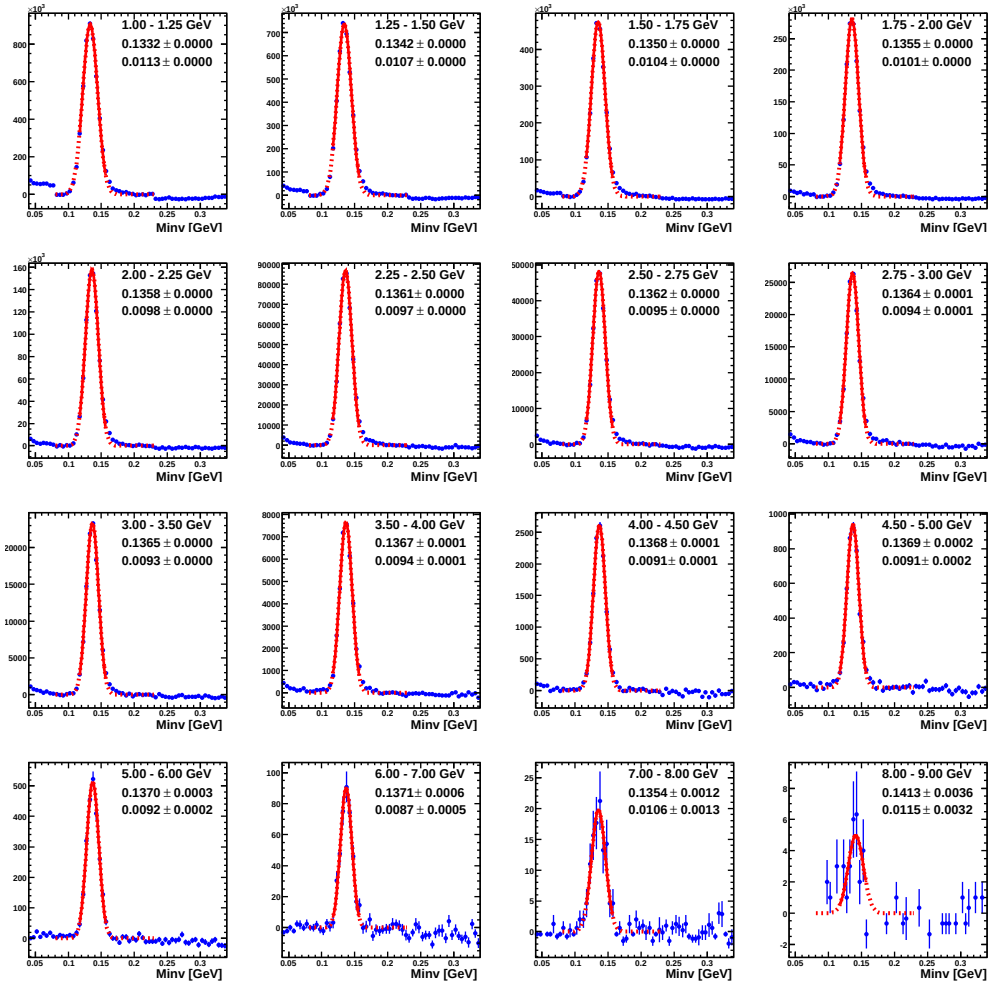

Figure 4.14: π^0 peaks in the PbSc sectors for various p_T selections. Details are the same as Fig-4.13. Note that more counts are observed for PbSc sectors than PbGl sectors. This reflects the differences in the total number of towers for the two types of calorimeters.

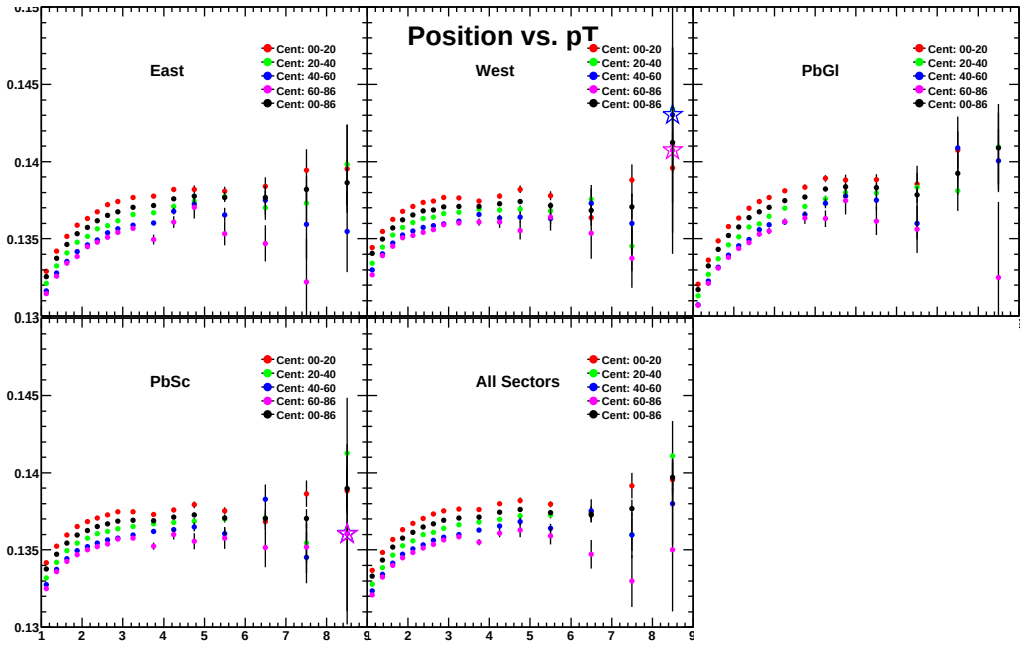

Figure 4.15: Survey results of the peak position for $\sqrt{s_{NN}} = 62$ GeV. See Text.

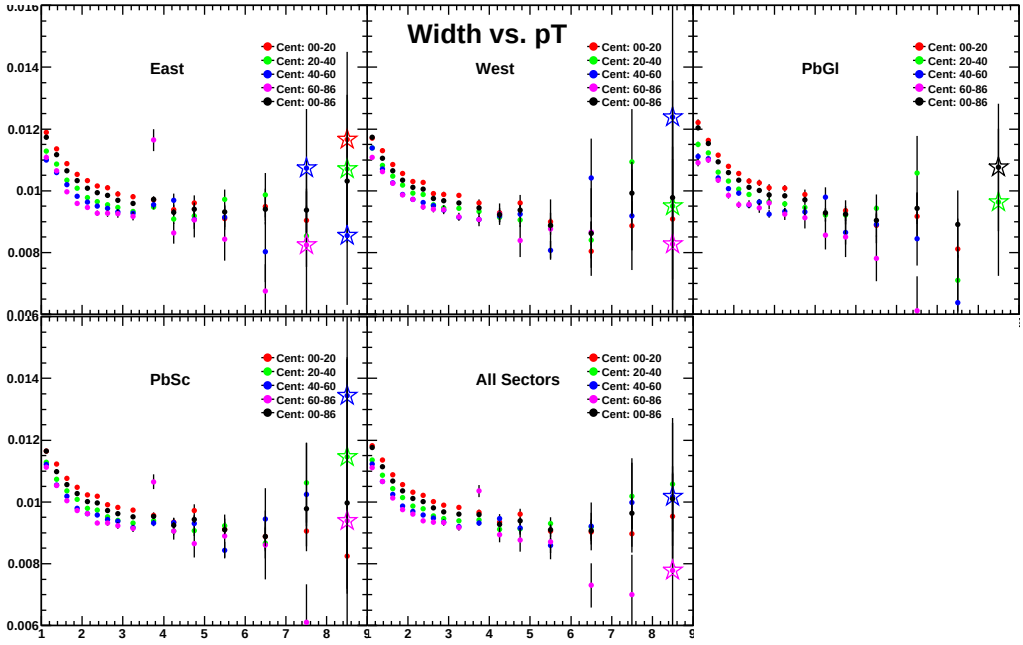

Figure 4.16: Survey results of the peak width for $\sqrt{s_{NN}} = 62$ GeV. See Text.

resulting data points with large error bars are marked by stars. Almost all the data points for the peak position and width follow a smooth trend, the features of which are explained in Sec-4.4.1. Any outliers, such as the width values of π^0's with $p_T \in (3.75, 4.00)$ GeV/c, in the centrality $60 - 86\%$ and constructed at the East arm and PbSc, are marked for additional investigation to ensure that robust π^0 peaks are built.

Once a π^0 peak is confirmed robust, we can specify an integration range and integrate over data points to extract the π^0 yield (cf. Fig-4.13 and Fig-4.14). The choice of integration range in this analysis is $(\mu - 2\sigma, \mu + 2\sigma)$, where μ and σ are expectation and standard deviation of the Gaussian fitting function. Results with varied integration ranges are also checked to help understand the associated uncertainty propagated to the final results.

The π^0 yield values in all p_T and centrality bins are presented in the form of π^0 raw spectrum in Fig-4.17 for 62 and 39 GeV respectively. For both

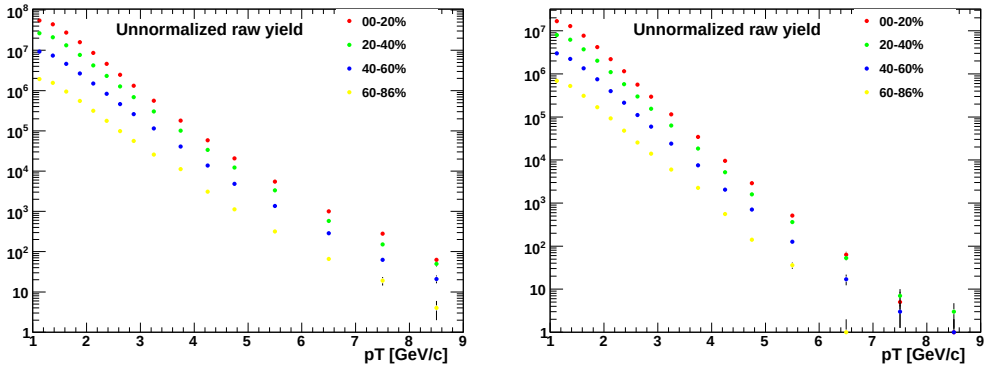

Figure 4.17: Uncorrected π^0 yield vs. p_T (raw spectrum). Data points are color coded, representing different centrality selections. $\sqrt{s_{NN}} = 62$ (left panel) and 39 (right panel) GeV.

62 and 39 GeV, the raw spectrum drops rapidly with increasing p_T. If the π^0 yield is enhanced by contamination (background fluctuation, fake π^0 from hot/warm towers, etc.), the corresponding data point would deviate from the linear decreasing trend on the semi-logarithm plot. It's noteworthy that the π^0 spectrum for 39 GeV has a steeper slope, which is expected because of the lower collision energy.

4.5 π^0 v_2 Measurements

4.5.1 Event Plane Detection

For v_2 measurement the second order event plane Φ_2 is necessary. The basics of Φ_n construction and calibration are documented in Sec-3.4 and Sec-3.6. Therefore, only the resolution factors of the calibrated Φ_2 are discussed in this section. From Eqn-3.10, we see that the resolution factor Res$\{\Phi_2\}$ is embedded into the raw v_2 measurement and needs to be canceled out by division. It represents the dispersion of Φ_2 around Ψ_2 and smears v_2 measurement, making the observed v_2^{raw} smaller than the "true" v_2.

The second order resolution factors measured with BBC, MPC, RXI, RXO and RXN are shown on Fig-4.18. We see that resolution factors in 62 GeV

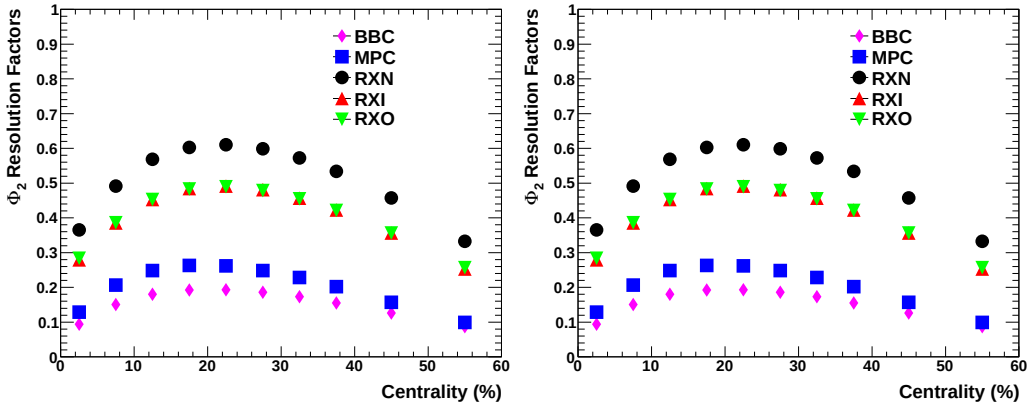

Figure 4.18: Res$\{\Phi_2\}$ vs. Centrality for BBC, MPC, RXI, RXO and RXN. $\sqrt{s_{NN}} = 62$ (left) and 39 (right) GeV.

for all detectors are higher than those in 39 GeV, which could be explained by the multiplicity difference. As explained in Sec-3.4.4, the resolution factors increase and then decrease with centrality; at very large centrality bins (peripheral collisions) the event planes might not be robust (cf. Fig-3.22 and Fig-3.23) but the resolutions are shown anyhow for reference.

In Sec-3.5, methods and benefits of event plane combination are discussed. RXI and RXO are routinely combined to give RXN. However, in [87], event planes in RXO are not used because it is relatively close to the central arm and suffers non-flow effects, particulary in the high p_T region that the paper focuses on. To achieve better resolutions for event plane detection, MPC and RXI are combined instead. For our analysis, the combination of MPC and RXI is tried as well. But due to the low multiplicities for 62 and 39 GeV collisions, the resolution of the MPC is poor. It peaks at around 0.26 and 0.18 for 62 and

39 GeV respectively, while at 200 GeV the resolution reaches as high as 0.52. One result of the poor resolution of the MPC is that even if RXI is combined with MPC, the increase in event plane resolution is very limited. In fact, if not handled properly the resolution for the combined detector becomes even smaller.

Moreover, at lower collision energy the jets are created much less frequently and the p_T reach in this analysis (cf. Fig-4.17) is also much lower than that of [87]. Therefore, non-flow effects in this analysis are not as prominent. For these two reasons, the RXN event planes are employed by default because of their good resolutions.

4.5.2 Raw v_2 Measurements

Raw v_2 governs the modulation of the π^0 yield in different angular bins relative to the event plane Φ_2. In our case, the π^0 yields are measured separately in six angular bins as shown in Fig-1.20. This means that the foreground and background distributions of the invariant mass m_{inv} and the corresponding subtraction are all performed independently in six angular bins.

One example for π^0 raw v_2 extraction is illustrated in Fig-4.19. On the top and middle panels, the π^0 peaks in the six angular bins are shown. The "angle" indicated on the panels refers to the azimuth of π^0 relative to Φ_2, i.e. a small "angle" value corresponds to the in-plane direction. The integrated yield values for the six bins are plotted in the bottom left panel. A functional form with v_2 modulation is used to fit the data points and the v_2 parameter that maximizes the likelihood is considered as the expectation value of v_2^{raw}. The error of v_2^{raw} is estimated in this process as well and the v_2^{raw} value with errors are also indicated inn the panel. The resolution factor corrected v_2 is also shown. The inclusive π^0 peak is shown on the bottom middle panel for reference.

To obtain an intuitive picture of the robustness and the limits of the v_2^{raw} extraction, the yield vs. angle plots (bottom left panel of Fig-4.19) for all the p_T bins in this analysis are demonstrated in Fig-4.20. For lower p_T bins where the statistics are abundant, the fitting curves and the data points agree with each other very well, demonstrating both robust measurement and correct model assumptions. For the high p_T bins, statistical fluctuations start to play a role in the fitting and eventually smear out the v_2 modulation almost completely. The information for the panels in Fig-4.20 can be compiled as a single v_2^{raw} vs. p_T curve.

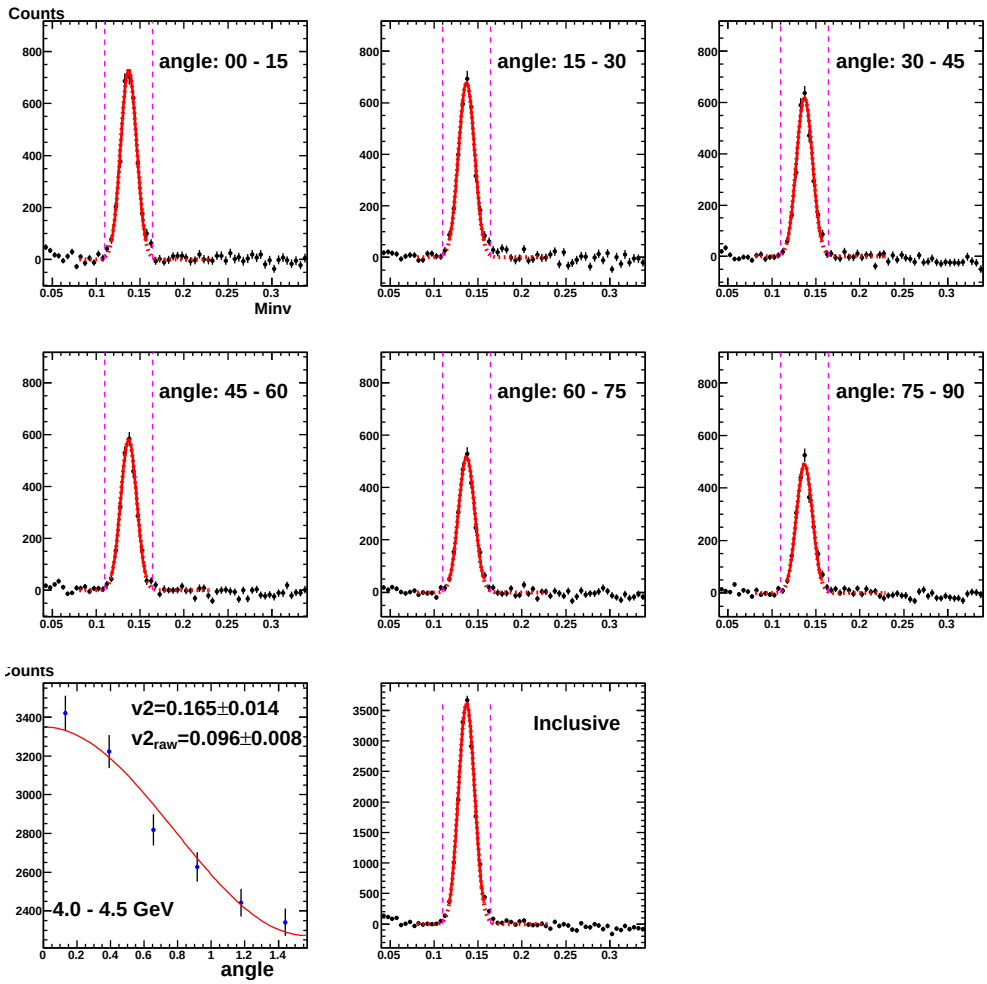

Figure 4.19: Raw v_2 extraction. π^0 peaks constructed in individual angular bins (cf. Fig-1.20) are shown from the most in-plane (angle: 0-15) to the most out-plane (angle: 75-90) bin. Bottom left panel shows π^0 yield values in the six angular bins and the functional fitting (red curve) used to extract $v_2^{\rm raw}$, which is printed along with the resolution corrected v_2. The inclusive (angular independent) π^0 peak is shown on the bottom middle panel. $p_T \in (4.0, 4.5)$ GeV, centrality $20-40\%$, $\sqrt{s_{NN}} = 62$ GeV.

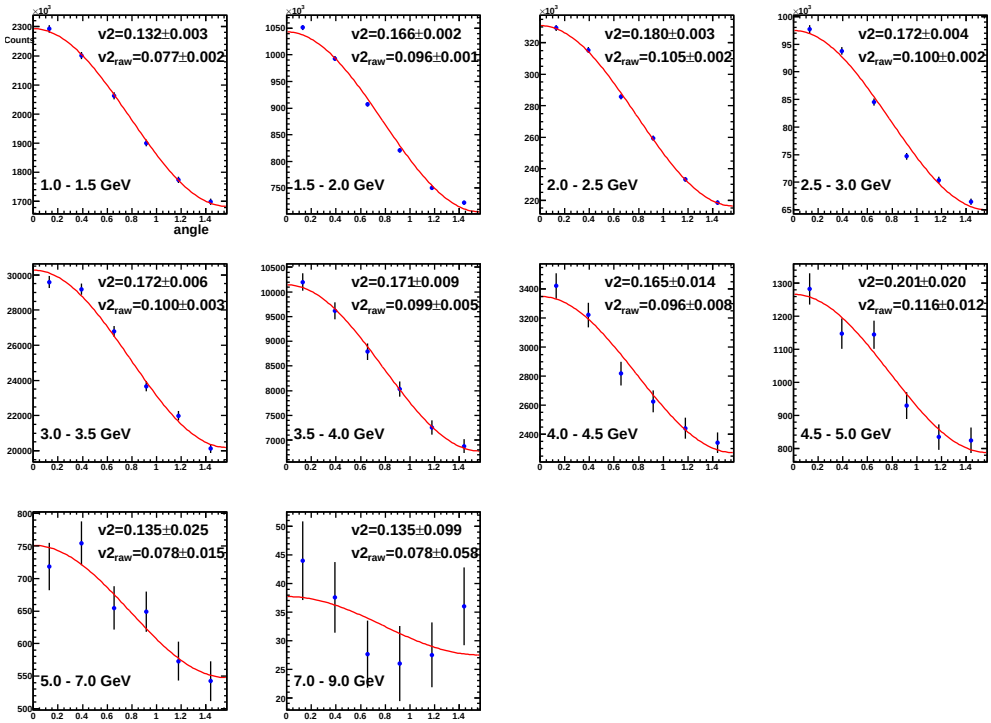

Figure 4.20: p_T dependence of raw v_2 (extraction). Each panel has the same style as the bottom left panel of Fig-4.19 and corresponds to a particular p_T bin. Centrality $20-40\%$, $\sqrt{s_{NN}} = 62$ GeV.

4.5.3 An Initial Look at v_2

With resolution factors and raw v_2 values ready, the calculation of v_2 is straightforward. Initial results of v_2 with only statistical error bars are displayed in Fig-4.21 for six centrality bins. Several common features of v_2 can

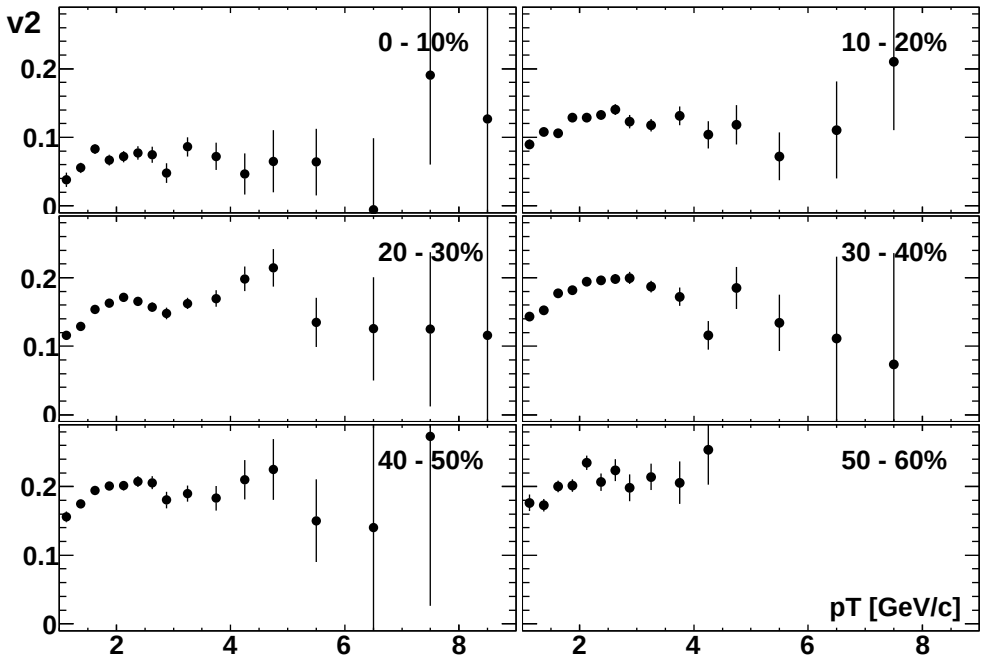

Figure 4.21: An initial look at v_2. Event planes are measured with the RXN detector. Only statistical errors are shown. $\sqrt{s_{NN}} = 62$ GeV.

be observed. v_2 values increase with p_T till around 2 to 3 GeV and then decrease slowly. In central collisions v_2 values are smaller since the eccentricity of the collision zone is lower. It's noteworthy that p_T starts from 1 GeV on the plot, therefore the v_2 curves appear to be flatter when compared to other measurements such as those in Fig-1.9.

4.6 Systematic Uncertainties

In virtually all measurements, there are factors that are known to affect the results but can not be 100% quantified. Consequently, the systematic uncertainty is introduced to give an estimation of the affect of these factors. In this π^0 v_2 analysis, systematic uncertainty mainly comes from the combination of sectors and non-flow effects in the raw v_2 measurement.

4.6.1 Sys. Unc. from Combination of Sectors

As discussed in Sec-4.4.1, additional fake π^0's might be included into the π^0 peak for the combined sectors because the individual π^0 peaks from different sectors do not perfectly overlap. The direct approach to estimate the uncertainty of this origin is to compare v_2 measured in different sectors and observe the discrepancies among them. Because v_2 for different sectors are not expected to be very different, ratio values of v_2 measured at each sector divided by v_2 from combined all sectors are plotted side-by-side to facilitate the comparison. In the left panel of Fig-4.22, we see that the differences between v_2

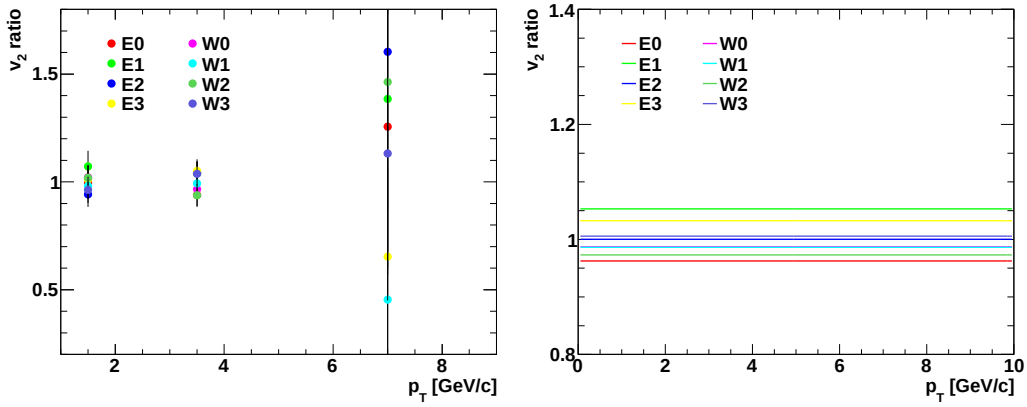

Figure 4.22: Comparisons of v_2 measured in individual EMCal sectors. Left panel: p_T dependence of ratio values, where v_2 measured in each sector serve as the numerator and v_2 from a combination of all sectors serve as the denominators. Right panel: horizontal line fittings of the ratio values on the left. Results are shown for centrality of $20-30\%$ for $\sqrt{s_{NN}} = 62$ GeV.

among sectors are not large. Note that to increase the statistical significance of the data points, p_T bins are combined to the extent that only 3 data points are left for each sector. Even so, the error bars are quite sizable, especially for the high p_T bin. To capture the behavior of each sector with a single number, we assume that the discrepancies among sectors are p_T independent (which is not strictly true, but enables a first order estimation) and fit the ratio values with horizontal lines, which are shown in the right panel of Fig-4.22. We see that the v_2 variations among sectors are less than 5%.

The comparison of v_2 for individual sectors shown in Fig-4.22 suffers from poor statistics. v_2 measurement at $20-30\%$ centrality normally has the best precision, but even in this case the figure indicates that the size of the error bars are on the same scale as the discrepancies among sectors. In other centrality selections and especially for 39 GeV collisions, the situation is worse.

Therefore, sectors on the east and west arms are grouped to allow maximum statistics for both groups. The results are shown in Fig-4.23 and Fig-4.24.

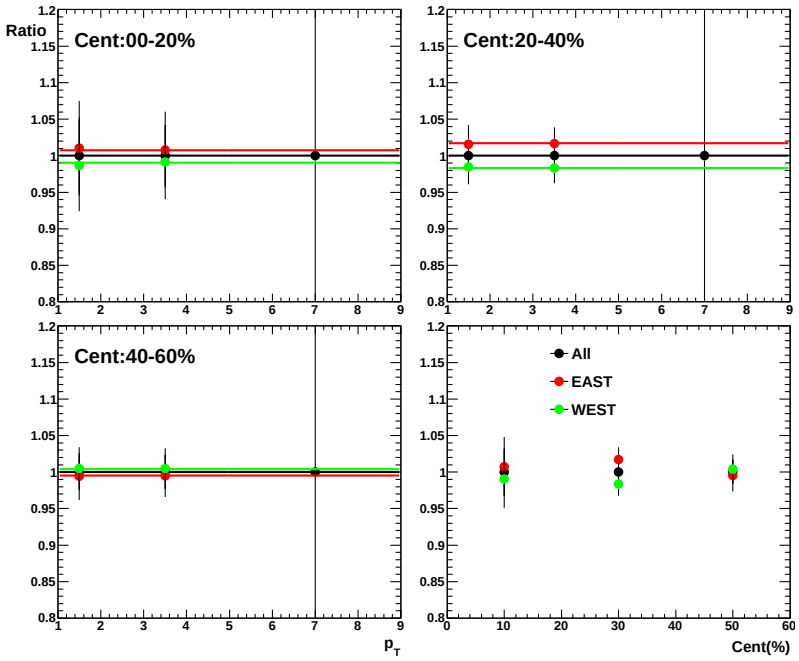

Figure 4.23: Comparisons of v_2 measured in the east and west EMCal arms in three centrality bins, $\sqrt{s_{NN}} = 62$ GeV.

The former graph shows information similar to that in Fig-4.22, with the ratio for data points and fitting lines drawn together. Three centrality selections are shown on the top panels and bottom left panel. Error bars still appear to be large compared to the discrepancies, however the values are only about 1%. Data points on the bottom right panel summertime the other three panels. The levels of the horizontal lines in the other three panels are assigned to data point values in the fourth panel and the corresponding fitting errors are plotted as error bars. Fig-4.24 is of a similar structure, the only difference is that the roles of centrality and p_T are interchanged. We conclude that the differences between v_2 measured in one single arm and v_2 with both arms are less than 1%. Together with observations from Fig-4.22, the combination of sectors doesn't seem to have a significant impact on the v_2 results.

4.6.2 Sys. Unc. from Res$\{\Phi_2\}$ Estimation

In this analysis, event plane resolutions are calculated with the two sub-events method (cf. Sec-3.4.5) by default. Res$\{\Phi_2\}$ values found from the 3 sub-events

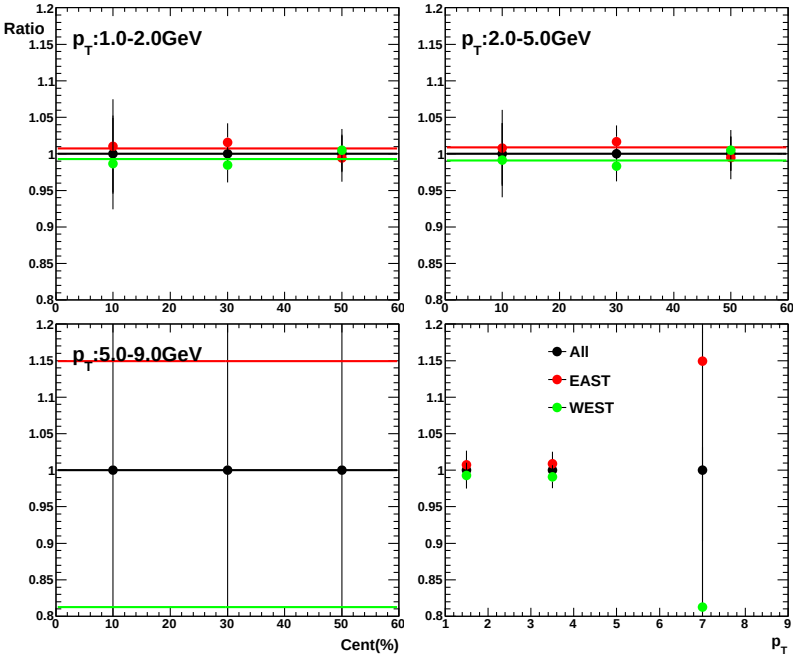

Figure 4.24: Comparisons of v_2 measured in the east and west EMCal arms in three p_T bins, $\sqrt{s_{NN}} = 62$ GeV.

method (cf. Sec-3.4.6) serve as a cross-check and allow us to estimate the errors associated with resolution factors. Since the combined RXN detector (inner and outer rings, south and north arms) is the target detector for the event plane determination (cf. Sec-4.5.1), to apply the 3 sub-events method the other two detectors are selected to be one component of BBC or MPC on the south arm and one component on the north arm; in total four combinations of three sub-events are available for resolution evaluation. Since the two assistant detectors are located in south and north arms respectively, auto-correlation between them are minimized. However, since both MPC and BBC sit at $|\eta|$ of $3 \sim 4$ and RXN sits at $|\eta|$ of $1 \sim 3$, there is no rapidity gap between the south assistant detector (MPCs or BBCs) and RXNs, and the same for the north side. Therefore, according to Eqn-3.15 and arguments in that section, the resolution factors calculated in the three sub-events method might be overestimated.

The comparisons of Res$\{\Phi_2\}$ obtained via the two and three sub-events method are shown in Fig-4.25. The values for the resolution ratio for four combinations of three sub-events are illustrated. The resolution factors for the two sub-events method serves as the denominators for the ratios. In general, resolution factors obtained via various combinations of three sub-events are consistent with the ones from the two sub-events method. In the most central

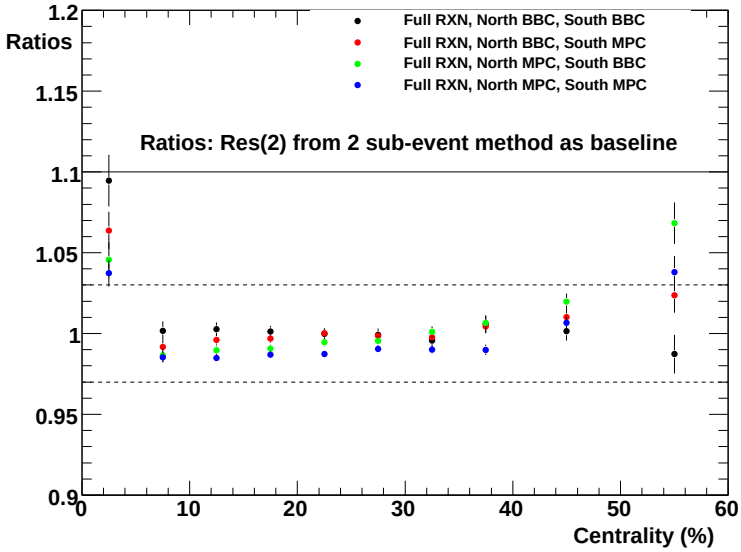

Figure 4.25: Comparisons of Res$\{\Phi_2\}$ calculated from two and three sub-events method (multiple combinations). Ratio values for resolution factors (for the RXN detector) are shown on the figure with resolutions from two sub-event method as the baselines (denominators). Four combinations of 3 sub-events are shown: RXN is combined with a south detector (BBCs, MPCs) and a north detector (BBCn, MPCn).

bin Res$\{\Phi_2\}$ from all combinations of three sub-events are more than 5% larger than Res$\{\Phi_2\}$ from two sub-events method. The same observation roughly holds for peripheral collisions as well. These observations are consistent with effects of non-flow mentioned above [29]. However, in a wide range of mid-central collisions, the resolutions agree within 1% across all configurations.

4.6.3 Sys. Unc. from Non-Flow Effects

Particles of an event might be correlated in ways other than the global azimuthal anisotropy. For example, particles from the same jet cone exhibit local correlations among themselves. The two source model of two particle correlation (cf. Eqn-1.5) is well manifested in Fig-1.17. v_n could be extracted from C_{Flow}; but if C_{Jet} is not excluded, the v_n values obtained are biased.

Since event planes are basically averaged azimuthal information of multiple particles, the above argument for two particle correlation applies also to the particle - event plane correlation that is employed to measure v_2 in this analysis. As shown in Fig-1.17, C_{Jet} could be excluded by requiring a sufficiently large η gaps between the two particles. Consequently, to prevent jet bias the detectors that construct event planes must be well separated in η from the detectors that measure to-be-correlated single particles. For v_n analysis at PHENIX, the single particles are measured in the central arms ($|\eta| < 0.35$) and the event planes are built in multiple detectors in different rapidity regions with $|\eta|$ of $1 \sim 4$, including BBC, MPC, RXI and RXO (cf. overview of the PHENIX detector at Chapter-2 and particularly Sec-2.1.5). Consequently, the comparisons of v_2 measured independently with Φ_2 in each of these detectors provides natural guidance for the estimation of non-flow effects. The study at 200 GeV with Run7 PHENIX data is published as part of [29]. RXO has the smallest rapidity gap relative to the central arm and it is reported that the non-flow effects are estimated to be less than 5% in mid-central collisions and 5% for most central and peripheral collisions.

In our analysis, the collision energy is lower and jets are less frequently created. The non-flow effects are expected to be smaller than those observed at 200 GeV. It turns out that the v_2 values measured with BBC and MPC event planes have large statistical fluctuations, as well as additional systematic uncertainties which result from the lower multiplicity environment. Therefore, v_2 measured with RXI and RXO event planes are compared to those measured with the combined RXN event plane. The results are summarized in Fig-4.26 and Fig-4.27, which are of the same style as Fig-4.23 and Fig-4.24 where v_2 from the east and west EMCal arm were compared. Ratio values of v_2 from RXI and RXO are plotted, with v_2's from the combined RXN as the denominators. The observation is quite similar to that for 200 GeV. From

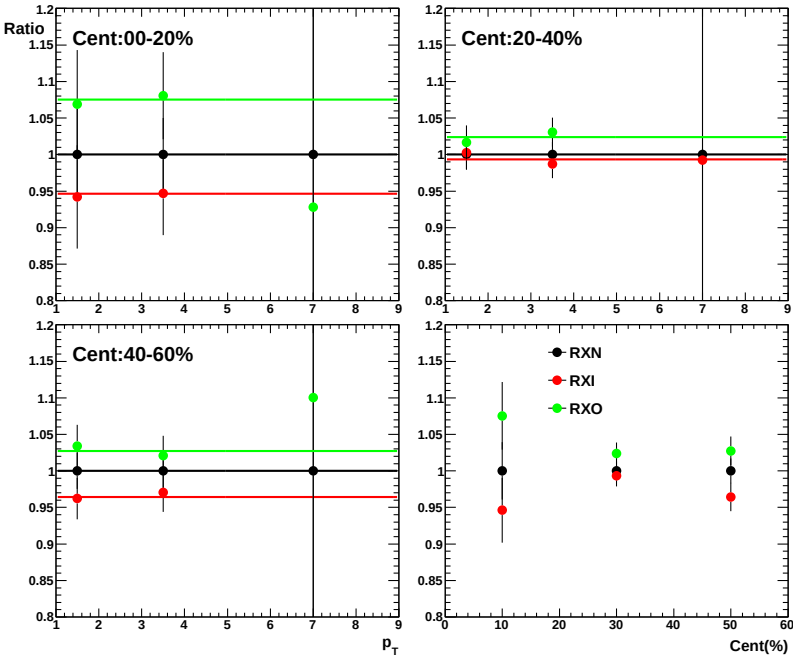

Figure 4.26: Comparisons of v_2 measured with RXI and RXO event planes in three centrality bins, $\sqrt{s_{NN}} = 62$ GeV.

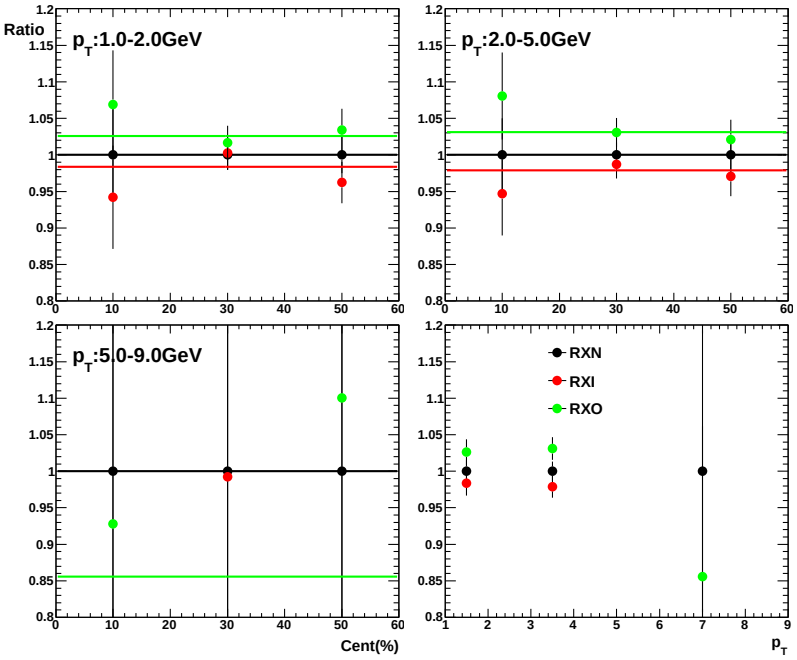

Figure 4.27: Comparisons of v_2 measured with RXI and RXO event planes in three p_T bins, $\sqrt{s_{NN}} = 62$ GeV.

Fig-4.26, it can be seen that the v_2 values for RXO and RXI agree within 5% for mid-central events; the discrepancies are larger for the most central and peripheral collisions. Jets are more likely to be created at hight p_T, therefore larger non-flow effects are expected for high p_T v_2. However, the statistics at high p_T (cf. Fig-4.26) is too small to draw a firm conclusion.

4.6.4 Summary

Other cross-checks were performed as well. They were proven to be minor contributors to the systematic uncertainty which include:

- variations in the trigger efficiency and the corresponding centrality definition (cf. Sec-3.2 and Sec-3.3).
- different peak integration regions (cf. Fig-4.13 and Fig-4.14);
- different π^0 peak fitting schemes, e.g. whether to fix the π^0 peak positions of the six angular bins to the same value extracted from the inclusive π^0 peak (cf. Fig-4.19).
- different fitting schemes of the yield vs. angle histogram (cf. Fig-4.20), e.g. using 18 angular bins instead of 6, modified χ^2 evaluation for the fitting, adding a $v_4\{\Psi_2\}$ term to the fitting function, etc.

Since the overall systematic uncertainty is a root-sum-square of all the components, the effects of the above factors are very limited.

To quantify systematic uncertainty, statistical errors should be suppressed as much as possible (by reducing the number of p_T bins, for example). However, the dataset at low collision energies are relatively small and the π^0 v_2 analysis is statistically limited. Therefore, the estimation of systematic uncertainties are in general difficult. The results are summarized in Tab-4.6.4 and Tab-4.6.4. Systematic uncertainty from different sources are then root-sum-squared to yield the overall values.

4.7 Results

π^0 v_2 values for Au+Au collisons at $\sqrt{s_{NN}} = 200$ GeV (from [87]), 62 GeV and 39 GeV are overlaid in Fig-4.28, Fig-4.29 and Fig-4.30 for centrality ranges of $0-20\%$, $20-40\%$ and $40-60\%$. Wide centrality bins are used to reduce statistical fluctuations. As mentioned in Sec-3.4.4, resolution factors should be calculated in narrow centrality bins. Therefore, instead of finding

Table 4.1: Summary of systematic uncertainty of π^0 v_2 for Au+Au $\sqrt{s_{NN}} = 62$ GeV.

source $\diagdown$ centrality	$0-20\%$	$20-40\%$	$40-60\%$
EMCal Sector Comb.	3[a]	2	2
Res$\{\Phi_2\}$	3	1	2
non-flow	3	1	2
other sources	2	2	2

[a] relative error in percentage

Table 4.2: Summary of systematic uncertainty of π^0 v_2 for Au+Au $\sqrt{s_{NN}} = 39$ GeV.

source $\diagdown$ centrality	$0-20\%$	$20-40\%$	$40-60\%$
EMCal Sector Comb.	3[a]	2	2
Res$\{\Phi_2\}$	4	2	3
non-flow	3	1	2
other sources	2	2	2

[a] at 39 GeV the statistical error bars are large and the estimation of systematic uncertainty is particularly difficult. Therefore the estimation of systematic uncertainty is sometimes also based on the observation at 62 GeV.

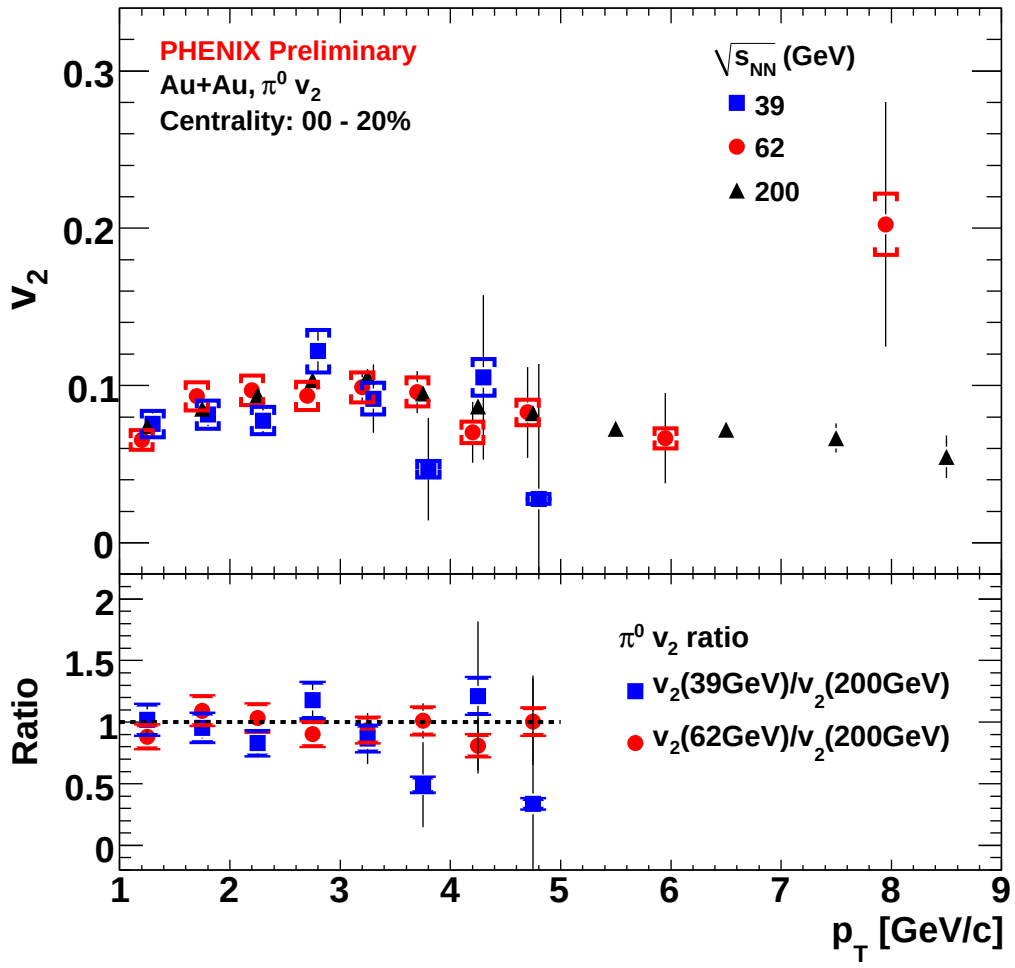

Figure 4.28: π^0 v_2 vs. p_T for Au+Au collisions at $\sqrt{s_{NN}} = 200$ GeV [87] (black triangles), 62 GeV (red dots) and 39 GeV (blue squares), for the centrality cut of $0-20\%$. Φ_2 are determined with combined RXI and MPC at 200 GeV and with RXN at 62 and 39 GeV. v_2 values are shown in the top panel, and v_2 ratios with v_2 at 200 GeV as baseline, are shown in the bottom panel. Vertical brackets around data points denote systematic uncertainties.

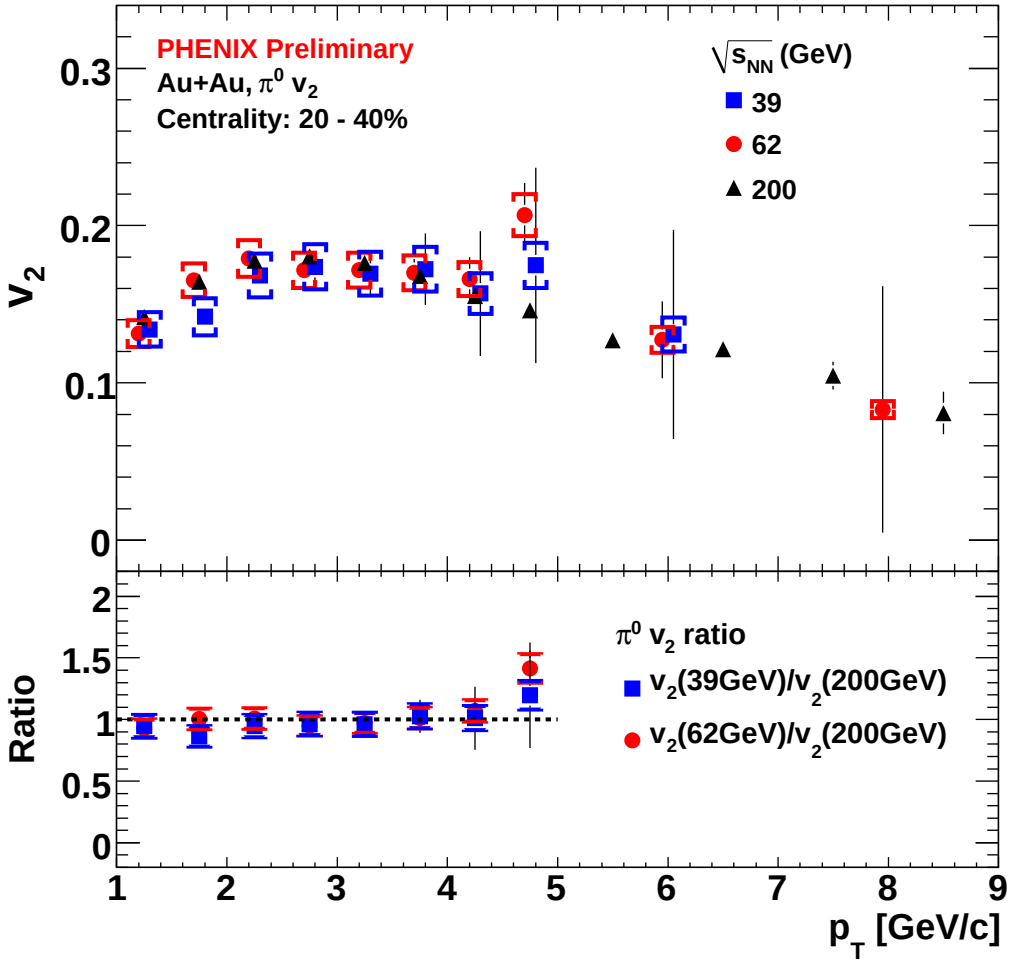

Figure 4.29: Same figure as Fig-4.28 for centrality $20-40\%$.

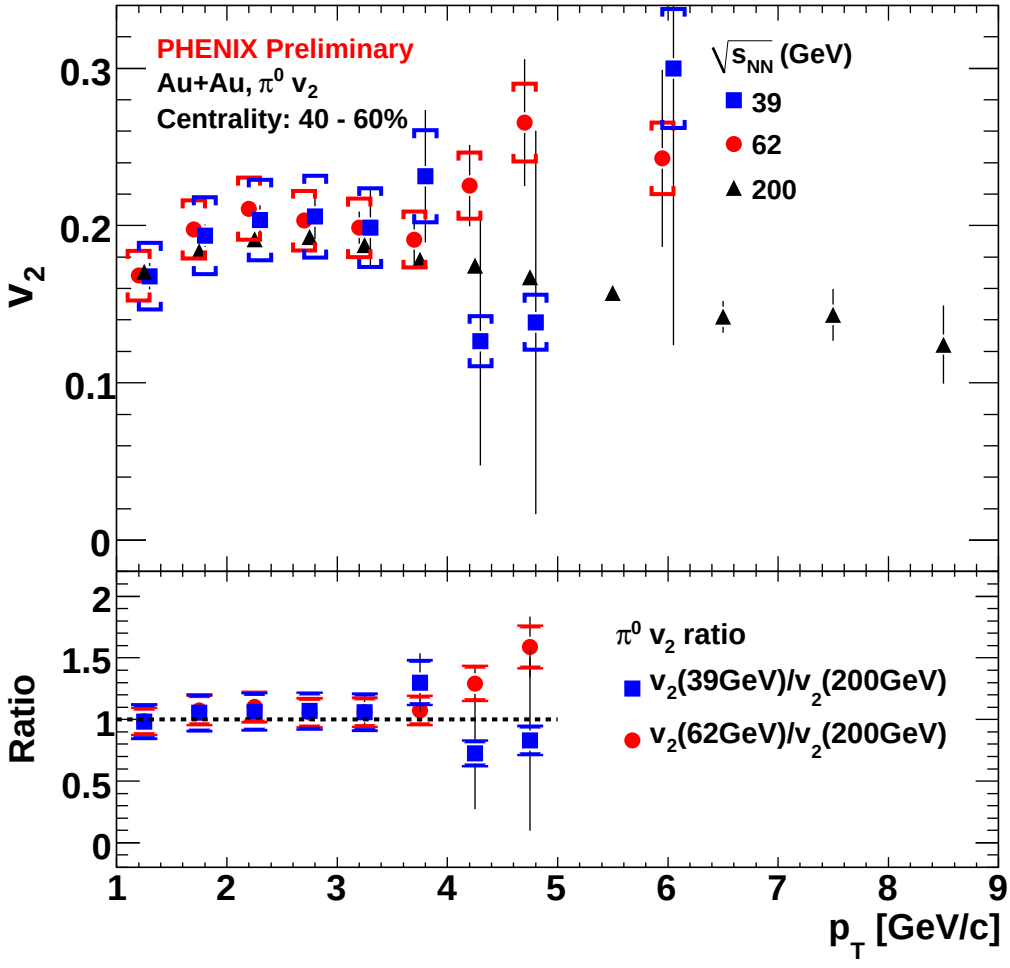

Figure 4.30: Same figure as Fig-4.28 for centrality $40-60\%$.

v_2^{raw} and Res$\{\Phi_2\}$ in wide centrality bins to calculate v_2 according to Eqn-3.10, the process is applied in finer centrality bins and resolution corrected v_2 are determined in these finer bins first; then they are combined into wider centrality bins with π^0 counts as the weighting factors. In this way, v_2 results are obtained for wide centrality bins with minimized centrality smearing effects in event plane determination.

Ratio values of v_2 at 62 and 39 GeV divided by v_2 at 200 GeV are drawn on each figure as well (bottom panels) to allow detailed comparisons among v_2 of the three beam energies. The main message is that in the low and intermediate p_T region, π^0 v_2 at 62 and 39 GeV are no different than those at 200 GeV, which is best observed for the $20-40\%$ centrality bin where the statistical errors are the smallest. In the $40-60\%$ centrality bin, v_2 values at 62 and 39 GeV seem to be greater, but as demonstrated in Fig-3.22 and Fig-3.23, event plane construction for peripheral events suffer from detector granularity effects and might underestimate Res$\{\Phi_2\}$ (and thus over-correct v_2). The agreement of v_2 suggests that the same mechanisms for flow and coalescence that explain v_2 at 200 GeV are likely to hold true for lower beam energies down to 39 GeV. v_2 at high p_T ($p_T > 6$ GeV) provide insights for the jet-suppression models (cf. Sec-1.8.3). However, the statistical fluctuation for the current measurement prevents us from drawing a firm conclusion on the latter topic.

Chapter 5

Inclusive Charge Hadron v_n Analysis

Charge hadrons are mostly composed of $\pi^{\pm}$, $K^{\pm}$ and $p(\bar{p})$. They are abundantly created in heavy ion collisions just as π^0's. Inclusive charge hadron measurements do not require particle identification, which limits the analysis in the following ways:

- particle identification becomes difficult at intermediate p_T and eventually becomes impossible as p_T increases (cf. Fig-2.13, also [49]);
- other than the very low p_T region where timing information from EMCal can be used, particle identification is limited to the acceptance of TOFW, TOFE and ACC, which covers less than one third of the PHENIX acceptance.

Therefore, an inclusive charge hadron analysis has higher p_T reach and better statistical significance. The latter advantage is particularly crucial for higher order v_n measurement. Analysis with identified particle species allow the examination of phenomenon such as quark number scaling (cf. Fig-1.13), and has been subsequently carried out at PHENIX.

The measurement of v_n, especially the higher order components v_3 and v_4 in this analysis, could provide additional constraint on the initial geometry profile of the nuclear matter and its evolution dynamics (cf. Sec-1.6.4). The method to measure v_3 and v_4 is generally the same as the one used in Chapter-4 for v_2 measurement: event planes are constructed at large $|\eta|$ first, raw v_n values are then measured relative to Φ_n and corrected by the Φ_n resolutions. However, the first thing we need to know is how to accurately measure charged hadrons.

5.1 Features of Charged Hadron Analysis

Unlike neutral pions that are considered secondary particles that need to be constructed from more primitive ones (photons), charged hadrons are measured directly based on the detector response. As in the neutral pion analysis, the most important character of a charged particle is its momentum.

5.1.1 Track Construction and Momentum Measurement

A charged particle in a magnetic field is subject to the Lorentz force which bends its track. Its momentum is directly reflected in the curvature of this track. Consequently, momentum measurement of a charged particle is performed via full construction of its track.

Details of track construction are presented in Sec-2.2.2. In summary, for each charged track the DC provides 12 hits of (x, y) measurement and 8 hits of z measurement. PC1 provides 1 hit of (x, y, z) measurement. In an event with hundreds of particles, thousands of hits are left in the DC and PC. All feasible associations of hits are considered as possible tracks, though most of them are combinatorial background. They are then screened by a Hough transformation, the results of which are the track candidates. These candidates, part of which are still accidental associations of hits, are then matched by hits registered on outer layer detectors, such as RICH, PC3 and EMCal. Fake tracks are likely to be rejected in the matching process.

With the map of magnetic field, charged particle momentum could be derived from the bending angle of each track (α in Fig-2.10). Particles with larger momentum bend less. For particles with $p_T \sim 1$ GeV/c, the typical bending angle is about 5 degrees.

5.1.2 Correction of Momentum Measurement

In the track construction algorithm, two assumptions are made:

1. tracks originate from the primary collision vertex of heavy ions, and
2. the primary collision vertex is located at the center of the beam pipe.

Both assumptions are not always valid. The first one doesn't consider charged particles created from particle decays that happen before the parent particles reach the drift chamber; the decays particles would be assigned high p_T by the algorithm, which is discussed later. The failure of the latter assumption is more relevant to our analysis since it affects all particles, not necessarily with high p_T.

If the beams of heavy ion bunches are off-centered in the beam pipe, instead of the assumption that they are centered with zero-valued (x, y) coordinates of the origins of all tracks, errors in α measurements are incurred and consequently propagate to momentum calculations. To remove momentum bias from this beam shift, corrections are applied to the α angles.

The first step of the beam shift correction is to measure the beam shift itself. It is done with zero field runs, which are data segments collected when the magnetic field of the PHENIX detector is intentionally turned off. Without magnetic field, charged particles travel in straight lines and if their origins are indeed located at the beam pipe center, the α angles should be zero. However, with a beam shift, small values of α (denoted as $\Delta\alpha$) are assigned to the constructed tracks, which are related to the actual beam position (Δx, Δy) for particles with azimuth ϕ as:

$$\begin{aligned} \sin\Delta\alpha &= \frac{-\Delta y\cos\phi + \Delta x\sin\phi}{R}, \\ \cos\Delta\alpha &= -\frac{\Delta x\cos\phi + \Delta y\sin\phi}{R} + 1 \end{aligned} \tag{5.1}$$

where R is the radius of the reference circle and equals 220 cm (cf Sec-2.10). (Δx, Δy) values are then extracted, commonly via a simultaneous fitting utilizing all the $\Delta\alpha$ and ϕ measurements.

Since the location of shifted beams may vary with time, (Δx, Δy) values are calculated within relatively small run groups. The correction for α and momentum measurements are straightforward with known (Δx, Δy) values of beam shift. For a beam shift of 1 mm, the effect on the momentum scale is roughly 0.5%.

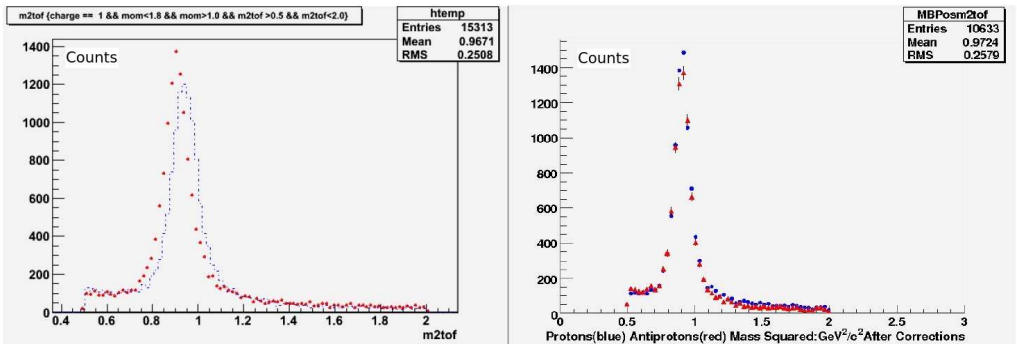

Figure 5.1: Mass square distributions of protons (blue) and anti-protons (red) measured at TOFE [128]. Left/Right panel shows distributions before/after the application of momentum scale correction.

In Fig-5.1, mass square distributions of protons and anti-protons measured in TOFE are plotted. The mass square values are calculated with Eqn-2.3, which is proportional to the square of the momentum of the track. Therefore, if the mass square peaks are at the expected location (the established proton mass), the momentum measurement is accurate. On the figure, we can see the effects of the beam shift and momentum scale correction; when they are implemented, the mass square peaks are adjusted to the right location.

5.1.3 Matching Cut on Charged Particle Tracks

The track candidates produced by the Hough transformation still contain a large portion of accidental associations of hits. Therefore, the projected points of each constructed track on the outer detectors (such as PC2, PC3 and EMCal) are matched to the hits of those detectors. A coincidence of track projection point and detector hit increases our confidence that the track corresponds to a real charged particle.

The variable used to characterize the matching between a track projection point and a detector hit is the distance between them on the detector sensor plane, commonly decomposed into a component along beam (z) direction and a component along azimuth (ϕ). For example, on PC3 the aforementioned distance is decomposed into variables referred to as $pc3\Delta z$ and $pc3\Delta\phi$. However, it would be more meaningful if the distances are normalized; otherwise, specific values of the above variables don't tell much about whether the distance can be considered small enough for a successful matching.

$pc3\Delta z$ and $pc3\Delta\phi$ are normalized by their RMS values; and the normalized variables are assigned names such as $pc3s\Delta z$ and $pc3s\Delta\phi$. However, the normalized values need to be calibrated prior to usage. The calibration process itself is iterative and straightforward. The p_T dependence of $pc3s\Delta z$ values before and after calibration for various *zed* selections are plotted in Fig-5.2. Before calibration, the $pc3s\Delta z$ distributions are off-center and have varying RMS values. The calibration process shifts the mean values to zero and scales the RMS values to unity. Matching calibration of $pc3s\Delta\phi$, and for PC2, EMCal, TOF, etc. were carried out and examined in the same fashion.

The effectiveness of a matching cut is illustrated in Fig-5.3. It can be seen that the spectrum with RMS cuts on PC2 and PC3 (i.e. requiring $pc3s\Delta z < 2.0$ and $pc3s\Delta\phi < 2.0$ for PC3, the same for PC2) follows an exponential drop with increasing p_T up to around 5 GeV, suggesting that most of the fake tracks are rejected in this p_T range. On the contrary, without matching cuts the spectrum contains a large contamination from accidentally associated hits, especially when p_T is above 2GeV. In the range of $p_T > 5$ GeV, significant background remains even after matching cuts are applied.

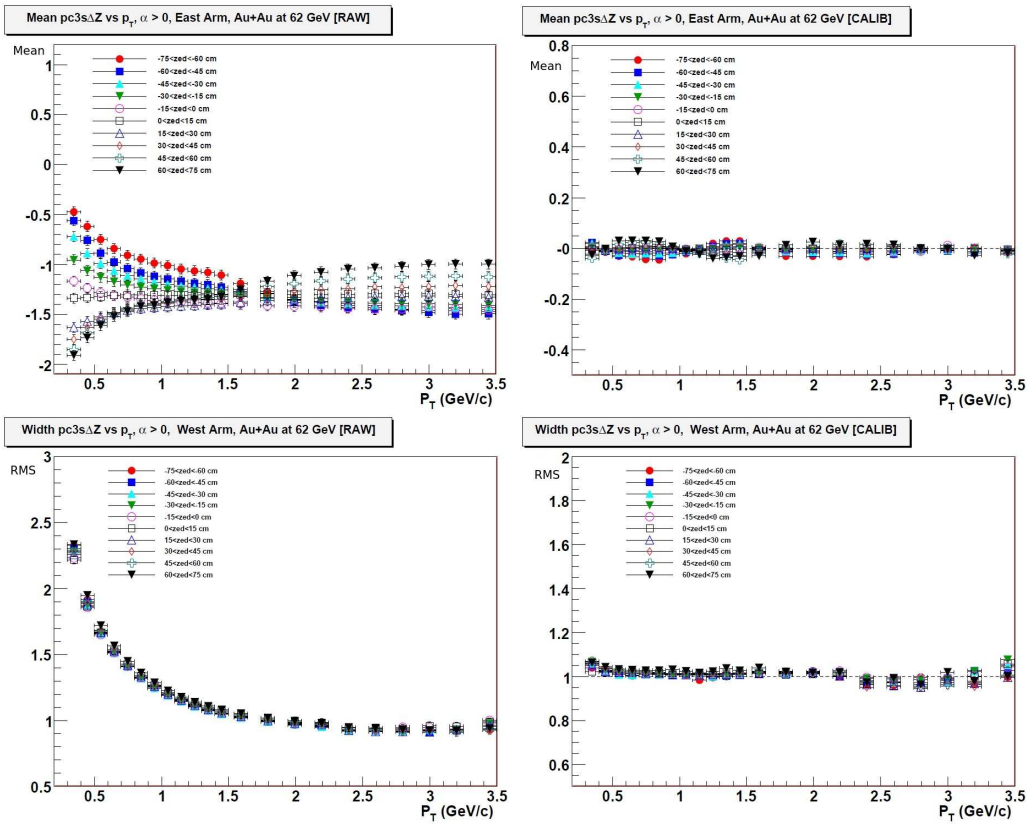

Figure 5.2: Calibration of matching variables. The mean (upper panels) and RMS (lower panels) values of $pc3s\Delta z$ are plotted as a function of p_T before (left panels) and after (right panels) the implementation of calibration. The calibration shown is for negatively charged particles ($\alpha > 0$) detected on the east arm. Different curves correspond to various *zed* selection, the value of which is in cm and represents the location along z-axis of the track projection point on the DC. $\sqrt{s_{NN}} = 62$ GeV.

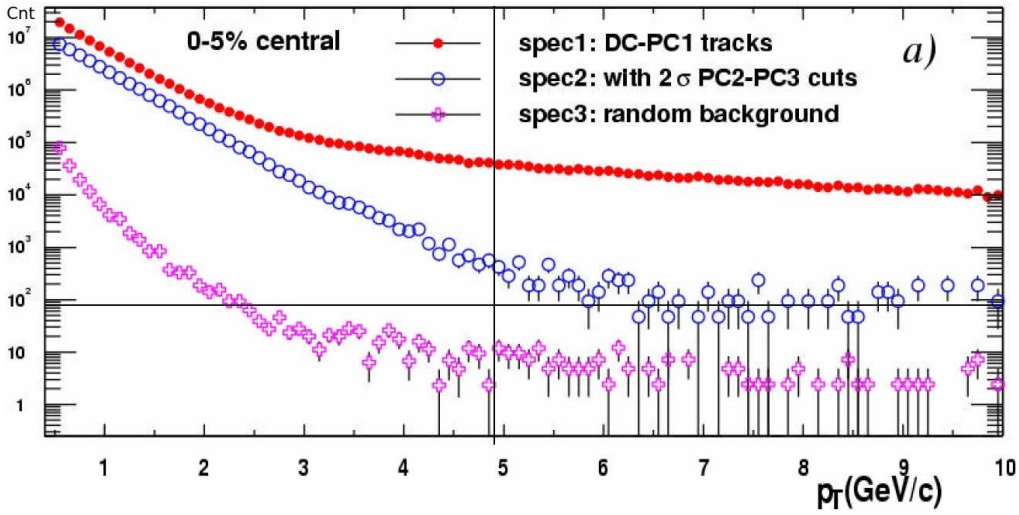

Figure 5.3: Effectiveness of matching cut. Unnormalized p_T spectrum are shown for tracks constructed with DC and PC1 without any matching cut (red dots), with RMS cuts at 2 for PC2 and PC3, and random background.

This high p_T background originates from secondary decays of hadrons such as $K^{\pm}$ and photon conversions (to $e^{\pm}$). For example, if a parent particle decay happens just in front of the DC, the decay products are likely to pass through the DC with very small bending angles and mimic high p_T particles. Such events are rare, but high p_T charged particles themselves are rare events and could be significantly contaminated in this way. However, the p_T reach of this v_n analysis is lower than 5 GeV and the sole usage of matching cuts is sufficient.

5.2 Event Planes, Especially for Higher Order v_n

5.2.1 Construction and Calibration

Several methods to construct, combine and calibrate event planes are discussed in Sec-3.4, Sec-3.5 and Sec-3.6 respectively. The Q-vectors are built according to Eqn-3.8 and Eqn-3.3 for all orders (up to 4 in this analysis); subsequently, raw Φ_n are calculated. The next step is to calibrate event planes. The official event plane calibrator employed in the analysis presented in Chapter-4, was written before higher order harmonics were pursued; therefore its capability is limited to the first two orders, direct and elliptical planes. To measure Φ_3 and

Φ_4, an enhanced calibrator was designed and implemented.

The method used to calibrate higher order event planes are exactly the same as the one for the first two orders. However, to study the calibration process some modifications are made into the enhanced calibrator (EC). When compared to the official calibrator (OC), the differences are:

- EC implements vertex-dependent flattening, while OC does not.
- EC implements flattening up to the 8th order of k in Eqn-3.32, while OC goes up to the 5th order.

In EC, a detector gain calibration is implemented explicitly before the application of any of the calibration steps discussed in Sec-3.6. This step is also implemented in OC (for lower level calibrators). The impact of the above differences in the calibration process to Φ_n and v_n is shown in Fig-5.7, and also Fig-5.19 and Fig-5.20. It's noteworthy that a slightly different calibrator, with everything the same as EC except that 10% centrality bins are used in both re-centering and flattening, is used for the analysis in [50] [129]. This calibrator has also been tried out in our analysis and the corresponding Φ_n and v_n are very similar to the ones calibrated with EC .

One more thing that's worth mentioning is that we employed a different procedure for the dead segment in RXI south. The new procedure is that an artificial gain (instead of default value "0") is assigned to the dead segment, which equals to the averaged gain of the two neighboring segments. The ordinary event plane construction and calibration steps then follow. The treatment should make the raw event plane distributions flatter, and thus less re-centering and flattening is needed. The effect of this dead segment is discussed in Sec-5.5.

5.2.2 Res$\{\Phi_3\}$ and Res$\{\Phi_4\}$

The most direct indicator of the feasibility of a v_n analysis is the event plane resolution. Large values of resolution factors suggest small dispersions for Φ_n and sizable raw v_n signals, which would not be easily blurred by the statistical fluctuations. Consequently, Res$\{\Phi_n\}$ values are always the first check for a v_n analysis, especially in our case because:

- we target higher order Φ_n, the resolutions of which tend to be smaller compared to Res$\{\Phi_2\}$;
- due to the decreased event multiplicity, values of Res$\{\Phi_n\}$ at lower beam energies are smaller than those at 200 GeV;

- the total number of events in each lower energy dataset is much smaller than the one for a typical 200 GeV dataset, and less statistics lead to greater fluctuations.

We have already seen Res$\{\Phi_2\}$ for various detectors at $\sqrt{s_{NN}} = 62$ and 39 GeV in Fig-4.18. While Res$\{\Phi_2\}$ for RXN detector (including RXI and RXO) are significant, Φ_2 built at BBC and MPC have only small resolution factors, especially for BBC. Therefore, it's doubtful that Φ_3 and Φ_4 can be constructed at MPC and BBC with sufficient precision.

Res$\{\Phi_n\}$ calculation starts from $\langle\cos[n(\Phi_n^S - \Phi_n^N)]\rangle$, the south-north correlation that is directly measured and roughly equals to $[\text{Res}\{\Phi_n\}]^2/2$ for poor resolutions (cf. Eqn-3.11). The Φ_3 and Φ_4 correlation values for BBC and MPC are illustrated on Fig-5.4 for 62 GeV collisions. It is observed that the

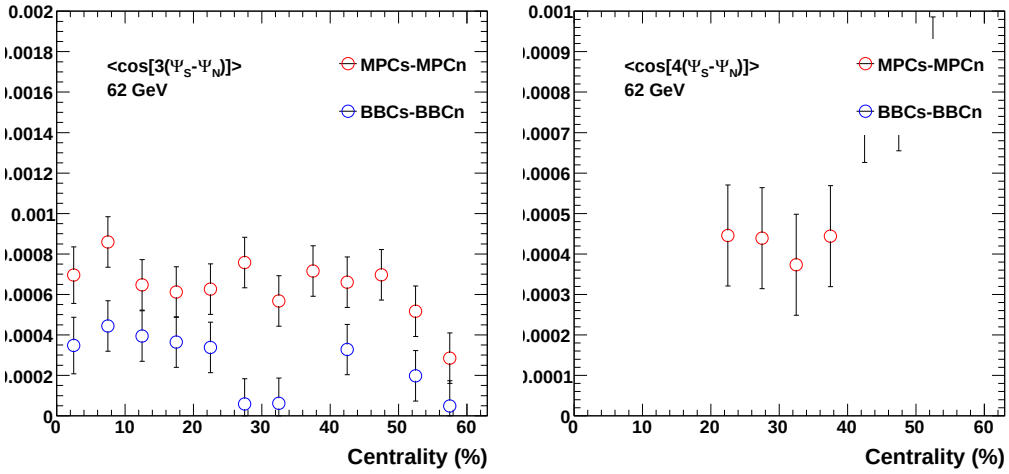

Figure 5.4: $\langle\cos[n(\Phi_n^S - \Phi_n^N)]\rangle$ vs. centrality of $n = 3$ (left) and 4 (right) for BBC and MPC. $\sqrt{s_{NN}} = 62$ GeV.

correlation values are extremely small with little statistical significance, and the corresponding resolution factors would be less than several percent. The same set of resolution factors are only worse for 39 GeV collisions. Therefore, Φ_3 and Φ_4 built at MPC and BBC are not used in the analysis.

In the next step we check the performance of the RXN detector. It has an inner ring (RXI) and an outer ring (RXO), and each ring has a south and a north component. Therefore we have 4 components to build the south-north correlation functions. In Fig-5.5, the south-north correlations for 4 combinations among the RXN components are drawn side-by-side and compared via ratio values. From the left panels on the graph, we observe sizable values for Φ_2 and Φ_3 correlations. The correlations for Φ_3 reach the peak values almost

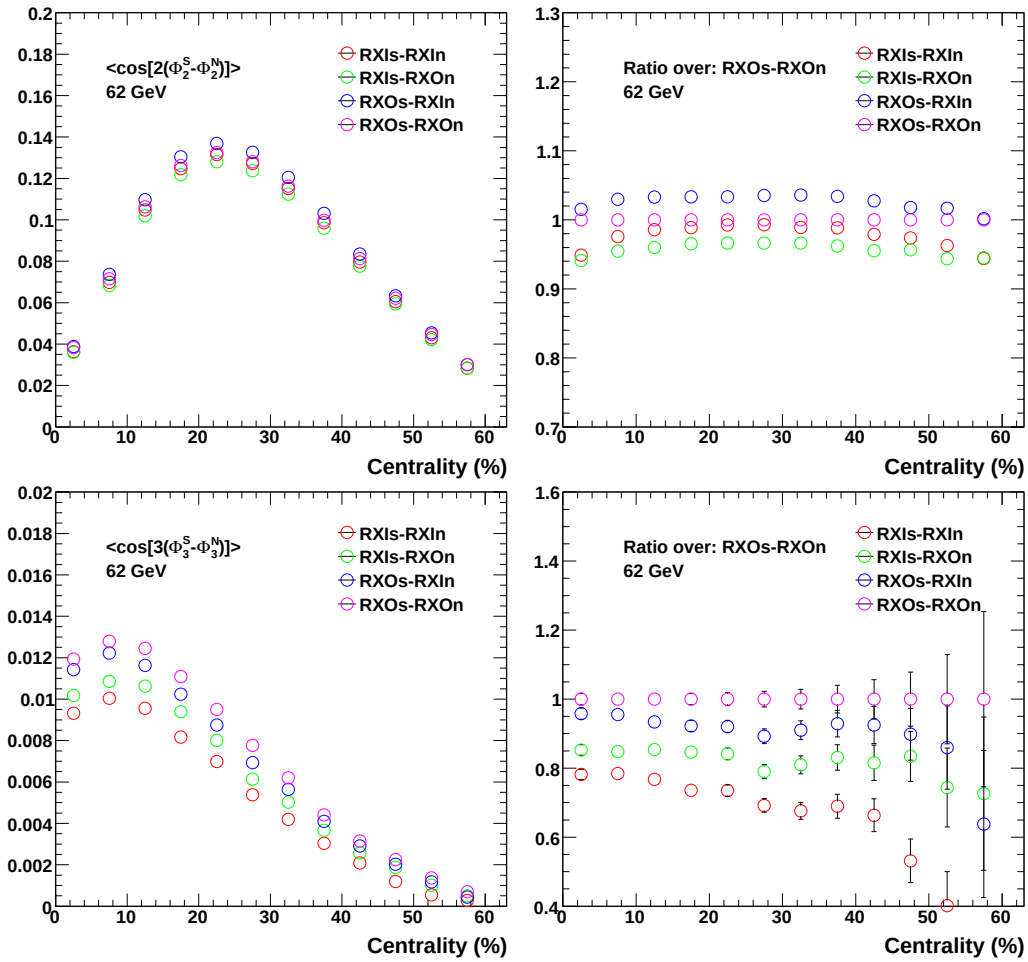

Figure 5.5: $\langle\cos[n(\Phi_n^S - \Phi_n^N)]\rangle$ vs. centrality of $n = 2$ (top panels) and 3 (bottom panels) for 4 RXN south-north combinations. Correlation values are shown on the left panels; ratios of correlations with RXOs-RXOn correlation as the baseline are shown on the right panels. $\sqrt{s_{NN}} = 62$ GeV.

in the most central collisions. This is because in contrast to v_2, v_3 for different centralities don't change much (discussed in Sec-1.6.4); consequently the resolution factors of Φ_3 mainly depend on event multiplicity, which decreases from central to peripheral collisions and results in the observed trend of the Φ_3 correlations. Robust Φ_4 correlations are observed as well; the curves are very much like those for Φ_3, only with smaller values.

As mentioned earlier, there is one dead segment in RXIs. Although this has been taken into account during the event plane calibration process, the resolution of RXIs is still expected to be lower than that of RXIn, because the accounting is meant to make the calibration process easier and does not have the capability to improve the inherent resolution of the detector. The lower resolution of RXI is best illustrated on the right two panels of Fig-5.5, where we observe that correlations of RXIs-RXOn are consistently smaller then those of RXIn-RXOs. The differences are around 10% for Φ_2 correlations and 20% for Φ_3 correlations. Since there are no known defects on RXO, RXOs and RXOn are considered identical. Therefore, according to Eqn-3.11 the event plane resolutions of RXIs are 10% and 20% lower than the ones of RXIn, for Φ_2 and Φ_3 respectively.

It is noteworthy that the comparisons between correlations of RXIs-RXOn and RXIn-RXOn can not be employed to derive the conclusion above, which is tempting because one common component RXOn is used and should just cancel out in the comparison. The reason is that correlations of RXIn-RXOn involve significant non-flow effects (10 to 20%); they are located at the same arm without any rapidity gap in between.

To cope with the imbalance between RXIs and RXIn, various methods to calculate resolutions are employed and discussed in Sec-5.5 All of these methods give consistent resolution for the combined RXI detector, and thus consistent RXN resolution. To achieve maximal resolution, the RXN detector is used for the final results and the resolution factors of RXN are plotted in Fig-5.6. Note that event planes here are calibrated with EC. Resolution factors decrease quickly for higher order event planes and Res$\{\Phi_4\}$ almost exhaust the sensitivity. The shapes of the curves are very similar to the south-north correlations shown in Fig-5.5, as they should be.

The Res$\{\Phi_2\}$ for RXN is also shown in Fig-4.18; the difference is that Φ_2 in that case is calibrated with FC. Therefore, we could compare Res$\{\Phi_2\}$ obtained with these two different calibrators and examine the impact of distinct calibration processes. The ratios of Res$\{\Phi_2\}$ with Φ_2 calibrated with FC and EC are illustrated on Fig-5.7. It can be seen that Φ_2 calibrated with FC has less dispersion in central collisions, while for peripheral collisions the performance of EC calibrated Φ_2 is better. The study has also been implemented

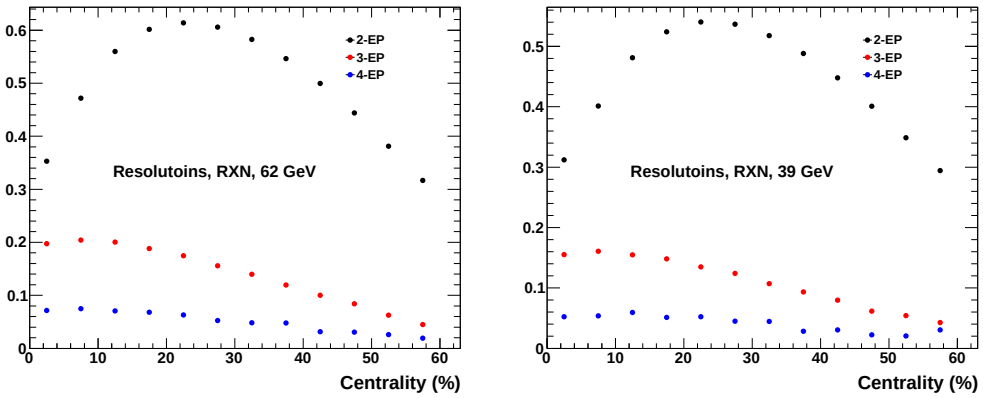

Figure 5.6: Res$\{\Phi_n\}$ vs. centrality measured with RXN for $n = 2, 3, 4$. $\sqrt{s_{NN}}$ = 62 GeV (left) and 39 GeV (right).

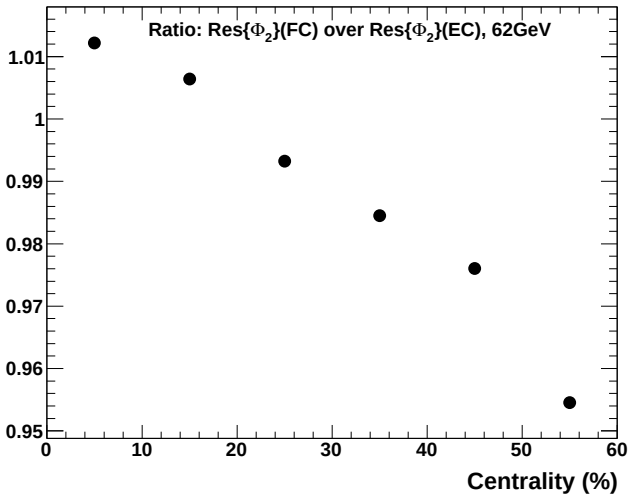

Figure 5.7: Comparisons of Res$\{\Phi_2\}$ for Φ_2 calibrated with FC and EC. Ratios of Res$\{\Phi_2\}$ values for the two methods are illustrated, with resolutions of Φ_2 calibrated with EC as the denominator. $\sqrt{s_{NN}} = 62$ GeV.

with 39 GeV data; the observations are almost the same.

5.3 QA

As for other analyses, QA is implemented to pick the data segments that are suitable for the charge hadron v_n measurement. QA results for resolution factors of Φ_2 calibrated with FC are shown in Fig-3.29 in terms of south-north correlation $\langle\cos[2(\Phi_2^S - \Phi_2^N)]\rangle$. Since we have shown that EC calibrated Φ_2 won't be much different (cf. Fig-5.7), similar QA results of EC calibrated Φ_2 are expected, which is confirmed by actual measurement. More importantly, Φ_3 and Φ_4 are constructed and calibrated with EC; they are checked in the same fashion as Φ_2 and thus not shown here.

Besides resolution factors, another approach to select runs for this analysis is to check the raw v_3 and v_4 values directly. The raw values are first found out in run groups, each of which contains 24 run segments (except the last one) and is assigned a run group number starting at 999900. The results are illustrated on Fig-5.8. The raw v_3 and v_4 values are very consistent among run

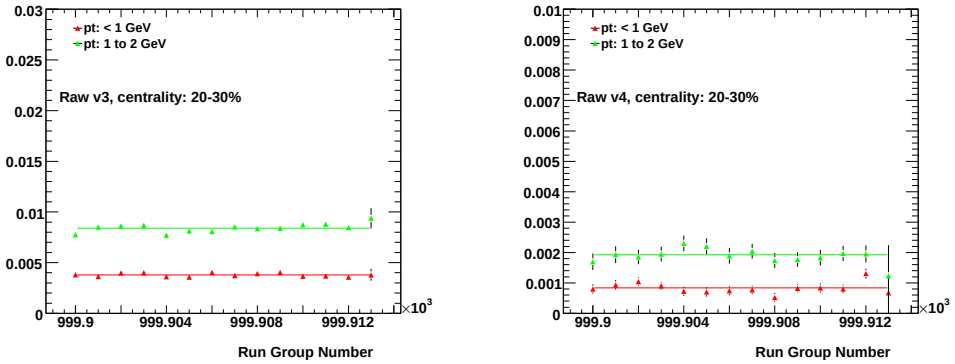

Figure 5.8: Run group QA of raw v_3 (left) and v_4 (right). Two p_T selections (red and green dots) are shown; lines indicate averaged values with inclusive data. Centrality $20-30\%$, $\sqrt{s_{NN}} = 62$ GeV.

groups. To exclude possible unsuitable run segments, the same type of plots for individual runs are produced. Though the statistical fluctuations are large on those plots, suspicious run segments can still be selected. They are further manually checked to avoid accidental rejection.

5.4 Effects of Non-Flow

The estimation of non-flow contamination to the v_n signal is a crucial part of quoting systematic uncertainties. Comparing v_n with Φ_n built with detectors sitting at distinct rapidity ranges can provide a handle for such an estimate. As discussed in Sec-5.2.2, MPC and BBC are not suitable for v_3 and v_4 analysis. Therefore, v_n measured at RXI and RXO are employed and compared, as was done in Sec-4.6.3. The inclusive charged particle measurements have much better statistics and thus allows a better estimate of non-flow effects.

v_n measured at 62 GeV with RXI and RXO are compared in terms of ratio values (over v_n measured with RXN) in Fig-5.9, Fig-5.10 and Fig-5.11,

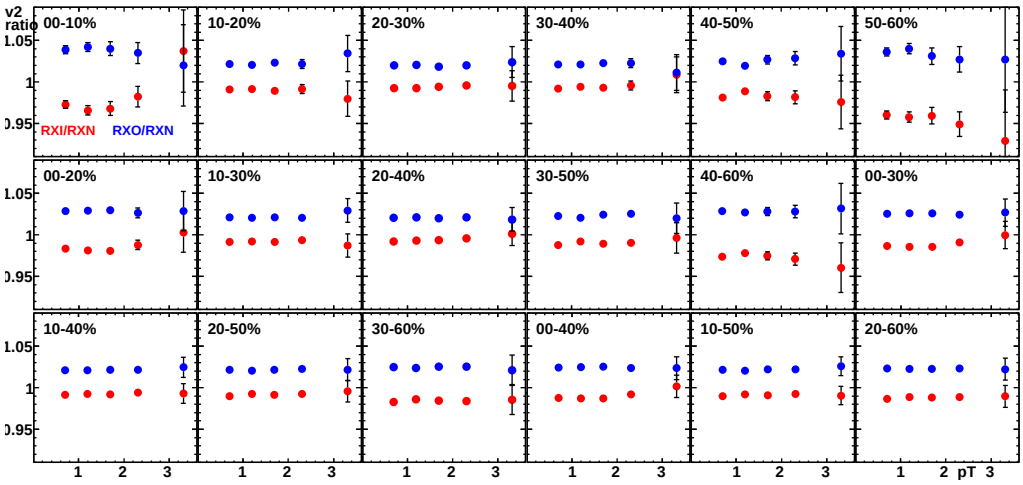

Figure 5.9: Comparisons of v_2 measured with RXI and RXO for various centrality selections. Ratio values of v_2(RXI)/v_2(RXN) and v_2(RXO)/v_2(RXN) are shown side-by-side as red and blue dots. Results are shown for $\sqrt{s_{NN}} = 62$ GeV.

respectively. For the v_2 ratios, unambiguous p_T independent differences between RXI and RXO are found, and v_2 measured with RXO are larger than those with RXI. This observation is consistent with our expectation of non-flow effects. The ratios deviate from unity by an amount of 3% in central and peripheral collisions and less than 2% in mid-central collisions.

For v_3 ratios, they don't exactly line up as v_2 ratios do. But the discrepancies are still rather limited, around $3-4\%$ for most of the centrality bins. For peripheral collisions, the statistical fluctuations become large and v_3 with RXI seem to be abnormally large. The ratios for v_4 cease to be p_T independent and for p_T less than 1 GeV the discrepancies between RXI and RXO are exceptionally large. The reasons for this is unknown and a larger systematic

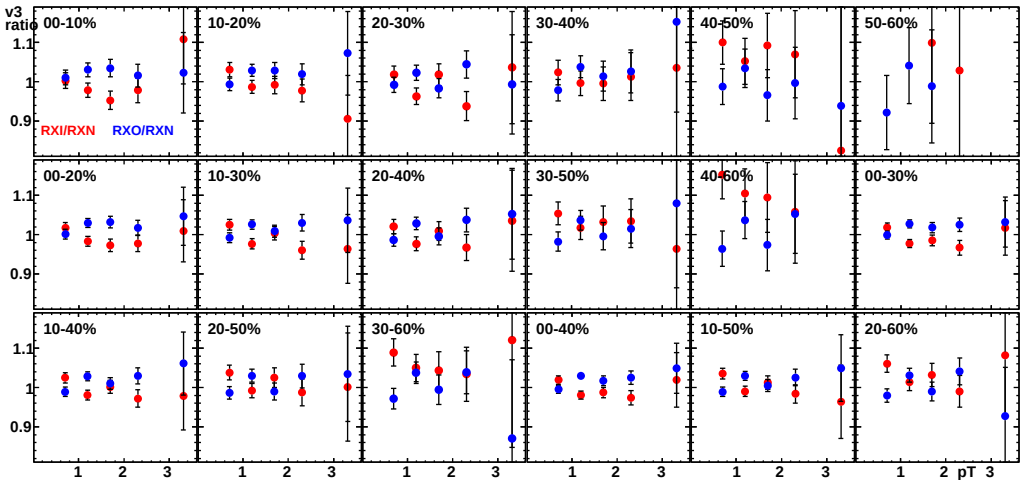

Figure 5.10: Same as Fig-5.9, except ratios of v_3 are illustrated.

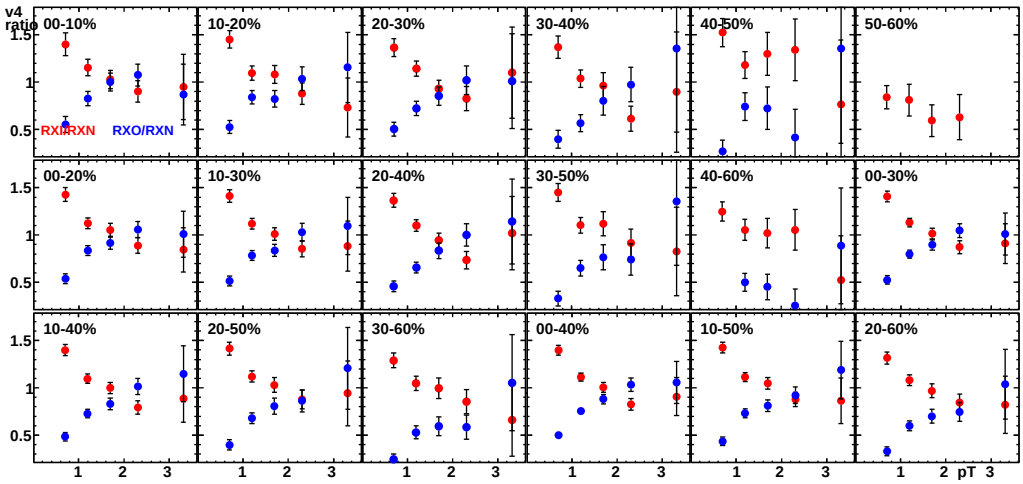

Figure 5.11: Same as Fig-5.9, except ratios of v_4 are illustrated.

uncertainty is assigned to v_4 at lower p_T. In peripheral collisions, multiplicity clearly drops to a critical level and this prevents an accurate determination of Φ_4, e.g. the ratios of RXO v_4 in the $50-60\%$ centrality bin completely falls out of bounds. In central and mid-central collisions, the differences are mostly less than 15%, except for the lowest p_T bin.

The estimation of systematic uncertainty from non-flow is tabulated in Tab-5.1 and Tab-5.2 for 62 and 39GeV respectively. Each column in the

Table 5.1: Systematic Errors of v_n at $\sqrt{s_{NN}} = 62$ GeV: non-flow

Cent. (%)	$0-10$	$10-20$	$20-30$	$30-40$	$40-50$	$50-60$
v_2 (% err.)	3	1	1	1	2	5
v_3 (% err.)	3	2	2	2	7	?[a]
v_4 (% err.)	15[b]	15[b]	15[b]	15[b]	?[a]	?[a]

[a] this centrality bin is not included in the final results.
[b] this estimation is for $p_T > 1.0$ GeV, otherwise the number is doubled.

Table 5.2: Systematic Errors of v_n at $\sqrt{s_{NN}} = 39$ GeV: non-flow

Cent. (%)	$0-10$	$10-20$	$20-30$	$30-40$	$40-50$	$50-60$
v_2 (% err.)	2	1	1	1	1	4
v_3 (% err.)	5	3	3	3	?[a]	?[a]
v_4 (% err.)	20[b]	25[b]	25[b]	30[b]	?[a]	?[a]

[a] this centrality bin is not included in the final results.
[b] this estimation is for $p_T > 1.0$ GeV, otherwise the number is doubled.

table denotes a specific centrality range. Note that for higher order v_n, the sensitivity of the measurement is exhausted in peripheral bins; they are not incorporated into the final results.

5.5 Comparison of v_n Measured with South or North Single Arm

The event plane detectors have two arms (south and north respectively), and Φ_n can be built individually with each of these arms. According to Eqn-3.11, resolution factors are easily accessible for event planes built in only one arm of the detector (denoted as $\mathrm{Res}\{\Phi_n^{\mathrm{S/N}}\}$). Therefore, if the raw v_n are also measured relative to only the south or north arm, v_n measured with one single arm can be calculated.

5.5.1 Res$\{\Phi_n^{S/N}\}$ from 2 Sub-Events Method

The two sub-events method is routinely employed at PHENIX to calculate resolution factors. One fundamental assumption of the two sub-events method is that the two sub-events, obtained in the south and north arms of a particular detector, are identical or as least have the same Res$\{\Phi_n\}$. Based on this assumption Res$\{\Phi_n^S\}$ and Res$\{\Phi_n^N\}$ are calculated according to Eqn-3.11, and the resolution of the combined detector can be further calculated. However as demonstrated in Sec-5.2.1, there is one dead segment in RXIs so that it is not identical to RXIn, i.e. the resolution for RXIs is lower.

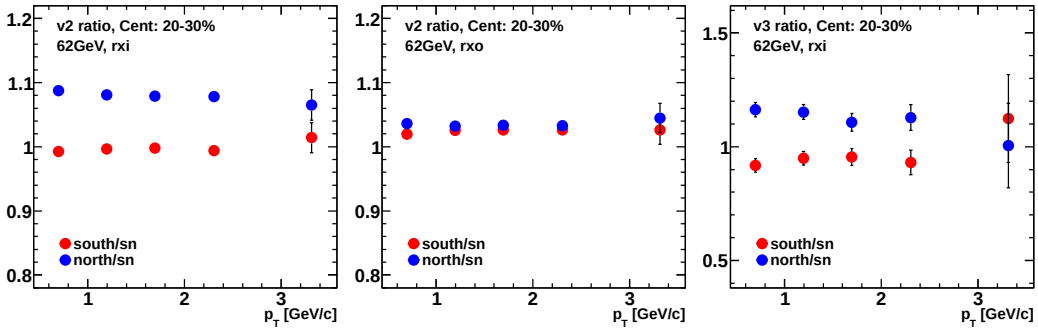

Figure 5.12: Comparisons of v_n measured with the south and north event planes; resolution factors are calculated with the **two sub-events method**. Red and Blue dots denote ratio values of v_n measured in the south and north arms over v_n measured with the combined detector (south and north). The left and middle panel shows v_2 ratios for RXI and RXO; the right panel shows v_3 ratios for RXI. Results are shown for events with centrality of $20-30\%$ for $\sqrt{s_{NN}} = 62$ GeV.

The results from v_n comparisons are illustrated in Fig-5.12. In the left panel, comparisons of the two arms of RXI are shown and we observe that the v_2 value measured with the north arm is greater than measured with the south arm; the differences are however p_T independent, suggesting an error in Res$\{\Phi_n\}$. This discrepancy is rooted in the fact that in the two sub-events method, Res$\{\Phi_n^S\}$ is assumed to be equal to Res$\{\Phi_n^N\}$, while in reality it is less. However, the multiplicity values of Res$\{\Phi_n^S\}$ and Res$\{\Phi_n^S\}$ are the south-north correlations and directly measured. Therefore, under the two sub-events method framework Res$\{\Phi_n^S\}$ is overestimated and Res$\{\Phi_n^N\}$ is underestimated. Since the resolution factor appears in the denominator when the v_n's are calculated, v_2 measured with the south arm would be over-corrected and smaller. Note that the 10% difference in v_2 values are quite consistent with the 10% difference between RXIs-RXOn and RXIn-RXOs correlations (cf. Fig-5.5); the

coincidence is not unexpected at all because the discrepancies exhibited on the two plots come from the same origin.

In the middle panel of Fig-5.12, the same comparisons are demonstrated with the RXO detector that has no known differences between its south and north arms. As expected, v_2 measured in the south and north arms agree with each other well. However, the v_2 values measured in the single arms seem to be several percent higher than the measurement with the combined arms. This issue will be re-visited shortly. In the right panel of Fig-5.12, the v_3 values obtained with RXI are compared in the same fashion. The observations are quite similar to those of the left panel.

The three sub-events method is a natural substitute in this situation where the two sub-events method is clearly inapplicable. However, as shown in Fig-5.4, BBC and MPC are incapable of measuring Φ_n beyond $n = 2$. Therefore, we only have RXI and RXO available for study, which are closely next to each other in η and make them unsuitable for the three sub-events study by themselves. For example, if an estimation of RXIs Φ_3 resolution is implemented with the three sub-events from RXIs, RXIn and RXOs, the correlation between RXIs and RXOs would be artificially enhanced by non-flow effects and the consequent RXIs resolution would be mistakenly larger. Thus the three sub-events method was restricted only to a study of Φ_2.

5.5.2 $\mathrm{Res}\{\Phi_n^{\mathrm{S/N}}\}$ from Effective 3 Sub-Events Method

As discussed in Sec-3.4.7, a hybrid of the two sub-events method and the three sub-events method yields the effective three sub-events method, where less detectors are needed compared to the requirement of the three sub-events method and nonidentical sub-events could be handled, such as the south and north arm of RXI.

With resolution factors calculated with an effective three sub-events method, comparisons of single arm v_n are illustrated in Fig-5.13, which has the same layout as Fig-5.12. Remarkably good consistency between v_n from the south and north arms is achieved for v_2 and v_3, RXI and RXO. The agreement is equally good for other centrality bins and for v_4 as well.

There is one remaining issue, however. The ratio values in Fig-5.13 are generally 3 to 4 percent larger than unity, indicating that v_n measured with the single arms are slightly higher than those measured with the combined arms. Again, the deviations from unity are mostly p_T independent, which suggests that there are uncertainties in the calculation of the resolution factors. In Sec-4.6.2, uncertainties of this type were estimated via the implementation of three sub-events method, which is limited to Φ_2 analysis as mentioned above.

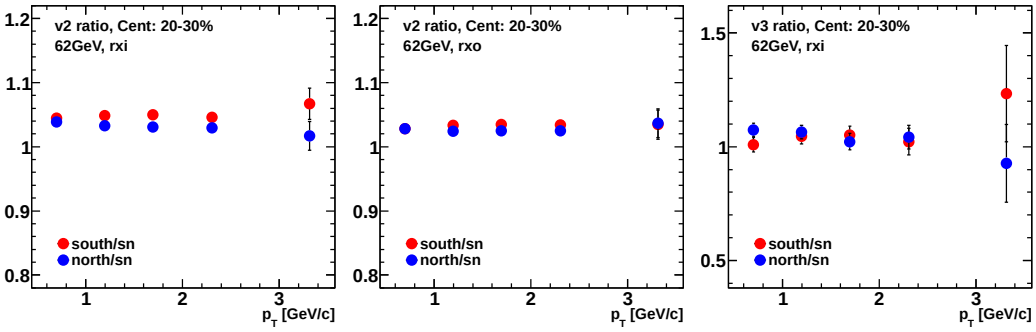

Figure 5.13: Same as Fig-5.12, but for resolution factors calculated with the **effective three sub-events method**.

5.5.3 $\mathrm{Res}\{\Phi_2^{\mathrm{S/N}}\}$ from 3 Sub-Event Method

Though only Φ_2 could be examined with the three sub-events method, an investigation is still worthy to pin-down the reasons for the v_2 ratio deviations from unity observed in Fig-5.13. If the uncertainties for the v_2 measurement are very well understood, we can be more confident about the assignment of systematic uncertainties for v_3 and v_4.

Ratio values for the resolution factors are illustrated in Fig-5.14. For these ratios, the values of the numerators are $\mathrm{Res}\{\Phi_2\}$ calculated with 4 combinations of 3 sub-events, and the denominators are $\mathrm{Res}\{\Phi_2\}$ obtained via the effective 3 sub-events method. They are of the same style as Fig-4.25, but the event planes shown here are calibrated with EC instead of FC. It is observed that the discrepancies among the four combinations are much larger in this case. The resolution values calculated with BBCs and BBCn (green dots) are more than 5% larger than those with MPCs and MPCn (red dots). This is to be compared to Fig-4.25 where the differences are less than 2% for most centralities. The reason for the BBC's poor performance with EC implemented is unknown. The MPC has very consistent performance when Fig-5.14 and Fig-4.25 are compared. Therefore, the following discussion is based on taking MPCn and MPCs to form sub-events.

The study of the 3 sub-events method suggests that $\mathrm{Res}\{\Phi_2\}$ of RXIs obtained via the effective 3 sub-events method are underestimated by more than 5%, where measurements of $\mathrm{Res}\{\Phi_2\}$ for RXIn and RXI are more accurate. For RXO, $\mathrm{Res}\{\Phi_2\}$ values are more consistent for the two methods. In the 3 sub-events framework, the comparisons of v_2 measured in the south and north arms are plotted in Fig-5.15, with the same style as Fig-5.12. We can see that v_2 measured with the two arms are now spread out to the two sides of the combined detector v_2, and the deviations from unity are less than 1%.

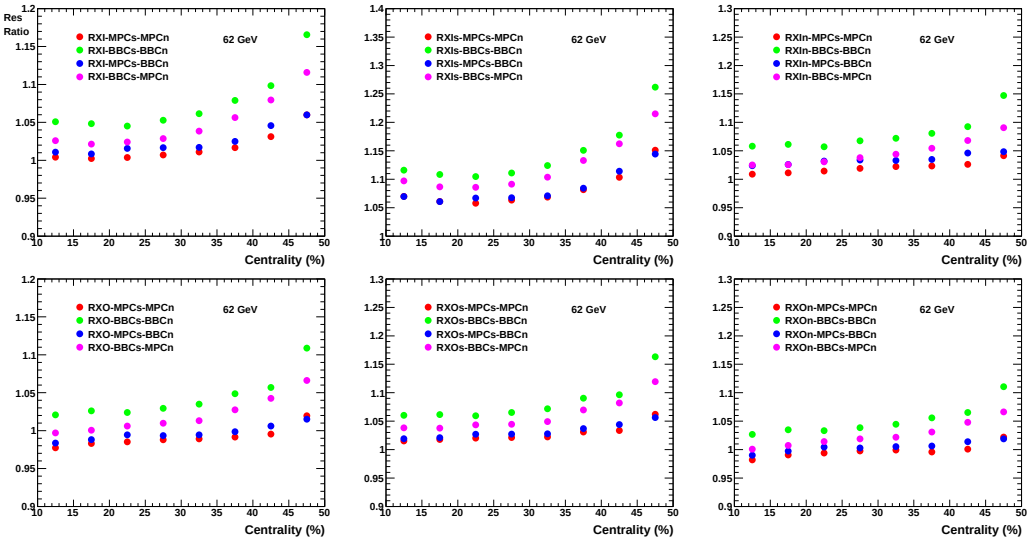

Figure 5.14: Comparisons of Res$\{\Phi_2\}$ obtained via the 3 sub-events method and the effective 3 sub-events method. For the ratio vs. centrality, the resolution factors for the effective 3 sub-events method served as the denominator. Resolutions factors for 4 combinations of the 3 sub-events, serve as the numerator. Ratios are shown for RXI (upper panels) and RXO (lower panels). For each detector, results are shown for the combined (left panels), as well as the south (middle panels) and north (right panels) arms. Results are shown for $\sqrt{s_{NN}} = 62$ GeV.

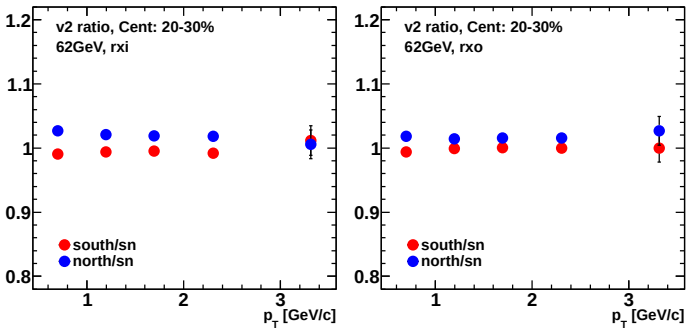

Figure 5.15: Same as the left and middle panel of Fig-5.12, but for resolution factors calculated with the **three sub-events method**.

By design the 3 sub-events method is the most robust. However, it utilizes the MPC which does not have the sensitivity to be applied to the v_3 and v_4 analysis. Therefore, the second best method, the effective 3 sub-events method is employed to estimate these resolution factors. The observations made for the v_2 analysis, where both methods are available, are used to guide the systematic uncertainty estimation for v_3 and v_4.

5.5.4 Differences between v_n with RXNs and RXNn

Since the final v_n results are based on Φ_n built at RXN, v_n measured at RXNs and RXNn are investigated and the discrepancies (possibly centrality dependent) are quoted as systematic uncertainties. As a result of the discussions in the previous sections, the effective 3 sub-events method is employed for the estimation of Res$\{\Phi_n\}$. The comparisons for v_2, v_3 and v_4 are presented in the familiar style in Fig-5.16, Fig-5.17 and Fig-5.18, respectively. Only comparisons for $\sqrt{s_{NN}} = 62$ GeV are shown; those for 39 GeV are quite similar, when statistics permit us to draw a firm conclusion.

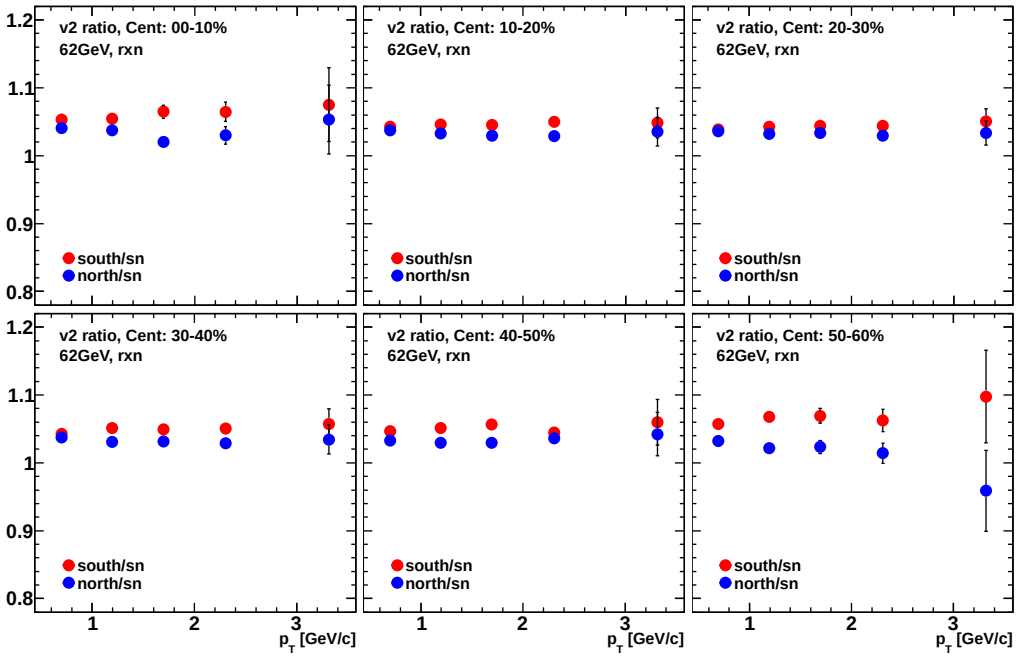

Figure 5.16: Comparisons of v_2 measured with RXNs and RXNn for various centrality bins. Red and Blue dots denote ratio values for v_2 measured from RXNs and RXNn over the ones from RXN. $\sqrt{s_{NN}} = 62$ GeV.

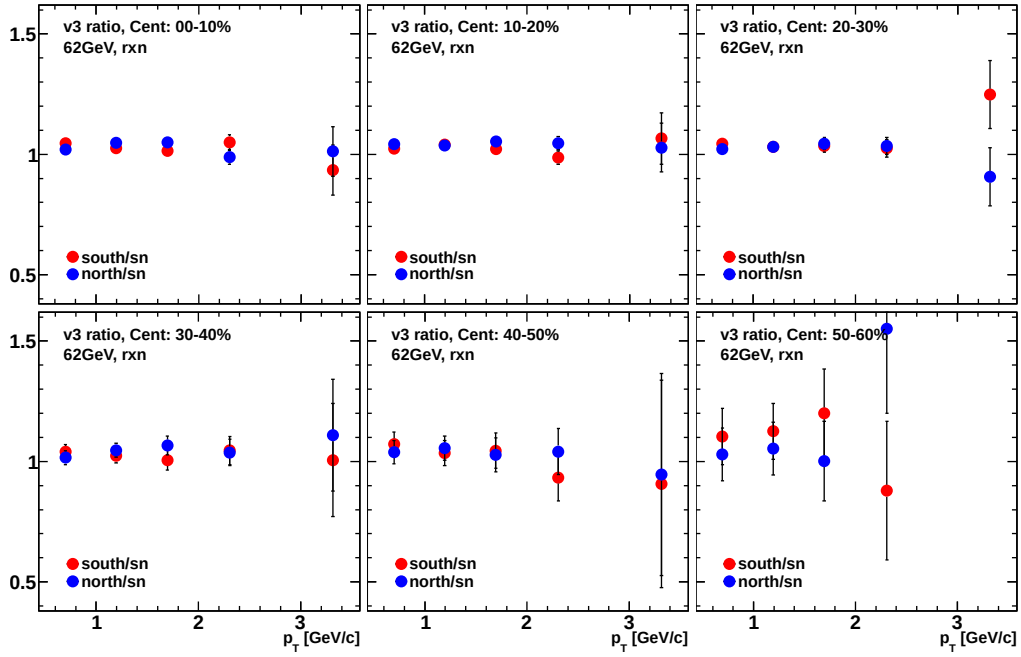

Figure 5.17: Same as Fig-5.16, but for v_3.

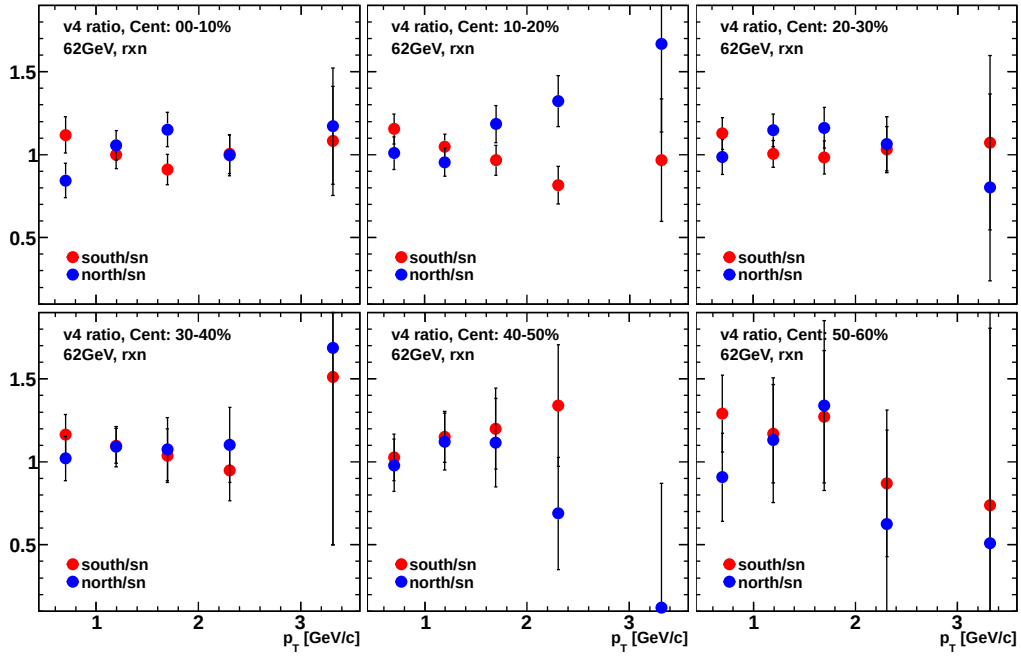

Figure 5.18: Same as Fig-5.16, but for v_4.

The observations from the figures are summarized as systematic uncertainty in Tab-5.3 and Tab-5.4 for 62 and 39GeV. Systematic uncertainties of

Table 5.3: Systematic Errors from Single Arm Measurement: 62GeV

Cent. (%)	$0-10$	$10-20$	$20-30$	$30-40$	$40-50$	$50-60$
v_2 (% err.)	3	1	1	1	1	3
v_3 (% err.)	3	1	1	1	2	?[a]
v_4 (% err.)	10	10	10	10	?[a]	?[a]

[a] this centrality bin is not included in the final results.

Table 5.4: Systematic Errors: single arm measurement: 39GeV

Cent. (%)	$0-10$	$10-20$	$20-30$	$30-40$	$40-50$	$50-60$
v_2 (% err.)	3	2	1	1	2	3
v_3 (% err.)	3	3	3	3	?[a]	?[a]
v_4 (% err.)	10	10	10	15	?[a]	?[a]

[a] this centrality bin is not included in the final results.

this type mainly comes from the uncertainty in event plane resolution measurement.

5.6 Systematic Uncertainty

The effects discussed in the previous two sections, Sec-5.4 and Sec-5.5, contribute to most of the systematic uncertainty in this analysis. However, there are other small sources that are not included for the measurements in this thesis. They include the following:

- formulae method vs. fit method to extract χ (and calculate resolution);
- BBC trigger efficiency;
- beam shift and momentum scale;
- track selection cuts;
- acceptance for tracks;

Many of these sources are discussed in Ref. [130]. Investigations of these effects show that their contributions to the overall uncertainty are minor compared to those discussed in the previous sections.

Finally, systematic uncertainties from all possible sources are summarized in Tab-5.5 for 62GeV and Tab-5.6 for 39GeV.

Table 5.5: Total Systematic Errors: $\sqrt{s_{NN}} = 62$GeV.

Cent. (%)	$0-10$	$10-20$	$20-30$	$30-40$	$40-50$	$50-60$
v_2 (% err.)	5	2	2	2	3	7
v_3 (% err.)	5	3	3	3	8	?[a]
v_4 (% err.)	20	20	20	20	?	?

[a] this centrality bin is not included in the final results.

Table 5.6: Total Systematic Errors: $\sqrt{s_{NN}} = 39$GeV.

Cent. (%)	$0-10$	$10-20$	$20-30$	$30-40$	$40-50$	$50-60$
v_2 (% err.)	4	3	2	2	3	6
v_3 (% err.)	7	5	5	5	?[a]	?
v_4 (% err.)	30	30	30	35	?	?

[a] this centrality bin is not included in the final results.

5.7 Cross Check with Other Measurements

In this analysis, v_n $(n = 2, 3, 4)$ of inclusive charge hadrons are measured for Au+Au collisions at 62 and 39 GeV. There are similar measurements carried out independently at PHENIX, the results of which are presented and compared in this section. Very good consistency is achieved across the separately implemented analysis and this fact lends us additional confidence about the measurements.

5.7.1 Comparisons with PHENIX Preliminary v_2

Preliminary results of inclusive charge hadron v_2 at 62 and 39 GeV were first shown at the Winter Workshop on Nuclear Dynamics in 2011. This analysis was performed before the v_n study shown here and FC calibrated Φ_2 were used [130]. Though v_2 measurement is not our main target, a cross-check of the v_2 values obtained here with PHENIX preliminary results could quickly tell us whether the analysis is trustworthy.

Comparisons of the two v_2 measurements are illustrated in Fig-5.19 and Fig-5.20 for $\sqrt{s_{NN}} = 62$ and 39 GeV. Unlike other comparisons, ratios of the two measurements are not directly accessible because different p_T binning

schemes are used. Therefore, the preliminary results are first fitted with a polynomial function and ratio values are then calculated as the v_2 results divided by the corresponding (p_T-wise) values on the curve. It is observed that v_2 values between the two methods agree with each other well, especially in the mid-central collisions. For the most central and peripheral centrality bin, the mostly p_T independent discrepancies could be as large as 3%, which are still well covered by the systematic uncertainties.

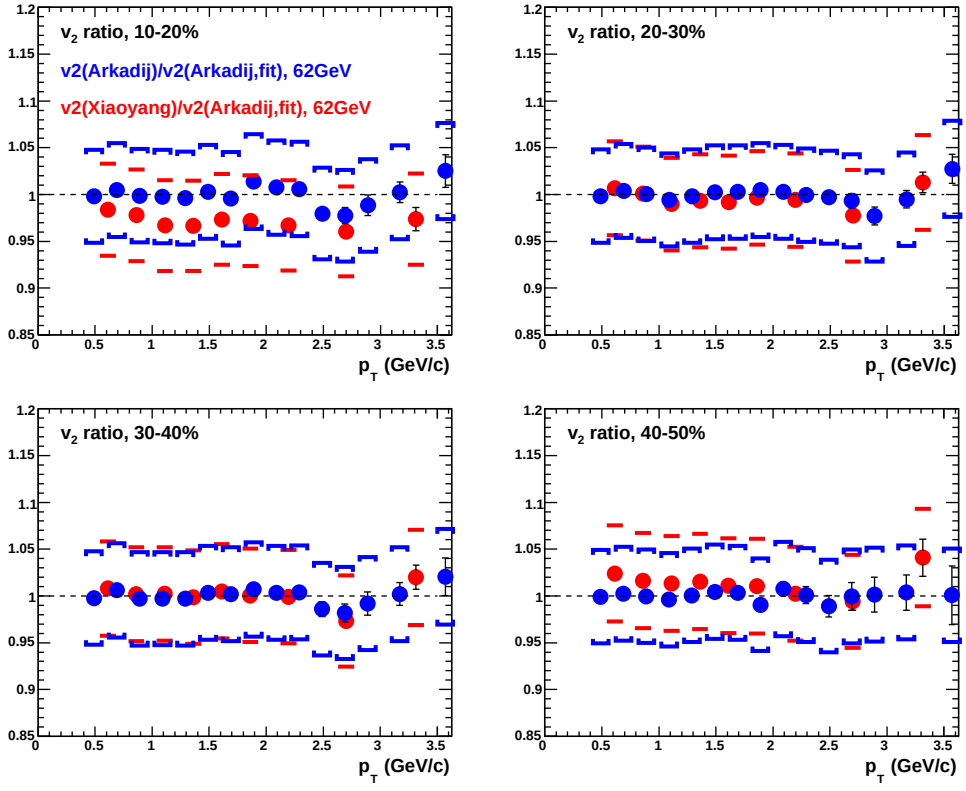

Figure 5.19: Comparisons of v_2 obtained in this analysis to PHENIX preliminary results, $\sqrt{s_{NN}}$ = 62 GeV. Preliminary v_2 vs. p_T results, denoted by the name of the main author as v_2[Arkadij], are first fitted with polynomial functions. The ratio values of v_2 results over the corresponding values on the fitting curve are illustrated, for both our v_2 results (v_2[Xiaoyang], red dots) and the preliminary results (v_2[Arkadij], blue dots). Systematic uncertainties are denoted by brackets. Four centrality selections are shown.

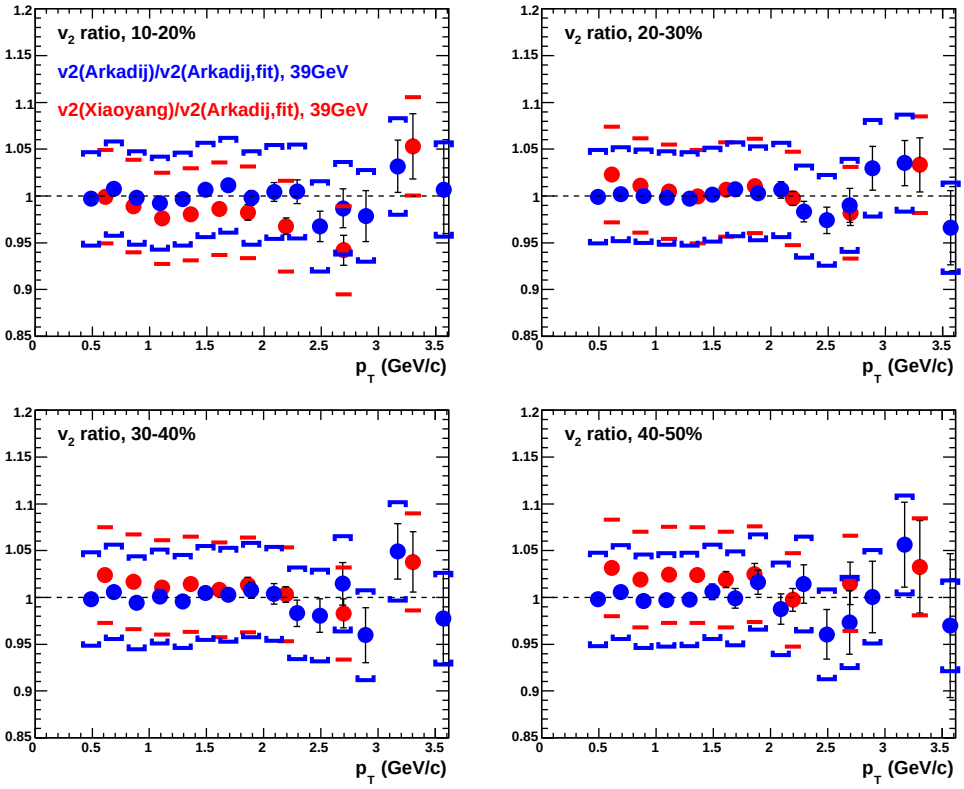

Figure 5.20: Same as Fig-5.19, but for $\sqrt{s_{NN}} = 39$ GeV.

5.7.2 Comparisons with PHENIX Preliminary v_n Extracted from Long Range Correlation Function

Besides measuring v_n via the construction of Φ_n (the event plane method), v_n could also be extracted from the two-particle correlation functions (cf. Sec-1.7.1). Measurement with this method is independently carried out at PHENIX and the results are employed here as a crosscheck for our measurement. To avoid a near-side jet contribution to the correlation function, a large $\Delta\eta$ separation between the two particles are necessary (cf. Fig-1.17), i.e. "long range". At PHENIX, to achieve a sufficient η gap between the two particles, one of them is selected as a charged track in the central arm, and the other is identified from the responses of one segment of the RXN detector. Therefore strictly speaking the second "particle" is not a real one but rather a collection of particles hitting the same segment. Nevertheless, the results won't be affected by this fact since factors of the second particle are dropped out in the calculation. It's also noteworthy that since Φ_n for our final results are constructed in RXN, the η gap in both measurements (with event plane method and long range correlation method) are the same.

Comparisons of v_2 measured with the two methods are presented in Fig-5.21. Results obtained with both methods are very consistent, especially for v_2 and v_3. Sensitivity of v_n measurement with RXN is exhausted for v_4 due to the segmentation of RXN (12 segments in azimuth), which is more obviously observed on v_4 measured with the long range correlation method. For results with other centrality selections, and for those at $\sqrt{s_{NN}} = 39$ GeV, the consistency between the two measurements are observed as well.

5.8 Results

The main results of inclusive charge hadron v_n measurement for Au+Au collisions at $\sqrt{s_{NN}} = 62$ and 39 GeV are presented in this section. Mid-rapidity $v_n\{\Psi_n\}$ $(n = 2, 3, 4)$ measured at PHENIX central arm are illustrated on Fig-5.22 as a function of p_T. The results are based on event planes constructed at RXN. Though it is relatively close to the central arm compared to BBC and MPC, it is the only detector that allows v_3 and v_4 measurement in the low multiplicity environment of collisions at $\sqrt{s_{NN}} = 62$ and 39 GeV. Systematic uncertainty of $v_n\{\Psi_n\}$ is discussed in the previous sections and summarized in Sec-5.6.

As shown on the figure, values of $v_2\{\Psi_2\}$ generally increase with p_T as hydrodynamics predict. $v_2\{\Psi_2\}$ for both beam energies increase steadily from central to peripheral collisions, consistent with an increasing second order ec-

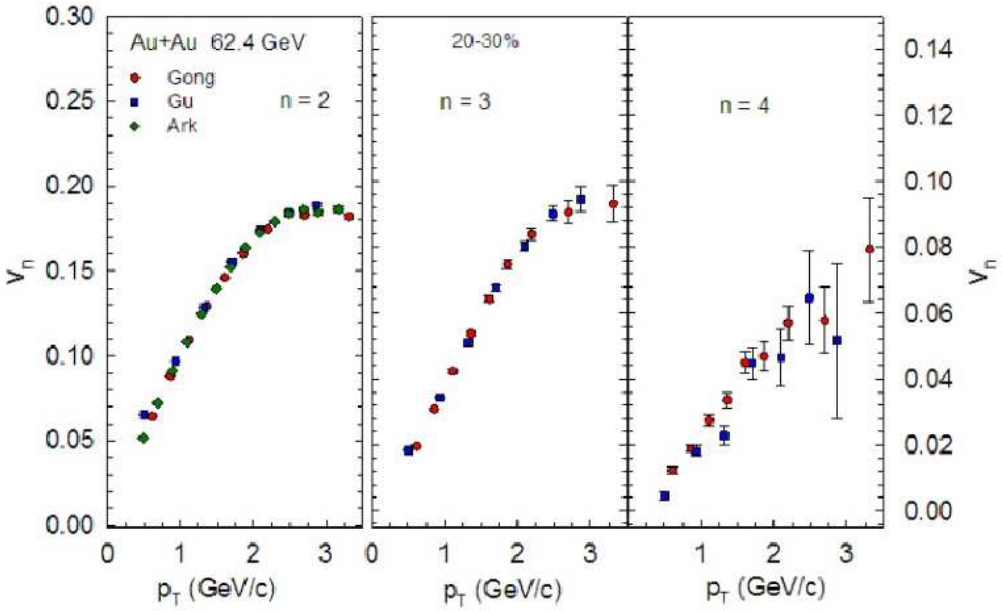

Figure 5.21: Comparisons of v_n obtained in this analysis (marked as "Gong", red dots) to v_n extracted from long range correlation function (marked as "Gu", blue squares). For v_2, results from Arkadij (marked as "Ark", green diamonds, cf. Fig-5.19) are also shown. Note that the vertical scales are different for v_2 (left panel) and v_3/v_4 (middle/right panel). Only statistical errors are plotted. Centrality: $20-30\%$, $\sqrt{s_{NN}} = 62$ GeV.

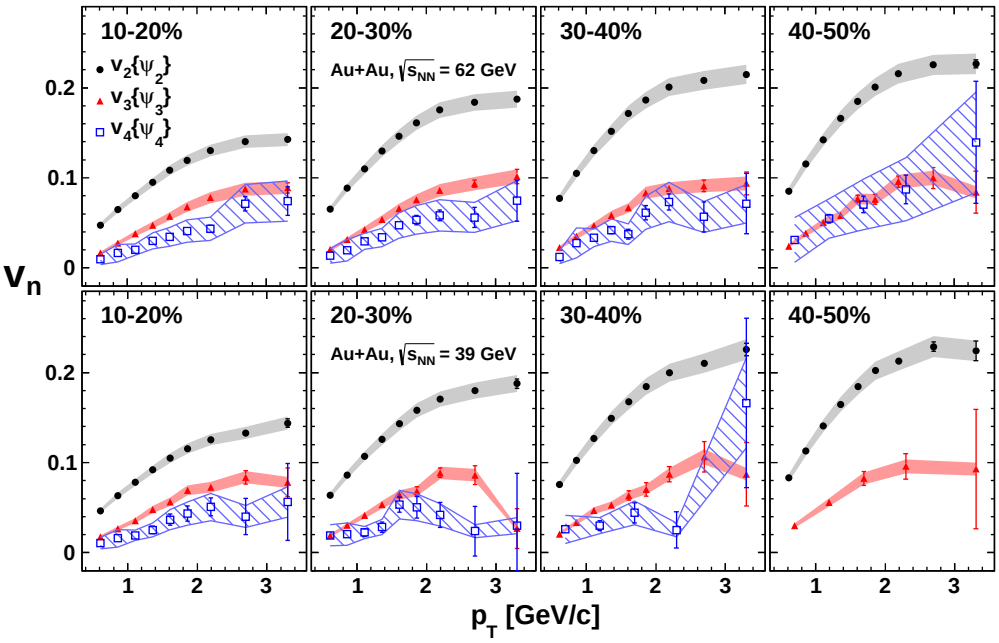

Figure 5.22: Inclusive charge hadron $v_n\{\Psi_n\}$ vs. p_T for $\sqrt{s_{NN}} = 62$ GeV (top panels) and 39 GeV (bottom panels). Four centrality selections are shown for each beam energy. Systematic uncertainties are indicated as grey (red) shaded areas for v_2 (v_3) and blue hatched areas for v_4.

centricity (ϵ_2). The values of $v_3\{\Psi_3\}$ and $v_4\{\Psi_4\}$ show a different centrality dependence, which is consistent with their origin from initial geometry fluctuations. An important observation that could already be spotted on this figure is that values of $v_n\{\Psi_n\}$ are roughly the same for the two beam energies. Moreover, these values are actually very consistent with those at 200 GeV [50].

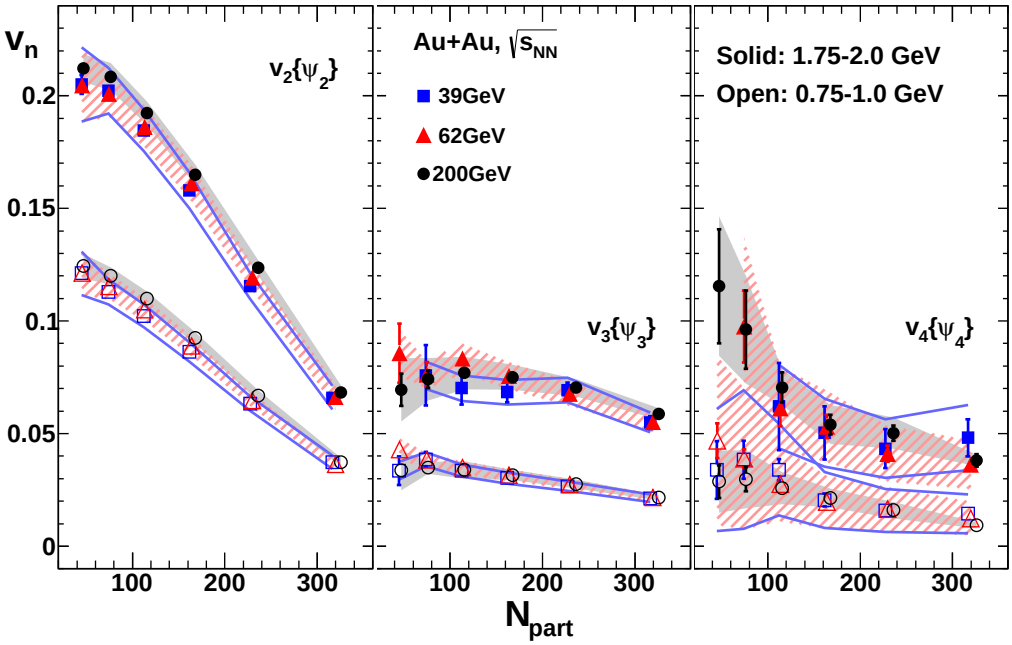

Figure 5.23: Inclusive charge hadron $v_n\{\Psi_n\}$ vs. $N_{\rm part}$: values of v_n at three beam energies, 39 GeV (blue squares) , 62 GeV (red triangles) and 200 GeV (black dots), are shown for two p_T selections. Systematic uncertainties are indicated as grey (red) shaded areas for beam energy of 200 (62) GeV and blue hatched areas for 39 GeV.

Fig-5.23 compiles $v_n\{\Psi_n\}$ measurements carried out in PHENIX at different beam energies, including previously published results at 200 GeV. Values of $v_n\{\Psi_n\}$ are plotted as a function of $N_{\rm part}$ and laid side by side for $\sqrt{s_{NN}} =$ 39, 62 and 200 GeV. The $v_n\{\Psi_n\}$ values observed at the low p_T range (Open symbols on the figure) reflect the soft physics domain where the application of hydrodynamics is justified by many analysis. A slightly higher p_T selection is presented to discern possible effects from non-equilibrated nuclear matter. From the left and middle panels of the figure we see very consistent $v_2\{\Psi_2\}$ and $v_3\{\Psi_3\}$ values in the beam energy range of 39 $\sim$ 200 GeV. Values of $v_4\{\Psi_4\}$ seem to agree with each other for different beam energies as well, but the large size of uncertainty prevents us from drawing a firm conclusion.

The N_{part} dependence of $v_n\{\Psi_n\}$ (especially for $n > 2$) has very strong discriminating power on initial geometry models. Models that describe $v_2\{\Psi_2\}$ well might fail to reproduce higher order $v_n\{\Psi_n\}$, as demonstrated in [50]. The similarity between $v_n\{\Psi_n\}$ values observed up to $n = 4$ suggest that the initial geometry conditions remain mostly unchanged for collision energies down to 39 GeV.

Chapter 6

Discussion and Conclusion

6.1 v_n Excitation Function

The v_n excitation function describes the functional relationship between v_n and $\sqrt{s_{NN}}$. Naturally, the trend of the function illustrates the beam energy scan results of v_n most directly. Besides measurements at 200, 62 and 39 GeV shown in the previous chapters, inclusive charge hadron v_2 has also been measured for 7.7 GeV at PHENIX with the Run10 dataset and the results are depicted on Fig-6.1. It is observed that for all p_T values, the corresponding

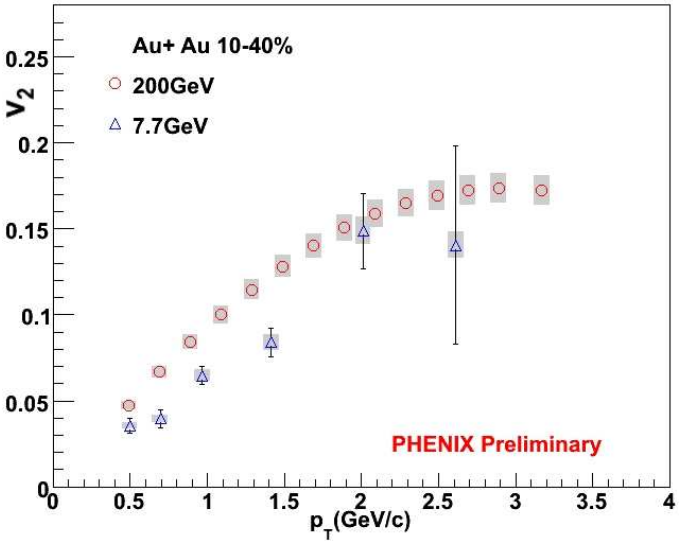

Figure 6.1: Inclusive charge hadron v_2 at $\sqrt{s_{NN}} = 7.7$ GeV [131]. v_2 values at 200 GeV are graphed for comparison. Systematic errors are indicated by grep bands. Results are shown for centrality $10 - 40\%$.

v_2's at 7.7 GeV are smaller than those for 200 GeV.

The other active experiment at RHIC, STAR, has produced rich results in the BES program as well. The Inclusive charge hadron v_2 measured by STAR is summarized in Fig-6.2. Note that in addition to all the collision energies

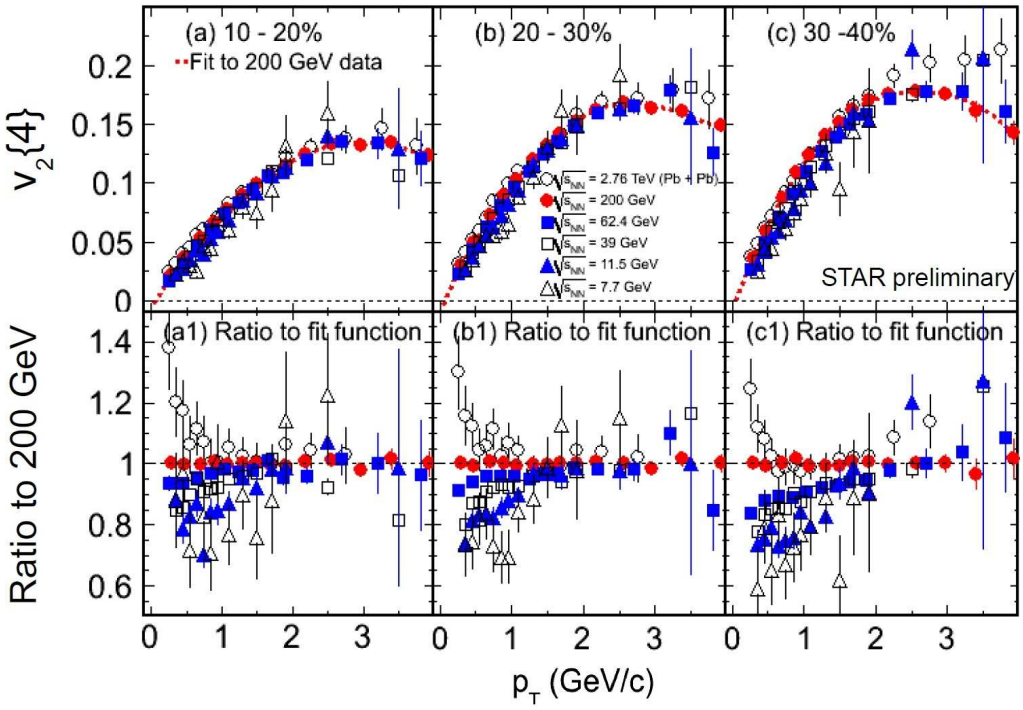

Figure 6.2: Inclusive charge hadron v_2 for various collision energies measured by STAR [132] and ALICE [133]. v_2 in three centrality bins are measured with the cumulant method and shown in the top panels. The ratios of v_2 at different collision energies over the fitted curves for the measurement at 200 GeV are plotted in the bottom panels. Results at RHIC energies of 200, 62, 39, 11.5 and 7.7 GeV along with result at LHC energy of 2.76 TeV are presented.

that have been discussed so far, STAR is capable of taking an extra dataset at $\sqrt{s_{NN}} = 11.5$ GeV during Run10.

Compiling all these results and including existing result at very low energy of 3 GeV from E895 [134], inclusive charge hadron v_2 from experiments operated on RHIC-AGS could be summarized on Fig-6.3 as v_2 excitation functions. Two selected p_T ranges are shown, and we observed that from $\sqrt{s_{NN}} = 200$ GeV to lower beam energies, the inclusive charge hadron v_2 values remain relatively the same down to $\sqrt{s_{NN}} = 39$ GeV. This observation is consistent with the one obtained from Fig-4.28 to Fig-4.30, where π^0 v_2 vs. p_T curves are laid side-by-side for 200, 62 and 39 GeV and very little difference is discerned.

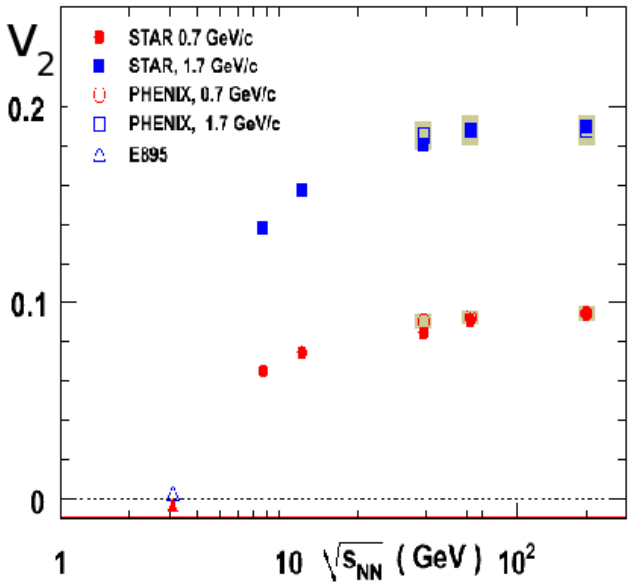

Figure 6.3: Excitation functions of inclusive charge hadron v_2. $\sqrt{s_{NN}}$ dependence of v_2 is illustrated with measurements from STAR (solid circles and squares), PHENIX (open circles and squares) and E895 (solid and open triangles). Two p_T selections are marked with red ($p_T \sim 0.7$ GeV) and blue ($p_T \sim 1.7$ GeV). Systematic errors are indicated as grey bands. See text.

On the other hand, in the low energy end of 11.5, 7.7 and 3 GeV v_2 drops quickly, and essentially reaches zero at AGS energy (E895 results). The BES program continued in 2011 and datasets at 27 and 19.6 GeV were collected at PHENIX, the analysis of which would yield results that fill into the gap between 39 GeV and 11.5 GeV on Fig-6.3. The connections between the two $\sqrt{s_{NN}}$ regions discussed above would be elucidated.

Higher order v_n's are difficult to measure at lower collision energies because of the worsening of event plane resolutions (cf. Sec-5.2). On the other hand, for experiments at the LHC, v_n up to $n = 6$ have been measured for Pb+Pb collisions at 2760 GeV. When results from LHC are incorporated, the excitation functions of v_n for $n = 2, 3, 4$ become available in the energy range of 39 to 2760 GeV, spanning two orders of magnitude in $\sqrt{s_{NN}}$. On Fig-6.4, the v_n excitation functions are plotted for two centrality and p_T selections. It is observed that regardless of centrality and p_T, v_n saturates in the full range of $\sqrt{s_{NN}}$ between 39 and 2760 GeV. This observation suggests that the nuclear matter created at very different collision energies might have similar initial geometry features and the evolving dynamics for them are also similar. Since the observed v_n in the final state are developed by the pressure gradient of the nuclear matter, a softening of nuclear matter equation of state is possible at high collision energies.

6.2 Selected Results of RHIC BES Program

Besides the inclusive charge hadron v_n and π^0 v_2 results discussed in the earlier sections, there are other results that could aid us toward a better understanding of the QGP phase diagram. Selected results that are more relevant to the dissertation are presented in this section.

6.2.1 Multiplicity

One basic observable of any collusion experiment is the multiplicity. It is conventionally normalized to unit rapidity and 2π azimuth and denoted as $\mathrm{d}N/\mathrm{d}\eta$. The multiplicity is further normalized by N_{part} and the resulting multiplicity per participating nucleon for various centrality bins (each corresponds to a particular value of N_{part}) are plotted on the left panel of Fig-6.5. PHENIX measurements at $\sqrt{s_{NN}} = 200$ GeV and 7.7GeV and ALICE and ATLAS measurements at 2.76 TeV are overlaid. Note that PHENIX results are scaled by constant factors for both energies. It can be seen that though the absolute values of multiplicity are much lower at RHIC energies as indicated by the size of the scaling factors, the shape of the N_{part} dependence curves are not changed

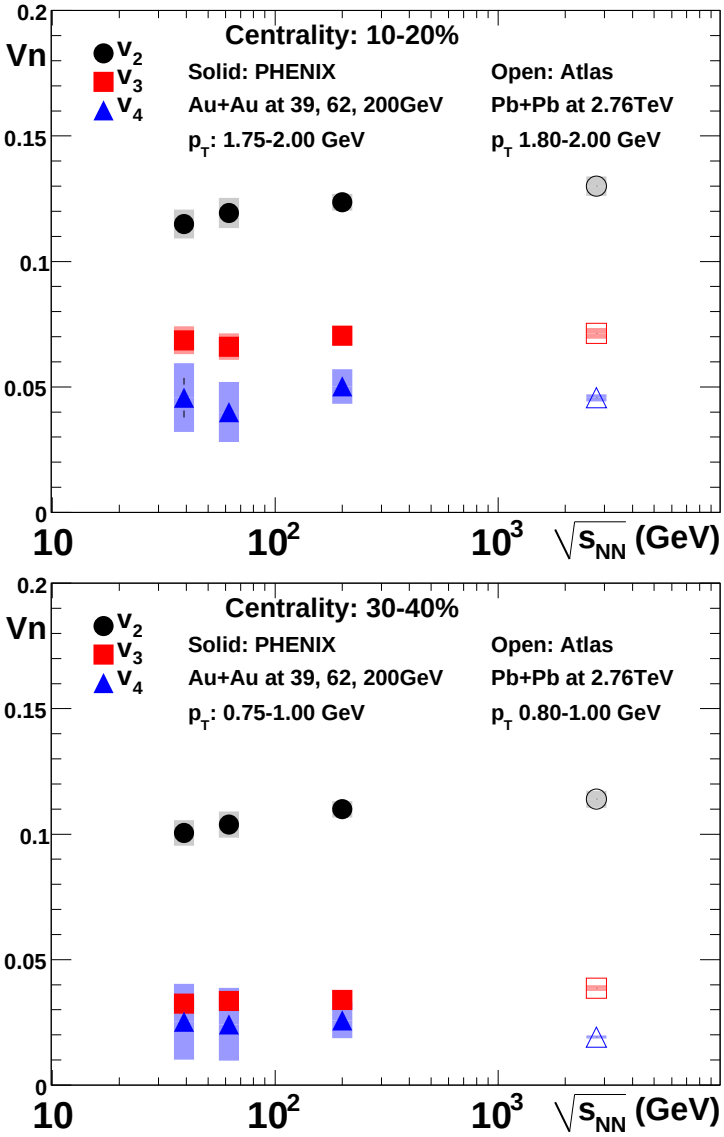

Figure 6.4: Excitation functions of inclusive charge hadron v_n, $n = 2, 3, 4$ (marked by black dots, red squares and blue triangles). Results from PHENIX at RHIC energies of 39, 62 and 200 GeV are denoted as solid symbols, while results from Atlas at LHC energy of 2760 GeV are denoted as open symbols. Systematic uncertainties are indicated by light color bands around the date points. Upper panel: centrality $10 - 20\%$, p_T $1.75 - 2.00$ GeV. Lower panel: centrality $30 - 40\%$, p_T $0.75 - 1.00$ GeV.

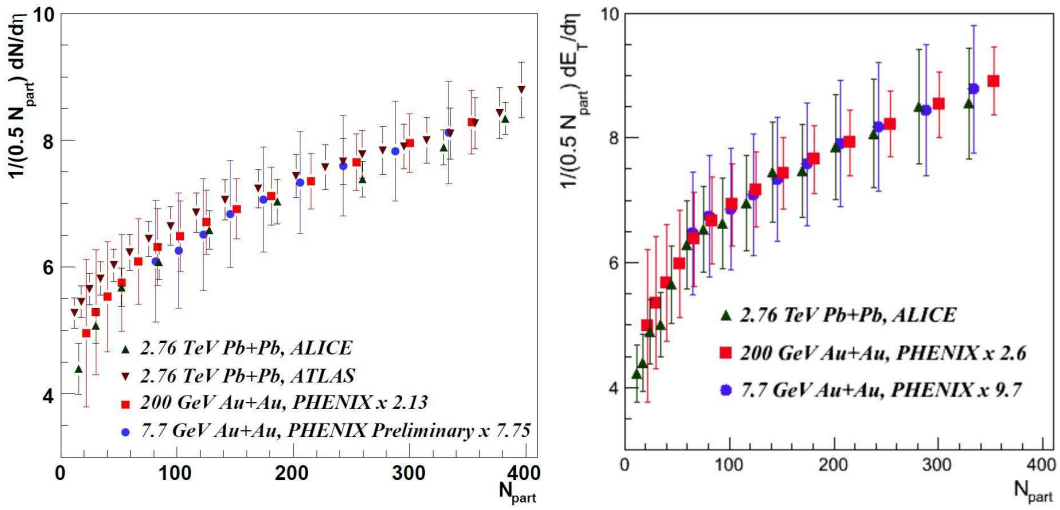

Figure 6.5: $\mathrm{d}N/\mathrm{d}\eta$ (left) and $\mathrm{dE}_T/\mathrm{d}\eta$ (right) divided by N_{part} for a wide range of centralities (characterized by N_{part}) [135]. Results from RHIC and LHC are compared. See text.

by much. If instead of counting the number of particles, we calculate the total transverse energy E_T in a particular acceptance, $\mathrm{dE}_T/\mathrm{d}\eta$ could be measured. On the right panel of the figure, measurements of $\mathrm{d}E_T/\mathrm{d}\eta$ are presented in a similar fashion as those of $\mathrm{d}N/\mathrm{d}\eta$ on the left panel.

When the beam energy is changed, one basic question is how the energy density of the created nuclear matter would change accordingly. One experimental observable that might help answer this question is the Bjorken energy density:

$$\epsilon_{Bj} \equiv \frac{1}{A_\perp \tau} \frac{\mathrm{dE}_T}{\mathrm{d}y}$$

where τ is the formation time and $A_\perp$ is the nuclei transverse overlap area estimated via Glauber-MC [136] [137]. $\frac{\mathrm{dE}_T}{\mathrm{d}y}|_{y=0}$ is obtained via multiplying $\frac{\mathrm{dE}_T}{\mathrm{d}\eta}|_{\eta=0}$ by a factor of 1.25 ± 0.05. Since the estimation of τ involves large uncertainty, the multiplicity of ϵ_{Bj} and τ is measured and shown. $\epsilon_{Bj}\tau$ measured in various centrality bins (N_{part}) for six RHIC energies are illustrated in Fig-6.6. For the most central collisions ($N_{\mathrm{part}} \sim 360$), there is a factor of $4 \sim 5$ times increase in $\epsilon_{Bj}\tau$. Since the values of τ are relatively insensitive to the collision energy, the increase mainly results from the change in mean p_T and multiplicity. Further calculations are necessary to extract the implication of this observation regarding the medium energy density.

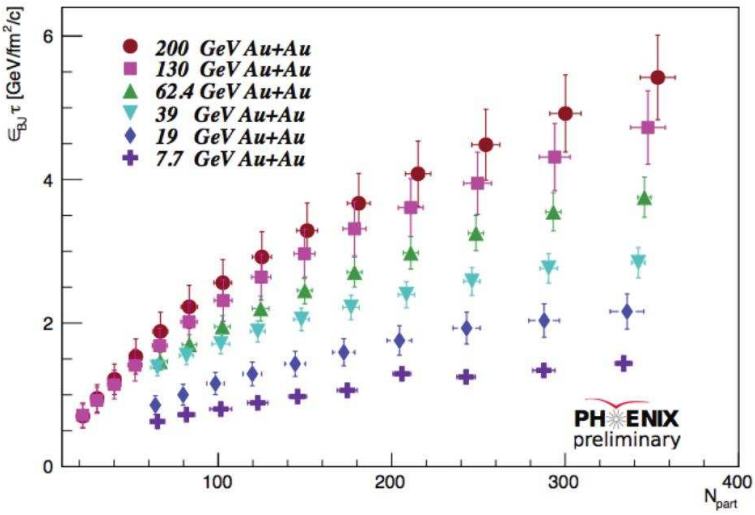

Figure 6.6: $\epsilon_{Bj}\tau$ vs. $N_{\rm part}$ for various collision energies of RHIC. Data points for 130 GeV are produced with Run1 data; those for 200 and 19 GeV are generated with Run2 data; the others are produced with Run10 data.

6.2.2 Identified Hadron v_2

By identifying particles we gain additional knowledge on them, such as their quark content. At 200 GeV, quark number scaling of v_2 was observed (cf. Sec-1.6.3), which indicates collective flow at the partonic level. At low beam energy collisions, the nuclear matter created may no long possess partonic degree of freedom, and v_2 scaling might be expected to fail.

PHENIX has measured v_2 of $\pi^{\pm}$, $K^{\pm}$ and $p(\bar{p})$ at $\sqrt{s_{NN}}$ = 62 and 39 GeV. The results are illustrated in Fig-6.7 as v_2 vs. p_T for the three particle

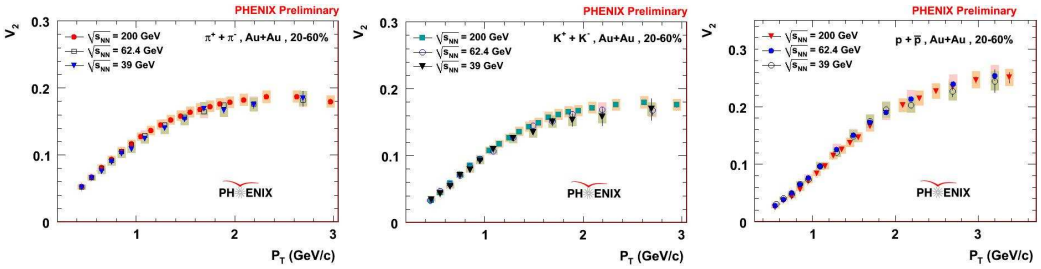

Figure 6.7: v_2 of several charge hadron species vs. p_T for $\sqrt{s_{NN}}$ = 39, 62 and 200 GeV at RHIC. Results of pion, kaon and proton are shown on the left, middle and right panel respectively.

species (on the three panels, respectively). Note that on each panel previous

results from 200 GeV collisions are included as well. As expected based on the observations of inclusive charge hadron v_2, at these three collision energies (200, 62 and 39 GeV) v_2 values are very similar for all three hadron species. Consistently, quark number scaling remains at 62 and 39 GeV, as explicitly

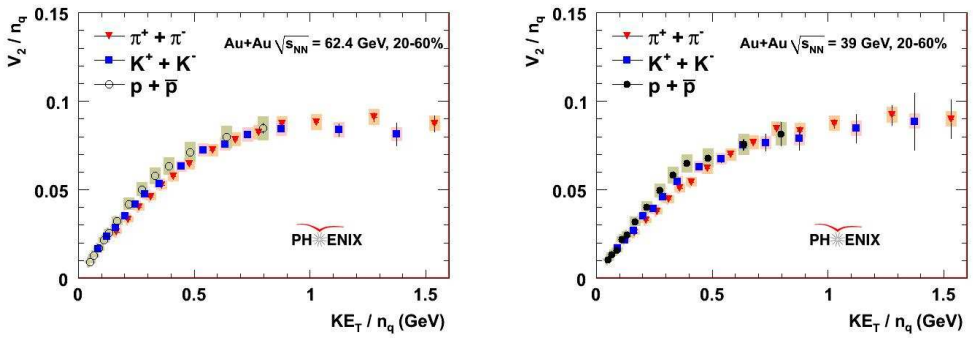

Figure 6.8: Quark number scaling of v_2 at $\sqrt{s_{NN}} = 62$ and 39 GeV, shown on the left and right panel respectively. v_2/n_q vs. KE_T/n_q curves for charge pions (red triangles), kaons (blue squares) and protons (black dots) are drawn side by side for both collision energies.

shown in Fig-6.8. We also note that in the neighboring region of $p_T \sim 0.4$ GeV, a small deviation from scaling is observed, which is especially obvious at $\sqrt{s_{NN}} = 39$ GeV. However, it's still fair to conclude that the quark number scaling holds down to 39 GeV.

STAR measured v_2 of various hadron species down to 11.5 GeV. The v_2/n_q vs. KE_T/n_q results of 39 and 11.5 GeV are illustrated in Fig-6.9. At $\sqrt{s_{NN}} =$ 39 GeV, curves representing different hadron species are roughly overlaid with each other, indicating a good scaling feature and consistent with the PHENIX measurement (cf. Fig-6.8). Whereas at $\sqrt{s_{NN}} = 11.5$ GeV, v_2 values for ϕ meson fall clearly apart from those of other hadrons. ϕ meson is known to have small hadronic interaction cross section, therefore its v_2 is mainly built up at the QGP phase, in contrast to other hadrons shown in the figure whose v_2's have greater contributions from hadronic gas phase. The smaller values of ϕ meson v_2 indicate that at 11.5 GeV the QGP phase might be less dominant in the nuclear matter evolution, compared to what's observed at higher beam energies such as 39 GeV.

6.2.3 π^0 R_{AA}

As discussed in Chapter-4, π^0's have been constructed at PHENIX for $\sqrt{s_{NN}} =$ 62 and 39 GeV. In particular, we have shown the raw π^0 spectrum in Fig-4.17.

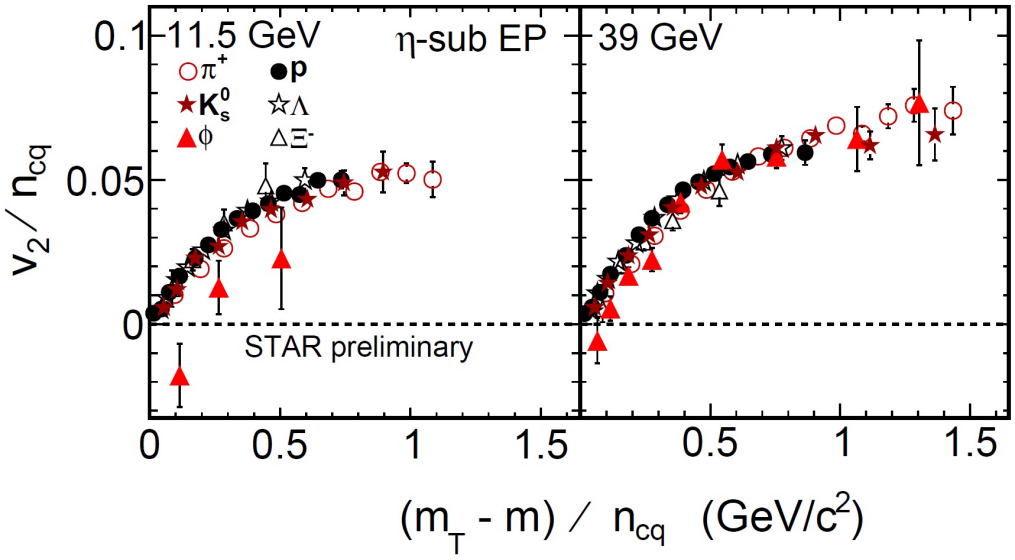

Figure 6.9: v_2/n_q vs. KE_T/n_q for several particle species at $\sqrt{s_{NN}} = 39$ (right) and 11.5 (left) GeV by STAR [138]. Note that v_2 for particles like π^- and $\bar{p}$ are not shown.

After the application of corrections mostly regarding detector efficiency and acceptance, the corrected π^0 spectrum could be obtained. When compared to the spectrum of p+p collisions at the same beam energy, the nuclear modification factors R_{AA} (cf. Eqn-1.7) are calculated.

PHENIX has measured π^0 spectrum for p+p collisions at $\sqrt{s_{NN}} = 62$ GeV with date generated in 2004 [139], which serves as a natural reference for the R_{AA} calculation at $\sqrt{s_{NN}} = 62$ GeV. So far RHIC hasn't performed any p+p collisions at $\sqrt{s_{NN}} = 39$ GeV. Therefore, results from Fermi-lab experiment E706, which effectively has collision energy of $\sqrt{s_{NN}} = 39$ GeV, are employed. Additional subtleties regarding the p+p references for both energies are discussed in [76].

π^0 R_{AA} vs. p_T results for $\sqrt{s_{NN}} = 200$ (red triangles), 62 (blue squares) and 39 (black circles) GeV are illustrated in Fig-6.10. Two centrality selections, $0-10\%$ and $40-60\%$, are shown on left and right panel respectively. p_T uncorrelated systematic errors are indicated by the color bars on the dotted baseline of unity. For each collision energy, R_{AA} values increase and then decrease with p_T, and eventually reach a plateau. This feature is well known (cf. Fig-1.19) and discussed in articles such as [140]. It's noteworthy that the p_T position of the turning point increases with $\sqrt{s_{NN}}$.

Two implementations of pQCD calculations (Vitev) are also shown for the most central bin. The solid lines of corresponding colors represent calculation

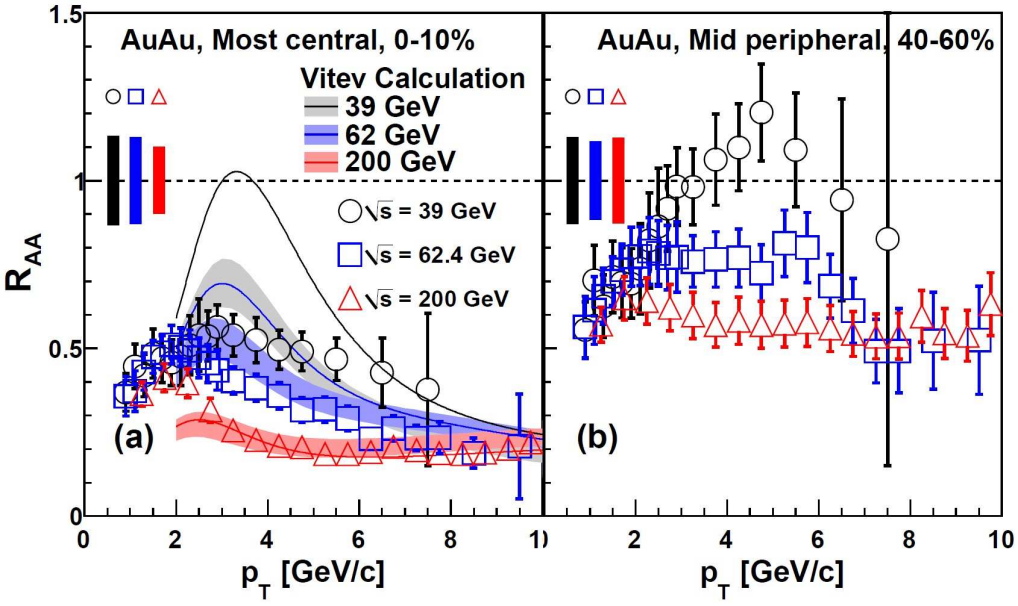

Figure 6.10: π^0 $R_{\rm AA}$ vs. p_T with model calculations [76]. See Text.

with ordinary Cronin-effect, and we could see that the results significantly over-predict $R_{\rm AA}$ for both $\sqrt{s_{NN}}$ = 62 and 39 GeV. The light-colored bands indicate calculation with Cronin-effect reduced to 1/2 of its regular size. For $\sqrt{s_{NN}}$ = 200 GeV, the reduction doesn't change the overall result much, while for $\sqrt{s_{NN}}$ = 62 GeV, the resulting $R_{\rm AA}$ band matches the data points much better. For $\sqrt{s_{NN}}$ = 39 GeV, the shape of the calculated $R_{\rm AA}$ is still not very consistent with the measurement.

For each collision energy, $N_{\rm part}$ could be simulated for each centrality bin and $R_{\rm AA}$ values of different $N_{\rm part}$ could be compared across beam energies. The results of $R_{\rm AA}$ (integrated over $p_T > 6$ GeV) for $\sqrt{s_{NN}}$ = 200, 62 and 39 GeV are re-compiled in this way and presented in Fig-6.11. For each energy, $R_{\rm AA}$ is close to unity for the most peripheral collisions, and then decreases as $N_{\rm part}$ becomes greater, which reflects the increasing size of medium created in more central collisions. The main feature is that $R_{\rm AA}$ of 200 and 62 GeV fall on the same curve, while those for 39 GeV are substantially larger, suggesting smaller suppression effect from medium on the energetic partons at $\sqrt{s_{NN}}$ = 39 GeV.

6.3 Conclusion

This dissertation study utilized dataset generated in the RHIC BES program, which is intended to probe the non-trivial μ_B region of the QCD phase diagram.

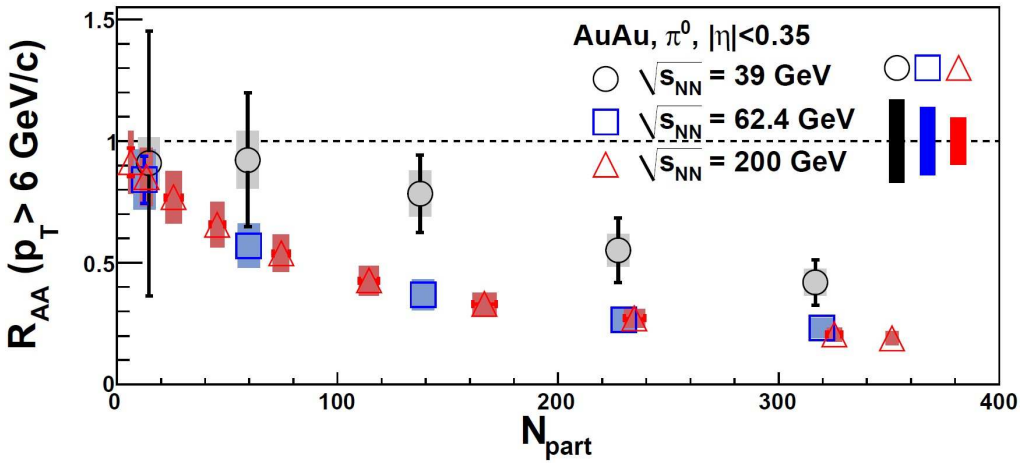

Figure 6.11: p_T integrated ($p_T > 6GeV$) π^0 $R_{\rm AA}$ vs. $N_{\rm part}$ [76]. $R_{\rm AA}$ from the three beam energies (cf. Fig-6.10) are compared side-by-side.

Inclusive charge hadron v_n were measured at $\sqrt{s_{NN}} = 62$ and 39 GeV. They are then compared to previous measurement at 200 GeV and corresponding results from other energies of the RHIC BES program. Results from LHC Pb+Pb collisions at $\sqrt{s_{NN}} = 2.76$ TeV are also incorporated for comparison. It was observed that v_n ($n = 2, 3, 4$) are essentially saturated beyond $\sqrt{s_{NN}} = 39$ GeV, which might indicate 1) the nuclear matter created in those energies have similar initial geometry profile and 2) the equation of state of nuclear matter is softened at higher beam energies. v_2 is measured for beam energies lower than 39 GeV as well, and its size exhibits a smooth decrease as $\sqrt{s_{NN}}$ becomes smaller and eventually reaches zero at AGS energy.

Because each hadron species has its own quark composition and different types of quarks have distinct behavior interacting with nuclear matter, v_n of identified hadrons could provide additional insights on the dynamic evolution of nuclear matter. Details of measurement of π^0 v_2 are discussed in this dissertation. Because π^0's are constructed from photon pairs, the analysis involves techniques different from those applied in charge particle analysis. It is found that π^0 v_2 of $\sqrt{s_{NN}} = 62$ and 39 GeV are very similar to those measured at $\sqrt{s_{NN}} = 200$ GeV, consistent with the saturation observed on inclusive charge hadrons. Though the bulk properties seem to remain largely unchanged, π^0 $R_{\rm AA}$ of 39 GeV are consistently larger than those of 62 and 200 GeV, which match within themselves very well. This observation suggests less suppression (or energy loss) of the energetic partons that traverse the medium created at $\sqrt{s_{NN}} = 39$ GeV.

v_2 results of other identified hadrons are presented as well. Saturation of v_2

down to $\sqrt{s_{NN}} = 39$ GeV for a large set of identified hadrons are observed at both STAR and PHENIX. Below 39 GeV, it's observed that ϕ meson v_2 are less than those of other particles, which might indicate that hadronic interactions become more dominant at $\sqrt{s_{NN}} = 11.5$ GeV.

Bibliography

[1] E. D. Bloom, D. H. Coward, H. DeStaebler, J. Drees, G. Miller, L. W. Mo, R. E. Taylor, M. Breidenbach, J. I. Friedman, G. C. Hartmann, et al., Phys. Rev. Lett. **23**, 930 (1969).

[2] M. Breidenbach, J. I. Friedman, H. W. Kendall, E. D. Bloom, D. H. Coward, H. DeStaebler, J. Drees, L. W. Mo, and R. E. Taylor, Phys. Rev. Lett. **23**, 935 (1969).

[3] M. Gell-Mann, Physics Letters **8**, 214 (1964), ISSN 0031-9163.

[4] G.Zweig, CERN Report p. TH.401 (1964).

[5] G.Zweig, CERN Report p. TH.412 (1964).

[6] D. J. Gross and F. Wilczek, Phys. Rev. Lett. **30**, 1343 (1973).

[7] H. D. Politzer, Phys. Rev. Lett. **30**, 1346 (1973).

[8] S. Bethke, Prog.Part.Nucl.Phys. **58**, 351 (2007), hep-ex/0606035.

[9] G. Sterman et al., Rev. Mod. Phys. **67**, 157 (1995).

[10] S. Durr, Z. Fodor, J. Frison, C. Hoelbling, R. Hoffmann, S. D. Katz, S. Krieg, T. Kurth, L. Lellouch, T. Lippert, et al., Science **322**, 1224 (2008), http://www.sciencemag.org/content/322/5905/1224.full.pdf.

[11] R. Tribble et al. (The Nuclear Science Advisory Committee) (2007).

[12] E. V. Shuryak, Physics Reports **61**, 71 (1980), ISSN 0370-1573.

[13] K. Adcox et al. (PHENIX Collaboration), Nucl.Phys. **A757**, 184 (2005), nucl-ex/0410003.

[14] F. Karsch, in: Lecture Notes in Physics **583**, 209 (2002).

[15] S. Afanasiev et al. (PHENIX Collaboration), Phys. Rev. Lett. **100**, 232301 (2008).

[16] M. P. McCumber, PhD thesis p. 13 (2009).

[17] R. J. Glauber, Phys. Rev. **100**, 242 (1955).

[18] D. Kharzeev, E. Levin, and M. Nardi, Nucl.Phys. **A730**, 448 (2004), hep-ph/0212316.

[19] D. Kharzeev and M. Nardi, Phys.Lett. **B507**, 121 (2001), nucl-th/0012025.

[20] A. Adare et al. (PHENIX Collaboration), Phys.Rev. **C81**, 034911 (2010), 0912.0244.

[21] R. J. Fries, V. Greco, and P. Sorensen, Ann.Rev.Nucl.Part.Sci. **58**, 177 (2008), 0807.4939.

[22] X.-N. Wang, Eur.Phys.J. **C43**, 223 (2005), nucl-th/0510043.

[23] S. Bass, M. Belkacem, M. Bleicher, M. Brandstetter, L. Bravina, C. Ernst, L. Gerland, M. Hofmann, S. Hofmann, J. Konopka, et al., Progress in Particle and Nuclear Physics **41**, 255 (1998), ISSN 0146-6410.

[24] M. Bleicher et al., J. Phys. **G25**, 1859 (1999), hep-ph/9909407.

[25] S. Afanasiev et al. (PHENIX Collaboration), Phys. Rev. Lett. **99**, 052301 (2007).

[26] F. Cooper and G. Frye, Phys. Rev. D **10**, 186 (1974).

[27] F. Cooper, G. Frye, and E. Schonberg, Phys. Rev. D **11**, 192 (1975).

[28] B. Alver and G. Roland, Phys. Rev. C **81**, 054905 (2010).

[29] A. Adare et al. (PHENIX Collaboration), Phys. Rev. Lett. **105**, 062301 (2010).

[30] D. Teaney, J. Lauret, and E. V. Shuryak, Phys. Rev. Lett. **86**, 4783 (2001).

[31] C. Adler et al. (STAR Collaboration), Phys. Rev. Lett. **87**, 182301 (2001).

[32] S. S. Adler et al. (PHENIX Collaboration), Phys. Rev. Lett. **91**, 182301 (2003).

[33] P. Huovinen, P. Kolb, U. W. Heinz, P. Ruuskanen, and S. Voloshin, Phys.Lett. **B503**, 58 (2001), hep-ph/0101136.

[34] U. W. Heinz, J.Phys.G **G31**, S717 (2005), nucl-th/0412094.

[35] J. M. Maldacena, Adv.Theor.Math.Phys. **2**, 231 (1998), hep-th/9711200.

[36] P. K. Kovtun, D. T. Son, and A. O. Starinets, Phys. Rev. Lett. **94**, 111601 (2005).

[37] P. Romatschke and U. Romatschke, Phys. Rev. Lett. **99**, 172301 (2007).

[38] M. Luzum and P. Romatschke, Phys. Rev. C **78**, 034915 (2008).

[39] K. Dusling and D. Teaney, Phys. Rev. C **77**, 034905 (2008).

[40] H. Song and U. Heinz, Phys. Rev. C **78**, 024902 (2008).

[41] P. Huovinen and P. Petreczky, Nucl.Phys. **A837**, 26 (2010), 0912.2541.

[42] A. Adare et al. (PHENIX Collaboration), Phys. Rev. Lett. **98**, 162301 (2007).

[43] M. Csanad, T. Csorgo, A. Ster, B. Lorstad, N. Ajitanand, et al., Eur.Phys.J. **A38**, 363 (2008), nucl-th/0512078.

[44] R. C. Hwa and C. B. Yang, Phys. Rev. C **67**, 034902 (2003).

[45] V. Greco, C. M. Ko, and P. Lévai, Phys. Rev. Lett. **90**, 202302 (2003).

[46] D. Molnár and S. A. Voloshin, Phys. Rev. Lett. **91**, 092301 (2003).

[47] B. Bonner, H. Chen, G. Eppley, F. Geurts, J. Lamas-Valverde, C. Li, W. Llope, T. Nussbaum, E. Platner, and J. Roberts, Nuclear Instruments and Methods in Physics Research Section A: Accelerators, Spectrometers, Detectors and Associated Equipment **508**, 181 (2003), ISSN 0168-9002.

[48] W. Llope, T. Nussbaum, G. Eppley, J. Velkovska, T. Chujo, S. Huang, B. Love, H. Valle, L. Ruan, Z. Xu, et al., Nuclear Instruments and Methods in Physics Research Section A: Accelerators, Spectrometers, Detectors and Associated Equipment **596**, 430 (2008), ISSN 0168-9002.

[49] A. Adare et al. (PHENIX Collaboration) (2012), 1203.2644.

[50] A. Adare et al. (PHENIX Collaboration), Phys. Rev. Lett. **107**, 252301 (2011).

[51] G. Aad et al. (ATLAS Collaboration) (2012), 1203.3087.

[52] K. Aamodt et al. (ALICE Collaboration), Phys. Rev. Lett. **107**, 032301 (2011).

[53] J. Velkovska and C. collaboration, Journal of Physics G: Nuclear and Particle Physics **38**, 124011 (2011).

[54] M. Gyulassy, I. Vitev, and X.-N. Wang, Phys. Rev. Lett. **86**, 2537 (2001).

[55] B. Betz, M. Gyulassy, and G. Torrieri, Phys. Rev. C **84**, 024913 (2011).

[56] A. Adare et al. (PHENIX Collaboration), Phys. Rev. C **78**, 014901 (2008).

[57] K. Adcox et al. (PHENIX Collaboration), Phys. Rev. Lett. **89**, 212301 (2002).

[58] N. Borghini, P. M. Dinh, and J.-Y. Ollitrault, Phys. Rev. C **62**, 034902 (2000).

[59] N. Borghini, P. M. Dinh, J.-Y. Ollitrault, A. M. Poskanzer, and S. A. Voloshin, Phys. Rev. C **66**, 014901 (2002).

[60] G. Aad et al. (ATLAS Collaboration), Phys. Rev. Lett. **105**, 252303 (2010).

[61] S. Chatrchyan et al. (CMS Collaboration), Phys. Rev. C **84**, 024906 (2011).

[62] Y. S. Lai, PhD thesis (2011).

[63] H. Caines (the STAR Collaboration), J.Phys.G **G38**, 124019 (2011), 1106.6247.

[64] N. N. Ajitanand, J. M. Alexander, P. Chung, W. G. Holzmann, M. Issah, R. A. Lacey, A. Shevel, A. Taranenko, and P. Danielewicz, Phys. Rev. C **72**, 011902 (2005).

[65] A. Sickles, M. P. McCumber, and A. Adare, Phys. Rev. C **81**, 014908 (2010).

[66] J. Adams et al. (STAR Collaboration), Phys. Rev. Lett. **91**, 072304 (2003).

[67] S. S. Adler et al. (PHENIX Collaboration), Phys. Rev. Lett. **97**, 052301 (2006).

[68] A. Adare et al. (PHENIX Collaboration), Phys. Rev. Lett. **104**, 252301 (2010).

[69] M. L. Purschke and the PHENIX Collaboration, Journal of Physics G: Nuclear and Particle Physics **38**, 124016 (2011).

[70] A. Adare et al. (PHENIX Collaboration), Phys. Rev. C **82**, 011902 (2010).

[71] A. Adare et al. (PHENIX Collaboration), Phys. Rev. C **83**, 024909 (2011).

[72] A. Adare et al. (PHENIX Collaboration), Phys. Rev. C **83**, 064903 (2011).

[73] A. Adare et al. (PHENIX Collaboration), Phys. Rev. C **84**, 044902 (2011).

[74] A. Adare et al. (PHENIX Collaboration), Phys. Rev. Lett. **101**, 162301 (2008).

[75] S. S. Adler et al. (PHENIX Collaboration), Phys. Rev. Lett. **98**, 172302 (2007).

[76] A. Adare et al. (PHENIX Collaboration) (2012), 1204.1526.

[77] A. Majumder and M. van Leeuwen, Progress in Particle and Nuclear Physics **66**, 41 (2011), ISSN 0146-6410.

[78] T. Renk, J. Ruppert, C. Nonaka, and S. A. Bass, Phys. Rev. C **75**, 031902 (2007).

[79] A. Majumder, C. Nonaka, and S. A. Bass, Phys. Rev. C **76**, 041902 (2007).

[80] G.-Y. Qin, J. Ruppert, S. Turbide, C. Gale, C. Nonaka, and S. A. Bass, Phys. Rev. C **76**, 064907 (2007).

[81] S. A. Bass, C. Gale, A. Majumder, C. Nonaka, G.-Y. Qin, T. Renk, and J. Ruppert, Phys. Rev. C **79**, 024901 (2009).

[82] S. S. Gubser, D. R. Gulotta, S. S. Pufu, and F. D. Rocha, Journal of High Energy Physics **2008**, 052 (2008).

[83] F. Dominguez, C. Marquet, A. Mueller, B. Wu, and B.-W. Xiao, Nuclear Physics A **811**, 197 (2008), ISSN 0375-9474.

[84] A. Adare et al. (PHENIX Collaboration), Phys. Rev. Lett. **98**, 172301 (2006).

[85] S. Afanasiev et al. (PHENIX Collaboration), Phys. Rev. C **80**, 054907 (2009).

[86] R. A. Lacey, N. N. Ajitanand, J. M. Alexander, X. Gong, J. Jia, A. Taranenko, and R. Wei, Phys. Rev. C **80**, 051901 (2009).

[87] A. Adare et al. (PHENIX Collaboration), Phys. Rev. Lett. **105**, 142301 (2010).

[88] S. Wicks, W. Horowitz, M. Djordjevic, and M. Gyulassy, Nuclear Physics A **784**, 426 (2007), ISSN 0375-9474.

[89] C. Marquet and T. Renk, Physics Letters B **685**, 270 (2010), ISSN 0370-2693.

[90] J. Jia and R. Wei, Phys. Rev. C **82**, 024902 (2010).

[91] K. Adcox et al. (PHENIX), Nucl. Instrum. Meth. **A499**, 469 (2003).

[92] M. Chiu (PHENIX Collaboration), AIP Conf.Proc. **915**, 539 (2007), nucl-ex/0701031.

[93] E. Richardson et al. (PHENIX), Nucl. Instrum. Meth. **A636**, 99 (2011), 1012.0873.

[94] W. Anderson et al. (PHENIX) (2011), arXiv/1103.4277.

[95] K. Adcox et al. (PHENIX), Nucl. Instrum. Meth. **A499**, 489 (2003).

[96] M. Aizawa et al. (PHENIX), Nucl. Instrum. Meth. **A499**, 508 (2003).

[97] L. Aphecetche et al. (PHENIX), Nucl. Instrum. Meth. **A499**, 521 (2003).

[98] S. H. Aronson et al. (PHENIX), Nucl. Instrum. Meth. **A499**, 480 (2003).

[99] H. Akikawa et al. (PHENIX), Nucl. Instrum. Meth. **A499**, 537 (2003).

[100] M. Allen et al. (PHENIX), Nucl. Instrum. Meth. **A499**, 549 (2003).

[101] C. Adler, A. Denisov, E. Garcia, M. Murray, H. Stroebele, and S. White, Nuclear Instruments and Methods in Physics Research Section A: Accelerators, Spectrometers, Detectors and Associated Equipment **470**, 488 (2001), ISSN 0168-9002.

[102] PHENIX (PHENIX), Systems Engineering and Integration (1995).

[103] A. Milov, PHENIX Analysis Note **461** (2005).

[104] I. Selyuzhenkov and S. Voloshin, Phys. Rev. C **77**, 034904 (2008).

[105] J. Koster, PhD thesis p. 38 (2010).

[106] M. Ippolitov et al., Nuclear Instruments and Methods in Physics Research Section A: Accelerators, Spectrometers, Detectors and Associated Equipment **486**, 121 (2002), ISSN 0168-9002.

[107] D. Ben-Tzvi and M. B. Sandler, Pattern Recognition Letters **11**, 167 (1990).

[108] S. C. Johnson et al., Proceedings of Computing in High Energy and Nuclear Physics (CHEP) (1998).

[109] L. Carlen et al., Nuclear Instruments and Methods in Physics Research Section A: Accelerators, Spectrometers, Detectors and Associated Equipment **396**, 310 (1997), ISSN 0168-9002.

[110] P. B. Nilsson et al., Nuclear Physics A **661**, 665 (1999), ISSN 0375-9474.

[111] A. Milov, PhD thesis p. 30 (2002).

[112] S. S. Adler et al. (PHENIX Collaboration), Phys. Rev. C **69**, 034909 (2004).

[113] G. David et al., IEEE Trans. Nucl. Sci. **47**, 1982 (2000).

[114] A. Bazilevsky (PHENIX), Internal Presentation (1999).

[115] S. S. Adler et al. (PHENIX), Nucl. Instrum. Meth. **A499**, 560 (2003).

[116] S. S. Adler et al. (PHENIX), Nucl. Instrum. Meth. **A499**, 593 (2003).

[117] D. Reynolds et al., PHENIX Analysis Note **947** (2010).

[118] K. Reygers, PHENIX Analysis Note **169** (2003).

[119] S. Mohapatra et al., PHENIX Analysis Note **924** (2010).

[120] A. M. Poskanzer and S. A. Voloshin, Phys. Rev. C **58**, 1671 (1998).

[121] J.-Y. Ollitrault (1997), nucl-ex/9711003.

[122] W. Holzmann et al., PHENIX Analysis Note **803** (2009).

[123] J. Lukasik and W. Trautmann (2006), nucl-ex/0603028.

[124] K. Nakamura and P. D. Group, Journal of Physics G: Nuclear and Particle Physics **37**, 075021 (2010).

[125] Y. Aramaki and D. Gabor, PHENIX Analysis Note **906** (2010).

[126] N. Novitzky et al., PHENIX Analysis Note **945** (2012).

[127] R. Wei et al., PHENIX Analysis Note **787** (2009).

[128] A. Morreale, PHENIX Analysis Note **622** (2009).

[129] S. Esumi, PHENIX Analysis Note **958** (2011).

[130] A. Taranenko, PHENIX Analysis Note **957** (2011).

[131] S. Huang, Winter Workshop on Nuclear Dynamcis (2011).

[132] S. Shi (STAR collaboration), Acta Phys.Polon.Supp. **5**, 311 (2012), 1111.5385.

[133] K. Aamodt et al. (ALICE Collaboration), Phys. Rev. Lett. **105**, 252302 (2010).

[134] P. Chung et al. (E895 Collaboration), Phys.Rev. **C66**, 021901 (2002), nucl-ex/0112002.

[135] J. Mitchell, Workshop on Fluctuations, Correlations and RHIC Low Energy Runs (2011).

[136] J. D. Bjorken, Phys. Rev. D **27**, 140 (1983).

[137] S. S. Adler et al. (PHENIX Collaboration), Phys. Rev. C **71**, 034908 (2005).

[138] S. Shi (STAR collaboration) (2012), 1201.3959.

[139] A. Adare et al. (PHENIX Collaboration), Phys.Rev. **D79**, 012003 (2009), 0810.0701.

[140] A. Adare et al. (PHENIX Collaboration), Phys. Rev. Lett. **101**, 232301 (2008).